uOttawa

L'Université canadienne
Canada's university

FACULTÉ DES ÉTUDES SUPÉRIEURES ET POSTDOCTORALES

uOttawa

L'Université canadienne
Canada's university

FACULTY OF GRADUATE AND POSTDOCTORAL STUDIES

Pauline Favero
AUTEUR DE LA THÈSE / AUTHOR OF THESIS

M.Sc. (Geography)
GRADE / DEGREE

Department of Geography
FACULTÉ, ÉCOLE, DÉPARTEMENT / FACULTY, SCHOOL, DEPARTMENT

Active Layer Detachment Morphology, Sedimentology and Mechanisms, Fosheim Peninsula, Ellesmere Island

TITRE DE LA THÈSE / TITLE OF THESIS

A. Lewkowicz
DIRECTEUR (DIRECTRICE) DE LA THÈSE / THESIS SUPERVISOR

CO-DIRECTEUR (CO-DIRECTRICE) DE LA THÈSE / THESIS CO-SUPERVISOR

EXAMINATEURS (EXAMINATRICES) DE LA THÈSE / THESIS EXAMINERS

L. Copland

A. Johnson

Gary W. Slater
Le Doyen de la Faculté des études supérieures et postdoctorales / Dean of the Faculty of Graduate and Postdoctoral Studies

Active Layer Detachment Morphology, Sedimentology, and Mechanisms, Fosheim Peninsula, Ellesmere Island

Pauline Favero

Thesis submitted to the
Faculty of Graduate and Postdoctoral Studies
In partial fulfillment of the requirements
For the MSc degree in Geography

Department of Geography
Faculty of Arts
University of Ottawa

Your file Votre référence
ISBN: 978-0-494-58209-1
Our file Notre référence
ISBN: 978-0-494-58209-1

ABSTRACT

Active layer detachments on the Fosheim Peninsula have been assumed to develop over periods of minutes to a few hours. This assumption played an integral role in the understanding of relationships between active layer detachment deposit morphology, morphometry and sedimentology and active layer detachment dynamics. Field observations of two failures at 'Big Slide Creek' on the Fosheim Peninsula in August 2005 showed that while one failure conformed to the pre-existing assumption of near-instantaneous formation, movement and cessation of movement, the other failure did not and exhibited progressive expansion over several days. Several active layer detachments known to have initiated in 2005 were visited in 2006 to assess whether active layer detachments known to have failed via a prolonged mode display surficial and internal morphological characteristics that are unique from active layer detachments known to have failed via a near-instantaneous mode and to evaluate the ability of the infinite slope model to adequately predict slope stability.

Results have indicated that active layer detachments known to have failed via a prolonged mode display a number of surficial and internal morphological characteristics that differ from those at active layer detachments known to have failed via a near-instantaneous mode. Based on Factor of Safety calculations, peak effective stress stability analysis indicates that Fosheim Peninsula slopes should be stable if pore-water pressures are not artesian, whereas residual effective stress stability analysis indicates that slopes greater than 6° on the Fosheim Peninsula are unstable even if pore water pressures are not artesian. Sensitivity analyses indicates that under peak conditions, Factors of Safety on Fosheim Peninsula slopes are most sensitive to changes in cohesion while under residual conditions, slope instability is related to increases in both slope angle and head of water above the slip plane.

ACKNOWLEDGMENTS

Thank-you to Dr. Antoni Lewkowicz for his patience and support throughout this thesis. Thank-you to the University of Ottawa and the Northern Scientific Training Program, Department of Indian Affairs and Northern Development for funding support as well as NSERC (through A. Lewkowicz). Thank-you to the Polar Continental Shelf Project, Natural Resources Canada (PCSP Contribution No. 030-09) for logistical support. Dr. Sai Vannipalli graciously provided geotechnical advice and allowed me the use of the Civil Engineering Department's Direct Shear Apparatus for the analysis of geotechnical parameters.

I wish to thank my family and Paul for encouragement and support throughout this endeavour. I could not have done it without you.

TABLE OF CONTENTS

LIST OF FIGURES

LIST OF TABLES

LIST OF SYMBOLS

Symbol	Unit	Description
ρ	g/cm^3	Bulk density
c	kPa	Cohesion
z	m	Depth to slip surface
l	m	Distance between two ends of failure block
c'	kPa	Effective cohesion
ϕ'	degrees	Effective internal angle of friction
σ'_n	kPa	Effective normal stress
σ'	kPa	Effective stress
Fs	unitless	Factor of Safety
g	m/s	Gravitational stress/acceleration (9.81 m/s)
D_w	m	Head of water above slide plane
ϕ	degrees	Internal angle of friction
LOI	%	Loss on ignition
LL	%	Liquid limit
ω	%	Moisture content
P/N	kPa	Normal load/force
σ_n	kPa	Normal stress
PL	%	Plastic limit
PI	%	Plasticity index
μ	kPa	Pore-water pressure
T/S	kN/m	Shear load/force
τ	kPa	Shear strength
β	degrees	Slope angle
A	m^2	Total area
c_u	kPa	Undrained shear strength
γ	kN/m^3	Unit weight of soil
γ_w	kN/m^3	Unit weight of water
m	unitless	Vertical height of water above slip surface
W	kN/m	Weight of failure block

M	g	Wet soil mass
V	cm^3	Wet soil volume

1 INTRODUCTION

1.1 Context of the Present Research

The most common type of landslide in northern regions is the active layer detachment (Dyke 2004). Active layer detachment morphology, morphometry and dynamics have been characterized at many locations in the Arctic and sub-Arctic, spanning a range of latitudinal locations and permafrost conditions (i.e. continuous or discontinuous). Active layer detachments are commonly classified based on morphology (compact, elongate or complex; see Lewkowicz and Harris 2005b). Assessments of failure history (instantaneous vs. prolonged) and dynamics (translational vs. compressional) have been based on description of the sedimentology of failure deposits (i.e. Mathewson and Mayer-Cole 1984; Lewkowicz 1990; Lewkowicz and Harris 2005b) and field observations (Lewkowicz 2007). These characterizations and assessments have led researchers to suggest relationships between the morphology, morphometry, and sedimentology of the active layer detachment deposit and the dynamics of the active layer detachment.

1.2 Statement of the Problem

Active layer detachments on the Fosheim Peninsula, although never observed in motion until recently, had been assumed to develop over periods of minutes to a few hours (Lewkowicz 2007). This assumption played an integral role in the understanding of relationships between active layer detachment deposit morphology, morphometry and sedimentology and active layer detachment dynamics (i.e. Mathewson and Mayer-Cole 1984; Lewkowicz 1990; Lewkowicz and Harris 2005b). However, field observations of two failures at 'Big Slide Creek' on the Fosheim Peninsula in August 2005 showed that while one failure conformed to the pre-existing assumption of near-instantaneous

formation, movement and cessation of movement, the other failure did not and exhibited progressive expansion over several days (Lewkowicz 2007).

Considering this new-found knowledge, an opportunity existed to return to the previously witnessed active layer detachments to either confirm or refute previous inferences between deposit morphology, morphometry and sedimentology and active layer detachment dynamics.

1.3 Research Objectives

The above-mentioned opportunity led to the following research objectives:

1. Assess whether in plan-form, active layer detachments known to have failed via a prolonged mode and those known to have failed in a near-instantaneous mode display unique sets of morphological characteristics.
2. Assess whether in section, the macro- and micro-structure of failures known to have failed via a prolonged mode differ from those failures known to have failed in a near-instantaneous mode.
3. Evaluate the ability of the infinite slope model to adequately predict slope stability by back-calculating the slope factor of safety using measured geotechnical properties and by providing a sensitivity analysis.

1.4 Active Layer Detachment Background

1.4.1 Definition

Material involved in active layer detachments is restricted to the active layer and involves detachment and downslope movement, primarily by sliding but sometimes including flow (Lewkowicz and Harris 2005a, 2005b), of an intact unfrozen soil mass and vegetation mat (Figure 1-1; Aylsworth et al. 2000). The frost table or the permafrost table acts as a lubricating slip plane and controls the depth of the failure (French 1988).

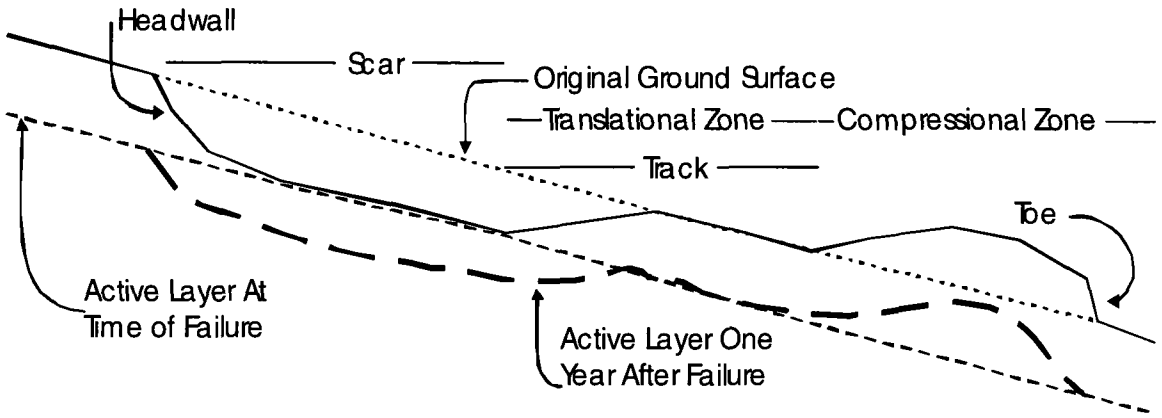

Figure 1-1. Idealized profile sketch of an active layer detachment. Note that not all active layer detachments exhibit a compressional zone with a thickened toe. Lengths range from approximately 30 m to over 600 m; depths/heights range from approximately 0.3 m to 1.0 m.

The term active layer detachment was first defined by Lewkowicz (1990) in response to the confusion surrounding the numerous terms used to describe the associated mass movement processes. Terminology used to describe similar slope processes included skin flow, active layer slope failure, earth flow, active layer glide, block glide, detachment failure, and active layer detachment slide (Lewkowicz 1988). Lewkowicz (1990) coined the term, active layer detachment, separating it from the above-mentioned terms by stipulating the slope process to be rapid, comprised of an intact mass of material, and not necessarily saturated.

1.4.2 Geographic Occurrence

Active layer detachments have been observed in the boreal forest zone of the Mackenzie River Valley (e.g. Mackay and Mathews 1973; McRoberts and Morgenstern 1973, 1974; Aylsworth et al., 2000; Dyke, 2000), the boreal forests of the Yukon (e.g. Huscroft et al. 2004; Lipovsky et al. 2006; Coates 2008), in the Alaskan tundra (e.g., Carter and Galloway 1981), in the Canadian Arctic Archipelago on Banks, Ellesmere and Melville Islands (e.g. Stangl et al. 1982; Cogley and McCann 1976; Edlund et al. 1989; Lewkowicz 1990, 1992; Harris and Lewkowicz 1993a, 1993b; Lamoureux and Lafrenière 2009) and in parts of Siberia (Leibman 1995; Leibman and Egorov 1996; Leibman et al.

2003). These locations encompass both Arctic and sub-Arctic regions, and permafrost conditions ranging from discontinuous in the Yukon to continuous in the High Arctic.

1.4.3 Triggers

Active layer detachments are triggered by an event or condition which permits rapid thawing of an ice-rich zone at the base of the active layer or within the top of permafrost (Harris and Lewkowicz 2000; Dyke 2004). The numerous triggers include high air temperatures (e.g. Edlund et al. 1989), summer rainfall events (e.g. Carter and Galloway 1981; Cogley and McCann 1976), rapid melting of an upslope snowbank (e.g. Mathewson and Mayer-Cole 1984), accumulated bright hours of sunshine (Lewkowicz and Harris 2005b), and surface disturbances such as fire (e.g. Mackay and Mathews 1973; Harry and MacInnes 1988; Savigny et al. 1995).

Prolonged periods of high summer air temperature lead to rapid thawing of the active layer triggering active layer detachments (Edlund et al. 1989; Harris and Lewkowicz 1993a; Lewkowicz and Harris 2005a, 2005b). Rapid thaw rates and progression of the thaw front into an ice-rich zone at the base of the active layer promote positive pore-water pressures (Harris and Lewkowicz 1993a). As a result, basal effective stress is reduced, creating a plane of low frictional strength upon which shallow downslope movement may occur (Harris and Lewkowicz 1993a).

High summer rainfall not only leads to the initiation of failures due to increased soil moisture contents and positive pore-water pressures but it also may lead to failure through strong ice lens development in the winter preceding failures (e.g. Lewkowicz and Harris 2005a, 2005b). For instance, water infiltrated to the base of the active layer from a late summer rainfall event may not drain completely prior to freeze-up allowing strong ice lens development. These ice lenses precondition the slope for failure the following summer when positive pore-water pressures develop during thaw of the lenses.

1.4.4 Frequency

The frequency of active layer detachments is difficult to determine with certainty because their initiation does not only depend on meteorological or environmental (e.g. surface disturbance due to fire) triggers but also conditions within the slope (Lewkowicz and Harris 2005a). For instance, redistribution of moisture within the active layer due to freezing and thawing (Lewkowicz and Harris 2005a) could lead to the development of an ice rich zone at the base of the active layer leading to high pore-water pressure upon thaw and an increased likelihood of failure. Solifluction is a second source of uncertainty since it can result in an unknown amount of shear strength reduction (Lewkowicz and Harris 2005a).

1.4.5 Morphology and Suggested Failure History

Active layer detachments are characteristically shallow and are commonly classified as either compact or elongate, but intermediate and complex forms occasionally develop (Figure 1-2; Lewkowicz and Harris 2005a). Landslide morphology is independent of latitudinal location and permafrost conditions (i.e. continuous or discontinuous) since a full range of morphological types has been observed at many latitudes (Lewkowicz and Harris 2005a). Active layer detachments most commonly occur on moderate slopes (10 – 25°), but failures on slopes as low as 3° have been recorded (Dyke 2000). Failures can develop on footslope, midslope or crestslope segments or can extend from the crestslope to the valley bottom (Lewkowicz and Harris 2005a). Active layer detachments reach widths of 50 m and lengths of 600 m, with failure depths up to 2 m (French 1996; Carter and Galloway 1981; Lewkowicz 1988).

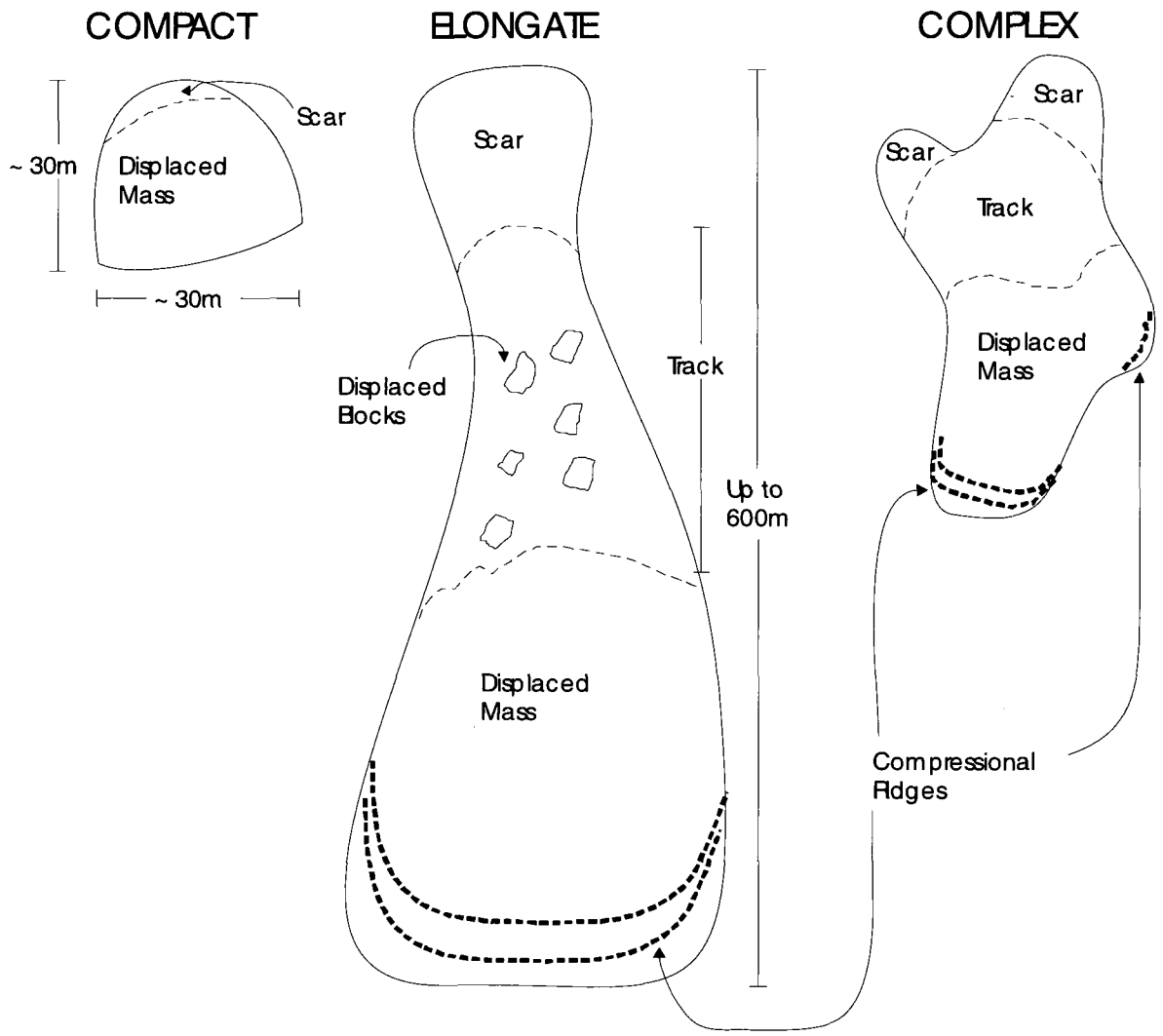

Figure 1-2. Idealized plan sketch of compact, elongate and complex active layer detachment morphologies.

1.4.5.1 Compact Morphology

Compact active layer detachments are typically bell-shaped with a curved scar headwall and a fairly straight edge running across the downslope part of the toe (Figure 1-3; Lewkowicz and Harris 2005b). The compact form is generally small (<30 m wide or long) and develops on convex slope segments where little resistance is offered to run-out (Lewkowicz and Harris 2005a). Lateral compression ridges are low to nonexistent, and sliding distances are often only a few meters, resulting in minimal internal deformation of the displaced mass (Lewkowicz and Harris 2005b). The failure history of compact active layer detachments likely involves an initial downslope movement of a major

block, potentially followed by progressive failure of upslope unsupported blocks (Lewkowicz and Harris 2005b).

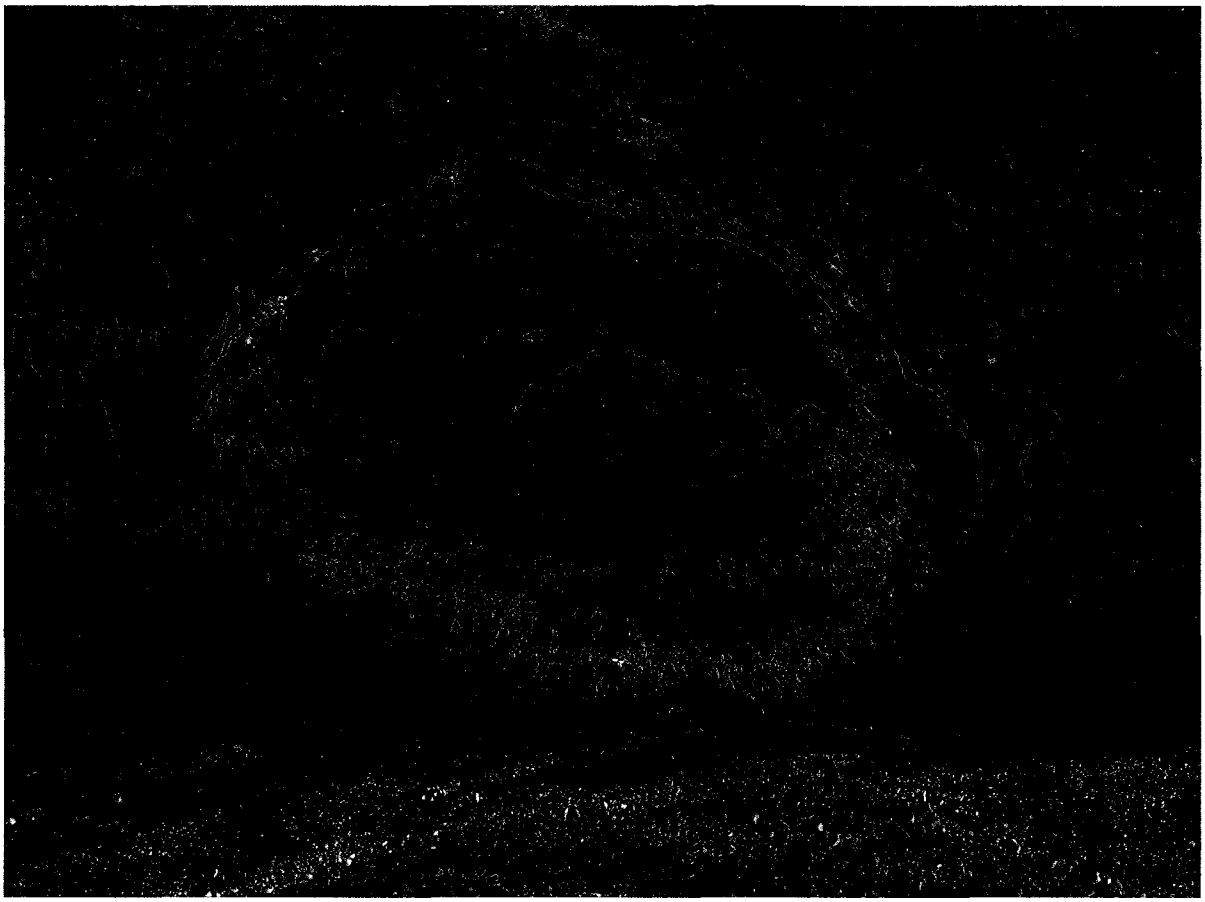

Figure 1-3. Example of a 15 m wide compact active layer detachment running from crest-slope to valley bottom. Photo taken at Black Top Creek in July 2006 of a failure inferred to have occurred in 2005.

1.4.5.2 Elongate Morphology

Elongated active layer detachments generally have trapezoidal or hour-glass shapes (Figure 1-4; Lewkowicz and Harris 2005b). Elongate failures may develop anywhere on the slope and sometimes extend from crest to valley bottom (Lewkowicz and Harris 2005b). Scar zones and tracks are bare or contain individual displaced blocks, and sediments in the toe zones may be severely deformed, suggestive of higher velocities and greater inertia during failure (Harris and Lewkowicz 2000; Lewkowicz and Harris 2005b). The failure history of elongated active layer detachments has been suggested to

involve either (1) failure initiation near the base of the slope with progressive failure of upslope unsupported blocks, or (2) failure initiation on the steeper upper part of the slope with displaced blocks progressively overloading the slope below (e.g. Mathewson and Mayer-Cole 1984; Lewkowicz and Harris 2005b).

Figure 1-4. Example of an elongate active layer detachment (approximately 20 m wide) running from crest-slope to valley bottom. Photo taken at "Big Slide Creek" in July 2006 of a failure inferred to have occurred in 2005.

1.4.5.3 Complex Morphology

A small percentage of active layer detachments have complex morphologies and cannot be classified as either compact or elongate (Figure 1-5; Lewkowicz and Harris 2005b). Complex forms may display more than one scar zone and conjoined toes forming broad sheets (Lewkowicz and Harris 2005b). In terms of failure history, complex forms may be representative of multiple failure events, some occurring within a

few minutes or hours of each other, whereas for others several days or even weeks may separate events (Lewkowicz and Harris 2005b).

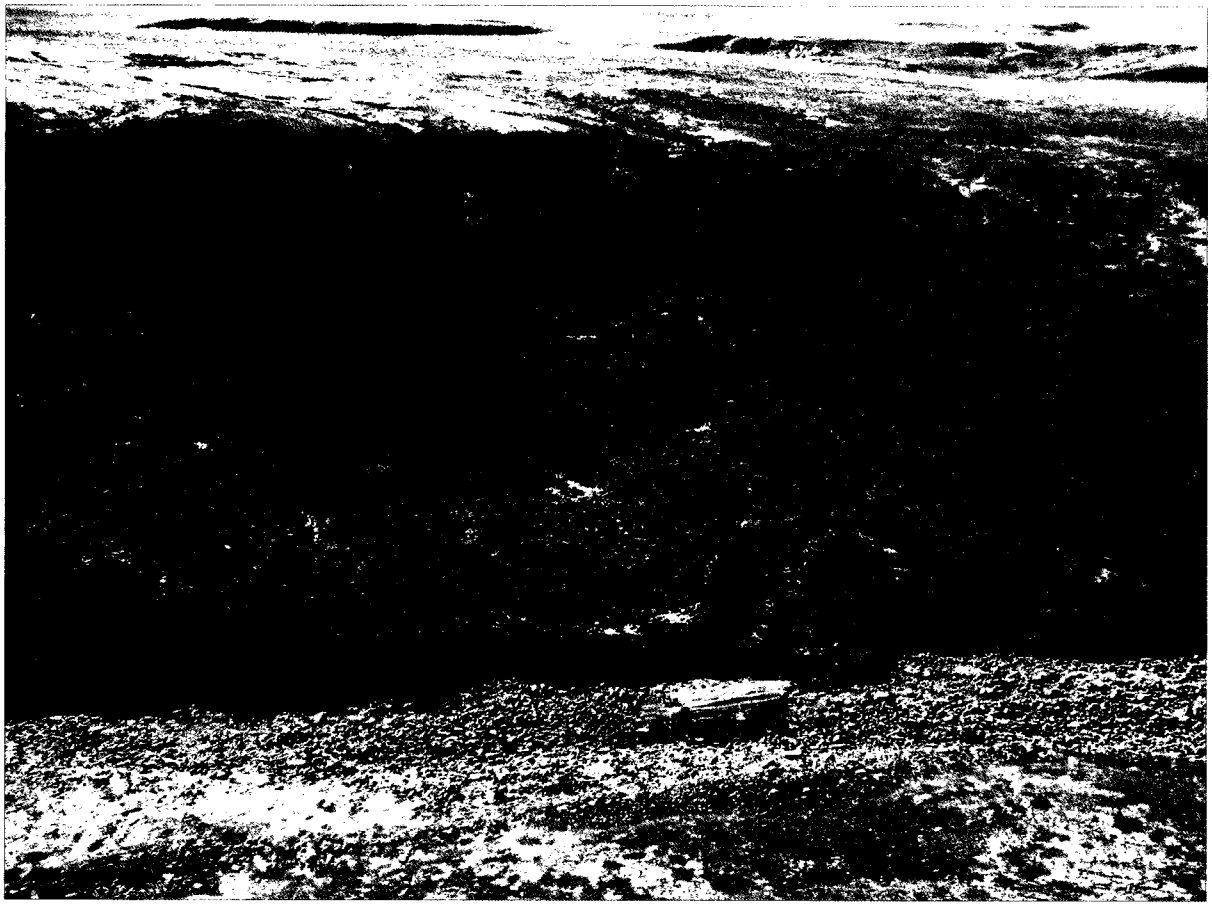

Figure 1-5. Example of a complex active layer detachment running from mid-slope to valley bottom. This failure is comprised of two to three tongues with another small failure to the right. The width of the two conjoined active layer detachments in the centre of the photo is approximately 30 m. Photo taken at Hot Weather Creek in July 2006 of a failure inferred to have occurred in 2005.

1.4.6 Slope Stability Analysis

A mass movement occurs due to a net imbalance between the forces tending to cause downslope movement and the shear strength resisting that movement (McRoberts and Morgenstern 1974). Analyses of slope stability have historically been performed using a deterministic method that makes use of the Limit Equilibrium theory to derive the Factor of Safety for the slope. The Factor of Safety is defined as the ratio between

resisting forces and those forces inducing movement. When the Factor of Safety approaches unity, failure is assumed to be imminent.

In deterministic methods, the Factor of Safety is derived by assuming that the variables involved are represented with certainty by a single value (El Ramly 2001). As a result, the variability of the factors governing slope stability is not accounted for. Employment of probabilistic methods and the concept of Probability of Failure are necessary to account for factor variability.

1.4.6.1 Limit Equilibrium Methods

Several methods of stability analysis have been developed which differ in the statics employed to derive the equation for the Factor of Safety and the assumptions adopted to solve the indeterminacy of the problem. In general, all methods use the Mohr-Coulomb failure criterion, given by the following equations (Selby 1993):

[1] $\tau = c_u$ (for total stress analysis);

[2] $\tau = c + \sigma_n \tan\phi$; and

[3] $\tau = c' + \sigma_n' \tan\phi'$ (for effective stress analysis);

where τ is shear strength (kPa); c_u is undrained shear strength (kPa); c is cohesion (kPa); c' is effective cohesion (kPa), as reduced by loss of surface tension; σ_n is normal stress (kPa); σ_n' is effective normal stress (kPa), which depends on the weight of the material (i.e. the normal stress (σ_n), and the pressure of water (μ; kPa) in the soil pores); ϕ is the angle of friction (degrees); and ϕ' is the angle of friction with respect to effective stresses (in degrees).

Hutchinson (1974) argued that where the rate of thaw was sufficiently rapid relative to the rate of drainage, resulting shear strengths are low and the active layer may slide under conditions approximating undrained. Under undrained or saturated conditions, soil strength is decreased because apparent cohesion is lost due to a reduction

in surface tension forces (Selby 1993). As a result, the shear strength must be calculated with effective stresses.

Stress is defined as force per unit area (Duncan and Wright 2005). Total stress (σ; kPa) is the sum of all forces, those transmitted through inter-particle contacts and those transmitted through water pressures, divided by the total area (Duncan and Wright 2005). Effective stress (σ'; kPa) includes only the forces that are transmitted through particle contacts (Duncan and Wright 2005). Effective stress cannot be measured directly but can be determined indirectly by finding the total normal stress (σ_n) and pore-water pressure (μ):

[4] $$\sigma' = \sigma_n - \mu$$

Total normal stress, or total force per unit area acting perpendicular to a plane, is defined as:

[5] $$\sigma_n = \frac{P}{A}$$

P (kN) represents the force normal to a plane that is applied over the area of the plane (A; m^2). By assuming point contact between particles, pore-water pressure will act over the entire area, A, of the plane (Bishop and Blight 1962). Consequently, Equation [3] is used for saturated conditions.

Pore-water pressure can be calculated from the following equation:

[6] $$\mu = \gamma_w m z \cos^2 \beta$$ (Selby 1993)

where γ_w is the unit weight of water (kN/m^3), m (unitless) is the vertical height of the water-table above the slide plane as a fraction of the soil thickness above the plane (Selby 1993; $m = 1.0$ if the water-table is at the ground surface and $m = 0$ if the water-table is just below the slide plane), z is the vertical depth to the slide plane (m), and β is the slope angle.

Pore-water pressure is considered neutral because it has normal stresses that act equally in all directions and no shear component (Holtz and Kovacs 1981). In contrast,

total and effective stresses can have both normal and shear components (Holtz and Kovacs 1981).

1.4.6.1.1 Significance of Cohesion

Cohesion represents the attraction between soil particles through direct bonding or due to water in small capillaries holding soil particles together under negative pore-water pressures (Holtz and Kovacs 1981). The angle of internal friction represents the frictional resistance among sediment grains (Holtz and Kovacs 1981). Cohesion is stress-independent while the angle of internal friction is stress-dependent (Holtz and Kovacs 1981). Cohesion and internal angle of friction values are obtained by plotting the results of a shear test on soil (Holtz and Kovacs 1981).

The shear strength parameters typical for cohesive (clay) and non-cohesive (sands and gravels) sediments are summarized in Table 1-1.

Table 1-1. Shear strength parameters for cohesive and non-cohesive sediments (after Craig 1997).

Sediment type	ϕ'(°)	c'(kPa)
sandy gravel	35-50	often assumed as 0
well graded sand, angular	33-45	often assumed as 0
silty sand	27-34	often assumed as 0
silt	30-32	often close to 0
clay	26-32	2-60

Cohesion is a function of grain size and/or conditions of confinement. When unconfined, sands and gravels are considered non-cohesive and without shear strength (Nash 1987). However, the shear strength of sands and gravels increases under confined conditions due to inter-particle friction and the interlocking of the particles (Towner and Childs 1972).

Clay, on the other hand, is considered a cohesive material as it generally exhibits significant shear strength even when unconfined. Such shear strength may be due to either direct bonding between clay particles or suction, also known as negative pore-

water pressure, within the clay (Nash 1987). Due to the low permeability of clay, its shear behaviour is separated into drained and undrained conditions (Craig 1997). When pore-water movement is restricted, a change in pore pressure directly affects the effective stresses and therefore the shear strength of the clayey sediment (Craig 1997).

1.4.6.2 Infinite Slope

Slope movement occurs when the shear stresses acting on the slope are greater than the opposing shear strength. The calculation of thaw slope stability can be approached using an infinite model that assumes a planar failure surface exists immediately above the permafrost table. In the infinite slope model, the slope is assumed to extend infinitely in all directions and sliding is assumed to occur along a plane parallel to the surface (Duncan and Wright 2005). Because the slope is infinite, the stresses will be the same on any plane that is perpendicular to the slope (Duncan and Wright 2005), such as the planes A-A' and B-B' (Figure 1-6). In addition, the forces on the two ends of the failure block will be identical in magnitude and opposite in direction, thus exactly balancing each other (Duncan and Wright 2005). Consequently, the forces on the ends of the failure block can be ignored in slope stability equations (Duncan and Wright 2005).

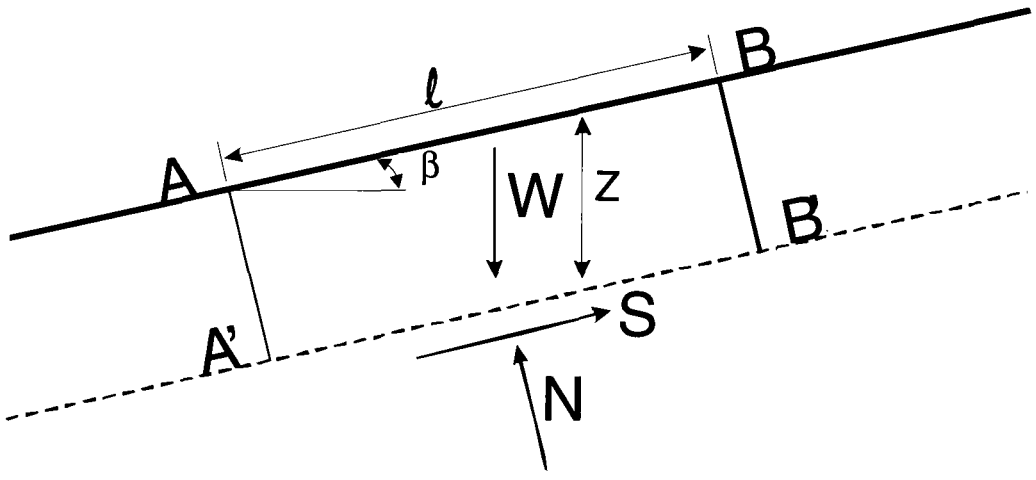

Figure 1-6. Infinite slope model with a planar slip surface (modified from Duncan and Wright 2005).

Summing forces in directions perpendicular and parallel to the slip plane gives the following equations for the shear force (S; kN/m) and normal force (N; kN/m) on the plane:

[7] $S = W \sin \beta$

[8] $N = W \cos \beta$

where W is the weight of the failure block (kN/m) and β is the inclination angle of the slope and slip plane, measured from the horizontal (in degrees).

For a block of unit thickness, the weight is expressed as:

[9] $W = \gamma l z \cos \beta$

where γ is the total unit weight of the soil (kN/m^3), which can be solved from the equation $\gamma = \rho g$ (ρ is density in g/cm^3; and g is gravitational acceleration, a constant of 9.81 m/s^2), l is the distance between the two ends of the failure block, measured parallel to the slope (m), and z is the vertical depth to the slip plane (m). Substituting Eqn. [9] into Eqns. [7] and [8] gives:

[10] $S = \gamma l z \cos \beta \sin \beta$

[11] $N = \gamma l z \cos^2 \beta$

The shear strength (τ; kPa) and normal stress (σ_n ; kPa) coincident on the slip plane are constant for an infinite slope and are obtained by dividing Eqns. [10] and [11] by the area of the plane ($l \cdot 1$), to give:

[12] $\tau = \gamma z \cos \beta \sin \beta$

[13] $\sigma_n = \gamma z \cos^2 \beta$

As shown previously, shear strength can also be solved from the Coulomb equation:

[2] $\tau = c + \sigma_n \tan \phi$ (drained conditions), or

[3] $\tau = c' + o_n' \tan \phi'$ (undrained conditions).

Solving for effective normal stress ($\sigma_n^{'}; \sigma_n^{'} = \sigma_n - \mu; \sigma_n^{'} = \gamma z \cos^2 \beta - \mu$) the modified Coulomb equation can be written as:

[14] $$\tau = c' + (\gamma z \cos^2 \beta - \mu) \tan \phi'$$

The factor of a slopes safety (*Fs*; unitless), which represents the factor by which the shear strength must be reduced so that the reduced strength is just in equilibrium with the shear stress (Duncan and Wright 2005), is summarized by the following equation:

[15] $$Fs = \frac{sum\ of\ resisting\ forces}{sum\ of\ driving\ forces}$$

Therefore, under effective stress conditions, *Fs* is given by:

[16] $$Fs = \frac{c' + (\gamma z \cos^2 \beta - \mu) \tan \phi'}{\gamma z \sin \beta \cos \beta}$$

Substituting for μ (see Equation [6] and rearranging, the *Fs* equation may be written as:

[17] $$Fs = \frac{c' + (\gamma - m\gamma_w) z \cos^2 \beta \tan \phi'}{\gamma z \sin \beta \cos \beta}$$

Harris and Lewkowicz (2000) wrote the above equation as:

[18] $$Fs = \left(1 - \frac{\gamma_w D_w}{\gamma z}\right) \frac{\tan \phi'}{\tan \beta} + \frac{2c'}{\gamma z \sin 2\beta}$$

where D_w is the head of water above the slip surface (m).

When pre-conditioning of the active layer shear zone by slow seasonal solifluction causes soil strength to reduce to near residual values, cohesion is reduced to close to zero (Lewkowicz and Harris 2005a). Under these conditions, Equation [17] can be reduced to:

[19] $$Fs = \frac{(\gamma - m\gamma_w) z \cos^2 \beta \tan \phi'}{\gamma z \sin \beta \cos \beta}$$

Harris and Lewkowicz (2000) wrote the above equation as:

$$[20] \quad Fs = \left(1 - \frac{\gamma_w D_w}{\gamma z}\right) \frac{\tan \phi_r'}{\tan \beta}$$

The pore water pressure on the slip surface is commonly expressed as the ratio r_u (unitless; Harris and Lewkowicz 2000):

$$[21] \quad r_u = \frac{\gamma_w D_w}{\gamma z}$$

Since γ is approximately twice the value of γ_w, the value of r_u is around 0.5 under hydrostatic conditions with the water table at the ground surface and a value of 1.0 indicates geostatic conditions (Harris and Lewkowicz 2000).

1.4.6.3 Primary Influences on Shear Strength

Several factors influence shear strength and ultimately slope stability. As each factor does not operate in isolation, exhibiting an influence on one another, it is not possible to determine their relative importance. These factors include particle size and shape, dry bulk density, soil water content, frost in soil, soil structure and fabric, plasticity, consolidation, salt removal, pre-conditioning, and desiccation. Details regarding the influence of several of these factors specific to permafrost environments on shear strength are presented below.

1.4.6.3.1 Frost in Soil

Ice lenses resulting from freezing of pore-water and migration of water to freezing fronts can have significant effects on the engineering behaviour of soils (Holtz and Kovacs 1981). Frost heave associated with volumetric expansion occurs during the freezing process, while increased water content and decreased strength is associated with the thawing process (Holtz and Kovacs 1981).

On thawing, the ice will melt and the soil skeleton must adapt to a new void ratio (Andersland and Ladanyi 1994). The amount of water generated from the ice melt may exceed the absorption capacity of the soil skeleton temporarily developing excess pore

pressures until drainage is complete (this is especially the case in fine-grained soils with low permeabilities; Andersland and Ladanyi 1994). If thawing is rapid enough, frozen ground may be transformed into a slurry of soil particles and water that is unable to support any significant load (Andersland and Ladanyi 1994).

1.4.6.3.2 Cryostructure

The shape and distribution of ice and sediment within frozen ground constitute its cryostructure (Murton and French 1994). Cyrostructures are visible to the naked eye and differences may be attributed to differences in freeze-thaw cycles and sediment texture (Murton and French 1994). Types of cryostructure include structureless, lenticular, layered, reticulate, crustal and suspended (Murton and French 1994). Features associated with the cryostructure itself and the nature of contact between different cryostructures may have implication on the stress state and the shear strength in and of the soil matrix (Murton and French 1994).

1.4.6.3.3 Pre-Conditioning

Small but progressive annual shear strain due to solifluction can result in a gradual reduction in shear strength at the base of the active layer (Harris and Lewkowicz 2000). Such slopes are said to be pre-conditioned for failure.

1.4.6.3.4 Dessication

Desiccation of the active layer by summer evaporation and two-sided freezing can lead to cryogenic hardening of active layer sediments (Harris and Lewkowicz 1993a). Cryogenic hardening increases shear strength, prohibiting the formation of shear planes.

1.4.6.4 Primary Influences on Shear Stress

A mass movement occurs when the average shear stress acting on a potential failure plane within an inclined mass of material exceeds the stresses that the plane of

material is capable of resisting (Chandler 1986). External factors such as slope oversteepening, earthquakes, and drawdown of external water levels contribute to increased shear stress (Chandler 1986). Oversteepening may result from erosion at the toe and/or loading at the crest of the slope (Chandler 1986).

1.4.6.5 Measuring Shear Strength

Several methods are available for determining shear strength, ranging from simple to complex. One simple method, the shear vane, and one complex method, the direct shear box, were employed during this study. The advantage of using the complex method is that the two shear strength parameters, cohesion and internal angle of friction, can be obtained whereas the simple method just provides a final shear strength value. Details regarding these methods are included in Chapter 4.

1.4.6.6 Summary of Slope Stability Analysis

Although simple to use and reasonably accurate, Limit Equilibrium methods of analysis have some drawbacks. One major drawback is the assumption that failure mechanism, slope geometry, groundwater pressure, and mean values of shear strength parameters are the same along the failure surface. These assumptions are not valid in the case of a progressive failure, such as the failures of quick clay slopes, where shear stress may vary considerably along the failure surface (Nash 1987).

A manner to account for the variability of the above parameters is the sensitivity analysis, in which one parameter is systematically varied in a sequence of analyses, while the others are held constant. Alternatively, the worst and best combination of certain parameters may be used in the analysis to define the upper and lower limits of Factor of Safety.

An alternative manner to deal with the uncertainties involved in the slope stability analysis is the probabilistic method. Generally, the same failure modes and

methods of analysis adopted in a deterministic approach are used, but the variability of the parameters governing slope stability is accounted for.

1.4.7 Active Layer Detachment Research Specific to the Fosheim Peninsula

Research specific to the Fosheim Peninsula has been separated into the main themes of morphology and failure history, morphometry, and slope stability analysis.

1.4.7.1 Morphology and Failure History

Lewkowicz (2007) describes the initiation and development of two active layer detachments at "Big Slide Creek" (BSC) in August 2005 (see Section 2.1.1 for location). The unique observations of active layer detachments in motion allowed the comparison of direct field observations with the pre-existing notion or assumption that active layer detachments develop over periods of minutes to a few hours. While one failure (BSC-2005-2) conformed to the pre-existing notion of almost instantaneous formation, the other (BSC-2005-1) did not.

Active layer detachment BSC-2005-1 initiated in a relatively wet cross-slope hollow near the top of a slope 650 m long. The angle of the slope at the point of initiation was approximately $16-19^{\circ}$ and the instantaneous rate of movement near the time of initiation was approximately 13 cm/min (7.8 m/hr). The main slide mass moved at rates of 1-5 m/hr over the next 5 hours following initiation. However, the front of the failure initially propagated at about 9 m/hr. The landslide attained its full length of 330 m over an estimated 80-120 hrs (3-5 days).

Three factors likely contributed to the stabilization of the detachment failure before it reached the foot of the slope (Lewkowicz 2007). First, the gradient gradually decreased downslope, reducing shear stress at the front. Second, the slight cross-slope depression that was controlling its path became deeper and consequently the toe was progressively confined, potentially increasing lateral resistance. Finally, the week of intense surface heating in July was followed by 4 days of significantly less hours of bright

sunshine and a consequent reduction in temperatures. This may have slowed thaw at the base of the active layer, resulting in reduced pore-water pressures in the slope.

Active layer detachment BSC-2005-1 is characterized by an asymmetrical Y-shaped scar, trailing blocks within the track zone that detached from the rear of the mass, headwall recession of 2-4 m, sidewall collapse, transverse ridges up to 75 cm high with an intact vegetation mat across the main side mass, brittle fracturing of the soil surface crust of transverse ridges as the slide mass front encountered drier parts of the slope, and complex discontinuous lateral compression ridges.

Active layer detachment BSC-2005-2 developed on the short valley slope opposite BSC-2005-1. The landslide was 39 m long, 24 m wide and consisted of a single mass which moved about 5 m on a $12-15^{\circ}$ gradient with an estimated velocity of 2 m/hr. The landslide virtually stabilized within 4 hours. At some point over the following 8 days, an additional 8 m of headwall retreat took place, but the position of the main slide mass remained unchanged during this period.

Active layer detachment BSC-2005-2 is characterized by a single displaced mass that is largely undisturbed with the exception of a single low compression ridge at its front where it had impacted stable terrain.

The observations of detachment failures in motion in 2005 generally confirm previous interpretations made from stratigraphic observations. They explain the range of deformation structures (shearing to complex folding; Harris and Lewkowicz 1993a, 2000; and Lewkowicz and Harris 2005a) which depend on the duration of the failure process as well as the precise location within the active layer detachment. At its simplest, block movement takes place virtually directly over the thaw plane. The intact slide mass is rafted on a layer of fluid mud that is usually less than 10 mm in thickness. This type of motion results in shearing deformation and was observed at the trailing edge of the main slide block at the start of BSC-2005-1 and at BSC-2005-2.

Internal structures varying from folds to shears to diapiric intrusions observed within excavated transverse ridges developed across the main slide mass (Mathewson and Mayer-Cole 1984; Harris and Lewkowicz 1993a; Lewkowicz and Harris 2005b) have been interpreted as relating to the speed of advance, the strength of the overlying vegetation mat, and the moisture condition of the sediments. Surface features at BSC-2005-1 showed both folding and compressive thickening. Field observations of dynamic loading by the moving slide mass and very low undrained shear strengths contributed to the formation of the surface features observed atBSC-2005-1. The combination of dynamic loading and very low undrained shear strength are believed necessary to allow detachment failures such as BSC-2005-1 to traverse very low-angled slope segments.

A study by Lewkowicz and Harris (2005b) found that mesoscale geomorphic factors (e.g. slope length, pre-existing cross-slope depressions, slope hydrology, and soil properties) exert significant control over active layer detachment morphology, making it difficult to compare statistically significant morphometric relationships between active layer detachments from one site to the next even within the same permafrost condition.

Lewkowicz and Harris (2005a) found that active layer detachments on the Fosheim Peninsula were triggered by short-term environmental variation (meteorological conditions). As part of the study, a surface heating index composed of the average product of daily hours of bright sunshine and daily air temperatures for periods of 9 – 13 days was developed to indicate the minimum meteorological conditions necessary to trigger active layer detachments on the Fosheim Peninsula.

Observations of failures from previous fieldwork and calculations from aerial photograph analysis have been tabulated, providing at least 50 years worth of data (Lewkowicz and Harris 2005a). Based on this data, Lewkowicz and Harris (2005a) showed that the annual initiation rate of active layer detachments for all three of the Fosheim Peninsula study areas is 2.6-6.2, 12.6, and 14.6 for the periods pre-1975, 1975-1987, and 1988-2000, respectively. This analysis suggests increasing numbers of active

layer detachments on the Fosheim Peninsula during recent years (Lewkowicz and Harris 2005a). This increase could be due to either (1) climate change, or (2) systematic underestimation of earlier landsliding activity. While evidence exists to support the first explanation, in order to substantiate this explanation or to rule out the second explanation, direct monitoring of active layer detachments on the Fosheim Peninsula would be required for at least a further decade.

Harris and Lewkowicz (1993a) investigated the form and internal structure of three active layer detachments located at Black Top Creek (BTC), BSC, and Hot Weather Creek (HWC; see Section 2.1.1 for location). Observations led the authors to conclude that active layer detachments on the Fosheim Peninsula occur in low- to medium-plasticity clays that contain some bands of silt and fine sand. The characteristic coherent slide blocks with minimal internal disturbance indicate that sliding takes place over a soft basal layer that is only a few mm's to several cm's thick (Harris and Lewkowicz 1993a). However, compression within the toe zone can result in severe folding and thrusting and the development of transverse ridges (Harris and Lewkowicz 1993a). This study showed that clay content and Atterberg limits do not provide sufficient information to predict active layer detachment failure mechanism. Two-siding freezing and summer evaporation can lead to cryogenic hardening of less cohesive soils, allowing them to maintain their integrity and fail by sliding rather than flow (Harris and Lewkowicz 1993a).

Harris and Lewkowicz (1993b) described in detail the micromorphology of the three active layer detachments investigated in their (1993a) paper. The micromorphology of a control site near the BTC slide was also described to provide information on soil structures in an area where active layer detachments are not likely to have occurred in the past. Their investigation indicated sediments associated with active layer detachments on the Fosheim Peninsula are for the most part hard and strongly structured becoming moist, unstructured, and soft near the base of the active layer. The

base of the active layer is also marked by a planar discontinuity, the basal shear zone, which corresponds with the presence of a fine sandy layer a few cm in thickness (Harris and Lewkowicz 1993b). Thin-sections indicated that sand grains in this layer are reoriented parallel to the shear zone plane yet may be locally disturbed by fluidization and water escape. These observations contrast with those of shear surfaces beneath shallow paleo-clayslides in Britain where shear planes are polished and are bounded by zones no more than a millimeter or so in thickness (e.g. Skempton et al. 1991). The strong prismatic and blocky structure of the upper part of the active layer may result from soil shrinkage during desiccation or ice segregation and the formation of ice veins during active layer freezing. The coherence of this structure suggests little alteration of the near-surface during sliding, supporting the conclusions of Harris and Lewkowicz (1993a).

Lewkowicz (1990) separated an active layer detachment into four morphological zones and proceeded to describe the appearance and characteristics of these zones. Firstly, the scar zone is the location from which material moves downslope. The floor of the scar zone is relatively smooth at the time of failure; however degradation of the upper horizons of permafrost following failure creates rills and gullies. The scar floor and the floor of the second zone, the track, frequently exhibit grooves or ridges that represent paths taken by individual blocks. The track zone, along which the mobilized material travels, may be bordered by lateral berms. The third zone, the toe or compression zone, is where the transported material accumulates. This zone is usually wider than the track zone and may exhibit thick accumulations of material and transverse ribbing caused by compressional forces. In some cases, a fourth zone is present, which is comprised of disturbed material to the sides and front of the main slide mass.

Lewkowicz (1990) obtained estimates of active layer detachment initiation frequency by comparing overlapping aerial photographs of BTC. Failure frequency

ranged from 0.2 failures/year for 1950-59 to 75 failures/year in 1988, giving a mean rate of 2 – 4 failures/year (assuming an activity period of 50 – 100 years). The aerial photograph comparison also suggested that failures will not recur at the same slope location for at least 6 years and that 15 years or more is required to have elapsed before failure recurrence becomes common.

1.4.7.2 Morphometry

Lewkowicz (1990) studied active layer detachments in BTC, HWC, and BSC. Active layer detachments were found to typically occur in silty or sandy materials on slopes that ranged from < 2 - > 40°. Failure lengths ranged from <10 – 700 m, widths from 5 -150 m, and depths from 0.2 – 0.65 m. Morphometrically, active layer detachments at BTC and BSC were similar while failures in HWC tended to be shorter, steeper, and had a higher percentage of scar zone. This difference is related to grain size distribution, where BTC and BSC are dominated by the silt sized fraction while HWC is dominated by sand.

1.4.7.3 Slope Stability Analysis

Effective stress calculations of two failures studied by Lewkowicz (2007) at "Big Slide Creek", BSC-2005-1 and BSC-2005-2, can account for initiation of movement. However, the advancement of the elongate failure, BSC-2005-1, across the lower part of the slope where gradients decrease to 3 – 7° is problematic (Lewkowicz 2007). Factor of Safety (Fs) remains greater than 1 even if it is assumed that the average thickness of the slide mass doubles and that the phreatic surface is at the ground surface. A total stress analysis indicates that on slopes of 3 – 7°, basal undrained shear strengths of 0.6-1.3 kPa, 1.0-2.2 kPa, and 1.4-3.3 kPa are required for Fs to equal unity for saturated slide masses averaging 0.6 m, 1.0 m, and 1.5 m in thickness, respectively (Lewkowicz 2007).

Given that the lower parts of the slope failed progressively at BSC-2005-1 rather than independently, the conditions required for instability apparently developed through

time. These conditions likely included increased shear stress imposed dynamically by the moving mass from upslope, as well as by compressive thickening of the thawed layer, higher moisture contents due to drainage of water from the thawing scar, and pronounced loss of strength due to liquefaction or remoulding once movement had begun (Lewkowicz 2007).

Observations in 2006 suggest that the required very low shear strengths can be achieved if pore-water pressures are sufficiently high. Several days of warm and sunny weather in July 2006 resulted in mud ejection occurring at Black Top Creek (BTC). Mean undrained shear strengths dropped to as low as 0.5 kPa near the base of the active layer.

Fieldwork conducted during the Lewkowicz and Harris (2005a) investigation demonstrated positive pore-water pressures at Fosheim Peninsula sites. Slope stability calculations indicated that antecedent pre-conditioning (e.g. basal shear zone strength reduction by annual solifluction) in addition to high pore-water pressures is required to activate failures on Fosheim Peninsula.

The stability of permafrost slopes on the Fosheim Peninsula was investigated by Harris and Lewkowicz (2000). The study examined the relationship between shear strength and active layer pore-water pressure at HWC and BSC. The study analyzed slope stability using a range of strength parameters and slope angles providing an indication of critical pore-water pressures necessary to initiate sliding. The study indicated that lower angled slopes (e.g. 5°) require pore-water pressures in excess of hydrostatic to initiate planar sliding. Thus lower angled slopes are only likely to suffer instability if the basal active layer is ice rich and thaw penetration is very rapid. Higher angled slopes (e.g. 20°) do not require high pore-water pressures to trigger landslides if slope stability is controlled by residual shear strength values (Harris and Lewkowicz 2000). Thus failure may occur on steeper slopes with ice rich active layer soils even if thaw rates are not excessive. Comparisons of analyses conducted using peak and residual

soil strength parameters demonstrated the sensitivity of slopes to shear strength and that any reduction in basal shear strength by processes such as solifluction would result in a significantly lowered factor of safety. Harris and Lewkowicz (2000) suggested that soils on the Fosheim Peninsula are pre-conditioned for failure due to a gradual reduction in the shear strength at the base of the active layer associated with annual solifluction shear strain.

1.5 Conclusions

Historical active layer detachment research has found that active layer detachments initiate in both discontinuous and continuous permafrost zones and are triggered by some event or condition that permits rapid thawing of the ice-rich zone at the base of the active layer or top of permafrost. Triggers include high air temperatures, summer rainfall events, rapid melting of an upslope snowbank, accumulated hours of bright sunshine, and surface disturbances such as fire. Thawing of the ice-rich zone promotes positive pore water pressures and reduced effective stress, creating a plane of low frictional strength.

The frequency of active layer detachments is difficult to determine because their initiation does not only depend upon meteorological and/or environmental conditions/triggers but also conditions within the slope. Frequency analysis suggests increasing numbers of active layer detachments on the Fosheim Peninsula during recent years.

Active layer detachments are commonly classified as compact or elongate but intermediate and complex forms occasionally develop. Compact active layer detachment failure history likely involves a single downslope movement of a block potentially followed by progressive upslope failure of the headwall. Elongated active layer detachment failure history may involve either initiation near the base of the slope followed by progressive upslope failure of the headwall or initiation near the crest of the

slope followed by progressive overloading of the slope below with the initial displaced block.

Stability analyses of slopes on the Fosheim Peninsula indicated that pore-water pressures in excess of hydrostatic are required to initiate planar sliding on lower angled slopes. However, high pore-water pressure is not a necessary condition since slope stability on the Fosheim Peninsula is also controlled by residual shear strength values since soils are pre-conditioned for failure due to a gradual reduction in strength associated with annual solifluction shear strain.

Recent observations of active layer detachments in motion on the Fosheim Peninsula suggest two modes of failure; one nearly instantaneous and one prolonged. The prolonged failure mode involved dynamic loading of the moving slide mass on downslope terrain. This observation in conjunction with very low undrained shear strengths helps to explain the observed folded and sheared surficial and internal structures of elongate failures and the ability of these failures to transverse very low-angled slope segments.

1.6 Thesis Structure

This thesis is written in a traditional format and is composed of six main chapters. The first and current chapter provides a background on active layer detachments and includes a review of active layer detachment literature specific to the Fosheim Peninsula. The second chapter describes the study area in terms of its landscape, climate and vegetation. The third chapter describes the field laboratory and analytical methods used to answer the research objectives while the fourth presents the results of the methods of analysis. The fifth chapter discusses the results and the sixth presents the conclusions of the research along with recommendations for future work.

2 STUDY AREA

2.1 Regional Landscape

2.1.1 Location

Fieldwork was carried out in July of 2006 at four lowland sites on the Fosheim Peninsula, Ellesmere Island (Figures 2-1 and 2-2; NTS map sheets 49G/9, 49G/15, 49G/16, and 340B/3). Ellesmere Island is part of the Queen Elizabeth Islands of the Canadian Arctic Archipelago. The Fosheim Peninsula is bounded to the west and south by Eureka Sound, to the north by Greely Fiord, and to the east by Canon Fiord and the Sawtooth Range.

The four study sites, located within 35 km of Eureka (80° N, 85° 41'W) and ranging from 1.6 to 11.5 km^2 in area are: Station Creek (SC; 79° 58'N, 85° 55'W), Black Top Creek (BTC; 79° 58'N, 85° 40'W), Hot Weather Creek (HWC; 79° 58'N, 84° 28'W), and "Big Slide Creek" (BSC; unofficial name; 79° 42'N, 84° 23'W). The SC, BTC, and HWC sites are largely below the Holocene marine limit of about 140 meters above sea level (m a.s.l.; Bell 1996) while the BSC site is located between the elevations of 150 and 360 m a.s.l. The lowlands of the Fosheim Peninsula are largely ice free but are surrounded by high mountain ranges supporting glaciers and ice caps (Bell 1996).

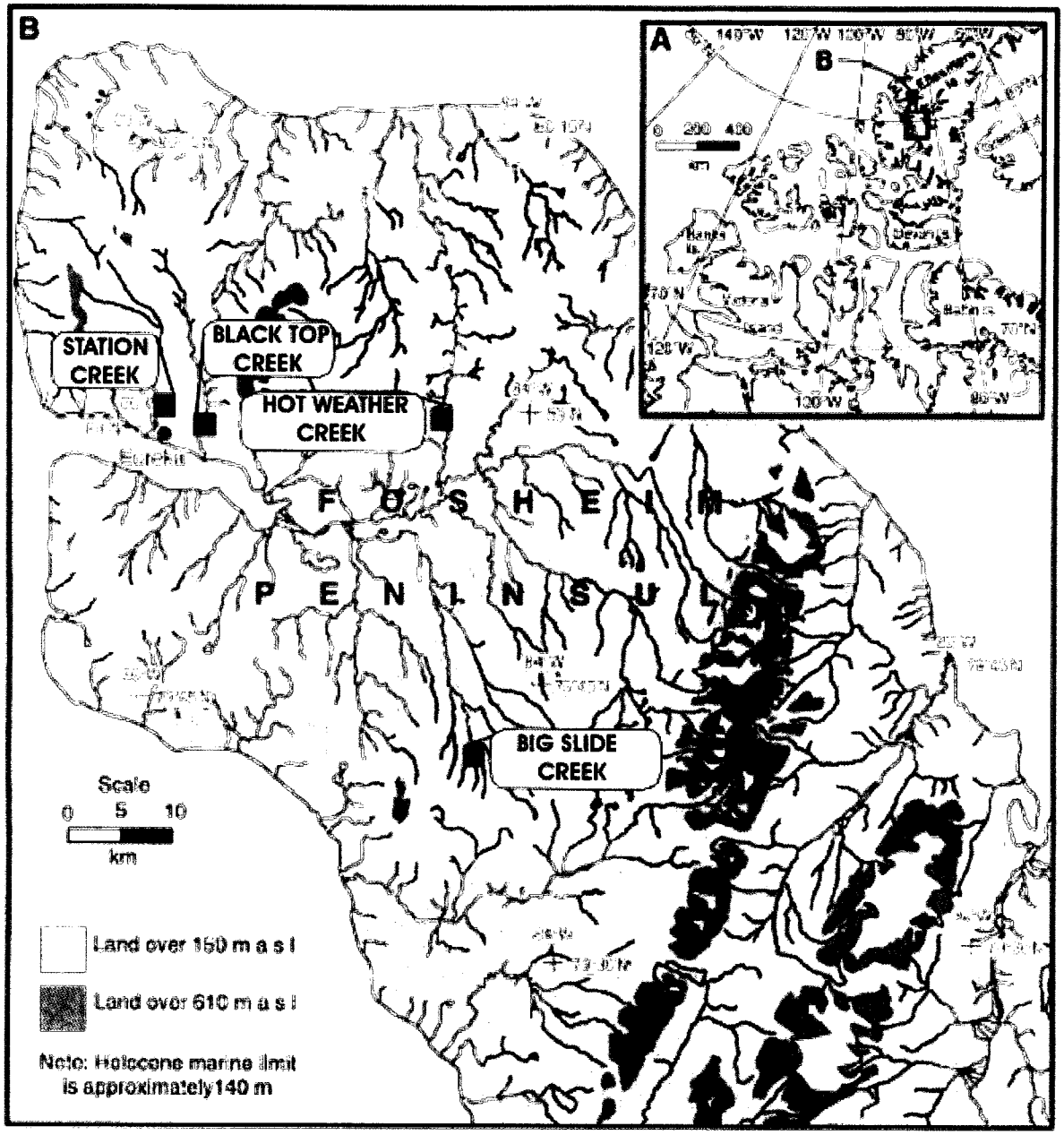

Figure 2-1. Location of the four lowland study sites on Fosheim Peninsula, Ellesmere Island (modified from Harris and Lewkowicz 2000).

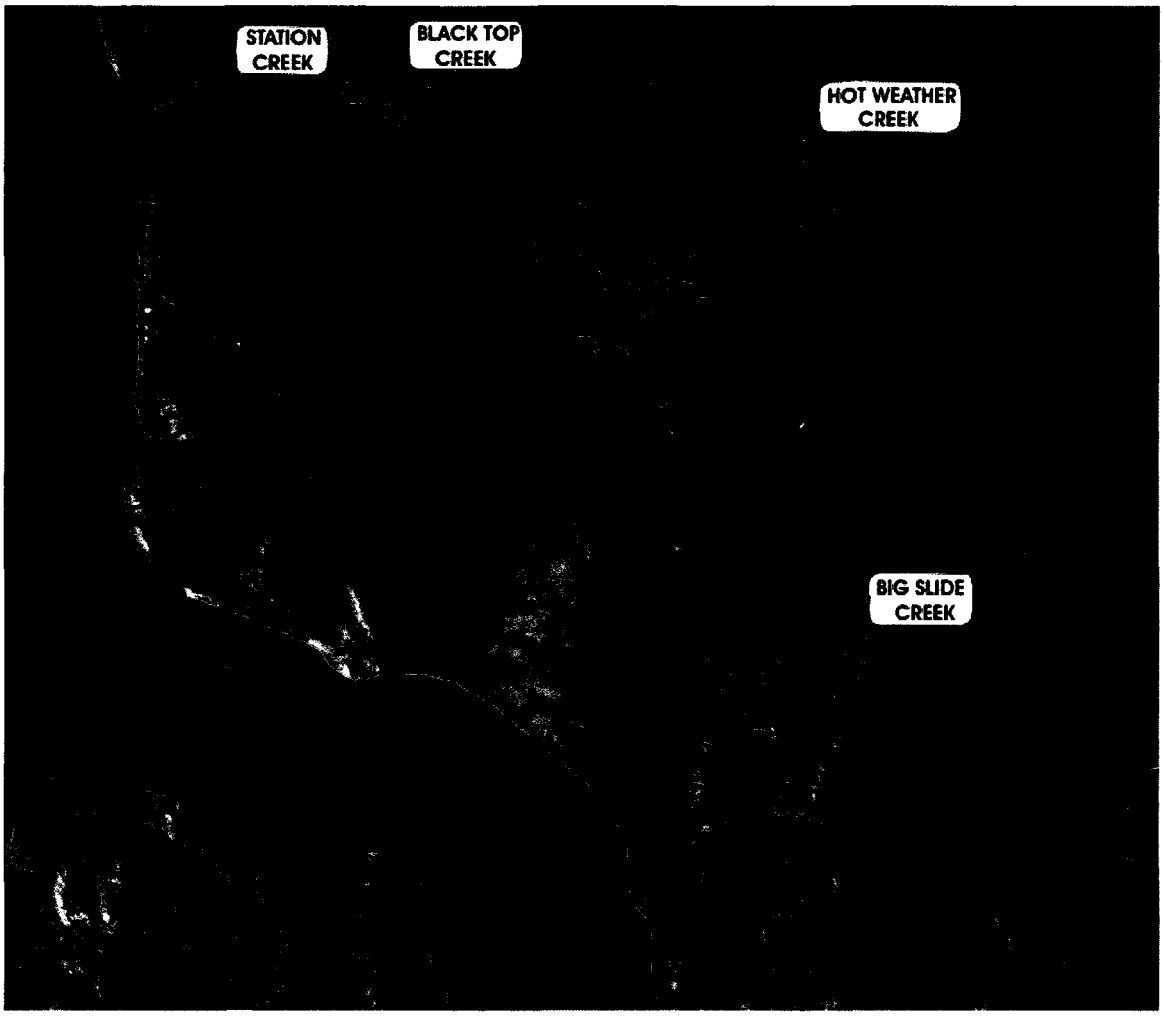

Figure 2-2. Satellite image (Landsat 7 launched April 15, 1999, date of coverage listed at 2000 ± 3 years) of the four lowland study sites on Fosheim Peninsula, Ellesmere Island (image accessed on July 5, 2009 from https://zulu.ssc.nasa.gov/mrsid).

2.1.2 Physiography

The Fosheim Peninsula is part of the Eureka Sound intermontane region between Axel Heiberg Island to the west and the bulk of Ellesmere Island to the east (Bell 1996). The study sites are located within the Eureka Sound Uplands physiographic zone of the Fosheim Peninsula (Roots 1963). The topography is subdued, with more than half of the landscape below 200 m a.s.l. and isolated ridges up to 840 m a.s.l (Bell and Hodgson 2000). The region exhibits a dendritic drainage system with many rivers displaying incised meanders in their lower reaches (Bell and Hodgson 2000). The Slidre River and its tributaries drain the interior of the peninsula and flow into the head of Slidre Fiord (Bell

1996). Gullying of poorly consolidated bedrock and raised marine fine-grained sediments has resulted in local badland topography (Bell and Hodgson 2000).

The HWC area consists of rolling lowland with a maximum elevation of 300 m a.s.l. (Kokelj and Lewkowicz 1999). HWC, a tributary of the Slidre River is characterized by a meandering morphology within a valley incised 25 to 50 m below the surrounding terrain (Kokelj and Lewkowicz 1999). HWC is bounded by the 820 m a.s.l. Black Top Ridge to the east and a polygon-network-dominated plateau to the west. BTC is characterized by meandering and braided morphologies in the upper and lower sections, respectively. BTC drains directly into Slidre Fiord. The eastern tributaries of the SC basin, located to the west of BTC, are incised within a polygon-network-dominated plateau, while the western tributaries of the SC basin drain a ridge that separates the basin from Eureka Sound. The SC basin drains directly into Slidre Fiord. The "BSC" basin is characterized by dendritic drainage of a broad, rolling lowland that drains to the north into the Slidre River. This broad rolling lowland is bounded to the southeast by the 1026 m a.s.l. Sawtooth Mountains.

2.1.3 Bedrock Geology

Fosheim Peninsula is underlain by the folded and faulted sedimentary rocks of the Sverdrup Basin geological structure (Thorsteinsson and Tozer 1970; Trettin 1989). The SC and BTC study sites are underlain by the poorly lithified shales, siltstones, sandstones, and mudstones of the Mesozoic Awingak, Deer Bay and Isachsen Formations (Geological Survey of Canada 1971a). The BSC and HWC sites are underlain by the sandstones, siltstones, shales, and coal of the Tertiary Eureka Sound Formation (Geological Survey of Canada 1971b).

2.1.4 Quaternary History and Surficial Deposits

Geomorphological and sedimentological evidence on the Fosheim Peninsula suggest at least two regional ice advances and sea-level transgressions followed by

regression (Bell and Hodgson 2000, Ó Cofaigh et al. 2000). The oldest known episode of regional glaciation, which covered the entire peninsula, occurred approximately 2.4 million years ago (Ma; Bell and Hodgson 2000; a minimum date is not reported). During the Late Wisconsinian, another episode of regional glaciation occurred where ice cover was extensive in southern and central Eureka Sound (Ó Cofaigh et al. 2000). Maximum glacial extents during the Late Wisconsinian occurred sometime after 28-27 thousand years (ka) before present (BP) and possibly <20 ka BP (Ó Cofaigh et al. 2000).

Throughout Ellesmere Island, deglaciation was underway by 9.5-11 ka BP (Bell 1996; Ó Cofaigh et al. 2000). Sea-level transgression reached a maximum level of 142-149 m a.s.l. between 10.6 and 8.7 ka BP (Bell and Hodgson 2000). Sea-level regression and landscape emergence caused relative sea level to fall to about 80 m a.s.l. by 7 ka BP, followed by a steady sea level decline to present-day levels (Bell and Hodgson 2000).

Generally, the surficial deposits consist of low- to medium-plasticity clays and silts of marine, glacial, and colluvial origin (Lewkowicz and Harris 2005b). Surficial deposits at HWC are the sandiest, SC deposits are the siltiest, and BTC soils contain the highest percentage of clay-sized sediments (this study).

2.1.5 Permafrost Conditions

The study sites are located within the continuous permafrost zone, with a permafrost temperature of about -15° C, extending to depths of about 500 m (Heginbottom et al. 1995). Active layer depths range between 0.5 to 0.9 m, with greatest depths found in sandy soils (Lewkowicz and Harris 2005a). Considerable inter-annual variation in active layer depth may occur at a single site.

The base of the active layer is characterized by high ice contents thought to have resulted from two-sided freezing (Harris and Lewkowicz 2000). Two-sided freezing (Mackay 1983) occurs in the late summer as a result of heat conduction downwards into the cold permafrost and upwards into the cold atmosphere (Harris and Lewkowicz 2000). This process leads to high concentrations of segregated ice immediately above the

permafrost table and a deficit of moisture in the upper and middle parts of the active layer (Mackay 1983; Harris and Lewkowicz 2000).

2.2 Regional Climate

The climate of the Fosheim Peninsula is cold and dry. Summer temperatures, however, are anomalously warm for this latitude (80° N) in the Canadian Arctic Archipelago (Edlund and Alt 1989). Climate data for the study areas was obtained from the closest Environment Canada climate station, Eureka, located at 79° 58' N and 85° 55' W, elevation 10.4 m a.s.l. From 1971 to 2000, the average monthly air temperature was 2.3, 5.7, and 2.6° C in June, July, and August, respectively (Table 2-1); all other monthly average air temperatures were below freezing (Environment Canada 2007). However, analyses (e.g. Alt et al. 2000) show that the Fosheim Peninsula lowland interior summer air temperatures are approximately 2 to 4° C warmer than Eureka. For the same period, the average June, July, and August monthly precipitation was 8.1, 12.5, and 14.9 mm, respectively (Table 2-1; Environment Canada 2007).

Table 2-1. Summary of climate data for Eureka.

	June	July	August
Average temperature (° C)	2.3	5.7	2.6
Average total precipitation (mm)	8.1	12.5	14.9

Data from Environment Canada (2007) for the period 1971-2000.

Monthly average air temperatures at Eureka from June to August 2005, the year when numerous active layer detachments occurred, were all greater than the long-term means (Table 2-2; Environment Canada 2007) with June showing the greatest departure from the average. Total monthly precipitation for June, July and August at Eureka were all less than the long-term means (Table 2-2) with August showing the greatest departure from the average.

Table 2-2. Eureka temperatures and precipitation for the summer of 2005 compared to the normal period, 1971-2000.

Month	Average monthly temperature (° C)			Total monthly precipitation (mm)		
	2005	Normal	Difference from normal	2005	Normal	Difference from normal
June	4.8	2.3	+2.5	6.4	8.1	-1.7
July	7.2	5.7	+1.5	12.4	12.5	-0.1
August	4.9	2.6	+2.3	10.0	14.9	-4.9

Data from Environmental Canada (2007).

Given that no measurable precipitation and only four trace events occurred at Eureka between July 22 and August 15, 2005, rainfall was eliminated as a triggering factor for the initiation of the 2005 active layer detachments (Lewkowicz 2007). Lewkowicz (2007) compared mean air temperatures and bright sunshine hours for the summer of 2005 to a surface heating index developed by Lewkowicz and Harris (2005a). Lewkowicz (2007) calculated index values for periods of 7-13 days but only the 7-day index ending on July 31, 2005 exceeded the threshold value. Hence one week of strong heating in the summer was sufficient to trigger numerous failures in the summer of 2005 (Lewkowicz 2007).

2.3 Regional Vegetation

The study area lies within the enriched prostrate shrub zone of the Canadian Arctic Archipelago with vegetation dominated by grasses, *Salix arctica* and *Dryas integrifolia* (Edlund and Alt 1989; Edlund et al. 2000). Flora on the Fosheim Peninsula is among the most diverse and abundant in the High Arctic (Lewis et al. 2005). Typical vegetation cover is up to 50% on the hummocky tundra and less than 20% on drier, more exposed slopes (Lewkowicz and Harris 2005a). Active layer detachment scars are largely vegetation-free and may remain so for decades on slopes underlain by marine sediments (such as SC, BTC and HWC); where salt is released following exposure and subsequent thawing of formerly perennially-frozen salt-rich marine sediments (Kokelj and Lewkowicz 1999).

3 METHODOLOGY

The methodology used in this thesis can be subdivided into field, laboratory and data analysis techniques (statistics, back analysis, and sensitivity analysis). The characterization of the 2005 active layer detachments on the Fosheim Peninsula follows that of Harris and Lewkowicz (1993a, 1993b and 2000), Lewkowicz and Harris (2005a and 2005b) and Lewkowicz (2007) with some minor modifications.

3.1 Field Techniques

Fieldwork was conducted in July 2006 to describe active layer detachments known to have occurred on the Fosheim Peninsula in 2005. Fieldwork involved both ground-based and aerial-based techniques. Fieldwork objectives were to describe and measure the active layer detachments and to collect samples for laboratory analysis.

3.1.1 Overview Mapping

3.1.1.1 Ground-based

Ground-based overview mapping was conducted in the Black Top Creek study area which was the most accessible of the four areas and the location where the largest amount of time was spent. Overview mapping involved describing active layer detachments known to have occurred in 2005 in terms of Global Positioning System (GPS) location, slope position, slope aspect, failure morphology, failure morphometry (length, width, scar length, and depth), failure morphology and features associated with movement (lateral berms, compression ridges, and grooves on scar and track floors). Failure morphology measurements were conducted with the aid of a 50 m tape measure and hand-held GPS unit. A total of 14 active layer detachments were described with this methodology.

3.1.1.2 Aerial-based

An aerial-based survey was conducted concurrently at Black Top Creek and Station Creek on July 22, 2006. Since extensive ground-based fieldwork was conducted at both of these sites, the purpose of this survey was to provide photographs to help elucidate failure morphology and morphometry.

3.1.2 Detailed Mapping

Detailed mapping was conducted at three active layer detachments at Black Top Creek, two at Station Creek, one at Hot Weather Creek, and one at "Big Slide Creek". Failure slope position was described as to whether the failure developed on foot-slope, mid-slope or crest-slope segments. When failures were located on the main valley side, slope position is in reference to the main valley, whereas failures located on local topography, e.g. the bank of a tributary to the main creek, slope position is in reference to the local topography. Failures were also classified as compact, elongate or complex based on their shape and measured dimensions (length and width).

Failures were mapped in the field using a 50 m tape measure, hand-held GPS unit, and Abney hand level. This detailed mapping allowed the construction of detailed site plans showing the scar, track, and depositional zones along with features associated with failure such as lateral berms, compressional ridges, grooves, displaced blocks and masses, disturbed zones in the adjacent terrain, and exposed ice wedge polygon networks. The detailed mapping also permitted the measurement of morphometric parameters (overall length and width, scar length and width, depth, and overall and scar failure angle) for use in future analyses.

3.1.3 Trial Pit Description

Trial pits were excavated in scar floors, tracks, displaced masses and toes to describe the macro-structure of the failure deposits and to locate the shear plane. Pits were excavated until the frost table was reached (from 0.5 – 1.4 m). Detailed sketches

were drawn of each trial pit. Cleaned trial pit faces were divided into units based on texture and structure while various other characteristics and features were noted. Unit depths and thickness were measured using a meter stick and 50 m tape measure.

Sediment texture was estimated in the field and confirmed later by laboratory grain size analysis. Sediments of mixed texture were described according to the dominant grain size, with subordinate grain sizes indicated by an adjective (e.g. silty sand; Whitlow 1995). In the case of very poorly sorted sediment, the names of the two dominant grain sizes are followed by that of the minor texture (e.g. silty sand with clay; Whitlow 1995). Sedimentary structures identified included: massive, stratified, laminated, lensed, columnar, prismatic, block, platy, granular, and cryoturbated (Brady and Weil 1996; Murton and French 1994). Other characteristics and features noted included: colour, clast shape and orientation, basal and upper contacts of units (sharp, gradational, inter-fingering, planar, irregular, undulating, horizontal, inclined, and truncated), buried organic horizons, deformation features (folds, thrust planes, and boudins) and fluidization features (flame structures; Fairbridge and Bourgeois 1978).

3.1.4 Sampling

Trial pits also facilitated the collection of both disturbed and undisturbed samples for subsequent grain size, moisture content, LOI, bulk density, Atterberg Limits, and shear strength analyses. Disturbed samples were only used for grain size, moisture content, LOI, and Atterberg Limits analyses. These samples were collected in Ziploc bags from trial pit walls, side-walls of the scar and track, and from the scar floor. Upon returning to Ottawa, all samples were immediately stored in a fridge and individual samples were not removed until selected for analysis.

Undisturbed samples were collected for shear strength analysis and subsequent grain size, moisture content, LOI, bulk density and Atterberg Limit analyses. Undisturbed samples were collected by pushing a 12 cm x 12 cm x 12 cm metal box into the trial pit wall and cutting around the box with a trowel to free it from the wall (Figure

3-1). The box was labeled with the sample identifier, upper side, down-slope direction, and approximate north direction. The open ends of the box were closed with a metal cover before wrapping the box several times with plastic wrap and then with aluminum foil.

Figure 3-1. Large and small metal sampling boxes prior to pushing into trial pit wall and freeing by cutting soil around the boxes with a trowel. Photo taken at Hot Weather Creek, HWC-2005-1, July 17, 2006.

Using the scale available at the Polar Continental Shelf Project laboratory in Resolute (model and accuracy of scale unknown), all samples less than 3300 g in mass were weighed on July 24, 2006. All samples, including those that were not weighed in Resolute, were weighed upon arrival in Ottawa on July 25, 26, or 28, 2006 using the Sartorius L610 (accuracy ± 0.005 g) or the Sartorius 1103 (accuracy ± 0.1 g) in the Geography laboratories or the Toledo No Springs Honest Weight (accuracy ~ ± 1 g) in the Civil Engineering laboratory.

3.1.5 *In-Situ* Shear Strength Testing

In-situ undrained shear strengths of fine-grained soils free of stones were measured in the field using a Geonor hand shear vane. The vane consists of four thin rectangular metal plates attached at right angles to a rod (Selby 1993). The vane was either pushed horizontally into a cleaned trial pit face or vertically into the scar floor and a torque was applied to the rod causing the blades to rotate and resistance to the turning motion was recorded directly in kPa, providing an indication of shear strength. Five repetitions were made at each location to provide an average peak undrained shear strength value.

3.2 Laboratory Techniques

The main objective of laboratory tests, conducted in the fall of 2006 was to further characterize the properties and structure of the soil involved in the active layer detachment. This objective was achieved by analyzing (1) the particle size distribution of sediment samples to confirm field estimates, by determining (2) soil moisture content and Loss on Ignition (LOI), (3) soil bulk density and unit weight, (4) Atterberg Limits, and (5) geotechnical parameters of undisturbed samples.

3.2.1 Particle Size Distribution

Soil samples were analyzed for particle size distribution using the laser particle size analyzer, Microtrac S3500. A representative sub-sample of approximately 100 g was separated from the sample. The sub-sample was oven dried at 105 ° C for 24 hours, after which it was ground by mortar and wooden pestle taking care not to pulverize the sample. The sub-sample was then weighed prior to re-hydrating with distilled water. After re-hydrating and mixing to form a muddy paste, a portion of the sub-sample was passed through a 2 mm sieve and set aside. The remainder of the sub-sample was poured onto the 2 mm sieve, only retaining the material that did not pass through the sieve. Organics were picked out of the material remaining on the sieve and the remaining

granular material was thoroughly washed, allowed to dry and weighed. The particle size distribution of the material remaining on the 2 mm sieve, i.e. the gravel fraction, was not further differentiated.

The material that had passed through the 2 mm sieve was then transferred to a 1000 mL beaker and subjected to three attacks with hydrogen peroxide over two days to remove organics. Following the last attack, the sub-sample was heated to burn off the hydrogen peroxide. At this point the sub-sample was re-hydrated slightly so as to allow the pouring of an approximately 20 g representative sub-sample into a vial.

As this work was conducted over several weeks, sets of approximately 18 samples were prepared at a given time. The vials comprising each set were then brought to the same weight by adding a dispersing agent, sodium hexametaphosphate, and allowed to sit overnight. The vials were then placed in a centrifuge and rotated at 3500 rpm for 30 minutes. The separated sodium hexametaphosphate was then decanted leaving a slightly moist sediment sample.

A 3 to 5 mL aliquot of appropriate consistency, i.e. slightly less viscous than cake frosting, was drawn from the vial using a metal spoon and placed in the particle size analyzer. The particle size analyzer was programmed to subject each sample to three runs and to report the average particle size distribution of the three runs. Three representative sub-samples of each sample were analyzed so the average particle size distribution reported for each sample is the result of nine runs.

3.2.2 Soil Moisture Content and LOI

Soil moisture content and LOI analyses were conducted on a representative sub-sample according to ASTM Standards 2216-98 (2004a) and methods outlined in Heiri et al. (2001), respectively. Approximately 30 g of soil was divided into three pre-weighed crucibles. The soil and crucible was then weighed and placed into an oven for 24 hours at 105 ° C, after which they were removed, allowed to cool and re-weighed. The moisture content (ω; %) is calculated from the following equation:

[22] $$\omega = \frac{m_2 - m_3}{m_3 - m_1} \times 100\%$$

where m_1 is the mass of the container (g), m_2 is the mass of the container and wet soil (g), and m_3 is the mass of the container and 105 ° C dried soil (g). The average of the three crucibles is reported as the moisture content for the sample.

The three crucibles were then placed in a muffle furnace set at 550 ° C for 5 ½ hours. The crucibles were then removed, allowed to cool and weighed. The LOI (%) is calculated from the following equation:

[23] $$LOI = \frac{m_3 - m_4}{m_3 - m_1} \times 100\%$$

where m_4 is the mass of the container and 550 ° C dried soil (g). The average of the three crucibles is reported as the LOI for the sample. LOI is a widely used method to approximate the organic content of sediments (Heiri et al. 2001).

3.2.3 Bulk Density and Unit Weight

The bulk density (ρ; g/cm^3) of six of the large undisturbed metal box samples was determined by slicing a 1 cm thick slice from the undisturbed soil in the box. Disregarding the effects of un-natural voids from sampling problems, the volume of each slice was estimated at approximately 144 cm^3. After weighing the slice, bulk density is calculated from the following equation:

[24] $$\rho = \frac{M}{V}$$ (Whitlow 1995)

where M is the wet soil mass (g) and V is the volume of the wet soil (cm^3).

Knowing the bulk density, the unit weight (γ; kN/m^3) can be calculated from the following equation:

[25] $$\gamma = \rho g$$ (Whitlow 1995)

where g is the acceleration due to gravity (9.81 m/s).

3.2.4 Atterberg Limits

Atterberg Limit tests, liquid limit (LL; %) and plastic limit (PL; %), were conducted on disturbed samples and undisturbed samples (following their use in direct shear tests) according to ASTM Standard D 4318. Atterberg Limit tests were not conducted on samples containing the suffix –SP and –TP since they are essentially a combination of sediment from above the shear or thrust plane (-ASP or –ATP) and sediment from below the shear or thrust plane (-BSP or –BTP).

The purpose of the liquid limit test is to find the moisture content of a soil at the boundary between the liquid and plastic states (ASTM 2004b). The undrained shear strength of a soil at the liquid limit is considered to be approximately 2 kPa (ASTM 2004b). The purpose of the plastic limit test is to find the moisture content of a soil at the boundary between the plastic and brittle states (ASTM 2004b).

Particle size distribution tests indicated that the majority of soils had little or no material greater than 425 μm in size and therefore it was deemed unnecessary to sieve the soil. An approximately 150 to 200 g representative sub-sample was prepared according to the wet preparation method for the multipoint liquid limit test and the plastic limit test.

3.2.4.1 Liquid Limit Test

The representative sub-sample was placed on a glass plate and mixed with distilled water to form a pasty consistency using a spatula. A portion of the sediment was then placed in the Casagrande liquid limit device, which consists of a brass cup and carriage (Figure 3-2). The sediment was leveled in the brass cup with a spatula and trimmed to a maximum thickness of 1.3 cm. The sample was then divided along the center line of the cup using the grooving tool (see Figure 3-2). The cup was lifted and dropped at a rate of two times per second by manually turning a hand crank. The lifting and dropping continued until the two halves of the sediment met at the bottom of the groove along a distance of 1.3 cm. The number of drops required for this to happen was

recorded. Using the spatula, an aliquot of the sample was collected from where it sutured and placed in a pre-weighed crucible. The weight of the moist sample and crucible was immediately recorded. All tools and the brass cup were cleaned and wiped dry before proceeding with the next portion of the representative sub-sample. The above steps were repeated another four times with new portions of the same sample, at decreasing degrees of wetness to obtain a total of five recorded number of drops, corresponding to each of the following drop ranges; 10-15, 15-20, 20-25, 25-30, and 30-35.

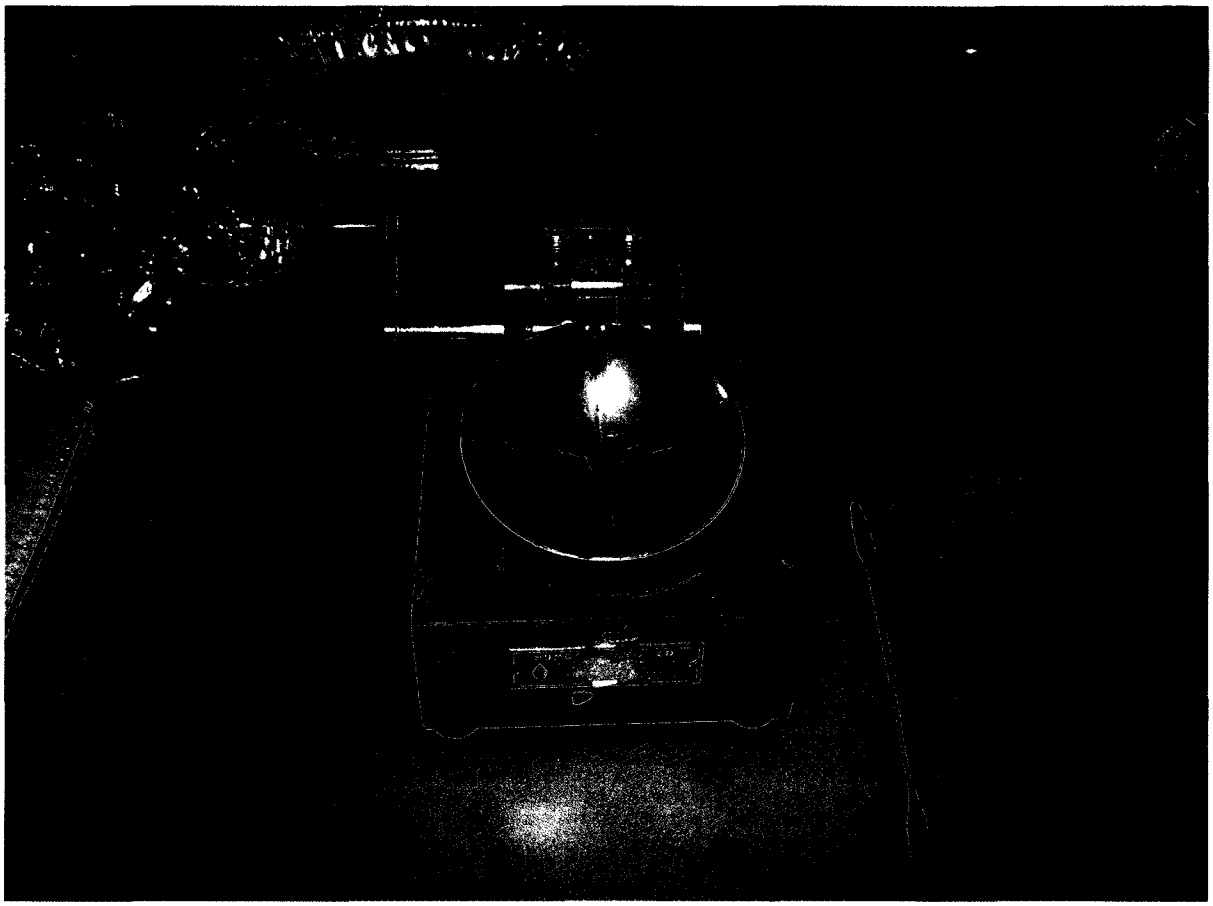

Figure 3-2. Casagrande liquid limit device with prepared and grooved soil sample.

The moist sample and pre-weighed crucible were then placed in a drying oven, set at 105 ° C, for 24 hours, after which the crucibles were removed, allowed to cool, and weighed. The gravimetric water content of the sample was then calculated from

Equation [22]. The gravimetric water contents of each of the five portions of the sample were then plotted against their corresponding number of drops on a semi-logarithmic graph. A regression line was drawn through the points to plot a "flow curve". The liquid limit was determined by taking the water content that intersected the flow curve at 25 drops.

3.2.4.2 Plastic Limit Test

The plastic limit test was performed using the hand rolled method. A portion of the wet sample was placed on the glass plate and hand rolled until it formed an approximately 1/8 inch thick thread. If at this point the thread did not show signs of crumbling, it was folded in two and rolled again until it was approximately 1/8 inch thick. This work was repeated until the thread would show signs of crumbling at 1/8 inch thickness. At this point, some of the crumbly material was placed in a pre-weighed crucible, immediately weighed and recorded.

The crumbly sample and pre-weighed crucible was then placed in a drying oven, set at 105 ° C, for 24 hours, after which the crucible was removed, allowed to cool, and weighed. The gravimetric water content of the sample was then calculated from Equation [22]. The gravimetric water content of the crumbly sample is considered representative of the plastic limit.

3.2.4.3 Plasticity Index

Based on the liquid limit and plastic limit test results, the plasticity index (PI) can be calculated from the following equation:

[26] $PI = LL - PL$

If either the liquid limit or plastic limit could not be determined, or if the plastic limit is equal to or greater than the liquid limit, the soil is reported as nonplastic (NP; ASTM 2004b). The significance of the plasticity index is that it reports the range of moisture contents over which a soil behaves plastically (ASTM 2004b).

3.2.5 Geotechnical Parameters

Shear strength parameters of soil samples collected on the Fosheim Peninsula were determined using a direct shear box. The direct shear box forces a failure plane to occur at a pre-determined location within a sediment sample (Bowles 1992). The sediment sample is placed in the shear box and split in half (Figure 3-3). Two forces are applied to the box during the test, one normal (P; N), applied vertically down onto the box, and the other is a shearing stress (T; N), applied horizontally.

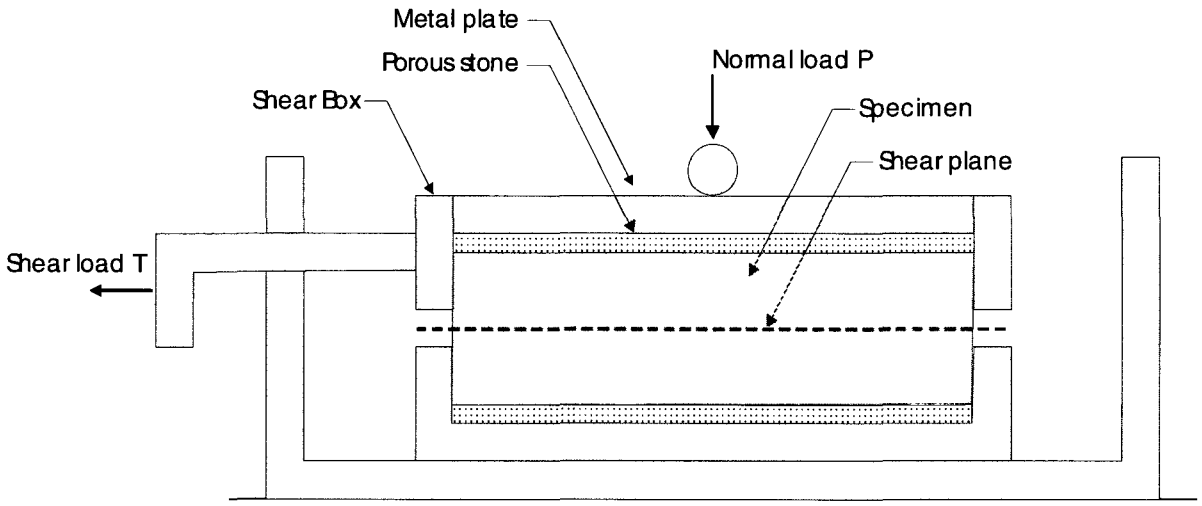

Figure 3-3. Direct shear test apparatus (modified from Duncan and Wright 2005).

During the direct shear test, the shear load (T) is applied to the test specimen causing the top of the shear box to move to the left relative to the bottom of the box (Duncan and Wright 2005). Eventually, the specimen will fail by shearing on a horizontal plane and the failure will be accompanied by development of a rupture or shear zone through the soil along the horizontal plane (Duncan and Wright 2005). As the top of the shear box moves relative to the bottom, the strength of the soil is mobilized and the particles within the shear zone are displaced from their original positions relative to adjacent particles (Duncan and Wright 2005). As a result, inter-particle bonds are broken, some particles themselves break, particles rotate, and particles slide along their contacts with adjacent particles (Duncan and Wright 2005). These

movements are resisted by the sources of shear strength in soils: the strength of inter-particle bonds, frictional resistance to sliding, and by forces from adjacent particles resisting displacement and reorientation (Duncan and Wright 2005).

The shear strength of soils is controlled by effective stress (Duncan and Wright 2005). The relationship between these two parameters can be graphically represented by the Mohr-Coulomb strength envelope (Figure 3-4; Duncan and Wright 2005). The strength envelope is developed by conducting direct shear tests on soils using a range of pressures and plotting the results on a Mohr stress diagram (Duncan and Wright 2005) where effective stress (σ') is plotted on the x-axis and shear stress (τ) is plotted on the y-axis. The strength envelopes are representative of the results of tests on undisturbed specimens, all cut from the same undisturbed sample and therefore all having the same pre-consolidation pressure (Duncan and Wright 2005). The strength envelope allows determination of the shear strength parameters; effective cohesion (c') and effective angle of internal friction (ϕ'), which can be used in Equation [3] to determine the undrained shear strength (τ):

[3] $$\tau = c' + \sigma'_n \tan \phi'$$

Although ring shear tests are preferable for measuring residual shear strengths because unlimited shear displacement is possible through continuous rotation, it is still possible to measure residual strength with the direct shear box by moving the top of the box back and forth relative to the bottom (Duncan and Wright 2005). In this way, direct shear tests are able to accumulate the displacements required for the determination of residual shear strength (Duncan and Wright 2005).

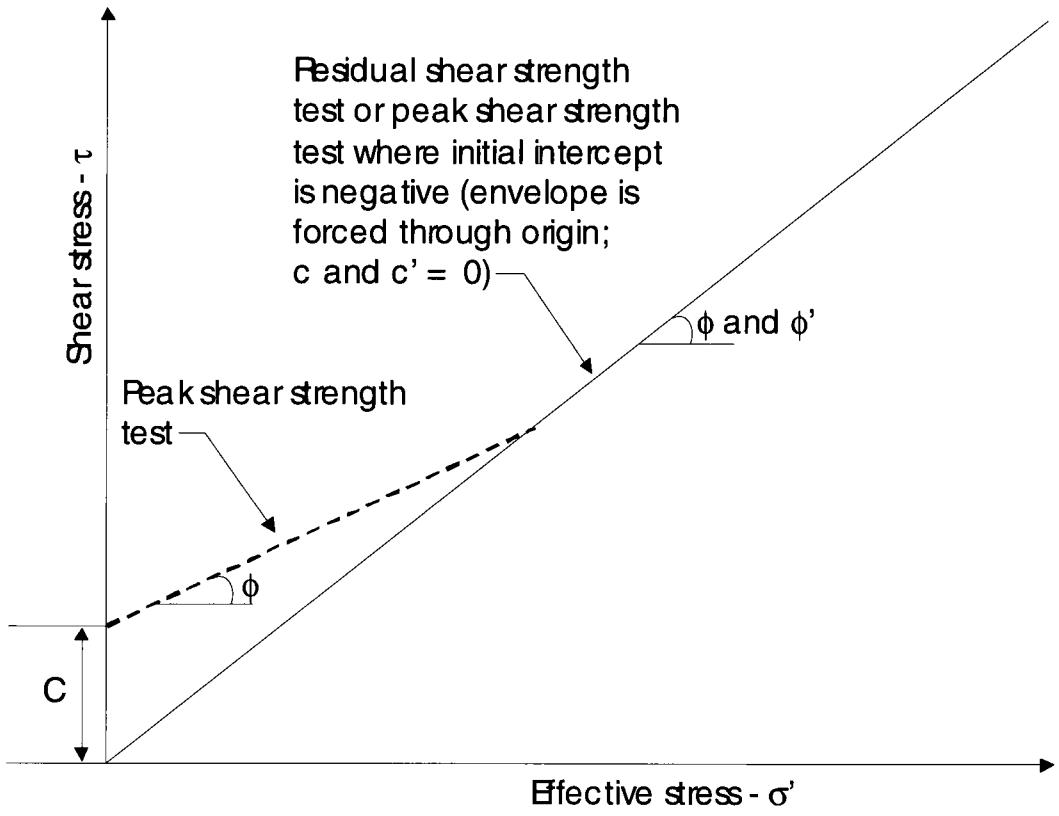

Figure 3-4. Effective stress shear strength envelope for a soil containing a clay component (modified from Duncan and Wright 2005).

There are three different categories of direct shear tests to choose from. They are the quick test, the consolidated-quick test, and the consolidated-slow test. For the quick test, the shearing force is applied as soon as the normal load is applied. Excess pore pressures develop due to soil grain reorientation (Bowles 1992). The direct shear box can be used to conduct the quick test by quickly increasing the normal and shear load (see Figure 3-3). However, this quick application of loads can result in higher measured strength due to strain rate effects (Duncan and Wright 2005). The consolidated-quick test applies the normal load and observes the vertical movement until settlement stops. The shearing force is then applied. The consolidated-slow test is similar to the consolidated-quick test but when the shear force is applied, it is applied so slowly (<0.01 mm/min) that no pore pressures develop in the soil (Bowles 1992).

For cohesive soil, the strength parameters are strongly influenced by the test method chosen, the degree of saturation, and if the sample is normally consolidated or overconsolidated (Bowles 1992). Shear strength parameters are normally given in terms of total stress (Bowles 1992). Unfortunately, the direct shear box test does not allow the determination of pore-water pressures during the test (Bowles 1992) and therefore shear strength parameters by default are given in terms of effective stress.

Soil conditions on the Fosheim Peninsula can be considered to approximate undrained since the rate of thaw is likely sufficiently rapid relative to the rate of drainage (e.g. Hutchinson 1974). These conditions can be approximated using the direct shear box by employing the quick test. However, by doing so strain rate effects may result in higher measured shear strengths (Duncan and Wright 2005). Triaxial tests would be better suited to undrained testing because drainage can be prevented by sealing the test specimens in impermeable membranes and tests are performed slowly enough to eliminate undesirable strain rate effects (Duncan and Wright 2005). However, time constraints and the large number of samples made it necessary to use the direct shear apparatus as several weeks would have been required to conduct a single undrained test using the triaxial apparatus.

The shear load (T) is recorded throughout the direct shear test until it reaches a maximum and begins to decrease or plateau, indicating that shear has occurred. The vertical and horizontal loads are each divided by the area of shear (area of the shear box; A; L^2; m), to compute the normal stress (σ_n) and maximum shear stress (τ):

[5] $$\sigma_n = \frac{P}{A}$$

[27] $$\tau = \frac{T_{(\max)}}{A}$$ (Duncan and Wright 2005)

When at least two values for maximum shear stress (τ) and effective stress (σ') are plotted on coordinate axes, effective cohesion (c') and effective internal angle of friction (ϕ') can be obtained. Effective cohesion is the y-intercept and effective internal angle of

friction is the inverse tangent of the slope of the line drawn through the points. The modified Coulomb equation (previously shown) is now satisfied:

[3] $\tau = c' + \sigma_n' \tan \phi'$

For cohesionless and residual soil, cohesion is assumed to be zero (Selby 1993) and the modified Coulomb's equation is simplified to:

[28] $\tau = \sigma_n' \tan \phi'$ (Selby 1993)

Both peak and residual shear strength tests were conducted because studies conducted by Skempton (1985) showed that once a failure has occurred and a continuous slickensided failure surface has developed, only the residual shear strength is available to resist additional sliding. Skempton (1985) found that peak shear strengths are attained at small strains corresponding to displacements in the order of 1 to 6 mm. However, it was found that even with effective stresses of ~600 kPa, displacements usually exceeding 100 mm are necessary before the strength of intact clay falls to a final steady residual value (Skempton 1985). In this study, a displacement of approximately 72 mm over three tests was deemed appropriate for the following reasons: Skempton (1985) found that strengths approaching a final steady residual value can be reached at displacements ranging from about 20% to 50% of the ideal; and particle re-orientation, and therefore the fall to residual strength, is complete at small displacements under high pressure (Skempton 1985).

Direct shear tests were carried out on intact samples using the equipment in the University of Ottawa Civil Engineering Geotechnical laboratory (Figure 3-5). Two to three 6 cm x 6 cm x 3 cm specimens were cut along the shear or thrust plane from the original 12 cm x 12 cm x 12 cm undisturbed sample. Care was taken to locate the shear or thrust plane as exactly as possible in the shear plane of the box and to arrange the specimen so that shearing followed the natural direction of movement. Where feasible, an additional two to three specimens were cut from the soil above and below the shear or thrust plane and subjected to direct shear tests.

Each specimen was subject to an initial run at an effective stress of 4.2, 7.2, or 10.8 kPa, to determine peak effective cohesion and peak effective internal angle of friction. This range of effective stresses was representative of the potential range of overburden pressures directed on soil at the shear plane at the time of failure. The shearing rate was set at 0.8 mm/min and applied until the sample had sheared (i.e., the vertical force had peaked). The test continued for a few readings past the peak shear stress (T_{max}). After the initial run, each specimen was then subject to three additional runs, at each of the following effective stresses; 30, 60, or 120 kPa, to determine residual effective internal angle of friction (residual effective cohesion is assumed to be zero). The selection of this range of effective stresses was somewhat arbitrary as the goal was to determine residual shear strength parameters in a short amount of time and higher effective stresses would help to achieve this goal. The second through fourth runs of the test were conducted after reversing the travel of the box while keeping the specimen loaded.

P (normal/vertical load/stress) applied at 4.2 kPa, 7.2 kPa, and 10.8 kPa for the peak shear strength tests and 30 kPa, 60 kPa, and 120 kPa for the residual shear strength tests
T (shear/horizontal load/stress) recorded during test
Δx (horizontal displacement) recorded during test
A (area of shear) 0.06 m x 0.06 m = 0.036 m^2

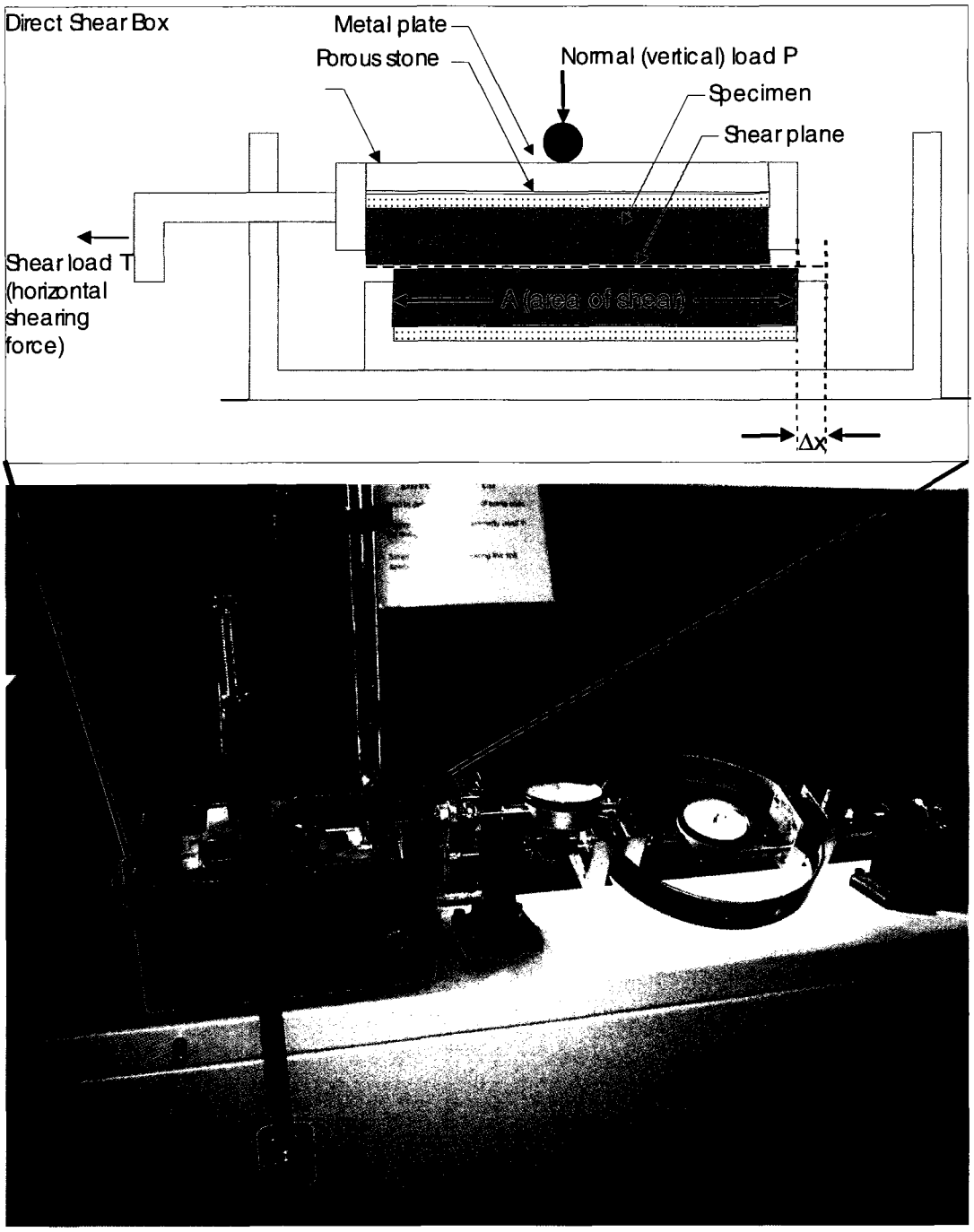

Figure 3-5. Direct shear apparatus at the Civil Engineering Department (University of Ottawa) used in the direct shear tests performed on undisturbed samples.

Two stress-displacement curves were plotted for each specimen; one for the peak shear strength test and a second which included all three residual shear strength tests. The stress-displacement curve plots the shear stress (T/A) against the horizontal displacement (Δx) for each vertical load (P). To simplify graph production, the peak stress-displacement curves from each of the peak direct shear tests (i.e., at the effective stresses of 4.2, 7.2, and 10.8 kPa) were plotted on the same graph and the three residual stress-displacement curves from each of the three residual direct shear tests (i.e., at the effective stresses of 30, 60, and 120 kPa) were plotted on the same graph.

The stress-displacement curves were used to determine the peak and residual maximum shear stresses (Figure 3-6). For the peak shear strength tests, the peak maximum shear stress is graphically represented by the peak of the graph (T_{max}/A) or the point at which the line begins to plateau (i.e., no change in T/A, either upwards or downwards). A peak maximum shear stress value was determined for each of the tests conducted at the effective stresses of 4.2, 7.2, and 10.8 kPa. Considering reduced strengths are expected under residual conditions due to strain concentration, particle re-orientation and polishing (Skempton and Vaughan 1993), the residual maximum shear stress is graphically represented by the point at which the line begins to plateau or drop. Since three runs were conducted for each effective stress of 30, 60, and 120 kPa, the lowest maximum shear stress value of the three runs was selected to represent the residual maximum shear stress value for each effective stress.

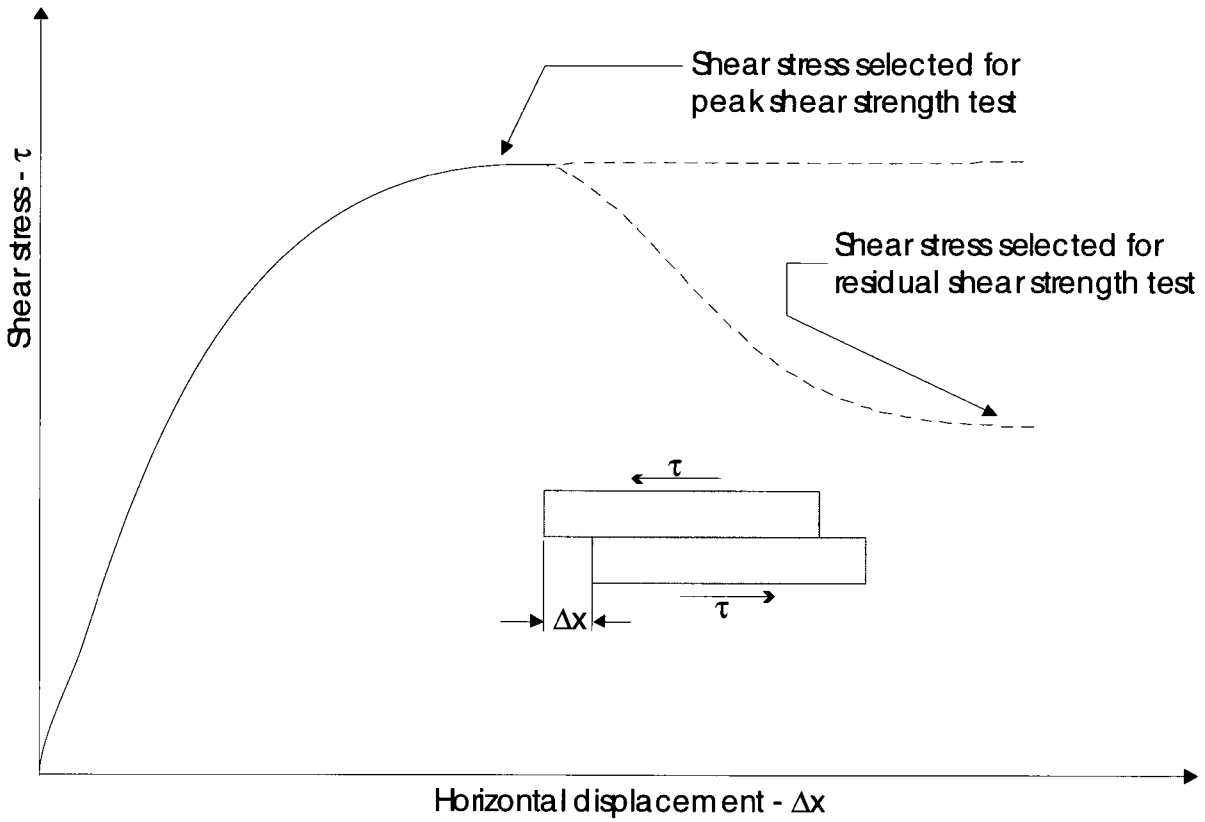

Figure 3-6. Stress-displacement curve showing selected maximum shear stress value for peak and residual direct shear tests (modified from Duncan and Wright 2005).

A graph was then produced plotting the maximum shear stress (τ) from each run against the corresponding effective stress (σ') of that run (4.2, 7.2, and 10.8 kPa in the case of the peak direct shear tests, and 30, 60, and 120 kPa in the case of the residual direct shear tests). A regression line was then drawn between the two to three points on the graph and the equation of this line was used to determine peak cohesion (y-intercept), and peak and residual internal angle of friction (inverse tangent of the slope of the line). In the case of the residual direct shear tests or where the intercept is negative in the peak direct shear tests, the y-intercept (cohesion) was set to 0 (see Figure 3-4).

In some instances, soil did not fill the entire 12 cm x 12 cm x 12 cm sampling box and voids were present along the sides of the box. In these cases, it was not possible to

cut three specimens from the plane of interest. In these cases, only two specimens were cut and tested, producing only two sets of cohesion and internal angle of friction results.

3.3 Analytical Techniques

Active layer detachment morphology and morphometry information gathered in the field and soil property and structure information gathered during the laboratory tests were analyzed to investigate the relationship between properties and to compare soil properties with field observations. This investigation was conducted with the aid of the following analyses: (1) classification of particle size, gravimetric water content, LOI, Atterberg limit, cohesion, and internal angle of friction data in terms of average size and sorting; (2) probability statistics between different populations of selected data; (3) descriptive statistics of morphometric parameters gathered in the field; (4) comparison of soil properties determined in the laboratory with failure characteristics observed and measured in the field; and (5) Factor of Safety calculations and sensitivity analyses using soil properties identified in the laboratory and measurements obtained from the field.

3.3.1 Classifying the Data

Statistical parameters were derived for the particle size, gravimetric water content, LOI, Atterberg limit, cohesion, and internal angle of friction results. Results were grouped into various populations including: failure site, study area, and samples collected from above, within, or below the shear or thrust plane.

3.3.1.1 Average Size and Sorting

The average size and sorting of particle size, gravimetric water content, LOI, Atterberg Limit, cohesion, and internal angle of friction data were investigated using the arithmetic mean and standard deviation (Moore and McCabe 1993). These calculations were conducted using the units of the parameter in question: % for particle size, gravimetric water content, LOI, and Atterberg limits; kPa for cohesion; and degrees for internal angle of friction.

The inclusive graphic standard deviation (*gs*) was calculated for each failure in phi units using the results from the Microtrac sediment analyses and the following equation:

$$[29] \quad gs = \frac{\phi 84 - \phi 16}{4} + \frac{\phi 95 - \phi 5}{6.6} \qquad \text{(modified from Folk 1980)}$$

The results were compared to a descriptive classification scale for sorting suggested by Folk (1980) to provide an indication of the degree of sorting for each failure (Table 3-1).

Table 3-1. Descriptive classification scale for sorting suggested by Folk (1980).

Inclusive Graphic Standard deviation (gs)	Degree of sorting
<0.35 Φ_{size}	very well sorted
0.35-0.50 Φ_{size}	well sorted
0.50-0.71 Φ_{size}	moderately well sorted
0.71-1.0 Φ_{size}	moderately sorted
1.0-2.0 Φ_{size}	poorly sorted
2.0-4.0 Φ_{size}	very poorly sorted
>4.0 Φ_{size}	Extremely poorly sorted

3.3.1.3 Probability

Probability (P) is defined as the probability of a certain event happening (Folk 1980). Through the use of a t-test (MS Excel, Data Analysis Tools, Two Sample Assuming Equal Variances), the probability of real differences existing between the means of two populations was examined. For significant results to exist, the t-stat should be less than t-critical and the p-value should be less than or equal to the significance factor (0.05; Moore and McCabe 1993).

3.3.2 Descriptive Statistics and Correlation Analysis of Morphometric Parameters

Descriptive statistics (average, standard deviation and range) were calculated for soil properties and the main morphometric parameters. Correlation analysis was used to determine if statistically significant relationships existed between the main

morphometric parameters of the failures; length, width, failure angle, and scar length. Correlation analysis was also used to determine if statistically significant relationships existed between particle size and morphometry. Descriptive statistics were also calculated for the main morphometric parameters of the two morphologic categories (compact and elongate) allowing comparison of the two categories.

3.3.3 Factor of Safety Calculations and Sensitivity Analysis

Calculations of slope Factor of Safety (Fs) were conducted using Eqns. [17] and [19]. This analysis was conducted using measured values for slope angle (β), effective cohesion (c'; both peak values measured from the direct shear tests and an assumed residual value of 0), effective internal angle of friction (ϕ'; both peak and residual values measured from the direct shear tests), depth to slip surface (z), and unit weight of soil (γ). Based on the fact that ice contents are high at the base of the active layer in continuous permafrost areas and thaw depths in the 2005 summer season were significant compared to previous years (Lewkowicz 2007), an assumed value of 1.0 was selected as the height of the piezometric surface above the shear plane expressed as a fraction of the total thawed layer thickness (m).

Sensitivity analyses of residual conditions were conducted for each failure using Eqns [18 and 20]. Depth to slip surface and unit weight of soil were kept constant and the relationship between factor of safety and the remaining five variables of the equations (peak internal angle of friction, peak cohesion, residual internal angle of friction, slope angle, and the head of water above the slip surface) was investigated. The selected ranges investigated for peak and residual internal angle of friction, peak cohesion, and slope angle were based on the maximum and minimum values determined from the direct shear tests and field observations while the head of water above the slip surface was simply varied from 0 to the ground surface.

Sensitivity analyses were conducted according to a method described by Prellwitz (1994) and modified by Haneberg (2000) that allows for a systematic evaluation of the

influence of changes in each of the independent variables on the calculated Factor of Safety. Normalized percent change in the i^{th} independent variable in a model, x_i, and the normalized percent change in the Factor of Safety are given by the following equations:

[30] $$\Delta x_i = \left(\frac{x_i - \bar{x}}{x_{max} - x_{min}} \right) \times 200\%$$ (from Haneberg 2000)

[31] $$\Delta Fs = \left[\frac{Fs(x_i) - Fs(\bar{x})}{Fs(\bar{x})} \right] \times 100\%$$ (from Haneberg 2000)

where $\bar{x}$ is the average value, x_{min} the minimum value, and x_{max} the maximum value of the i^{th} variable. The sensitivity of the Factor of Safety to variations in each independent variable is assessed by allowing x_i to vary continuously from x_{min} to x_{max}, calculating ΔFs and Δx_i for each value of x_i, and then plotting ΔFs versus Δx_i (Haneberg 2000).

4 RESULTS

The purpose of this chapter is to present field observations, sediment properties obtained during laboratory analysis, and information gained regarding slope stability through back calculations and sensitivity analysis.

4.1 Field Observations

4.1.1 Failure Distribution

Information from the 2006 field visit has been compiled to produce maps of each study area showing the approximate location of the active layer detachments inferred to have initiated in 2005 and studied in 2006 (Figures 4-1, 4-2, 4-3, and 4-4). These maps are representative of each of the four study areas on the Fosheim Peninsula, Station Creek, Black Top Creek, Hot Weather Creek, and "Big Slide" Creek (see Figure 2-1).

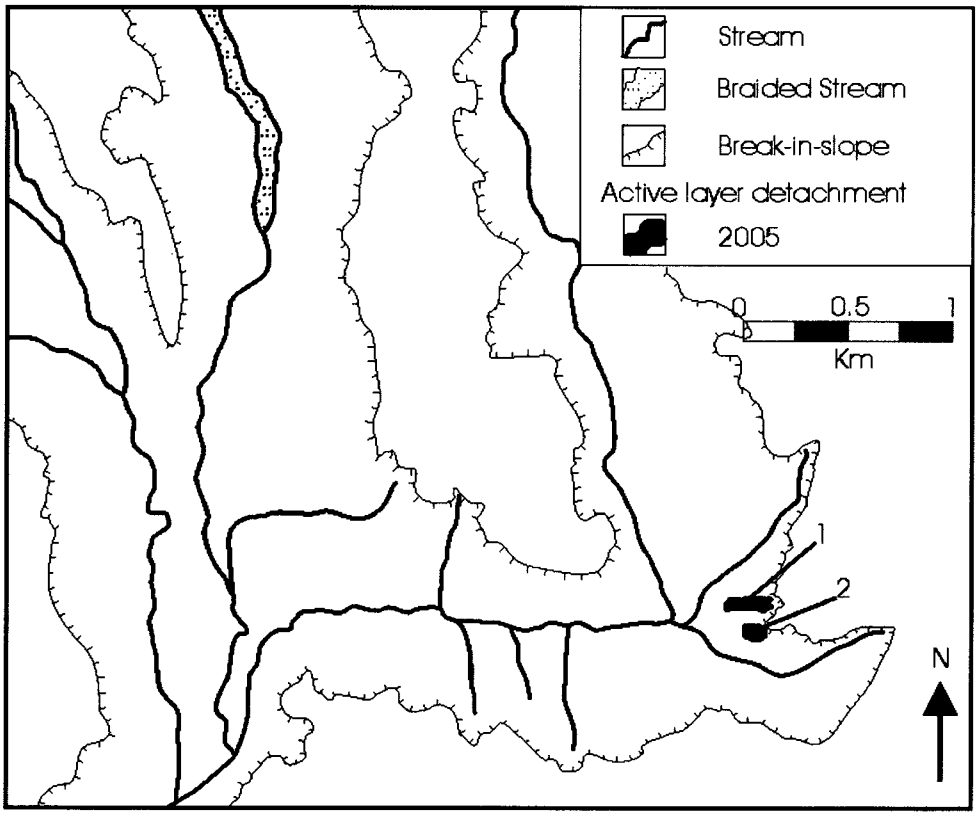

Figure 4-1. Map of 2005 active layer detachments studied at Station Creek. Source map 1298A Geology Slidre Fiord, Geological Survey of Canada, 1971.

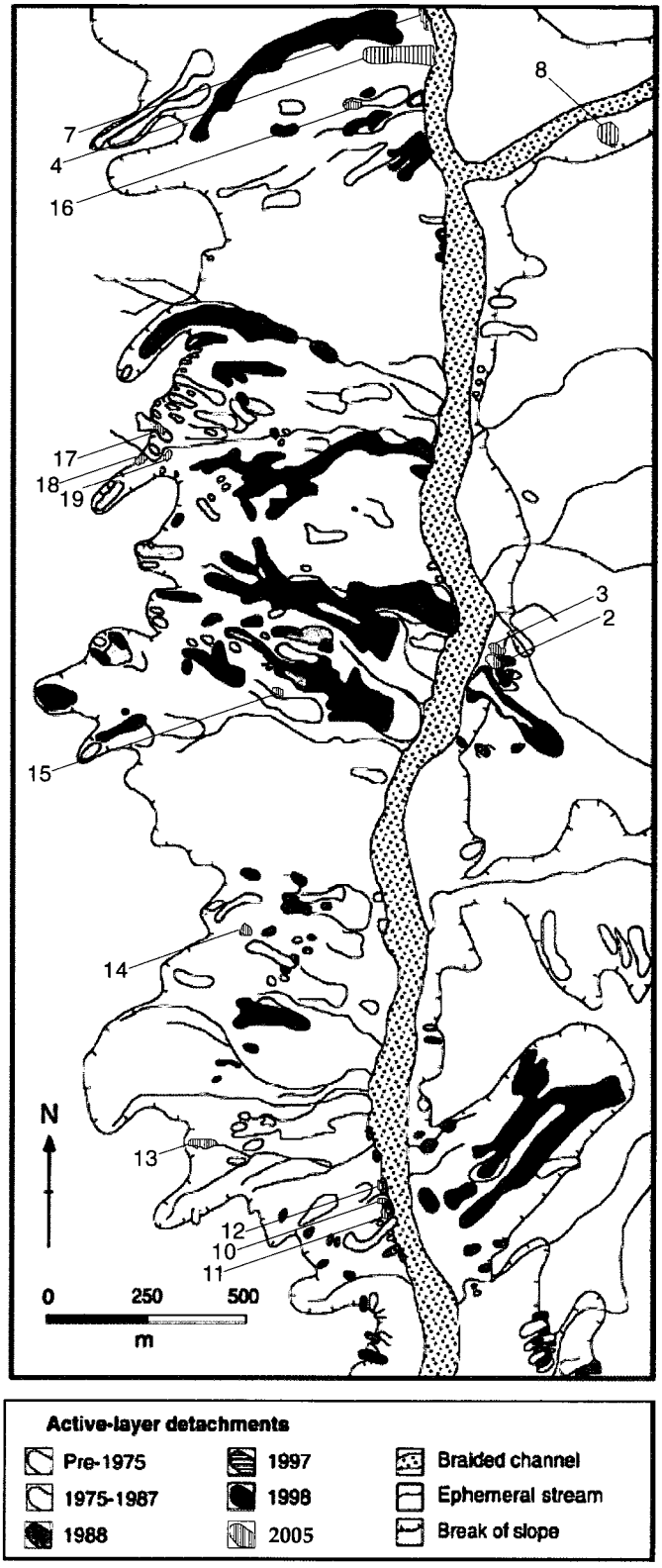

Figure 4-2. Map of 2005 active layer detachments studied at Black Top Creek. Modified from Lewkowicz and Harris (2005b) and updated to summer 2005.

Figure 4-3. Map of the 2005 active layer detachment studied at Hot Weather Creek. Modified from Lewkowicz and Harris (2005b) and updated to summer 2005.

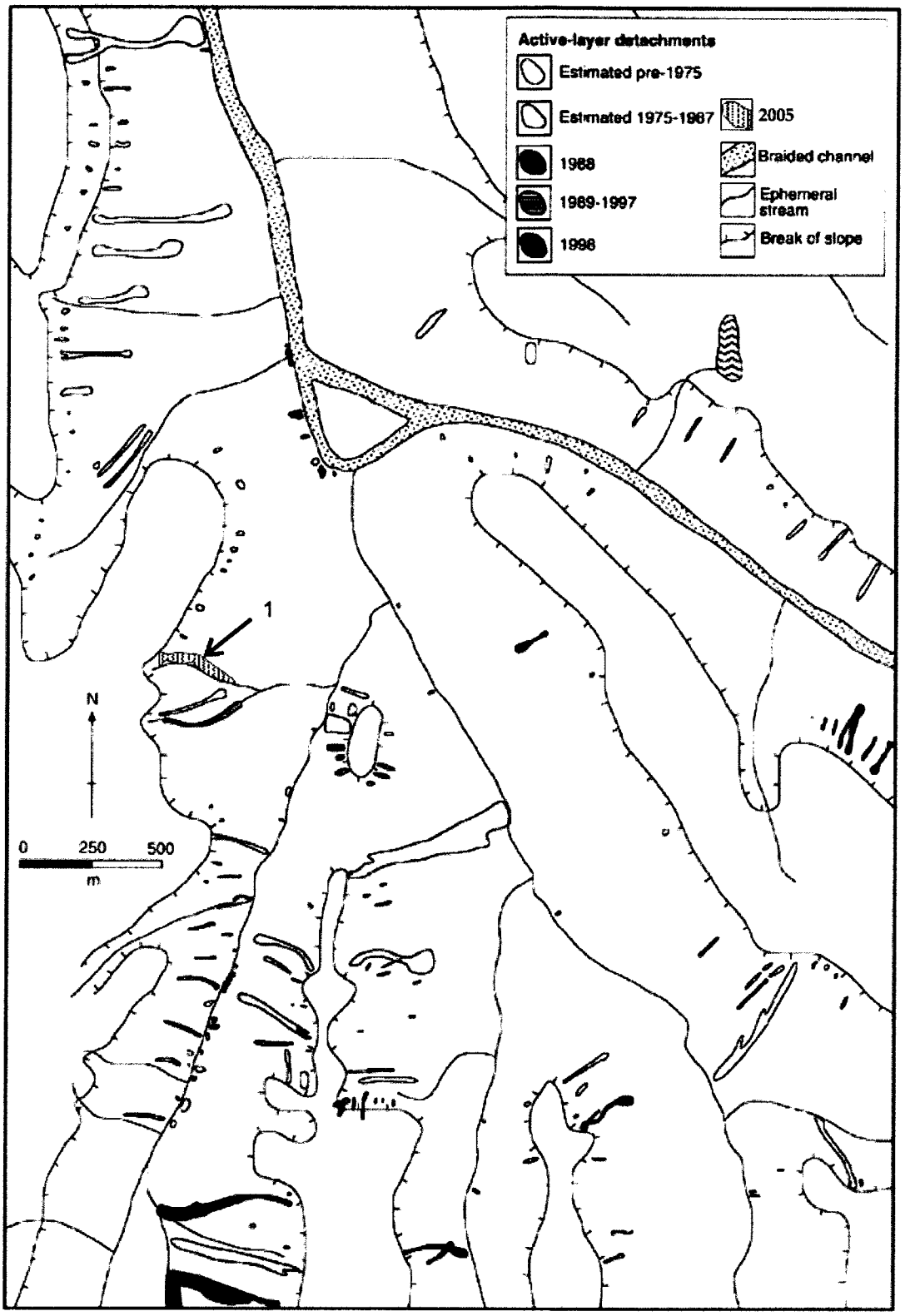

Figure 4-4. Map of the 2005 active layer detachment studied at 'Big Slide Creek'. Modified from Lewkowicz and Harris (2005b) and updated to summer 2005.

4.1.2 Failure Morphology and History

Active layer detachments can be classified morphologically as compact, elongate, or complex (Lewkowicz and Harris 2005a). Active layer detachments representative of each form were observed on the Fosheim Peninsula (Table 4-1). Eleven failures were identified as having a compact morphology, six were elongate, and two were complex. Comparisons between study areas in terms of morphological dominance cannot be undertaken as only one failure was investigated in each of the HWC and BSC sites, and only two failures were investigated in the SC study area.

Table 4-1. Initiation location and failure form of 2005 active layer detachments on the Fosheim Peninsula.

Failure	Northing	Easting	Initiation location	Failure Form
SC-2005-01	8882235	526410	mid-slope	Elongate
SC-2005-02	8882135	526420	mid-slope	Elongate
BTC-2005-02	8881183	526000	crest-slope	Compact
BTC-2005-03	8881207	526013	crest-slope	Compact
BTC-2005-04	8883485	525250	mid-slope	Elongate
BTC-2005-07	8882560	525352	crest-slope	Complex
BTC-2005-08	8882235	525752	crest-slope	Compact
BTC-2005-10	8879736	525620	crest-slope	Compact
BTC-2005-11	8879726	525623	crest-slope	Complex
BTC-2005-12	8879716	525617	crest-slope	Compact
BTC-2005-13	8879937	525180	mid-slope	Elongate
BTC-2005-14	8880450	525280	crest-slope	Compact
BTC-2005-15	8881083	525588	crest-slope	Compact
BTC-2005-16	8882360	525102	crest-slope	Compact
BTC-2005-17	8881485	525302	crest-slope	Compact
BTC-2005-18	8881474	525256	crest-slope	Compact
BTC-2005-19	8881472	525317	crest-slope	Compact
HWC-2005-01	8878744	549923	crest-slope	Elongate
BSC-2005-01	8848864	552225	mid-slope	Elongate

Table 4-1 also indicates the local initiation location for each failure (see Section 3.1.2 for discussion of local initiation locations). Five elongate failures initiated at a mid-

slope location. All compact and complex failures, in addition to one elongate failure, initiated at crest-slope locations.

Detailed ground surveys of seven failures, representative of each morphology type and study area, provide information regarding morphological characteristics specific to each failure. Morphological characteristics include overall length, maximum width, scar length, scar height, slide mass thickness, scar floor gradient, slide mass gradient and overall gradient. Scar length measurements are approximate because given the time between failure initiation and investigation (1 year), headwall recession took place in some cases and it was difficult to quantify the recession due to disintegration and/or rotation of collapsed blocks and to definitively attribute the collapsed block to headwall recession as opposed to sidewall collapse. In addition, potential dynamic loading of downslope terrain and movement via compression rather than translation, would result in the formation of a track zone and in some cases it was difficult to establish the boundary between the scar zone and track zone. Additional morphological characteristics described include lateral compression ridges, side disturbed zones, lateral gashes, transverse compression ridges, and other features characteristic of the main displaced block(s) and trailing blocks. Such morphological characteristics and features provide clues as to failure initiation, progression and termination history.

The stratigraphy of active layer detachment sediments were described with the aid of trial pits excavated in scar floors, tracks, displaced masses, compression ridges, and toe zones. Between one and three trial pits were excavated at each of the seven failures and were described in detail.

4.1.2.1 Station Creek Study Area

Two failures from the SC study area, SC-2005-01 and SC-2005-02, were described in detail (see Figure 4-1).

4.1.2.1.1 SC-2005-01

The morphological features of SC-2005-01 are displayed on Figure 4-5 while the sedimentological features of three trial pits are displayed in Figures 4-6 through 4-8. Figure 4-9 illustrates the inferred failure history of SC-2005-01.

Failure Morphology

Active layer detachment SC-2005-01 is comprised of an asymmetrical Y-shaped scar zone with each arm attaining a depth of approximately 0.5 m (Figure 4-5). The gradient of the northern scar floor ranged between 3 and 12°, while the southern scar floor gradient ranged between 3.5 and 13°. The northern and southern scar zones had attained total lengths of approximately 85 and 57 m, respectively. Maximum widths of the northern and southern scar zones were 36 and 38 m, respectively. Numerous blocks of varying sizes (0.5 – 7 m diameter and up to 0.5 high) were located within each scar zone. Several ice wedges, trending both cross-slope and parallel-slope, were exposed at the headwalls and edges of each scar zone. Active thermokarst activity (ice melt) was occurring at the exposed ice wedge locations.

The inferred track zone was 12 m long, had a maximum width of 36 m and a 2° gradient. The scar and track zone floors were characterized by uneven surfaces marked by grooves and dissected by rills. The track zone was also characterized by numerous trailing blocks (0.5 – 2 m diameter and up to 0.5 m high) and several ice wedges were exposed along the edges. Shallow mudflows accumulated at the rear of the displaced mass, partially covering the track and trailing blocks for a distance of 10 – 15 m.

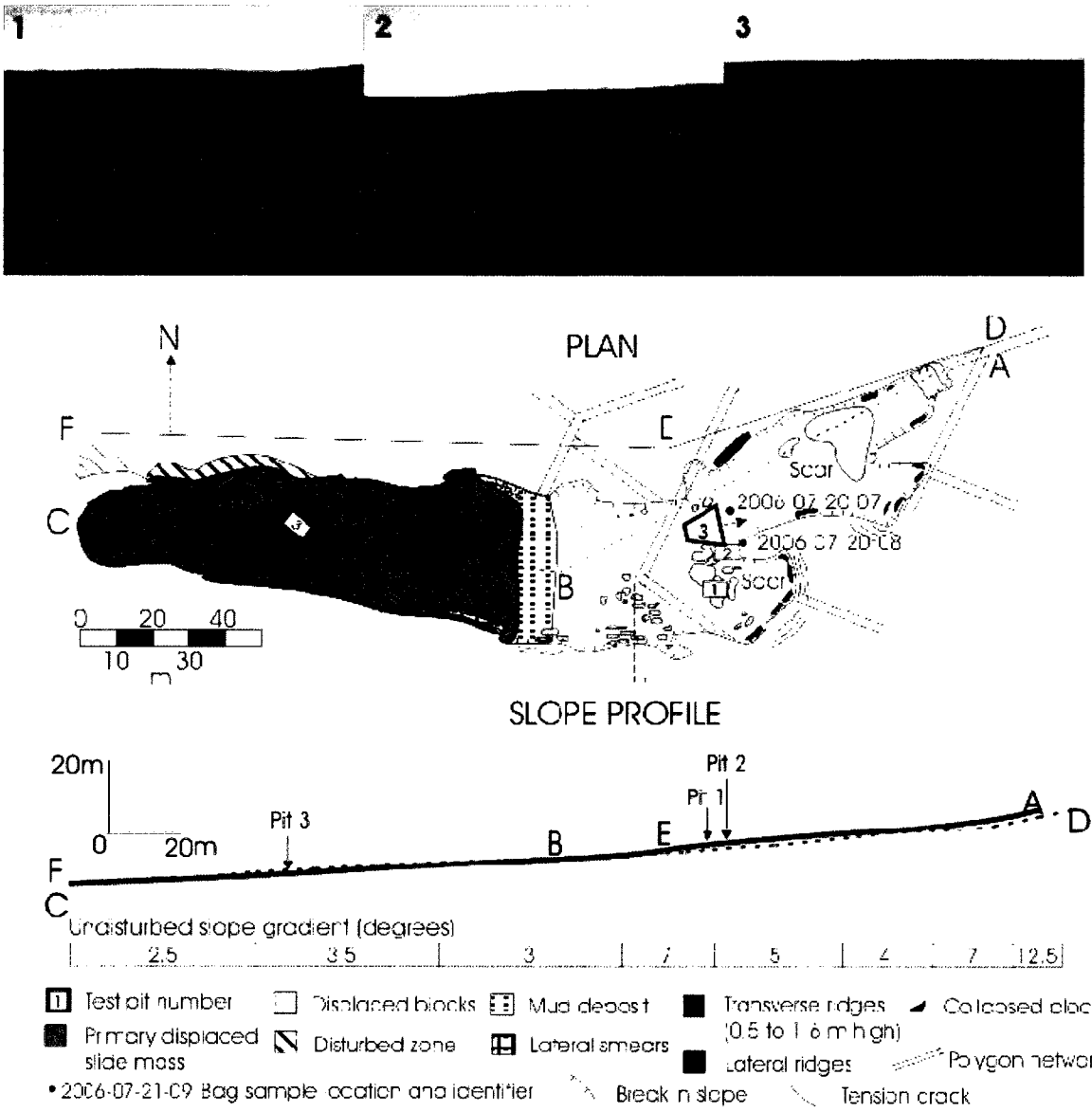

Figure 4-5. Plan and profile of elongate failure, SC-2005-01. Sketch movement direction towards the left. Sketch developed from a combination of field mapping with tape measure and GPS, and aerial mapping from helicopter surveys. Photo locations and orientation are shown on the map. Photo 1 shows the shear gash and side disturbed zone along the northern margin of the failure. Photo 2 shows the lateral ridge along the southern margin of the failure. Photo 3 shows the bare scar floor with evidence of thermokarst activity.

The displaced mass was approximately 121 m long with a maximum width of 47 m and ranged in gradient from 1.5 - 6°. The displaced mass is characterized by two sets of transverse ridges, up to 1.6 m high with an intact vegetation mat. The dominant set of

ridges trends E-W while the second set trends ESE-WNW. Some water had seeped through the displaced mass to fill hollows between the ridges. Both edges of the displaced mass were marked by vertical shear gashes extending approximately 0.5 m to the thaw plane. Lateral compression ridges up to 1.7 m high, some with smearing on the inside wall, were observed along both edges. Within the displaced mass, adjacent to the southern edge, was a unique whitish patch of dry soil with minimal vegetation. This patch could be traced upslope 23 m to a similar patch of ground within the adjacent undisturbed terrain. Adjacent to the northern margin of the displaced mass, near the front, was an extensive disturbed zone approximately 50 m long and up to 5 m wide. The central part of the displaced mass was generally 0.5 m thicker than the active layer in the adjacent terrain.

The front of the displaced mass was marked by a gradual disappearance of transverse ridges. Where the front encountered drier, hummocky terrain, the transverse ridges were comprised of broken hummocks, 0.15 – 0.35 m high, which had overturned in some cases.

Failure Stratigraphy

Three trial pits were excavated at SC-2005-01. The first two trial pits, TP 1 and TP 2, were located on the downslope side of trailing blocks within the scar zone (see Figure 4-5). The integrity of the blocks and the presence of grooves on the adjacent scar floor suggest that the blocks were sitting on the original failure plane.

TP 1 was comprised of two units; an upper dry to slightly moist, soft to stiff sandy silt unit with some clay and increasing clay content with depth sharply separated from a lower moist, soft clayey silt unit (Figure 4-6). The upper unit had no plasticity while the lower unit displayed moderate plasticity. The sharp boundary between the two units was the perceived failure plane. Pockets and flames of the lower unit noted within the upper unit were suggestive of fluid escape and plastic deformation associated with overloading.

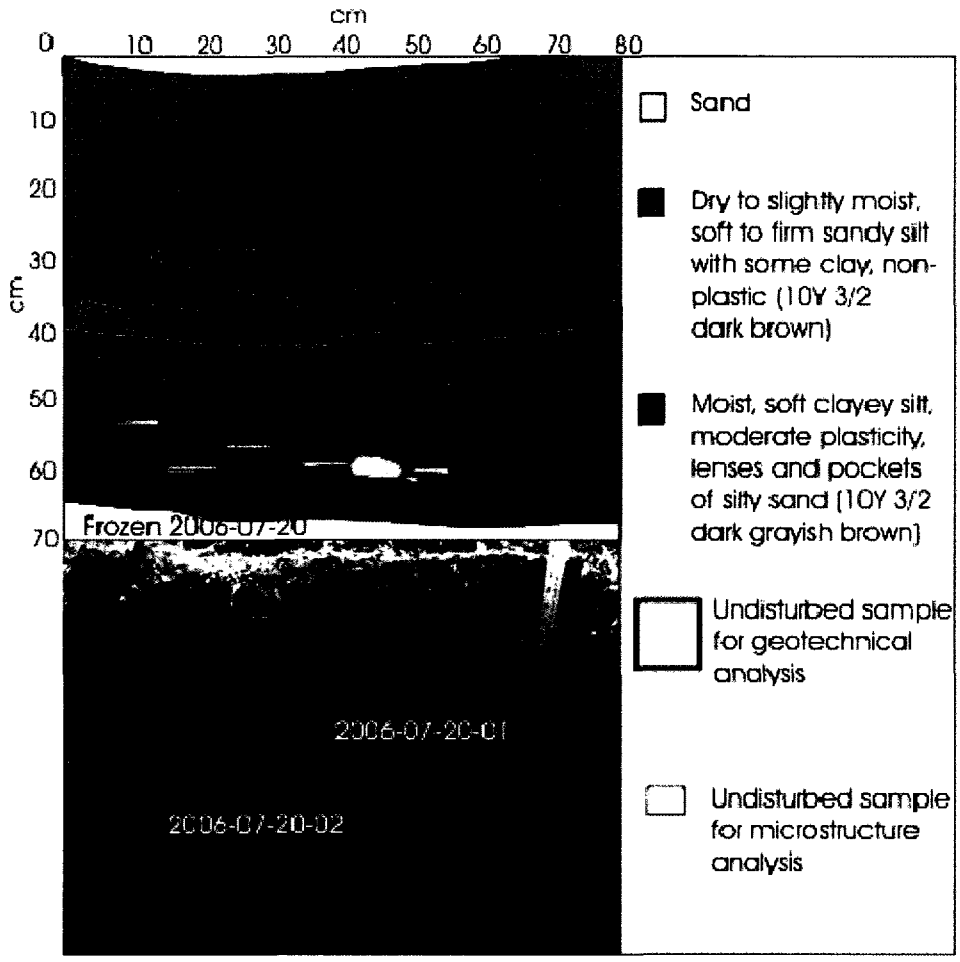

Figure 4-6. Trial pit description of TP 1 excavated on downslope side of a trailing block within the scar zone of SC-2005-01. Trial pit face is transverse to movement direction.

Significant cryoturbation of dry, non-plastic hummocks and silt to clayey silt sediments were noted in the near-surface of TP 2 (Figure 4-7). The perceived failure plane was bounded by an upper dry to slightly moist, stiff silty clay with blocky structure unit and a lower moist, soft, clayey silt with some sand and no structure unit. Below these units were numerous sand units distinguished from each other by colour.

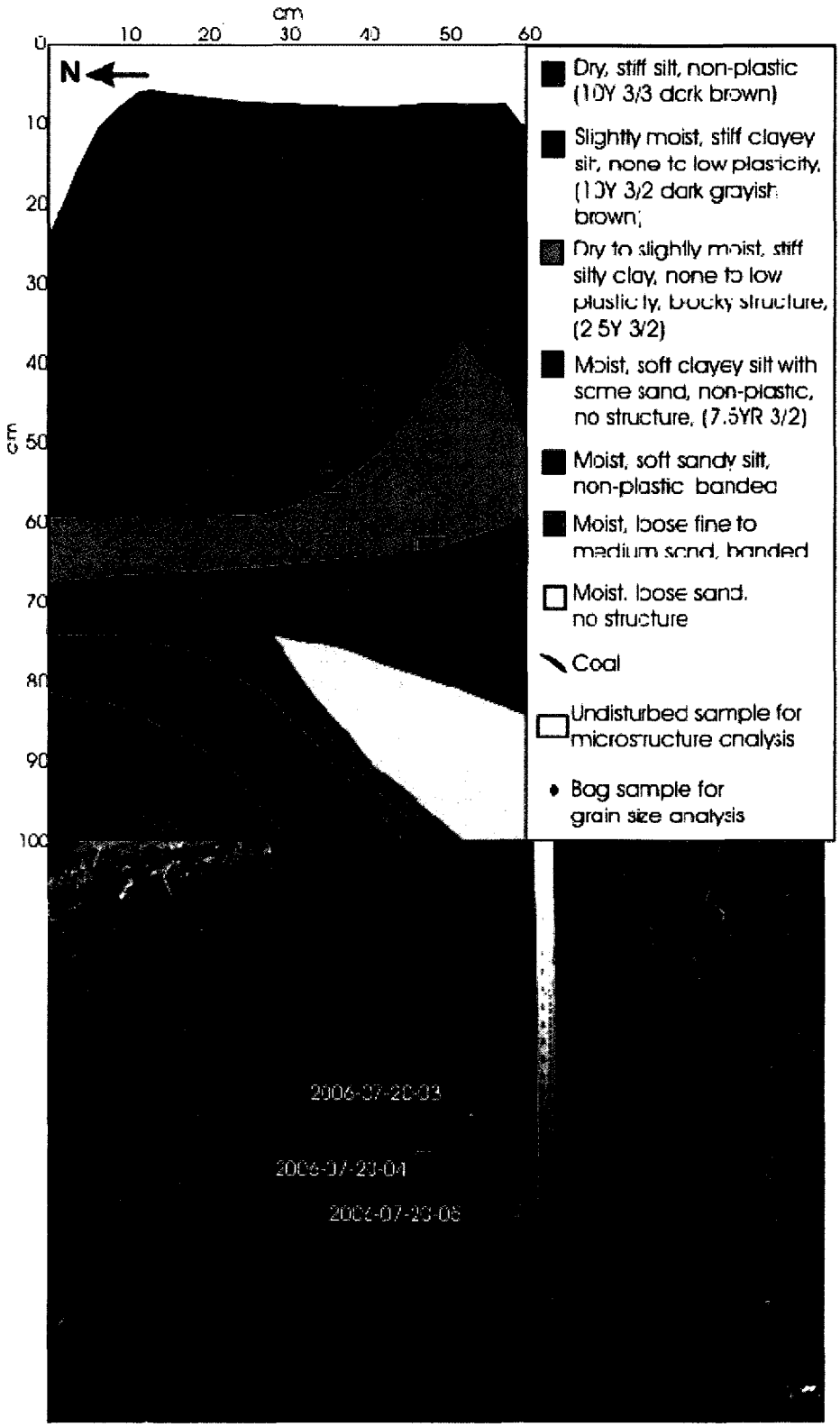

Figure 4-7. Trial pit description of TP 2 excavated on downslope side of a trailing block within the scar zone of SC-2005-01. Trial pit face is transverse to movement direction.

The third trial pit, TP 3 (Figure 4-8), was excavated across a transverse ridge within the compression zone. A moist to wet, soft, clayey silt unit overlain by a 0.06 m thick intact vegetation mat was exposed within the trial pit wall. Overturning of the vegetation mat had occurred on the downslope side of the ridge as evidenced by buried green organics. Pockets and stringers of moist, loose sand with some silt were injected upwards into the clayey silt unit. These upward injection features are suggestive of fluid escape associated with overloading. Because surface aggradation had occurred at this site, the failure plane could not be observed at it was beneath the frost table.

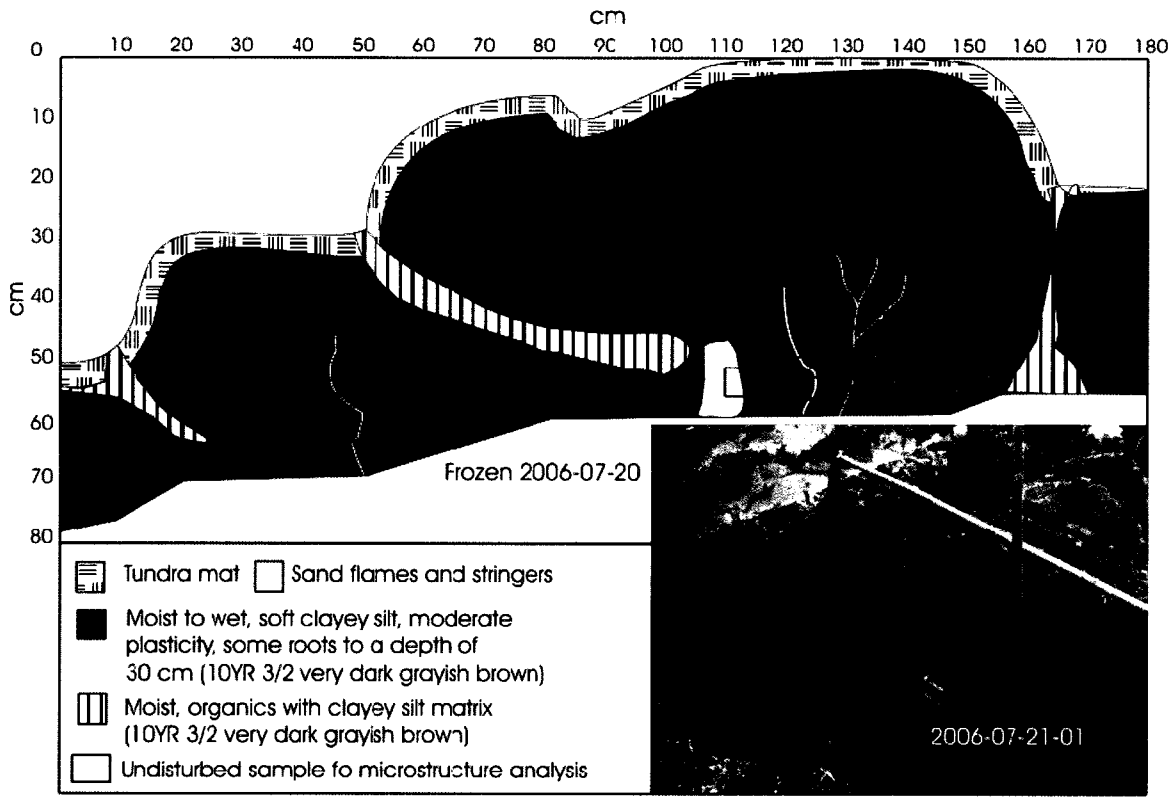

Figure 4-8. Trial pit description of TP 3 excavated across a transverse ridge within the compression zone of SC-2005-01. Trial pit face is parallel to movement direction (towards the left).

Inferred Failure History

Field mapping and trial pit description indicated that SC-2005-01 occurred in two movements (Figures 4-5 and 4-9). This conclusion is based on the observation of two

sets of transverse ridges within the displaced mass, pronounced lateral compression ridges, and disturbed zones in the adjacent terrain. The initial movement coincides with the southern branch of the asymmetrical Y-shaped scar zone. Mass movement started by sliding at a mid-slope location where the gradient of the adjacent undisturbed terrain is between 4 and 7°. Rates of movement are inferred to have been slow, prolonged and discontinuous.

Figure 4-9. Aerial view of SC-2005-01 showing primary and secondary displaced masses and associated scar zones, displaced blocks and extensive side disturbed zone.

The displaced mass travelled downslope within a moist cross-slope depression. Marginal shear gashes and large lateral compression ridges with smears on the inside (indicative of continued movement of the displaced mass) were created as the mass moved downslope. The transverse ridges were created as the moving mass thickened as it encountered more resistant downslope material. The lack of a pronounced terminal

push ridge at the front of the displaced mass suggests that the displaced mass gradually stopped moving.

The combination of loss of downslope support and thermokarst activity caused recession along a NE-SW trending ice wedge forming the northern branch of the asymmetrical Y-shaped scar zone. The second displaced mass released from this recessional activity travelled over the track of the initial movement before impacting the southern edge of the initial track zone, creating a large 1.6 m high lateral compression ridge. Following impact, the second displaced mass changed direction and began to travel downslope in a WNW direction before catching up to and appending to the trailing edge of the initial displaced mass. This impact created the second set of transverse ridges observed within the displaced mass which trended to the WNW. The second set of ridges superimposed themselves on the ridges of the initial movement. The second set of ridges did not extend to the front of the displaced mass but were directed towards the northern edge of the initial displaced mass. Compression associated with the second mass extended into the un-mobilized terrain to the north of the failure, near the front, and created an extensive disturbed zone.

Injection features noted within the compression zone deposits suggested escape of fluid from the saturated failure plane during overloading and thickening of the displaced mass as it moved downslope. Movement appears to have ceased due to a reduction in slope, down to 2.5°, and the termination of loading at the trailing edge of the failure block from the impact of additional displaced blocks. The amount of downslope movement of the combined block was at least 23 m.

Ongoing tertiary activity occurred following the initial movements from the north and south branches of the Y-shaped scar zone. This activity included additional headwall recession releasing blocks (particularly in the northern branch of the scar zone), the development of tension cracks, the collapse of blocks within the headwall complex and along the sidewalls of the scar zone, and upslope recession along ice wedges

exposed within the headwall complex and along the edges of the track zone. The blocks released from the headwall complex as a result of tertiary activity only traveled small distances (up to 4 m) and came to rest before reaching the trailing edge of the amalgamated displaced mass.

4.1.2.1.2 SC-2005-02

The morphological features of SC-2005-01 are displayed on Figure 4-10 while the sedimentological features of one trial pit is displayed in Figures 4-11. Figure 4-12 illustrates the inferred failure history of SC-2005-02.

Failure Morphology

Active layer detachment SC-2005-02 is characterized by three displaced masses and is mainly comprised of a scar zone and compression zone (Figure 4-10). The scar zones of the primary and secondary displaced masses were distinguishable. The primary displaced mass scar zone was characterized by a scarp height of approximately 0.7 m and a scar floor gradient ranging between 7 - 14.5°. The maximum length and width of the primary displaced mass scar zone were 15 m and 42 m, respectively. The secondary displaced mass scar zone was characterized by a scarp height of approximately 0.75 m and a scar floor gradient ranging between 7 - 19°. The maximum length and width of the secondary displaced mass scar zone were 42 m and 32 m, respectively. One large displaced block (approximately 5 m diameter) and several smaller blocks (0.5 – 2.0 m diameter) were located within the scar zone. The edges of the scar zone were marked by 1.0 – 1.5 m high lateral push ridges. The uneven scar floor was marked by grooves and dissected by rills.

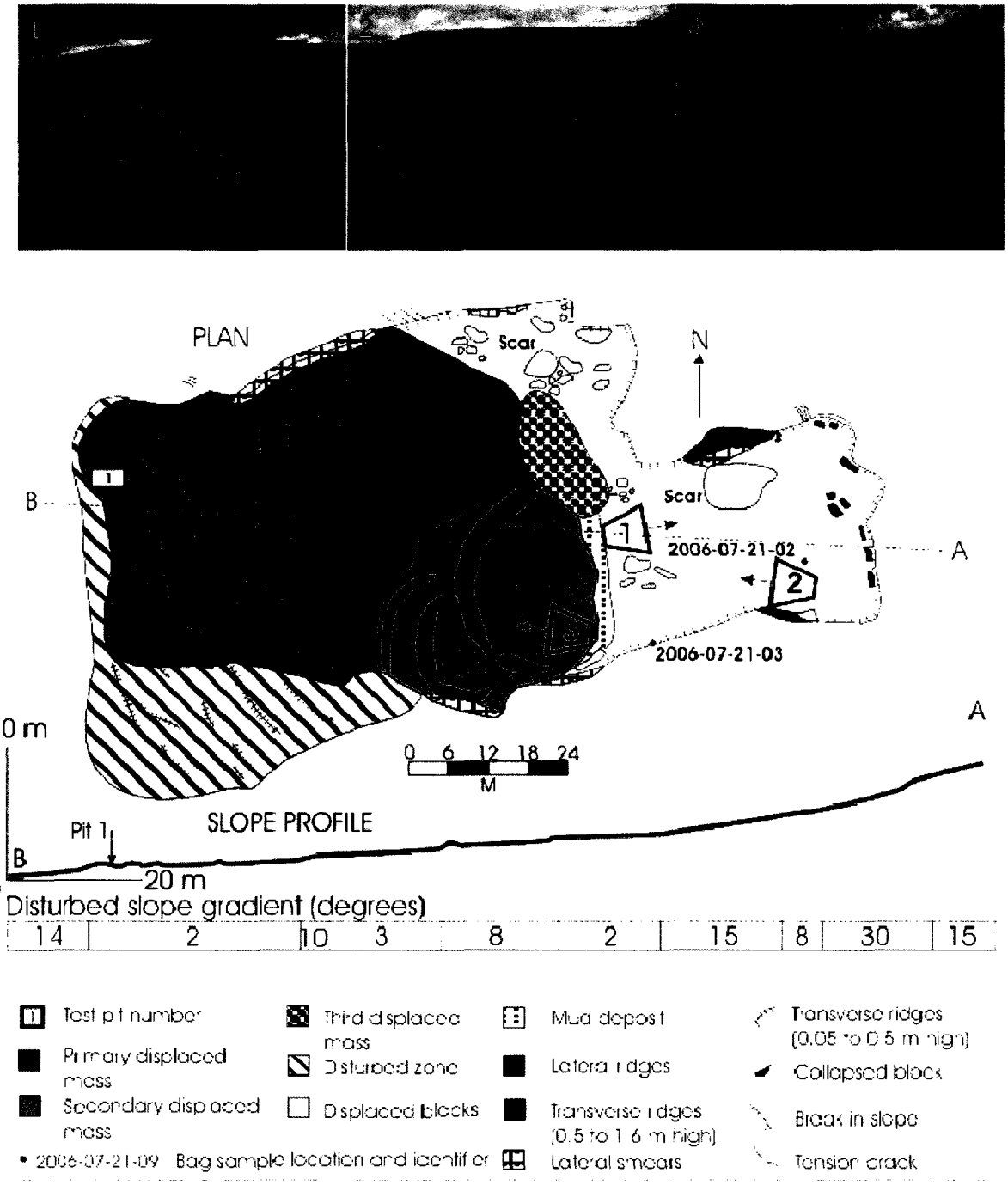

Figure 4-10. Plan and profile of complex-elongate failure, SC-2005-02. Sketch movement direction towards the left. Sketch developed from a combination of field mapping with tape measure and GPS, and aerial mapping from helicopter surveys. Photo locations and orientation are shown on the plan. Photo 1 shows the scar floor with some trailing blocks and evidence of thermokarst activity. Photo 2 shows the displaced mass. Photo 3 shows the large transverse ridge within the secondary displaced mass with smearing on the upslope side.

The maximum length and width of the primary displaced mass were 66 m and 48 m, respectively, with an overall gradient of 9.5°. The upper half of the primary displaced mass was flat and relatively undisturbed. The lower half of the primary displaced mass was characterized by two sets of transverse ridges, representing two distinct height categories. Both sets of ridges trended in an E-W direction. The first set of transverse ridges was 0.5 – 1.6 m high, flat-topped or peaked and typically found near the front of the displaced mass. The second set of transverse ridges were typically found up gradient of the first set of ridges, yet still within the lower half of the primary displaced mass, and were 0.05 – 0.5 m high. Many of the second set of ridges exhibited brittle fracturing.

The entire front of the primary displaced mass was marked by a 1.0 – 1.2 m high terminal compression ridge. Beyond the compression ridge, both to the west and south, was an extensive disturbed zone marked by 0.05 – 0.5 m high transverse ridges, many of which exhibited brittle fracturing. The down gradient and southern limit of the disturbed zone was marked by a gradual disappearance of the transverse ridges.

The maximum length and width of the secondary displaced mass was 30 m and 29 m, respectively with a gradient of approximately 3°. Located within the interior of the secondary displaced mass was a 1 m high ridge with smearing on the upslope side of the ridge. The southern edge of the secondary displaced mass was marked by a 0.2 – 2.0 m high lateral ridge with smearing on the interior side of the ridge. The front of the secondary displaced mass is embedded within the interior of the primary displaced mass. The front was characterized by 0.05 – 0.5 m high transverse ridges.

Attached to the trailing edge of both the primary and secondary displaced masses was a large oblong-shaped third displaced mass. The third relatively undisturbed displaced mass was approximately 5 m long and 15 m wide with an overall gradient of 3.5°. A compression ridge was not observed at the front of the third displaced mass.

Failure Stratigraphy

One trial pit, TP1, was excavated across the terminal compression ridge (see Figure 4-10). Plastic deformation is suggested by the wavy contact between the upper hard clayey silt unit and the lower lens of soft to stiff clayey silt (Figure 4-11). Sand flames within the latter unit suggest fluid escape associated with overloading. A thin layer of green organics is embedded within the upper hard clayey silt unit on the downslope side of the terminal push ridge. The green nature of the organics suggests that the ground surface within which they are rooted had been relatively recently over-ridden by the overlying sediment.

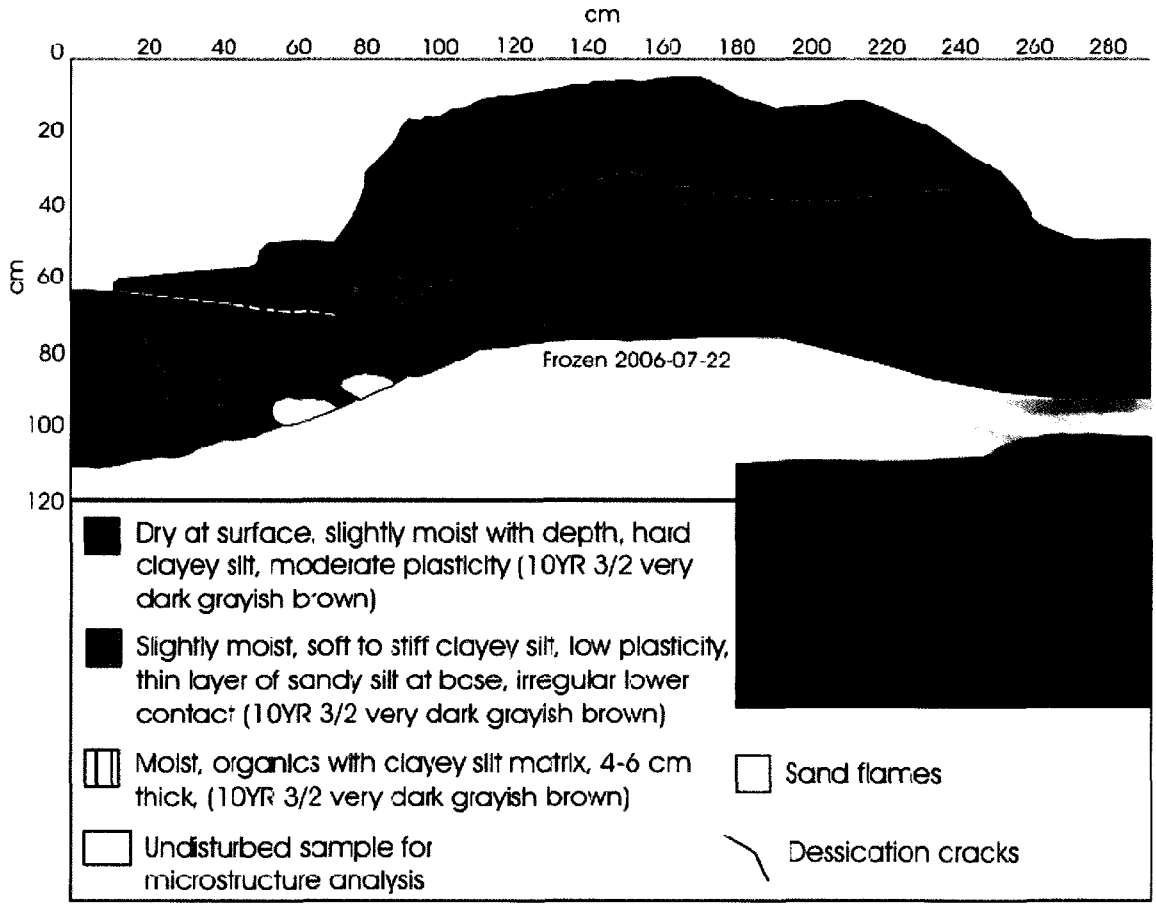

Figure 4-11. Trial pit description of SC-2005-02 TP1 across terminal transverse push ridge. Movement direction towards the left.

Inferred Failure History

Field mapping and trial pit description indicated that SC-2005-02 occurred in three movements (Figures 4-10 and 4-12). Rates of movement are inferred to have been rapid, prolonged and discontinuous. Movement of the primary displaced mass appears to have started by sliding at a mid-slope location where the gradient of the adjacent undisturbed terrain was approximately 14°. The primary displaced mass travelled downslope at least 15 m. The movement was comprised of the initial translational sliding followed by compression evidenced by presence of transverse ridges within the displaced mass and a large terminal push ridge at the front of the mass. The transverse and terminal push ridges were created as the primary displaced mass ploughed into stationary downslope terrain. Ultimately, the extensive height (1.2 m) and width (1.5 m) of the terminal push ridge prevented further movement. Within the lower half of the primary displaced mass are numerous small and large transverse ridges of which most displayed brittle fracturing. The absence of an intact vegetation mat and/or soil surface crust on the transverse ridges suggests the failure did not follow or encounter a pre-existing moist cross-slope depression and that all movement occurred within pre-existing dry terrain. The majority of the compression in the northern half of the primary displaced mass appears to have been taken up by compression within the mass (forming the transverse ridges) and from impact with the adjacent undisturbed terrain (forming the large lateral compression ridge along the north edge of the mass). Whereas, the majority of the compression in the southern half of the primary displaced mass appears to have been taken up by the adjacent terrain (forming an extensive disturbed zone downslope of the terminal push ridge that is characterized by numerous small transverse ridges).

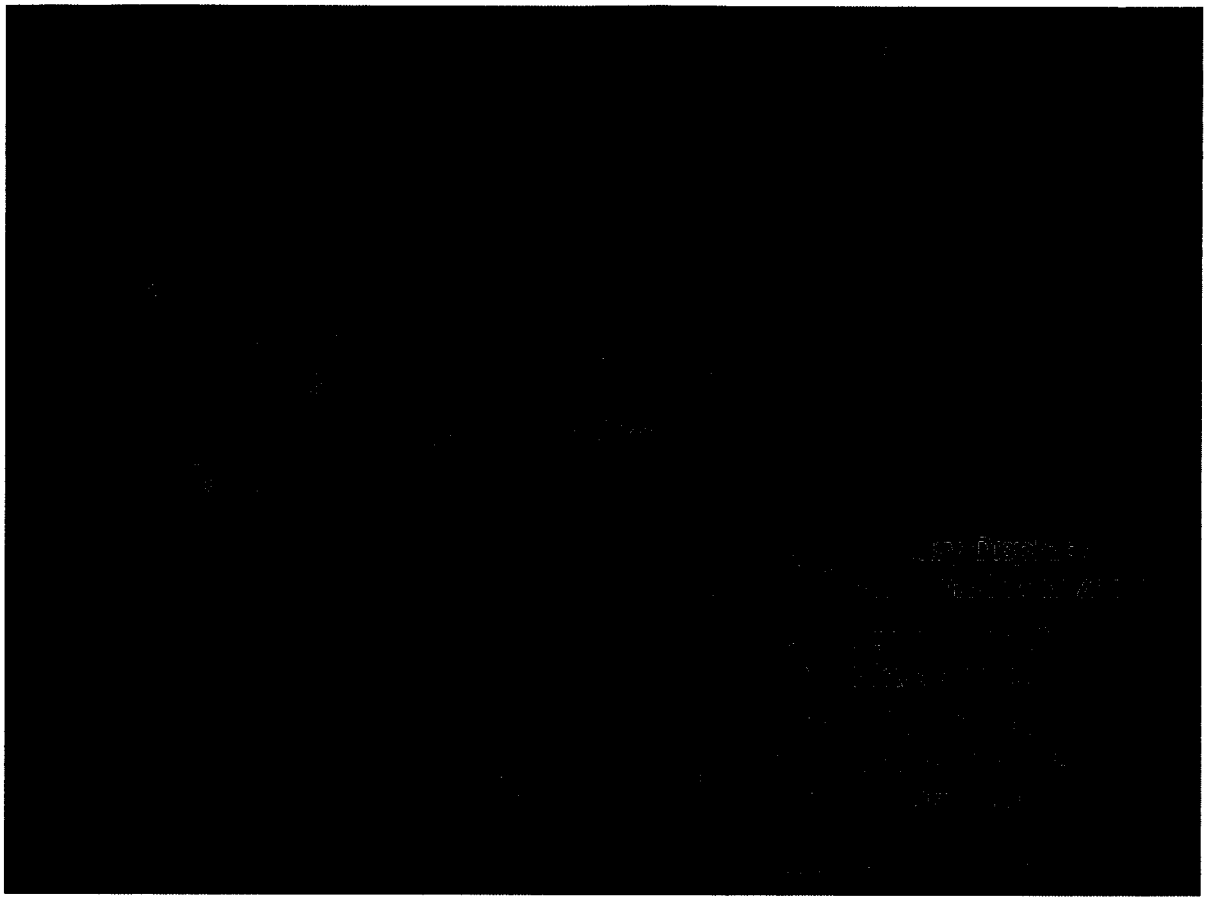

Figure 4-12. Aerial view of SC-2005-02 showing primary and secondary displaced masses and associated scar zones, displaced blocks, and frontal disturbed zone. The failure visible in the top left corner of the photo is SC-2005-01.

The dry ground surface conditions within the primary displaced mass and adjacent terrain contrasts with evidence of plastic deformation and fluid escape at the failure plane. This suggests that while the surface of the displaced mass remained as an intact, rigid block, thawing of the frost table created saturated low strength conditions along the failure plane.

Sliding of the secondary displaced mass appears to have been associated with the loss of support from the previous primary movement. The secondary displaced mass detached and travelled downslope on gradients ranging from 7 to19°. Large lateral compression ridges were formed along the edges of the scar zone as the mass moved downslope for approximately 42 m. The secondary displaced mass moved into a gap left

between the trailing edge of the primary displaced mass and the adjacent intact terrain (see Figure 4-10 for an example of a similar gap along the northern edge of the primary displaced mass). As the secondary displaced mass ploughed into the now stationary primary displaced mass, some small and large transverse ridges were created within the secondary displaced mass. In addition, a 1.2 m high lateral compression ridge was created along the southern edge as the secondary displaced mass impacted the adjacent terrain.

The presence of a ridge, transverse to the direction of movement with smearing on the upslope side, within the secondary displaced mass suggests that the secondary displaced mass originated within the footprint of a historical failure. The ridge likely represents a lateral smear and/or push ridge related to the historical failure (the footprint of which extends further to the south of SC-2005-02) that was entrained during the movement of the secondary displaced mass. The location of the lateral smear within the stationary secondary displaced mass, e.g. near the front, suggests that the secondary displaced mass experienced minimal counter-clockwise rotation as the mass filled the gap between the primary displaced mass and the adjacent terrain (Figure 4-13).

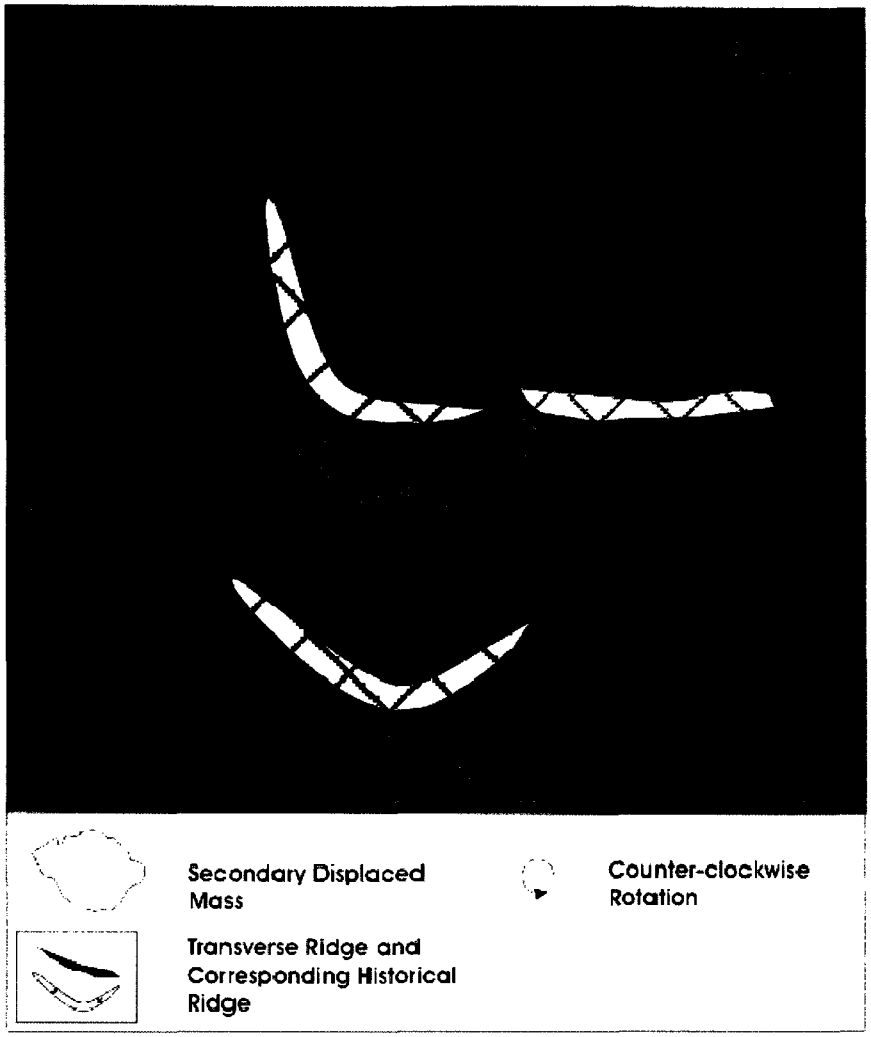

Figure 4-13. Aerial view of SC-2005-02 showing the rotation of the secondary mass, the original orientation of two transverse ridges within the mass prior to rotation and the corresponding ridges from a historical failure, and the final orientation of the transverse ridges within the mass.

Sliding of the third displaced mass also appears to have been associated with the loss of downslope support from the previous primary movement. The third displaced mass detached and travelled downslope on a very steep gradient for approximately 15 m before coming to a rest at the trailing edges of both the primary and secondary displaced masses. The lack of a terminal push ridge and transverse ridges within the third displaced mass suggests that movement was entirely by sliding and that there was no movement by compression.

At some point following movement of the third displaced mass, recession of the headwall led to mobilization of a large (5 m diameter) block. This block detached from the north corner of the headwall and travelled downslope approximately 15 m before coming to rest within the scar zone of the secondary displaced mass.

4.1.2.2 Black Top Creek Failure Morphology

Three failures from the BTC study area were described in detail. These are BTC-2005-04, BTC-2005-08, and BTC-2005-13 (see Figure 4-2).

4.1.2.2.1 BTC-2005-04

The morphological features of BTC-2005-04 are displayed in Figure 4-14 while the sedimentological features of three trial pits are displayed in Figures 4-15 through 4-17. Figure 4-18 illustrates the inferred failure history of BTC-2005-04.

Failure Morphology

Active layer detachment BTC-2005-04 is characterized by a single displaced mass and a significant track zone (Figure 4-14). The scar zone is characterized by a scarp height of approximately 0.8 m and a scar floor gradient of 6 - 15°. Maximum scar zone length and width were 28 m and 30 m, respectively. Numerous tension cracks were located along the headwall and sidewalls of the scar zone. Several collapsed blocks (0.5 – 2.0 m diameter) had detached from the headwall and sidewalls and were sitting on the scar floor. Several trailing blocks (0.5 – 1.0 m diameter) were also resting on the scar floor. The scar floor was marked by grooves and dissected by rills. Supra-permafrost groundwater from the scar zone and the surrounding terrain formed a small creek that meandered over the track zone and displaced mass, ponding just upslope of the Black Top Creek top of bank.

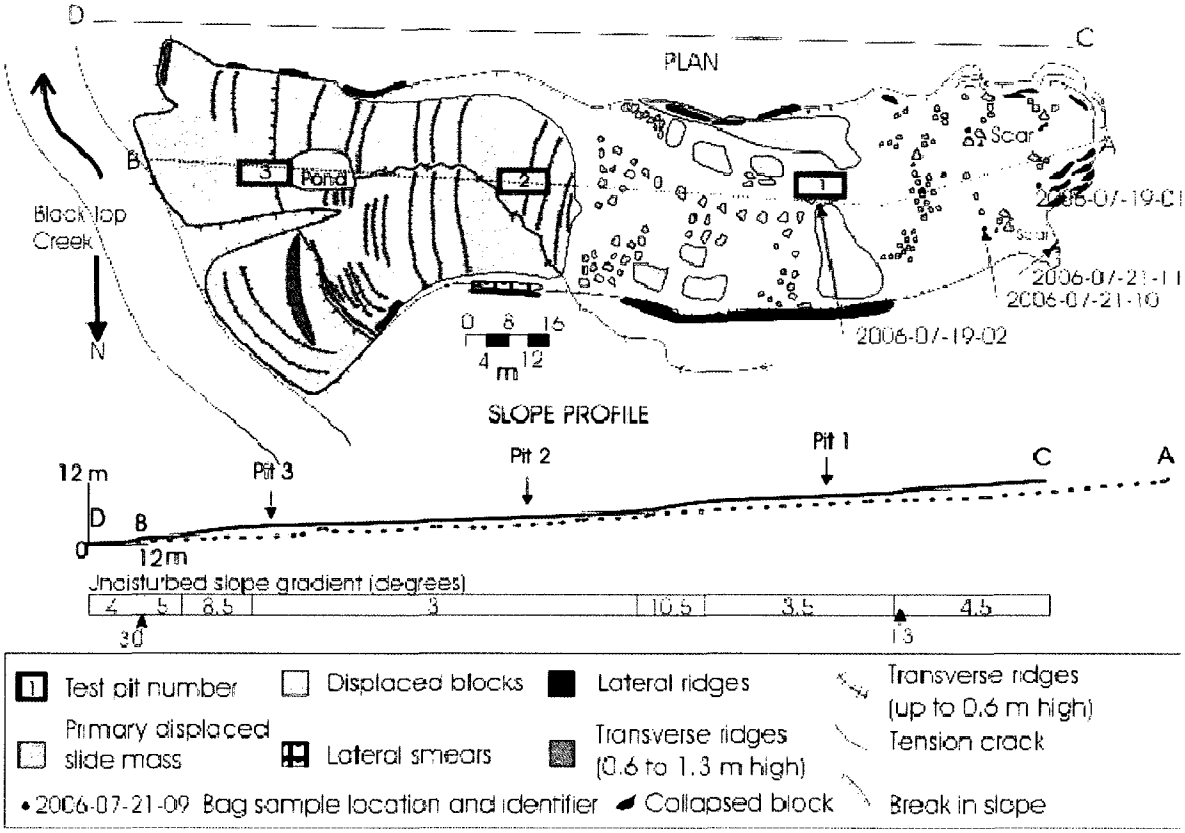

Figure 4-14. Plan and profile of elongate failure, BTC-2005-04. Sketch movement direction towards the left. Sketch developed from a combination of field mapping with tape measure and GPS, and aerial mapping from helicopter surveys.

The track zone length and width were measured as 70 m and 36 m, respectively. The overall gradient of the track zone ranged between 2 - 5°. The track zone was characterized by an uneven surface that was marked by grooves and dissected by rills. Numerous trailing and collapsed blocks (0.5 – 2.0 m diameter and approximately 0.7 m high) were resting on the track zone floor. Two large blocks (10 m and 15 m diameter, each approximately 0.7 m high) were resting on the track zone floor, the larger of which appeared to have impacted the southern edge of the track zone. Adjacent to the impact location was a 1.0 m high lateral compression ridge. An ice wedge was exposed along the southern edge of the track zone.

The length and width (measured at the Black Top Creek top of bank) of the displaced mass were measured as 80 m and 30 m, respectively. The slope gradient ranged

between 0 - 11° with the exception of the Black Top Creek top of bank where a bulge was observed. The slope gradient of the downslope side of the bulge was 20° while a 25° drop in slope was measured on the upslope side of the bulge. Minimal vegetation covered the displaced mass and numerous transverse ridges, trending E-W and up to 0.6 m high, were observed over the entire length of the displaced mass. Most of the transverse ridges displayed brittle fracturing. The northern edge of the displaced mass was marked by a 0.7 m high lateral compression ridge with smearing on the inside wall. Discontinuous lateral compression ridges, up to 0.8 m high, were also present along the southern edge of the displaced mass. A significant vertical shear gash was located between the displaced mass and the adjacent intact terrain on both margins, upslope of the Black Top Creek top of bank.

The toe of the displaced mass spilled over the Black Top Creek top of bank and down onto the active floodplain. The front of the displaced mass was marked by a large nearly vertical drop (up to 2.5 m). A pre-existing barrier at the top of bank caused a division of the displaced mass into a northern and southern lobe. Several transverse ridges ranging from 0.5 – 1.2 m high and up to 4 m wide were located within both lobes. Lateral compression ridges, up to 0.7 m high, were observed along the southern edge of the southern lobe.

Failure Stratigraphy

Three trial pits were excavated at BTC-2005-04 (see Figure 4-14). TP 1 was located on the downslope side of a trailing block within the track zone (Figure 4-15). The integrity of the block suggested that the block was likely sitting on the original failure plane. TP 1 was comprised of three units, all stiff clayey silt, distinguished from each other by structure. The presence of 1 to 4 mm diameter cryoaggregates dominated the structure of the upper unit, followed by a vertically elongated blocky structure containing blocks up to 20 mm in length. The failure plane was found within the third unit which exhibited a blocky to structureless structure.

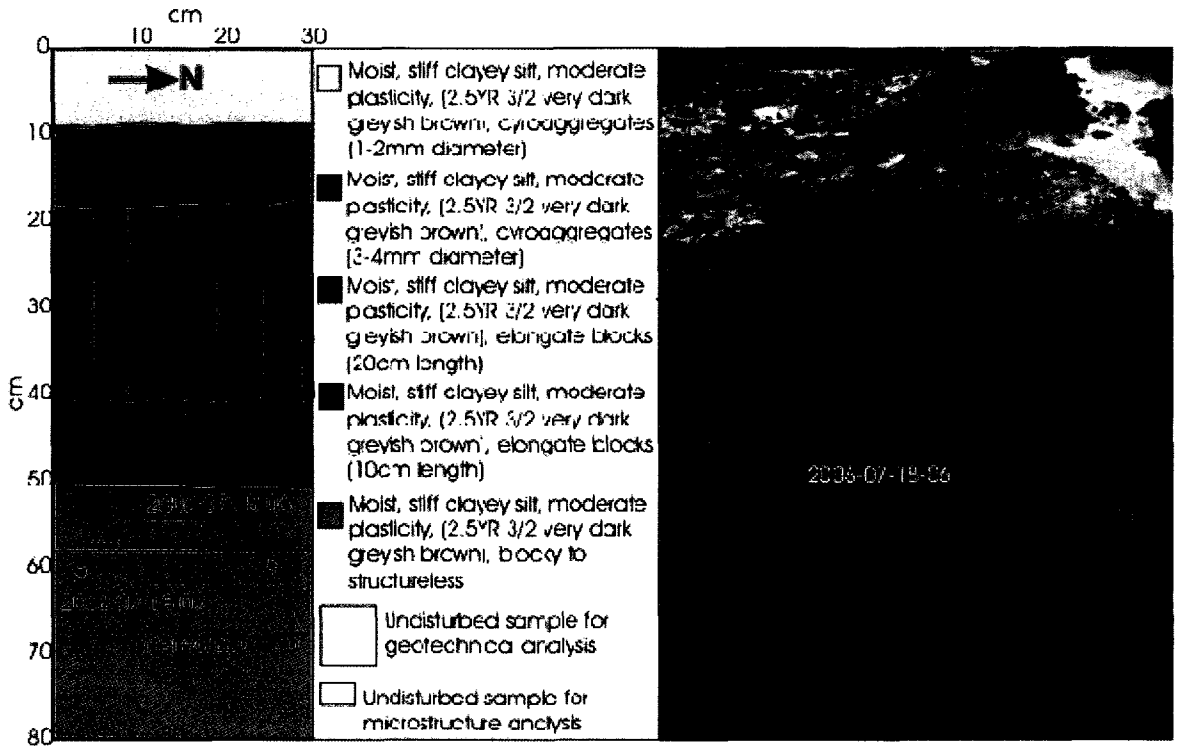

Figure 4-15. Trial pit description of BTC-2005-04 TP 1 excavated on downslope side of a trailing block within the track zone, transverse to the direction of movement.

TP 2 was excavated across a transverse ridge within the compression zone and was comprised of three units (Figure 4-16). All units consisted of clayey silt, distinguishable by their consistency and structure. Within the second unit (dry, non-cohesive cryoaggregate structure) were several emergent shear planes likely associated with compression of the displaced mass as it moved downslope. Insufficient depth of thaw prevented direct observation of the failure plane.

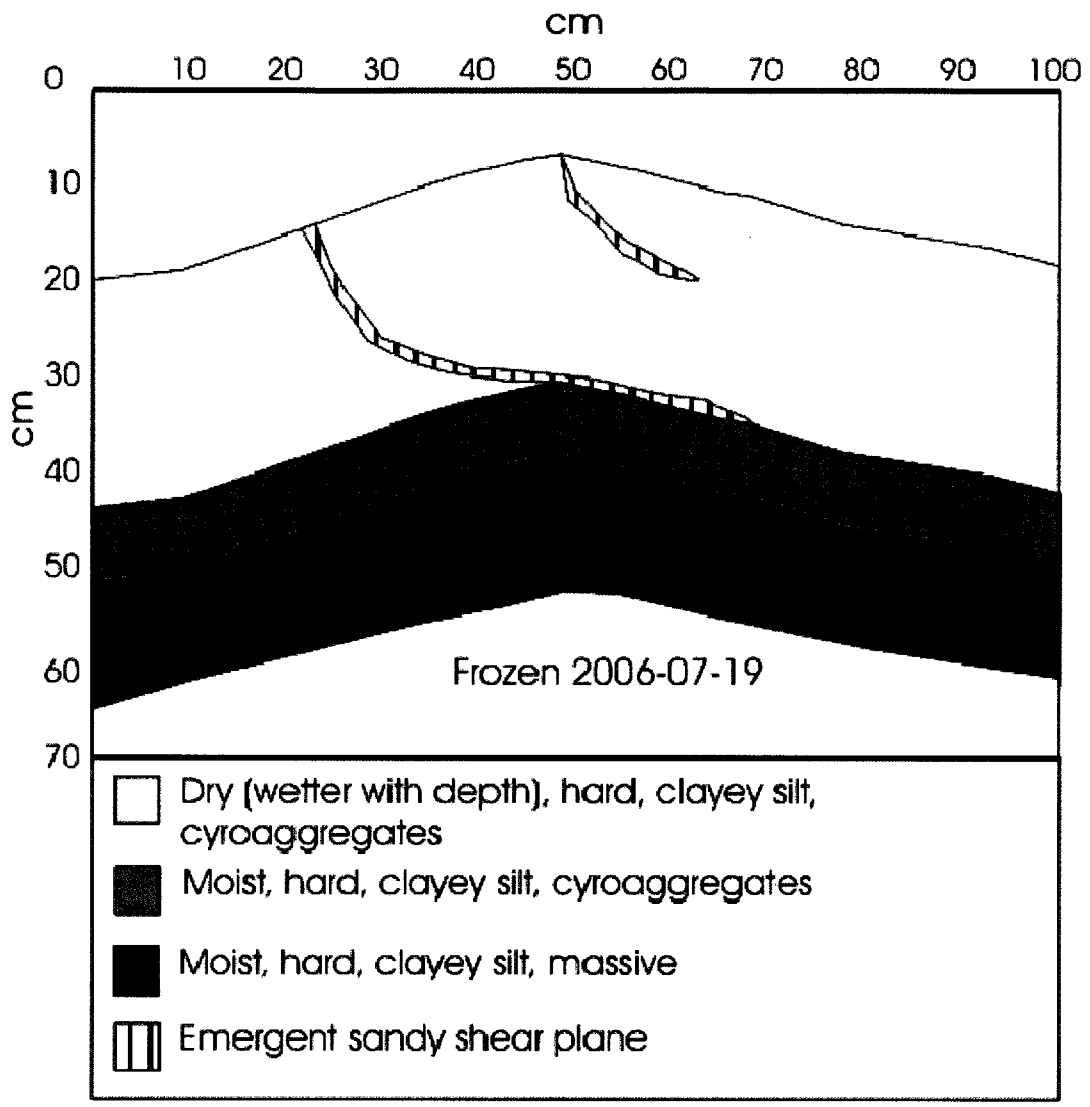

Figure 4-16. Trial pit description of BTC-2005-04 TP 2 across transverse ridge within the compression zone. Movement direction towards the left.

The third trial pit, TP 3, was a 5 m long trench excavated across a wide transverse ridge within the compression zone at the Black Top Creek top of bank (Figure 4-17). Exposed within the trial pit wall was a moist, soft, moderately cohesive, structureless clayey silt with sand unit overlain by a thin dry, brittle, cryoaggregate structured clayey silt unit. Within the lower unit, several emergent shear planes drew a moist, stiff, moderately cohesive, structureless clayey silt unit up towards the surface in the downslope direction. Buried organics on the downslope side of the ridge indicated over-

riding of the intact vegetation mat or over-turning of the transverse ridge. Insufficient thaw prevented direct observation of the failure plan.

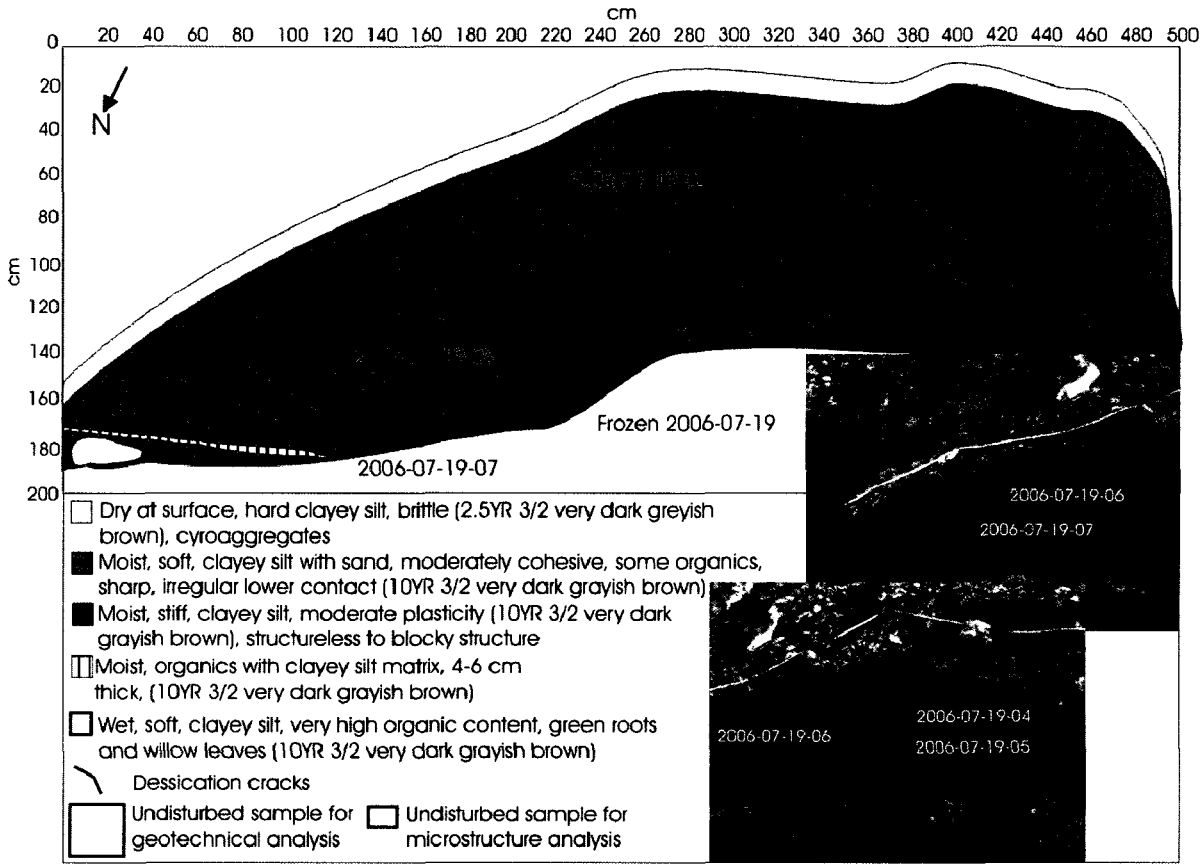

Figure 4-17. Trial pit description of BTC-2005-04 TP 3 across transverse ridge within the compression zone at the Black Top Creek top of bank. Direction of movement towards the left.

Inferred Failure History

Field mapping and trial pit description indicated that BTC-2005-04 occurred as a single movement (Figures 4-14 and 4-18). Rates of movement are inferred to have been slow, prolonged and continuous. Movement started by sliding at a mid-slope location where the gradient of the adjacent undisturbed terrain is generally 4°, with localized slopes of 13°. The displaced mass moved downslope approximately 95 m.

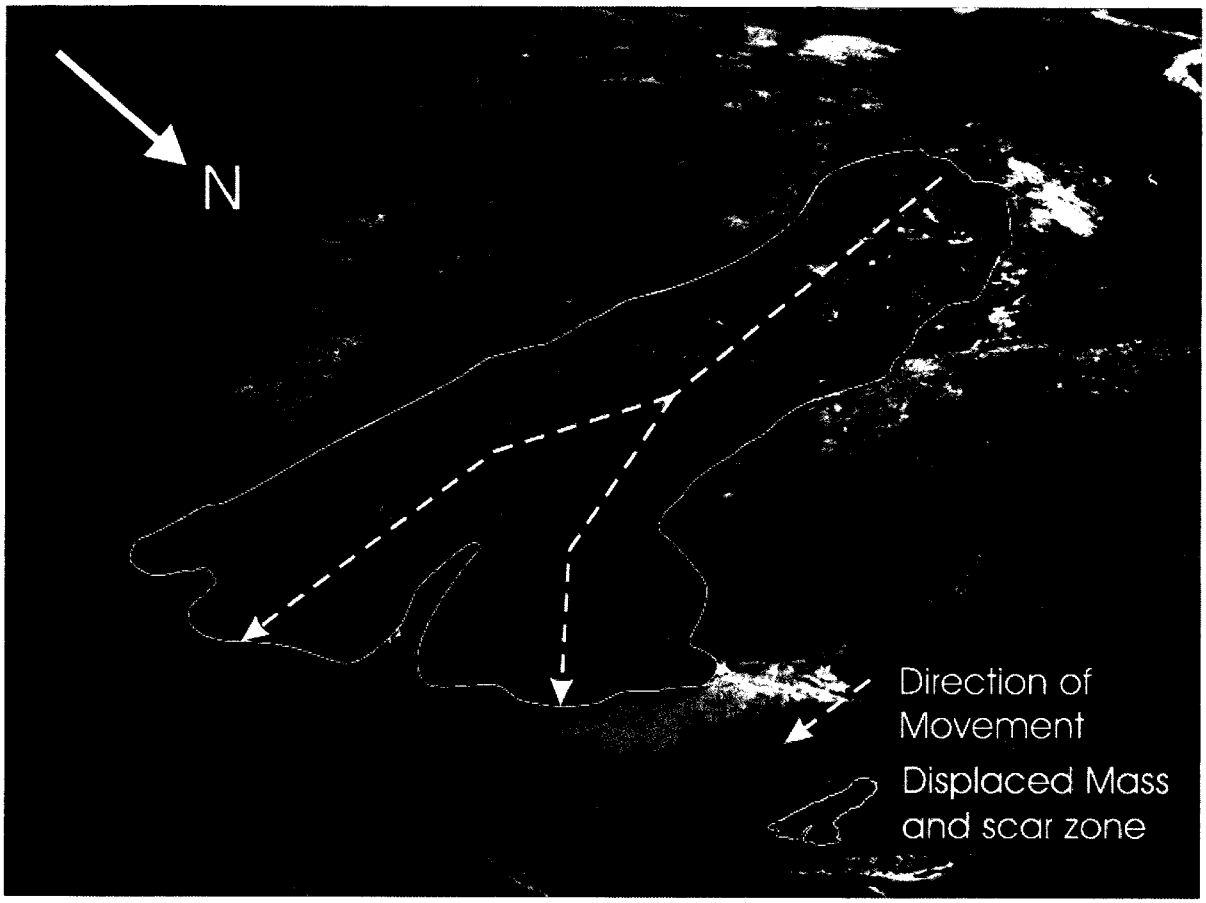

Figure 4-18. Aerial view of BTC-2005-04 showing a single primary displaced mass and associated scar zone, displaced blocks, and the two lobes of the toe zone.

The first 40 m of movement was characterized by a lack of lateral compression ridges suggestive of downslope movement with minimal frictional resistance from the adjacent intact terrain and downslope terrain. The remaining 45 m of movement are characterized by discontinuous lateral compression ridges on both margins of the displaced mass. This observation along with the presence of sedimentological features such as emergent shear planes, folding, and buried organic horizons within the displaced mass suggests compressive movement involving moist deformable sediments.

Within the displaced mass are transverse ridges that were created as the moving block thickened when encountering more resistant material downslope. Wide vertical shear gashes at each margin of the failure immediately upslope of the bank crest suggest a velocity increase as the displaced mass spilled out over the bank crest and down onto the

Black Top Creek floodplain. These were created as the sudden increase in velocity caused the trailing half of the displaced mass to pull away from the failure margins created by the leading front of the displaced mass.

The sudden increase in velocity likely caused a thinning of the displaced mass upslope of the bank crest. The thinning reduced the weight of the upslope material contributing to the stabilization of the displaced mass. The pronounced vertical front of the toe zone is likely the result of erosion by Black Top Creek during the 2006 snowmelt as opposed to toe zone characteristics at the time of stabilization.

Following the primary failure, recession of the headwall due to loss of support from the initial failure led to the release of two large blocks. The large blocks detached and traveled downslope on gradients that ranged from 2 to 6°. One block (approximately 24 m long and 10 m wide) traveled approximately 40 m from the northern corner of the headwall, impacting the southern margin of the initial failure, creating a lateral compression ridge before coming to a rest. The second block (approximately 16 m long and 20 m wide) appears to have come to a rest within the track zone, likely due to a reduction in slope gradient or resistance from mud on the track zone floor associated with melt of the exposed floor or supra-permafrost water entering the failure depression.

4.1.2.2.2 BTC-2005-08

The morphological features of BTC-2005-08 are displayed on Figure 4-19 while the sedimentological features of one trial pit are displayed in Figure 4-20. Figure 4-21 illustrates the inferred failure history of BTC-2005-08.

Failure Morphology

Active layer detachment BTC-2005-08 was characterized by a single displaced mass and an insignificant track zone (Figure 4-19). The scar zone is characterized by a scarp height of approximately 0.3 m and a scar floor gradient of 18 - 24°. Maximum scar zone length and width were 9 m and 16 m, respectively. Numerous tension cracks were

located along the headwall and sidewalls of the scar zone. Several collapsed blocks (0.5 – 2.0 m diameter) had detached from the headwall and sidewalls and were sitting on the scar floor. Evaporation of supra-permafrost groundwater led to salinization of the scar floor.

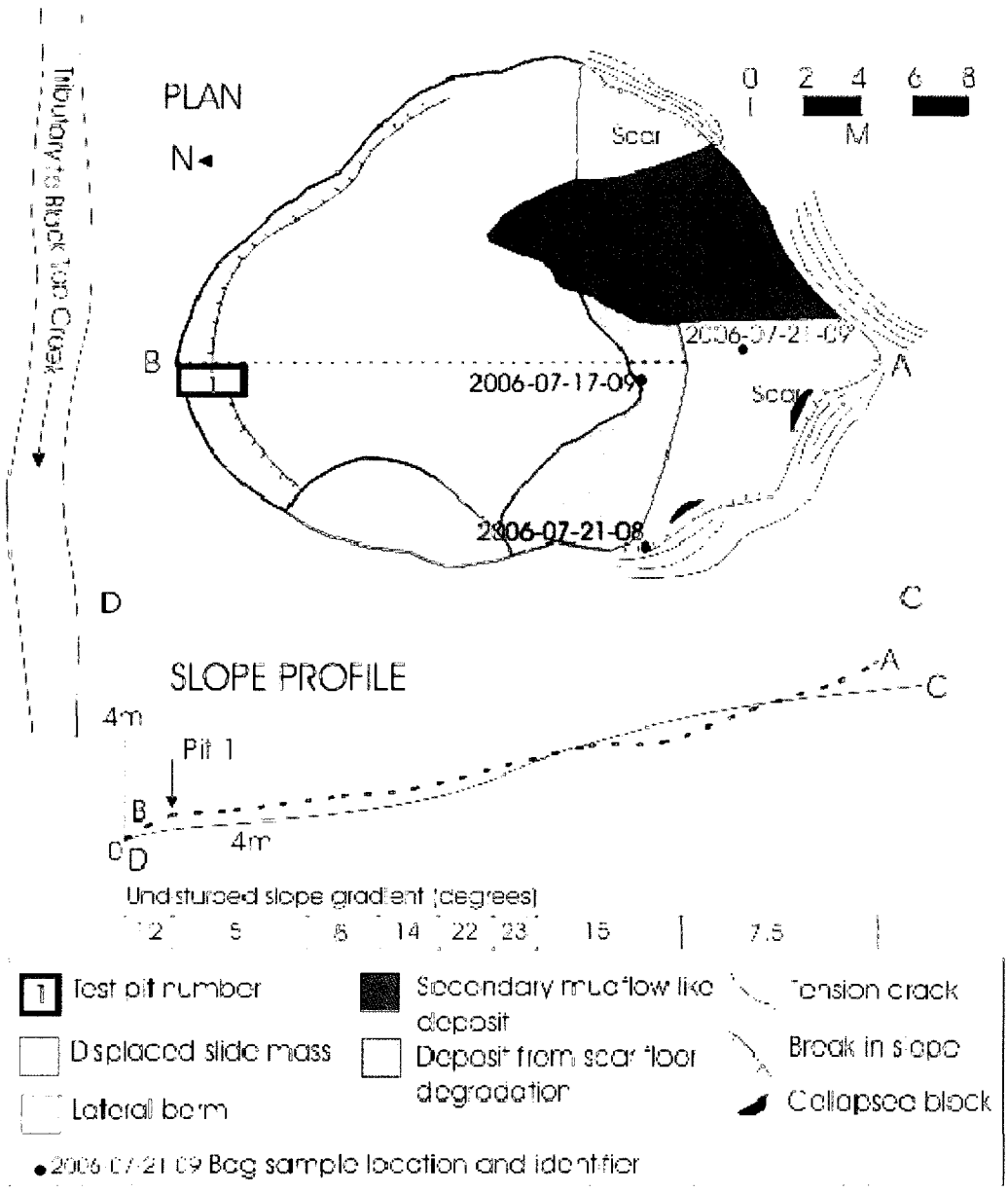

Figure 4-19. Plan and profile of compact failure, BTC-2005-08. Movement direction towards the left. Sketch developed from a combination of field mapping with tape measure and GPS, and aerial mapping from helicopter surveys.

Mudflow deposits from the exposed scar floor had accumulated at the rear of the displaced mass. The mudflow deposits are representative of two movements; one set appears to relate to widespread wasting of the scar zone, while the second set appears associated with localized wasting of the eastern portion of the headwall. Disintegration of the trailing edge of the displaced mass was not observed and there were no trailing blocks in the scar zone.

The maximum length and width of the bare displaced mass were measured as 16 m and 18 m, respectively. The slope gradient ranged between 12 - 23°. The western half of the displaced mass was marked by a 0.3 m high wide berm. The surface of the displaced mass was largely undisturbed, i.e. there are no transverse ridges. The entire front of the displaced mass was marked by a sharp drop (approximately 0.8 m) as the mass ran out onto the floodplain of a tributary to Black Top Creek.

Failure Stratigraphy

One trial pit, TP 1, was excavated across the toe of the failure (Figures 4-19 and 4-20). A buried organic layer that ran the entire extent of the trial pit separated the over-riding material from the lower intact sediment. The presence of green organics within the buried layer suggests that the surface was buried during recent movement.

The material overlying the buried organic layer was comprised of two units; an upper soft clayey silt unit and a lower very soft sandy silt unit. The contact between the two units was sharp. Within the lower unit are sand flames and lenses of clayey silt, suggestive of fluid escape and deformation associated with overloading, downslope movement, and high moisture content. The lower unit straddled the buried organic layer in the upslope portion of the trial pit.

Largely intact undeformed sediment was located below the buried organic layer in the downslope portion of the trial pit. Immediately below the buried organic layer was moist, soft, banded sandy silt with clay unit. Within this unit were pockets of organic-rich moist soft sandy silt with clay and lenses of slightly moist loose sand. The

boundary of these pockets and lenses with the enclosing sandy silt with clay unit was sharp.

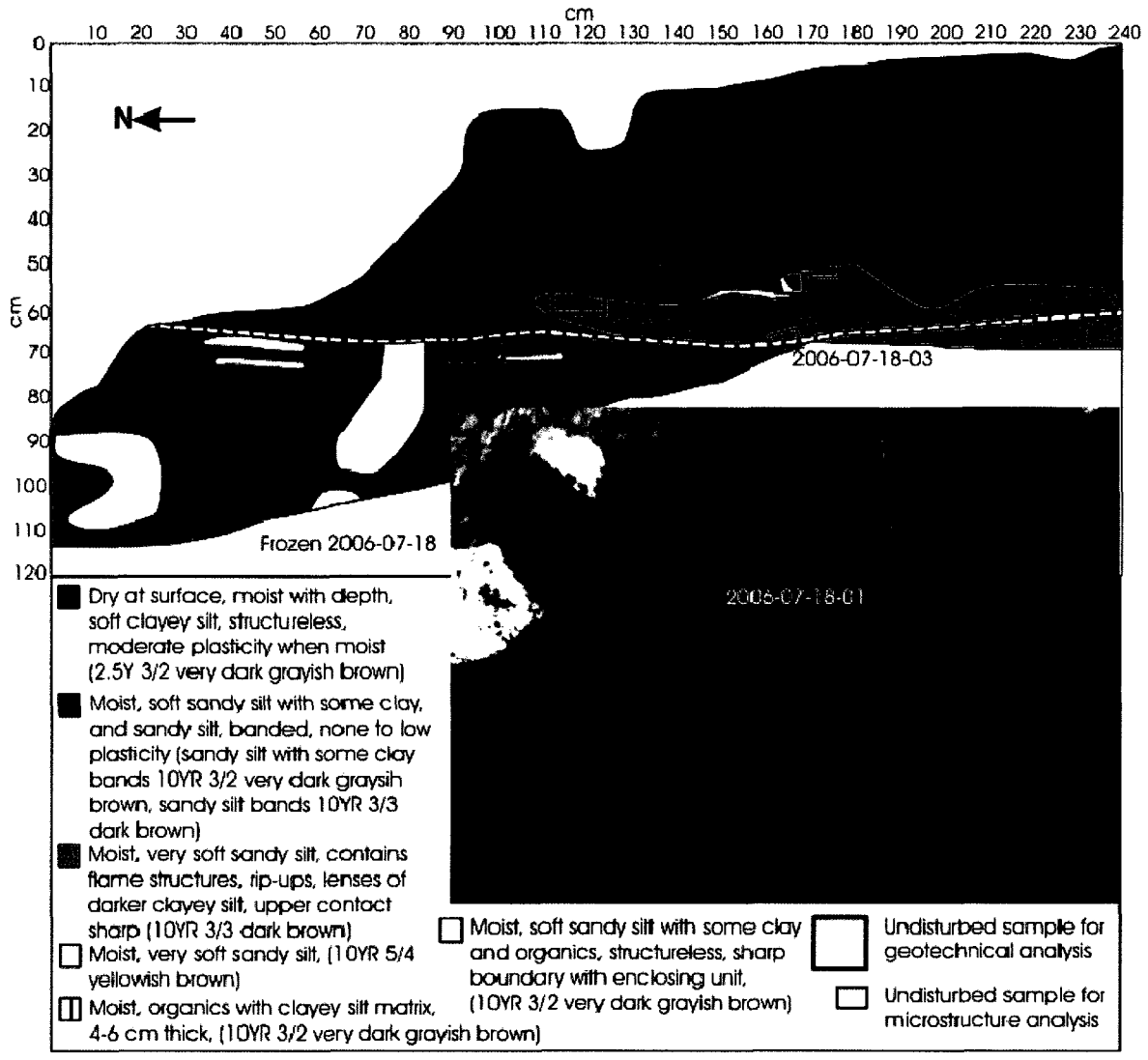

Figure 4-20. Trial pit description of BTC-2005-08 TP 1 across terminal transverse ridge. Movement direction towards the left.

Inferred Failure History

Field mapping and trial pit description indicates that BTC-2005-08 was made up of a single displaced mass indicative of a single movement (Figures 4-19 and 4-21). Rates of movement are inferred to have been rapid. Movement of the displaced mass appears to have started by sliding at a crest-slope location where the gradient of the adjacent

undisturbed terrain was between 7.5 and 15°. The undisturbed nature of the displaced mass, e.g. lack of transverse ridges and trailing blocks, indicates a singular, near-instantaneous movement. The displaced mass ran out approximately 7 m onto the floodplain of a tributary to Black Top Creek before coming to a rest.

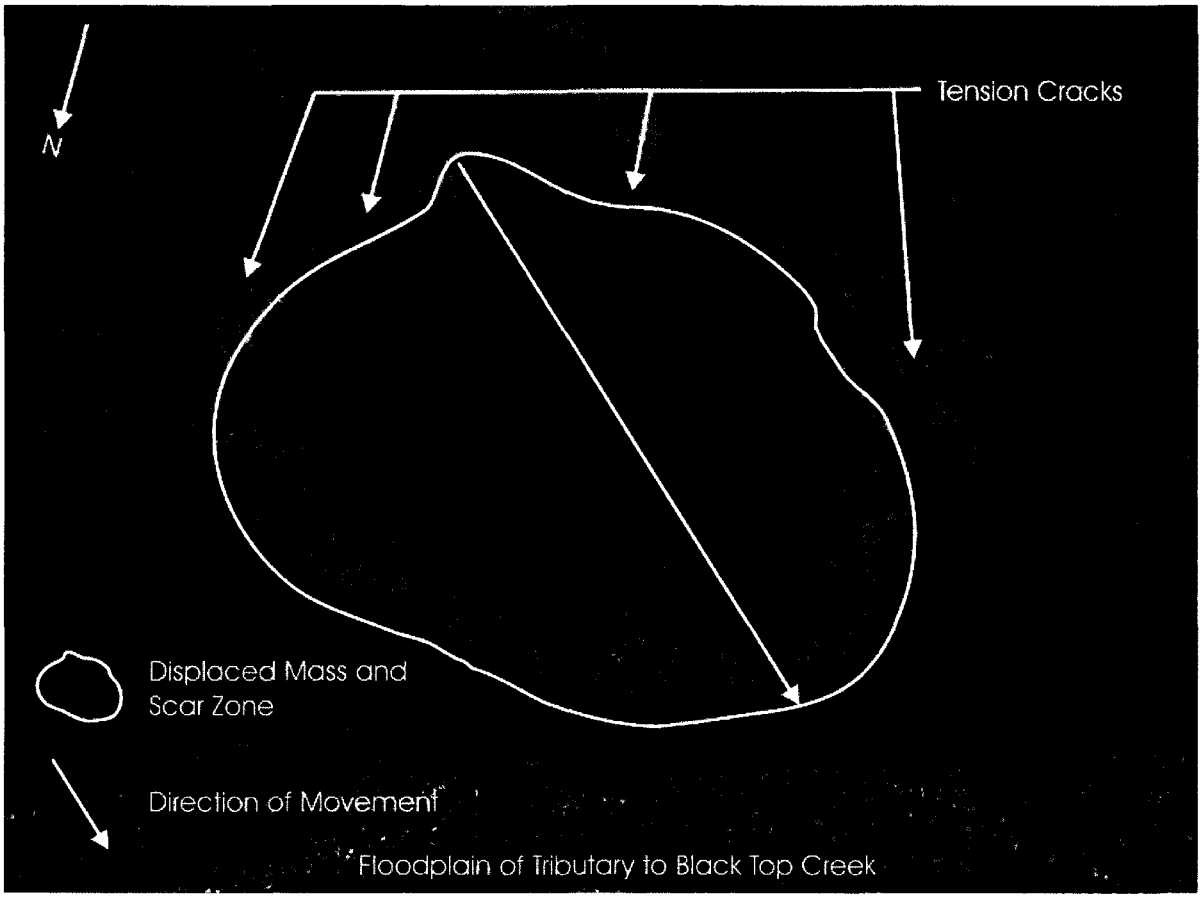

Figure 4-21. Aerial view of BTC-2005-08 showing single displaced mass and associated scar zone, and tension cracks in unmobilized adjacent terrain.

Following the singular, near-instantaneous movement, erosion and recession of the headwall and scar zone led to significant deposition of mud at the rear of the displaced mass. Extensive tension cracks surrounded the headwall and sidewalls of the scar zone. As these cracks widened, blocks eventually collapsed into the scar zone where they immediately came to rest.

4.1.2.2.3 BTC-2005-13

The morphological features of BTC-2005-13 are displayed on Figure 4-22 while the sedimentological features of three trial pits are displayed in Figures 4-23 to 4-25. Figure 4-26 illustrates the inferred failure history of BTC-2005-13.

Failure Morphology

Active layer detachment BTC-2005-13 was characterized by a single displaced mass and an insignificant track zone. The scar zone was characterized by a scarp height of approximately 0.7 m and a scar floor gradient of 0.5 - 22°. Maximum scar zone length and width were both 13 m. The headwall and sidewalls of the scar zone were characterized by tension cracks, collapsed blocks (0.5 to 3.2 m in diameter) and collapsed dry hummocks (generally 0.4 m in diameter). The scar floor was characterized by grooves and rills associated with movement of trailing and collapsed blocks. Flow shapes on the scar floor were suggestive of ductile deformation associated with thaw of the floor. Degradation of the exposed scar floor and supra-permafrost water entering failure depression generated mudflows over the scar floor and track floor. The mudflows accumulated at the rear of the displaced mass.

The maximum length and width of the displaced mass were 37 m and 18 m, respectively. The slope gradient ranged between 4 - 8°. Numerous transverse ridges, up to 0.3 m high, were found within the compression zone of the displaced mass. Some of the ridges displayed an intact vegetation mat while others exhibited vertical gashes oriented parallel to the direction of movement. Several large shear gashes were present within the interior of the displaced mass. The gashes were oriented both parallel to and at an angle to the direction of movement. Near the rear of the displaced mass, vertical shear gashes up to 0.37 m wide were found along both margins of the failure. Mid-block was a zone of disturbed hummocks characterized by a paucity of transverse ridges.

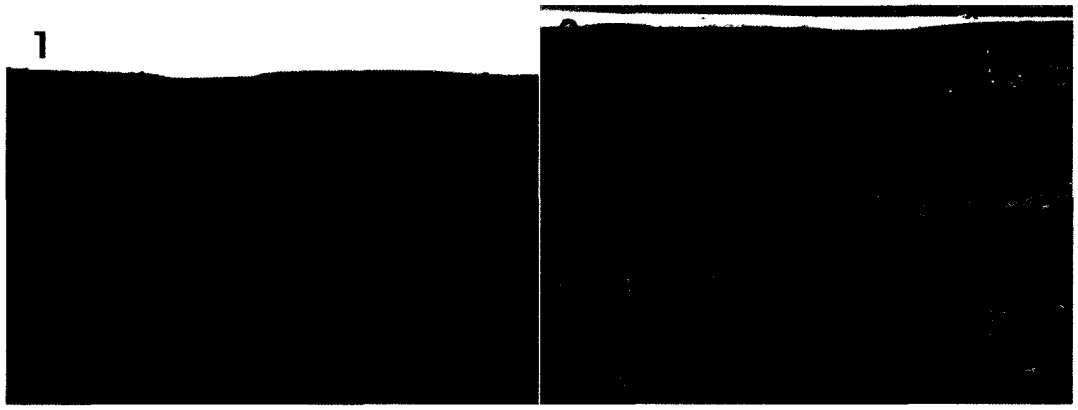

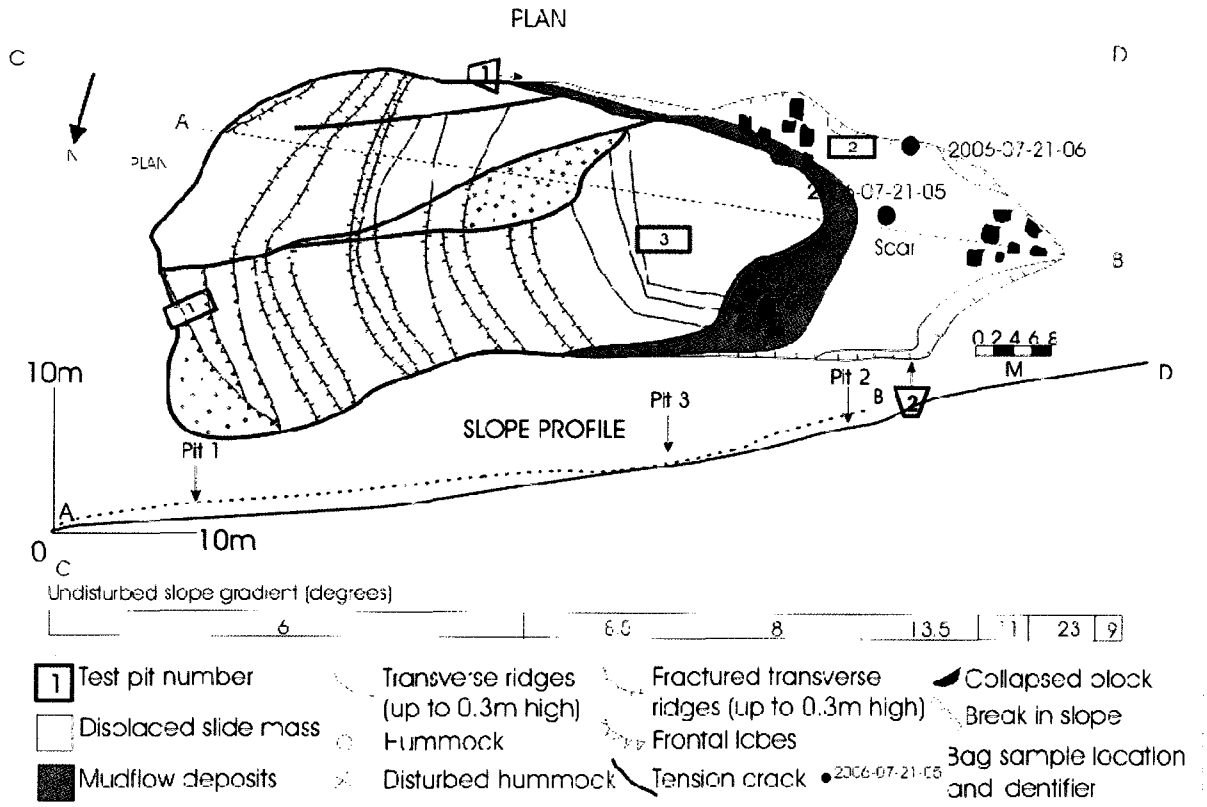

Figure 4-22. Plan and profile of elongate failure, BTC-2005-13. Movement direction towards the left. Sketch developed from a combination of field mapping with tape measure and GPS, and aerial mapping from helicopter surveys. Photo locations and orientation are shown on the plan. Photo 1 shows the shear gash along the southern margin of the failure. Photo 2 shows the scar zone of the failure.

The front of the displaced mass was marked by a small 0.23 m high frontal lobe that was characterized by overturned hummocks. The front of the displaced mass

funneled into a pre-existing moist vegetated cross-slope depression. Downslope of the frontal lobe was a 2 m wide zone of disturbed intact hummocky terrain.

Failure Stratigraphy

Three trial pits were excavated at BTC-2005-13 (see Figure 4-22). TP 1, excavated across the frontal lobe at the toe of the failure, was comprised of a single unit: dry to slightly moist, soft to stiff, low to high plasticity clayey silt with pockets and stringers of sand (Figure 4-23). The presence of several buried organic layers indicated overturning of the transverse ridges and frontal lobes.

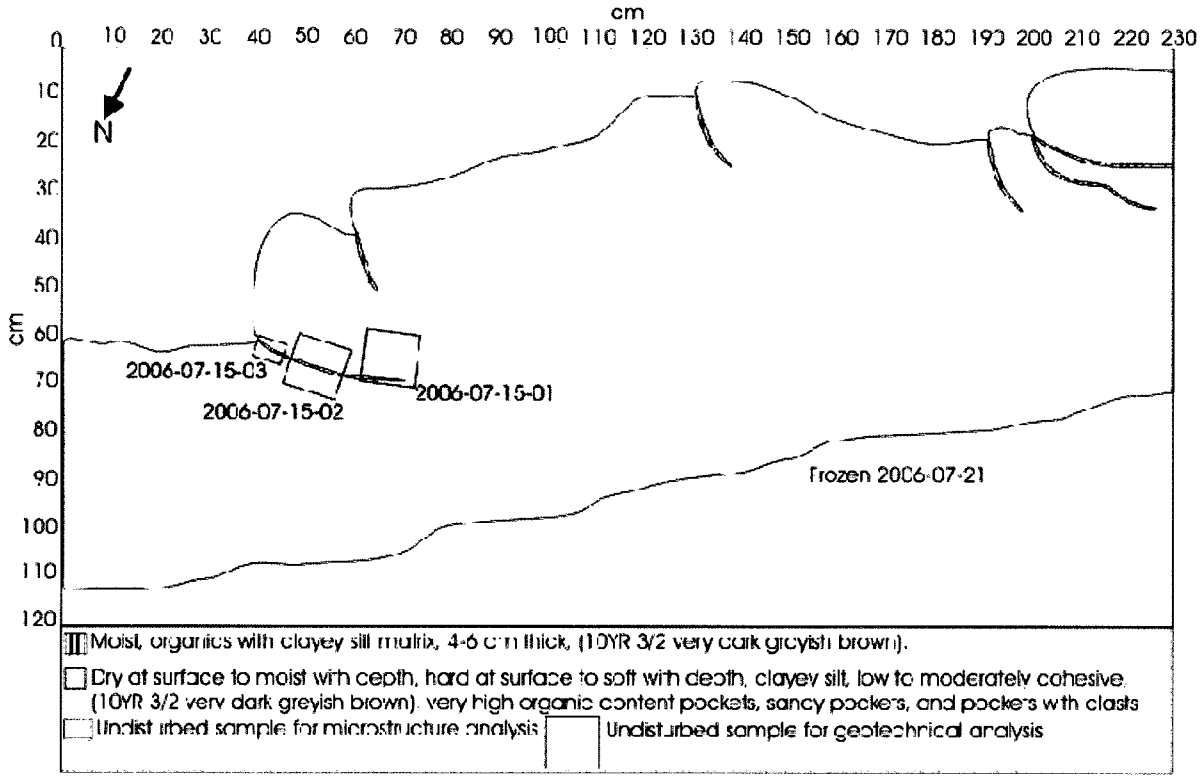

Figure 4-23. Trial pit description of BTC-2005-13 TP 1 across terminal transverse ridge. Movement direction towards the left.

TP 2 was located on the inward facing side of a block that had collapsed from the southern margin into the track zone (Figure 4-24). TP 2 was comprised of three units. The upper unit was a dry to moist, stiff, cryoturbated silt with minor sand and clay. Within this unit were pockets of clayey silt. An irregular, sharp boundary separated the upper unit from the unit below, a moist, medium stiff to stiff, moderately plastic,

vertically elongated blocky (approximately 2 cm diameter blocks) clayey silt to silty clay unit. Separating this unit from the bottom unit was a flat, sharp boundary inferred to represent the failure plane. The bottom unit was described as wet cryoturbated (1 to 2 mm diameter cyroaggregates) silty clay to clayey silt.

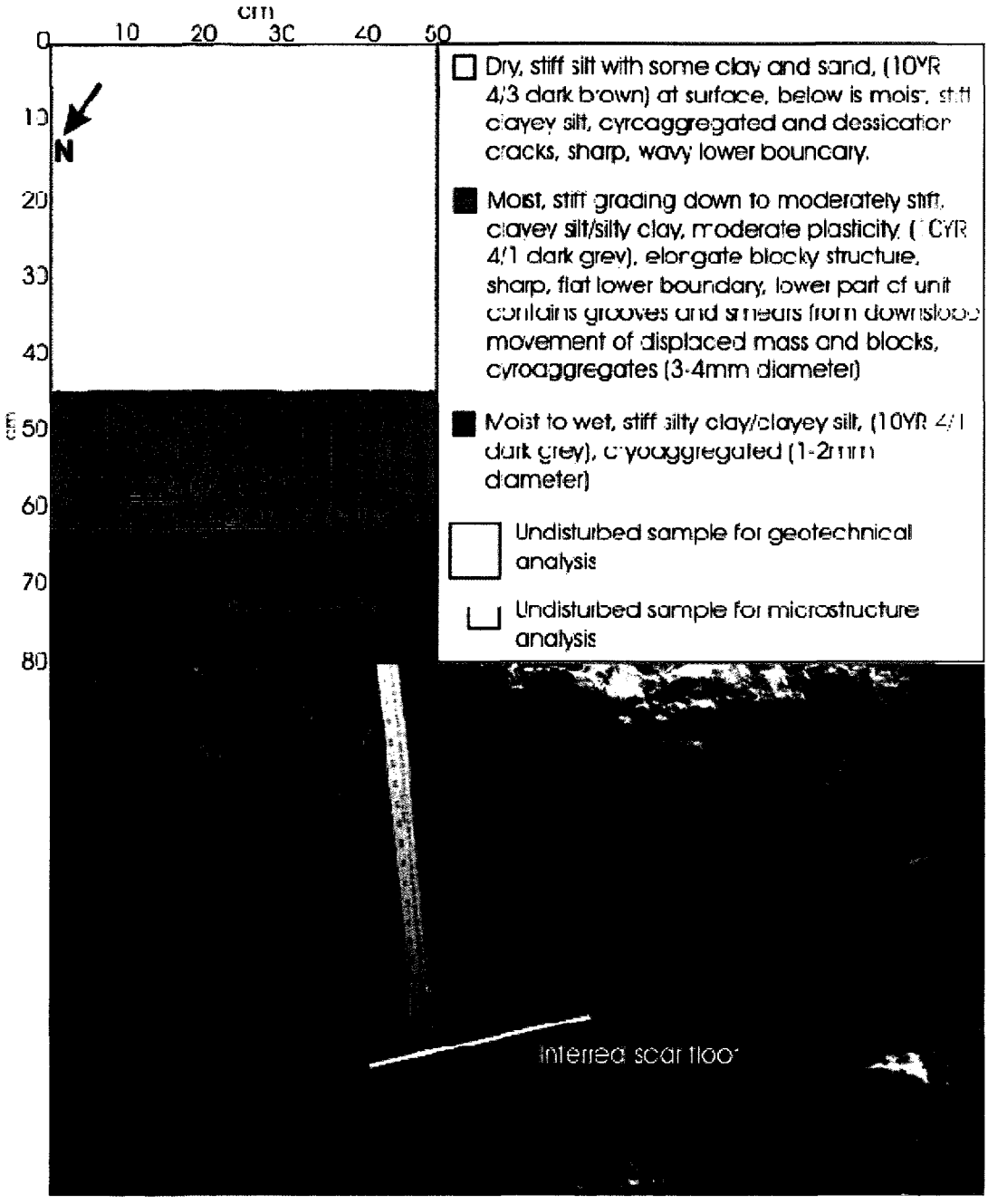

Figure 4-24. Trial pit description of BTC-2005-13 TP 2 excavated on inward facing side of a block within the track zone. Movement direction towards the left.

The third trial pit, TP 3, was excavated within a relatively undisturbed portion of the displaced mass and comprised three units (Figure 4-25). The main unit visible above the thaw plane was a moist, soft to stiff, non-plastic to low plasticity, structureless clayey silt. Within this unit were several pockets and lenses of a moist, soft, low to medium plasticity clayey silt unit that had higher clay content than the main unit above the thaw plane. Below the thaw plane was a moist, stiff, blocky structured clayey silt unit.

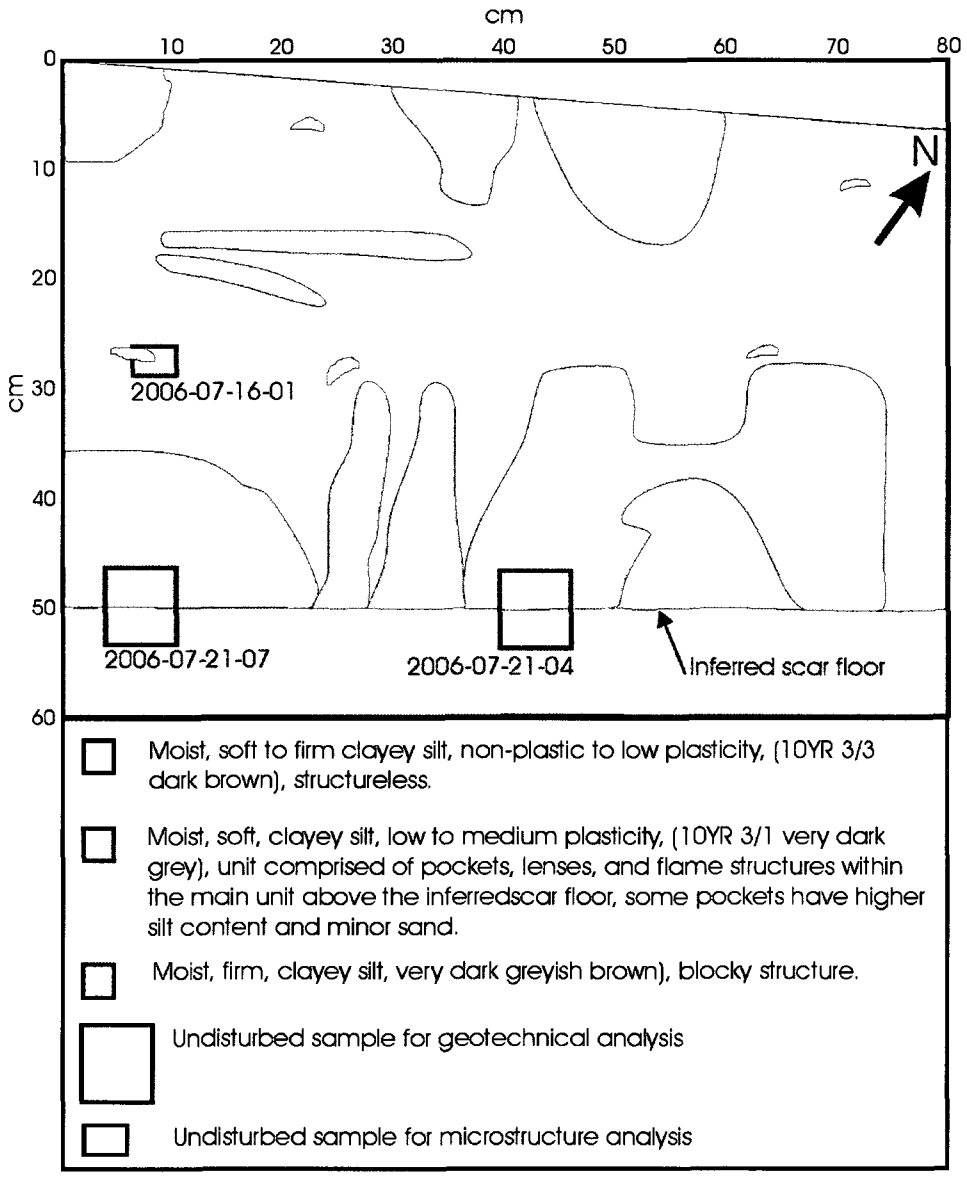

Figure 4-25. Trial pit description of BTC-2005-13 TP 3 excavated within an undisturbed portion of the displaced mass. Movement direction towards the right.

Inferred Failure History

Field mapping and trial pit description indicated that BTC-2005-13 is made up of a single displaced mass indicative of a single movement (Figures 4-22 and 4-26). Rates of movement are inferred to have been slow, prolonged and continuous. Movement of the displaced mass appears to have started by sliding at a mid-slope location. The gradient of the adjacent undisturbed terrain was between 8 and 13.5°. While the failure occurred as a single movement, the disturbed nature of the lower part of the displaced mass (the presence of transverse ridges) indicates prolonged compression. The transverse ridges are also suggestive of considerable resistance of the downslope terrain to movement. Significant resistance of a drier portion of the slope near the southern side of the toe zone resulted in a shear gash oriented parallel to the direction of movement within the block. Material to the south of the gash stopped moving while material to the north of the gash continued moving downslope within a pre-existing moist vegetated cross-slope depression. The depression offered comparatively less resistance. The initial movement of the displaced mass combined with prolonged compression and disturbance of the downslope terrain resulted in a cumulative 15 m of displacement.

Mudflows within the scar and track zones ponded at the rear of the displaced mass and partially covered trailing blocks within the track zone. The mudflows developed from thawing of the exposed scar floor and from supra-permafrost water entering the failure depression from the surrounding terrain. While some grooves from block movement over the scar floor were still visible, other portions of the scar floor thawed sufficiently that features suggestive of ductile deformation were visible. Subsequent erosion of the headwall due to loss of support led to tension cracks, collapse of blocks, and collapse of individual hummocks.

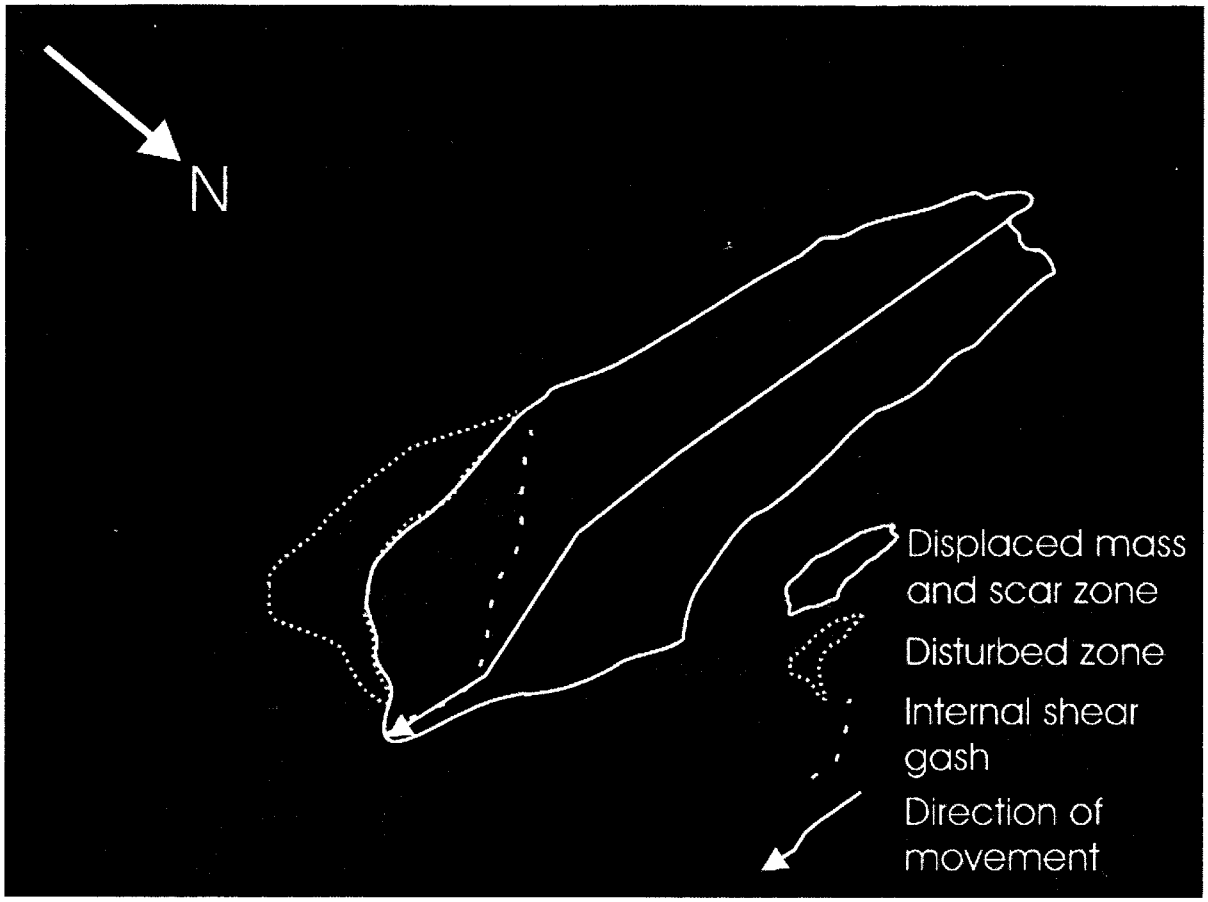

Figure 4-26. Aerial view of BTC-2005-13 showing single displaced mass and associated scar zone, and large internal shear gash within the compression zone.

4.1.2.3 Hot Weather Creek Failure Morphology

One failure from the HWC study area, HWC-2005-01, was described in detail (see Figure 4-3).

4.1.2.3.1 HWC-2005-01

The morphological features of HWC-2005-01 are displayed on Figure 4-27 while the sedimentological features of one trial pit is displayed in Figure 4-28. Figure 4-29 illustrates the inferred failure history of HWC-2005-01.

Failure Morphology

Active layer detachment HWC-2005-01 was characterized by a single displaced mass and an insignificant track zone (Figure 4-27). The scar zone was characterized by a scarp height of approximately 0.6 m and a scar floor gradient of 18 - 24°. Maximum scar zone length and width were 18 m and 30 m, respectively. Exposed within the headwall of the scar zone was an ice wedge trough. Tension cracks surrounding the ice wedge were observed and significant melting of the ice wedge contributed to collapse of blocks from the headwall into the scar zone and the generation of meltwater that entered the depression created by the failure. The floor of the scar zone was marked by secondary thermokarst. There were no trailing blocks from disintegration of the rear of the displaced mass in the scar zone.

The maximum length and width of the displaced mass were 54 m and 25 m, respectively. The slope gradient ranged between 5.5 - 10°. Numerous transverse ridges, up to 0.5 m high, were found within the compression zone of the displaced mass. The sides of the displaced mass were separated from the adjacent terrain by pronounced vertical shear gashes. The adjacent terrain was typically dry and hummocky exhibiting evidence of historical active layer detachments. The entire front of the displaced mass was marked by a sharp drop, 0.5 m, down to the downslope terrain. Beyond the toe was a small disturbed zone characterized by slightly tilted hummocks.

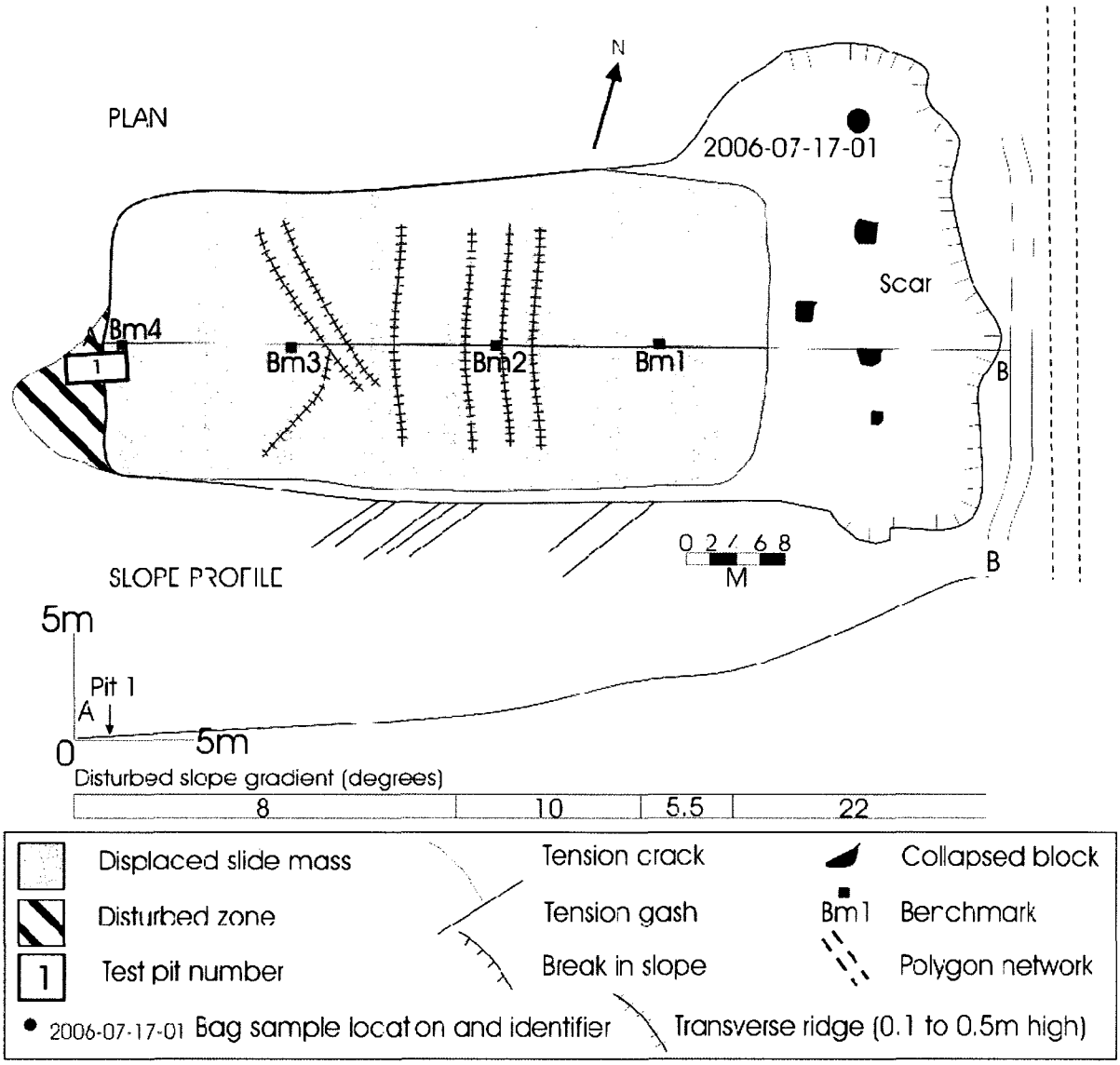

Figure 4-27. Plan and profile of elongate failure, HWC-2005-01. Movement direction towards the left. Sketch developed from a combination of field mapping with tape measure and GPS, and aerial mapping from helicopter surveys.

Failure Stratigraphy

One trial pit, TP 1, was excavated across the toe of the failure (Figures 4-27 and 4-28). Minimal evidence of disturbance was noted. Material exposed within the trial pit was relatively homogeneous soft to firm clayey silt with black coal fragments. Within this unit was a vertical zone of loose sand that appeared to be deformed slightly in a downslope direction.

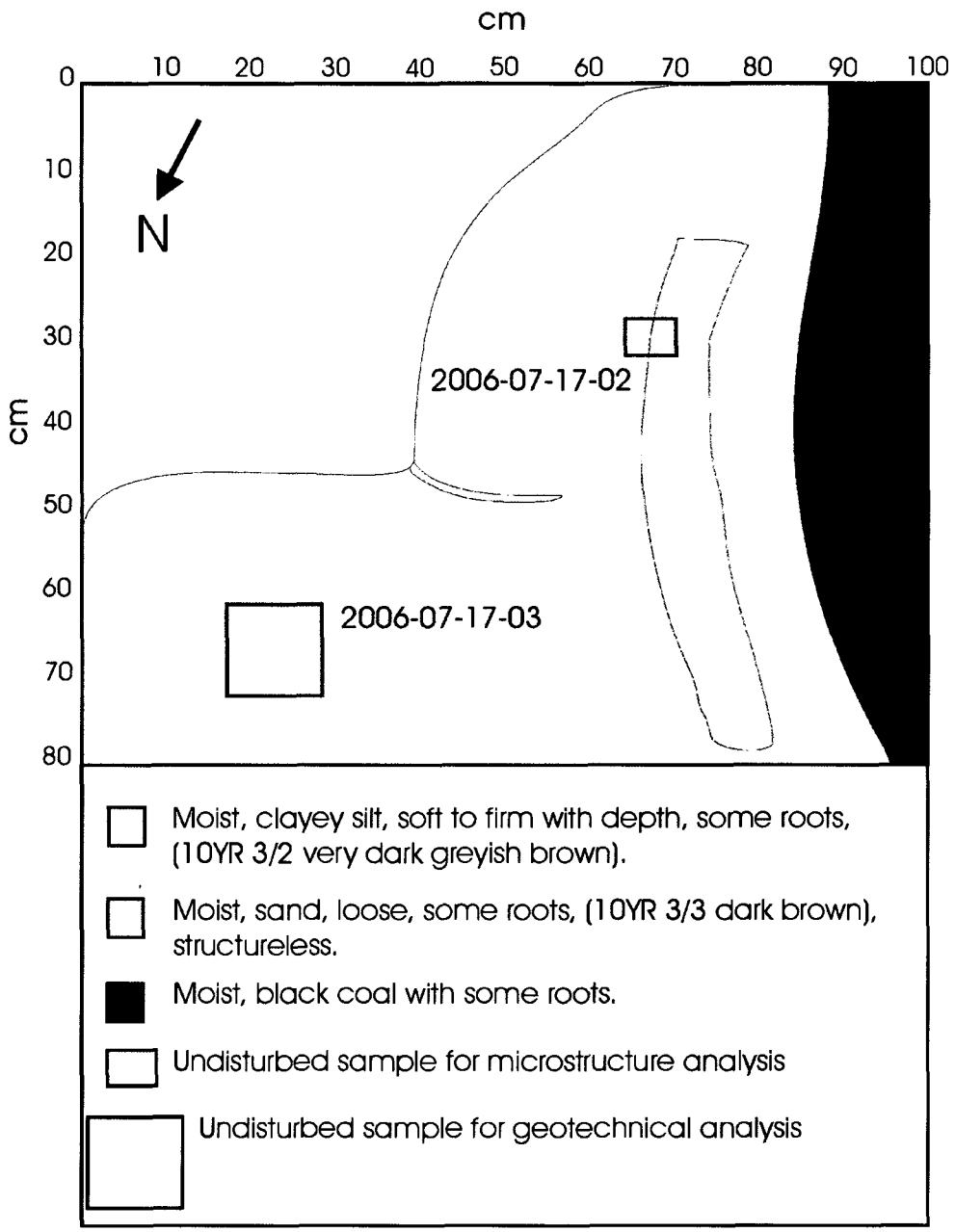

Figure 4-28. Trial pit description of HWC-2005-01 TP 1 excavated across the toe of the failure. Movement direction towards the left.

Inferred Failure History

Field mapping and trial pit description indicated that HWC-2005-01 was made up of a single displaced mass indicative of a single movement (Figures 4-27 and 4-29). Rates of movement are inferred to have been slow, prolonged and continuous. Movement of the displaced mass appears to have started by sliding at a nearly crest-slope location

which is also the location of a cross-slope ice wedge. The gradient of the adjacent undisturbed terrain is approximately 10°. While the failure occurred as a single movement, the disturbed nature of the displaced mass, suggested by the presence of transverse ridges, indicates prolonged compression. The transverse ridges are also suggestive of considerable resistance of the downslope terrain to movement. The initial movement of the displaced mass combined with prolonged disturbance of the downslope terrain resulted in a total 18 m of displacement. Following the instantaneous movement of the displaced mass and prolonged disturbance of downslope terrain, erosion of the headwall due to exposure of the ice wedge led to tension cracks, collapse of blocks and melt of the exposed cross-slope ice wedge.

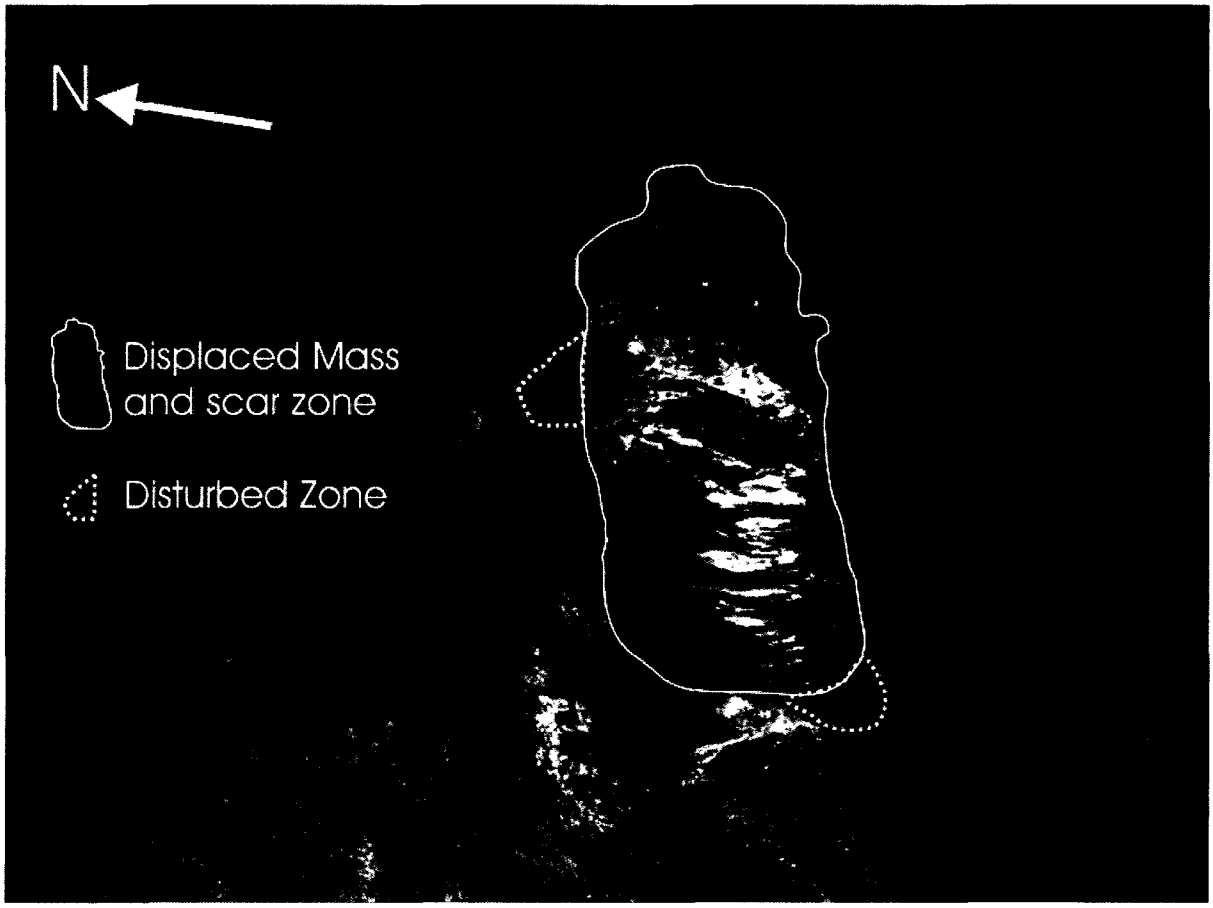

Figure 4-29. Aerial view of HWC-2005-01 showing single displaced mass and associated scar zone.

4.1.2.4 "Big Slide" Creek Failure Morphology

One failure, BSC-2005-01, from the BSC study area was described in detail (see Figure 4-4). The characteristics and history of this failure have been previously described in detail by Lewkowicz (2007).

4.1.2.4.1 BSC-2005-01

The morphological features of BSC-2005-01 are displayed on Figure 4-30 while the sedimentological features of one trial pit is displayed in Figure 4-31. Figure 4-32 illustrates the inferred failure history of BSC-2005-01.

Failure Morphology

Active layer detachment BSC-2005-01 was characterized by an asymmetrical Y-shaped scar zone, a significant track zone and a thickened compression zone (Figure 4-30). The scarp height of both the northern and southern branches of the asymmetrical scar zone were approximately 0.6 m. The gradient of the northern branch scar floor ranged between 16 – 19° while the southern branch scar floor gradient was approximately 14° (Lewkowicz 2007). The northern branch of the scar zone attained a maximum length and width of 10 m and 20 m, respectively. The southern branch of the scar zone attained a maximum length and width of 25 m and 20 m, respectively. Collapsed blocks released from tension cracks along the headwall and sidewalls of the scar zone were resting within the scar zone. A large displaced block (25 m long and 15 m wide), resting both within the scar zone and track zone, was blocking the exit of the northern branch of the asymmetrical Y-shaped scar zone. The scar floor was marked by grooves and dissected by rills.

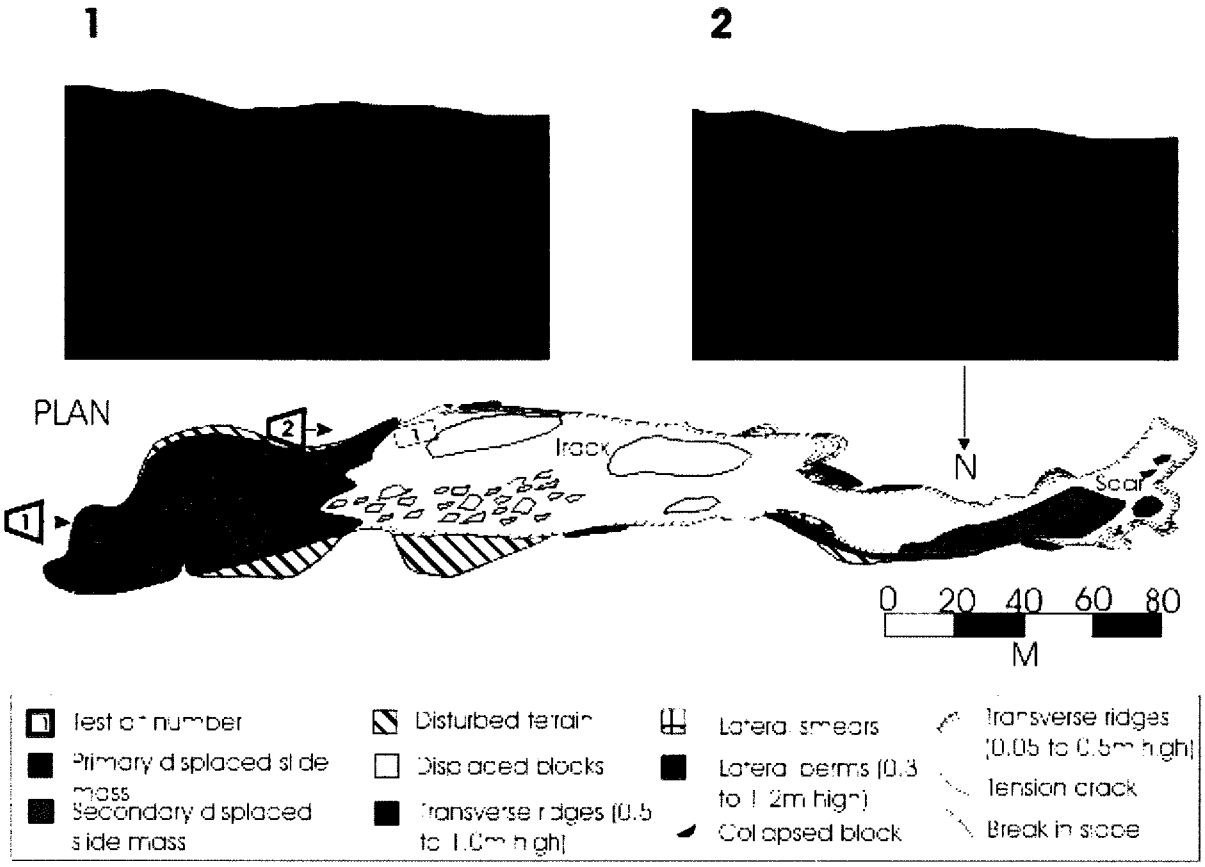

Figure 4-30. Plan and profile of elongate failure, BSC-2005-01. Movement direction towards the left. Sketch developed from a combination of field mapping with tape measure and GPS, and aerial mapping from helicopter surveys. Photo locations and orientation are shown on the map.

The track zone maximum length and width were 220 m and 40 m, respectively. The overall gradient of the track zone ranged between 5 – 10° (Lewkowicz 2007). The track zone was marked by grooves and dissected by rills. Numerous trailing and collapsed blocks were resting on the track floor. Aside from the large displaced block, there were three large displaced blocks resting in the track zone. The largest block was 25 m long and 25 m wide. The edges of the track zone was characterized by complex discontinuous 0.5 – 1.2 m high lateral compression ridges that were smeared along the inside wall. The intact adjacent terrain to the north of the track zone exhibited two disturbed zones. The upslope disturbed zone, approximately 20 m long and 5 m wide, was immediately downslope of where the large displaced block impacted the northern margin of the track zone. The downslope disturbed zone was 40 m long and 20 m wide.

Two areas of retrogressive slumping were observed along the southern margin of the track zone.

The main displaced mass was 75 m long and 40 m wide, with a slope gradient that ranged between 3 - 7° (Lewkowicz 2007). The main displaced mass was characterized by numerous transverse ridges up to 0.5 m high with an intact vegetation mat. The transverse ridges curved upslope at the edges of the failure. The curved transverse ridges exhibited brittle fracturing where vertical gashes extended across the ridges, approximately normal to the movement direction. The trailing edge of the main displaced mass was characterized by shear gashes along the margins. The downslope termination of the shear gashes coincides with the point where the displaced mass was thicker than the adjacent intact terrain (up to 0.9 m higher). The front of the displaced mass funneled into a pre-existing moist vegetated cross-slope depression. The front was marked by a 0.3 m high frontal lobe. Degradation of the exposed scar floor and supra-permafrost water entering failure depression generated mudflows over the scar floor and track floor. The mudflows accumulated at the rear of the displaced mass (Lewkowicz 2007).

Failure Stratigraphy

TP 1 was excavated across the shear plane within the track zone on the north side of a small transported block resting on the shear plane (Figures 4-30 and 4-31). The shear plane was identified by the presence of green organics separating the small transported block from the underlying intact sediment. Both the small transported block and the intact sediment were described as moist stiff clayey silt. Some gravel was noted within the intact sediment. Another buried organic layer representative of a historical failure was noted 0.28 m below the current shear plane.

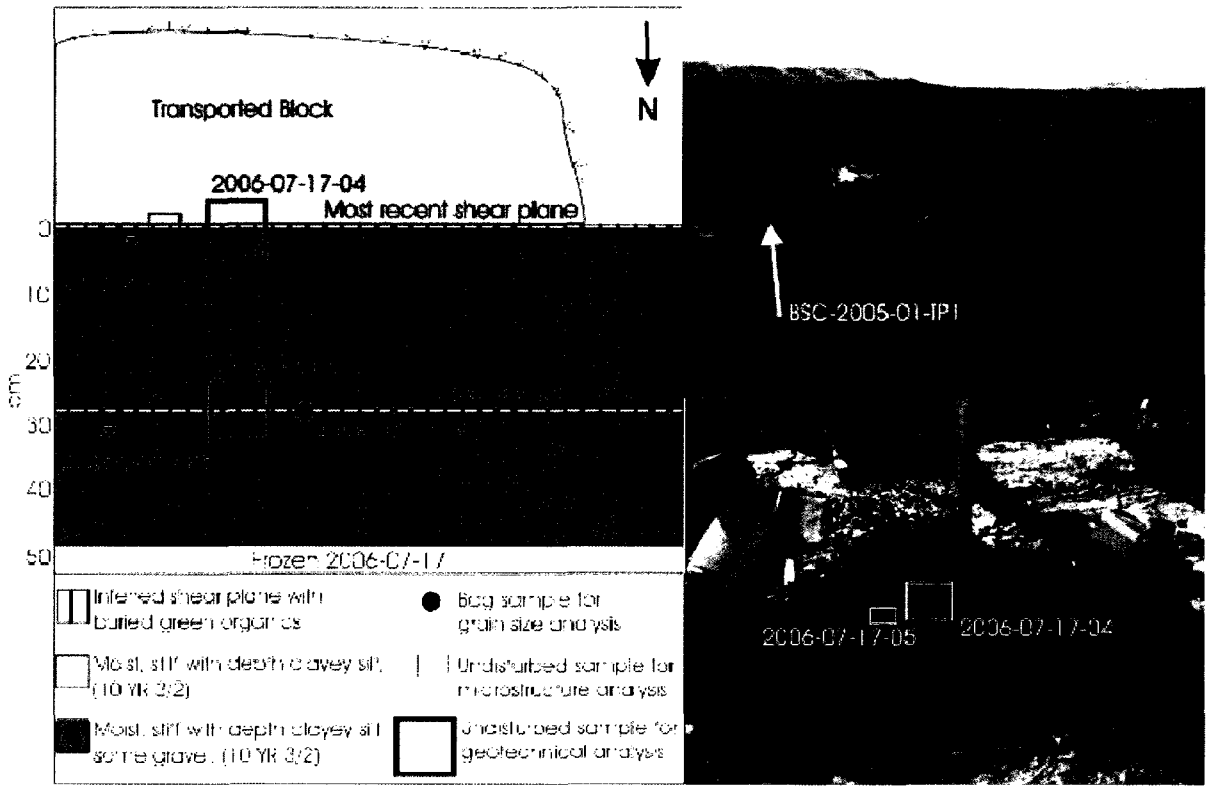

Figure 4-31. Trial pit description of BSC-2005-01 TP 1 excavated across the shear plane within the track zone. Movement direction towards the left.

Inferred Failure History

Field mapping and trial pit description indicated that BSC-2005-01 was made up of two main displaced masses indicative of two movements, a significant track zone and a thickened compression zone (Figures 4-30 and 4-32). Rates of movement are inferred to have been slow, prolonged and discontinuous. Movement of the primary displaced mass appears to have started by sliding at a mid-slope location within a moist cross-slope hollow (Lewkowicz 2007). Movement likely started on the northern branch of the asymmetrical Y-shaped scar zone where gradient of the adjacent undisturbed terrain was between 16 and 19° (Lewkowicz 2007). Grooves and rills created by the initial northern branch movement were crossed by grooves and rills (Lewkowicz 2007) created by secondary movements from the southern branch of the Y-shaped scar zone.

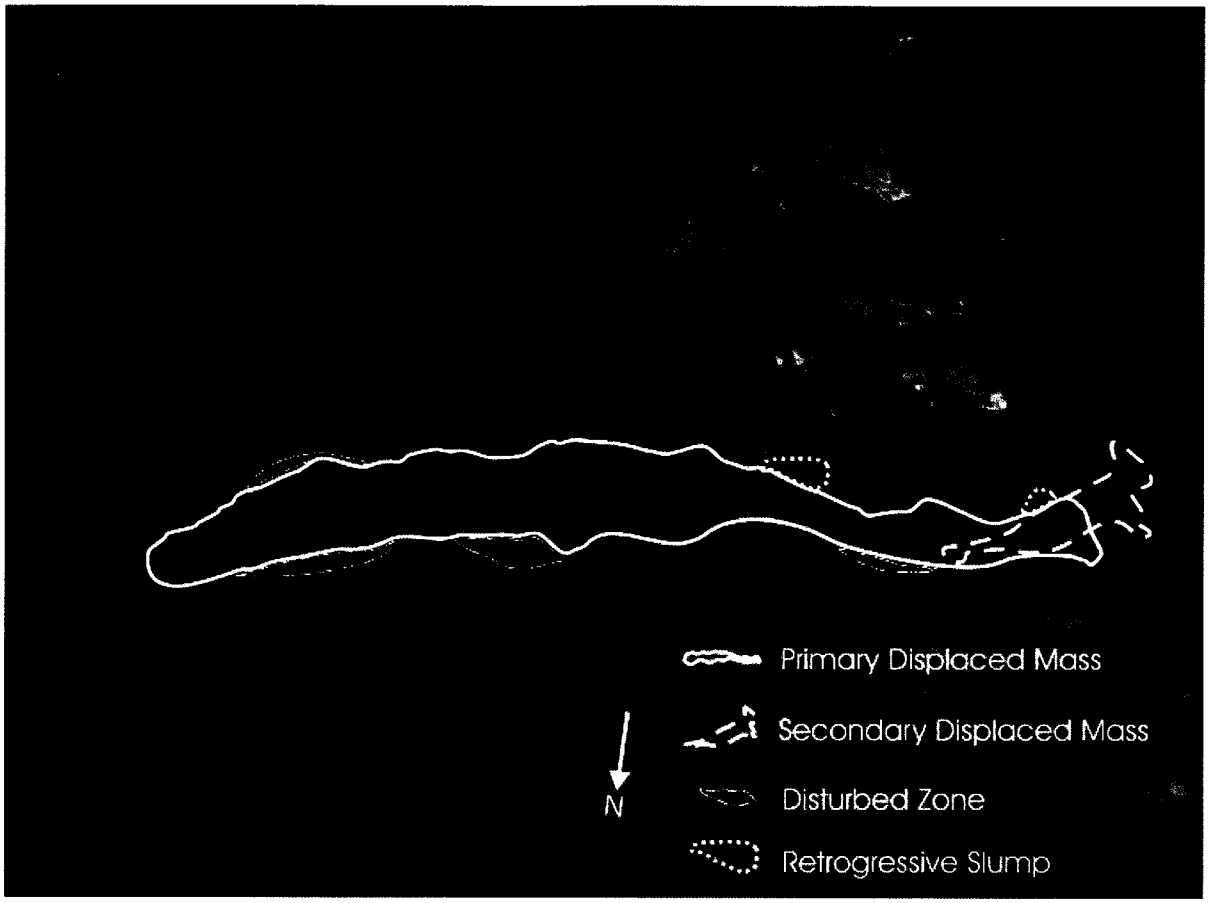

Figure 4-32. Aerial view of BSC-2005-01 showing primary and secondary displaced masses along with retrogressive slumps and disturbed zones. Movement is towards the left.

Observations by Lewkowicz in 2005 (Lewkowicz 2007) indicated that the primary displaced mass initially moved at rates of 1 – 5 m/hr; however the front of the failure initially propagated at about 9 m/hr. This higher rate of movement was due to mobilization of material downslope (Lewkowicz 2007).

Vertical shear gashes formed along the margins of the failure between the mobile mass and the intact adjacent terrain. Large, complex, discontinuous lateral compression ridges also formed along the margins of the failure where blocks impacted the margins of the failure, or where the direction of movement changed as the orientation of the pre-existing depression changed, or where the pre-existing depression narrowed (Lewkowicz 2007). Beyond the lateral compression ridge, disturbance of the adjacent intact terrain was noted in the form of small disturbance ridges.

As the primary displaced mass moved downslope, widening and interaction with the adjacent intact material created transverse ridges that curved upslope. Gashes across the ridges oriented in the direction of movement are the result of brittle fracturing. The fracturing may be the result of the encounter of the moving block with more resistant material associated with drier conditions, higher strength material, or a combination of both.

Sliding of the secondary displaced mass, forming the southern branch of the Y-shaped scar zone appeared to be associated with loss of support from the initial movement. The secondary displaced mass detached and traveled downslope on a gradient of approximately 14°, over the bare scar floor created by the initial movement (Lewkowicz 2007). Smearing along the inside of the lateral compression ridge along the northern margin created by the initial movement occurred as the secondary displaced mass impacted the northern margin and continued moving downslope. The impact also created a disturbed zone characterized by ridges within the adjacent intact terrain.

Tertiary movements occurred in the form of additional recession of the headwall and tension gashes along the margins of the track zone. In some cases, collapsed blocks fell into the scar zone and track zone. Some of the larger blocks were able to develop enough inertia to move through the accumulated mud on the scar and track floors and catch up with the primary and secondary displaced masses (Lewkowicz 2007). Smaller blocks were not able to travel significant distances downslope and came to rest within the scar or track zones.

The toe of the primary displaced mass was characterized by a tongue of material that funneled into an increasingly narrow pre-existing vegetated moist cross-slope depression. Stabilization of the landslide may be related to three factors: gradual decrease in slope and associated reduction in shear stress; narrowing and deepening of the depression potentially increasing lateral resistance; and a reduction in bright sunshine hours resulting in reduced pore-water pressures (Lewkowicz 2007).

Lewkowicz (2007) estimated that the failure attained its full length of 330 m in an estimated 80 – 120 hours (3 – 5 days).

4.1.3 Failure Morphometry

The plan dimensions of the active layer detachments studied show considerable variation (Table 4-2). The number of failures measured at the BTC study area (15) is sufficient to permit discussion of failure plan dimensions and planform. Comparisons between sites have not been made due to insufficient numbers of measured failures at the SC, HWC, and BSC study areas.

Table 4-2. Plan dimensions and planform of 2005 active layer detachments on the Fosheim Peninsula.

Failure	Maximum width (m)	Maximum length (m)	Scar length (m)	Average failure angle (°)	Scar failure angle (°)	Deposit failure angle (°)	Depth (m)	Scar length (% total length)	Length to width ratio
SC-2005-01	47	218	85	4	3-13	2-6	0.5	39	4.6
SC-2005-02	48	108	42	8	7-19	3-10	0.7	39	2.3
BTC-2005-02	10	12	4	35	-	18		34	1.1
BTC-2005-03	9	18	7	28	-	-		38	2.1
BTC-2005-04	36	178	28	7	6-15	0-20	0.8	16	4.9
BTC-2005-07	48	17	4	18	-	-		24	0.4
BTC-2005-08	18	35	9	13	18-24	12-23	0.3	26	1.9
BTC-2005-10	16	27	5	13	13	12		19	1.7
BTC-2005-11	27	18	4	18	-	-		22	0.7
BTC-2005-12	20	12	1	13	-	-		8	0.6
BTC-2005-13	18	50	13	8	1-22	4-8	0.7	26	2.8
BTC-2005-14	23	20	6	20	30	10		28	0.9
BTC-2005-15	15	7	1	12	-	-		14	0.5
BTC-2005-16	16	17	3	9	13	3-11		15	1.1
BTC-2005-17	11	31	18	13	11	15		58	3.0
BTC-2005-18	-	23	6	18	27	9		24	-
BTC-2005-19	17	7	2	21	-	-		29	0.4
HWC-2005-01	25	72	18	15	18-24	6-10	0.6	25	2.9
BSC-2005-01	40	320	25	8	14-19	3-7	0.6	8	8.0

Notes: "-" indicates not measured or calculated.

The widths of the BTC study area failures are skewed to the right due to the presence of two relatively wide failures, BTC-2005-04 (36 m) and BTC-2005-07 (48 m; Figure 4-33). Failure lengths are also skewed to the right (Figure 4-34). With the exception of BTC-2005-04, failure lengths are $\leq$ 50 m and most failure angles are $\geq$ 12°. Given that the BTC valley sides are long to moderate in length, this information reflects the fact that failures originating at crest-slope locations do not reach the valley bottom. Scar length expressed as a proportion of the entire length of the failure ranges from 8 to 58% at the BTC study area with all but two failures (BTC-2005-03 and BTC-2005-17) less than 35% indicating relatively short or non-existent track zones (see Table 4-2).

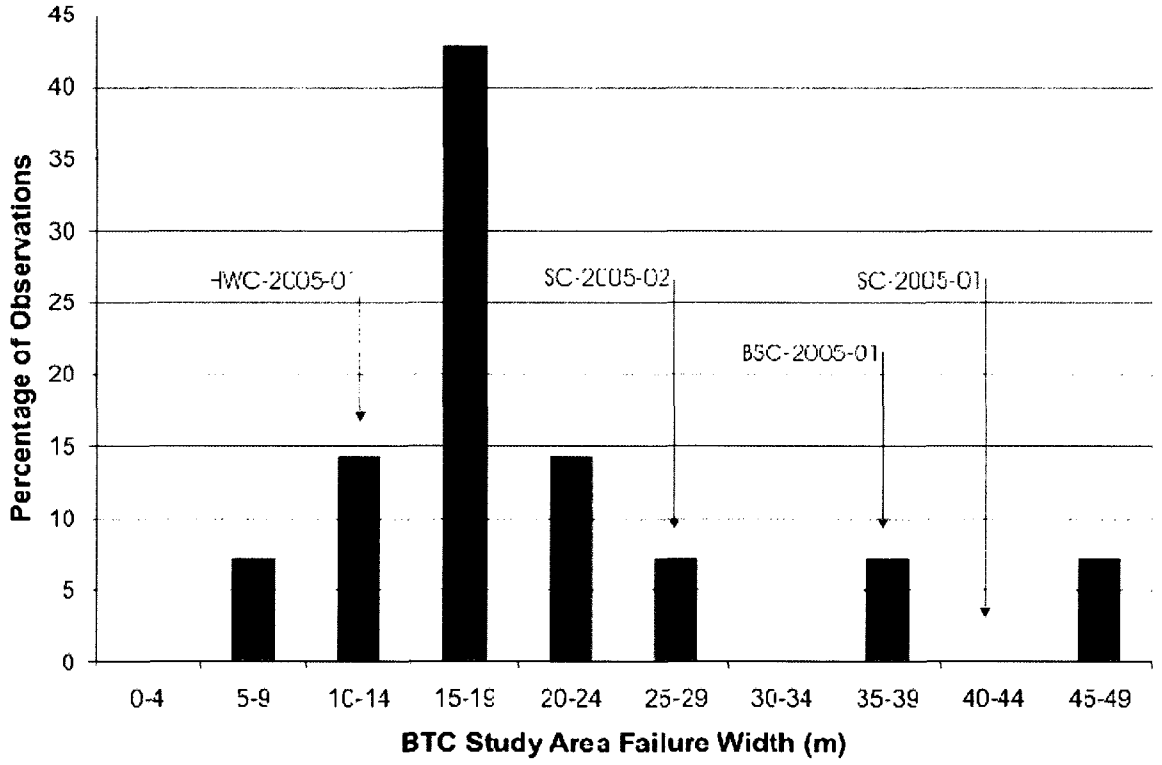

Figure 4-33. Histogram of failure width for 2005 active layer detachments at the BTC study area indicating the category into which the failures from the SC, HWC, and BSC study areas would fall.

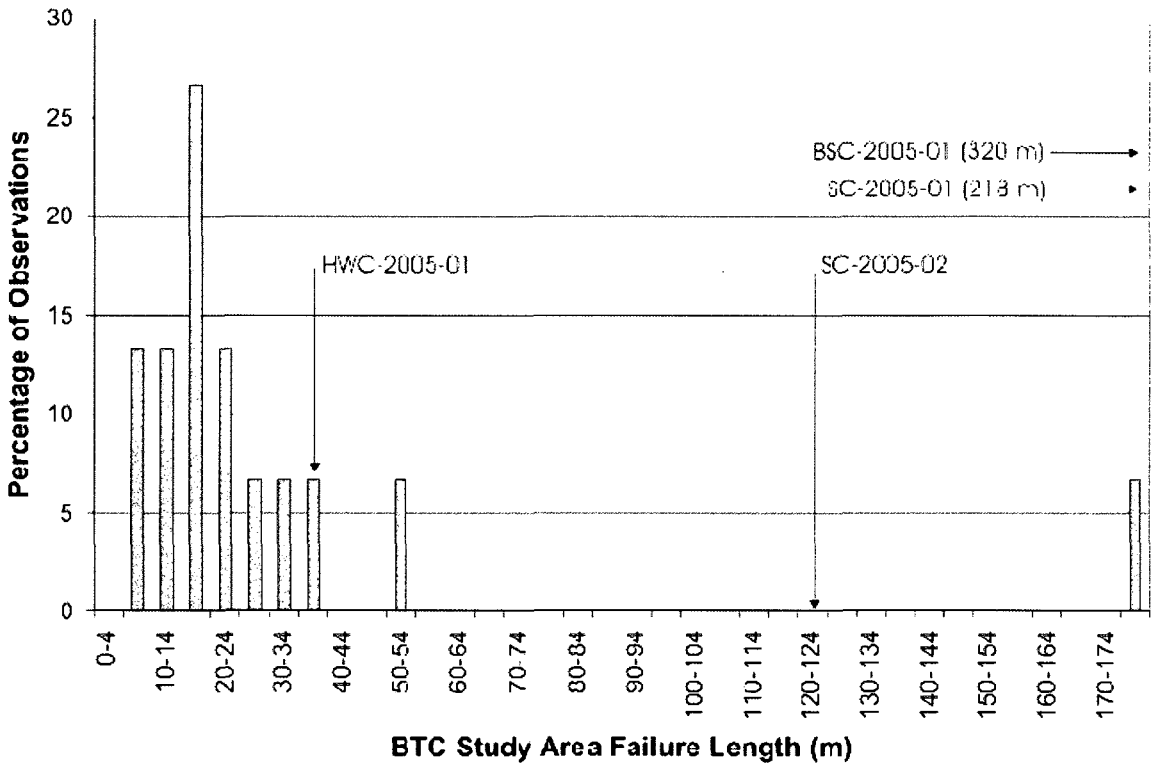

Figure 4-34. Histogram of failure length for 2005 active layer detachments at the BTC study area indicating the category into which the failures from the SC, HWC, and BSC study areas would fall.

The planform of failures can be examined using ratios of length-to-width (see Table 4-2). For the BTC study area, the length-to-width ratio distribution is skewed to the right (Figure 4-35). Approximately 35% of failures at the BTC study area have ratios < 1 which signifies compact failures with lengths less than widths. The remaining 65% of failures at the BTC study area have ratios > 1, signifying elongate morphology.

Correlation analysis has been conducted on plan dimensions at the BTC study area to determine if statistically significant relationships exist between the main morphometric variables (Table 4-3). The analysis did not indicate any relationships significant at the 5% level.

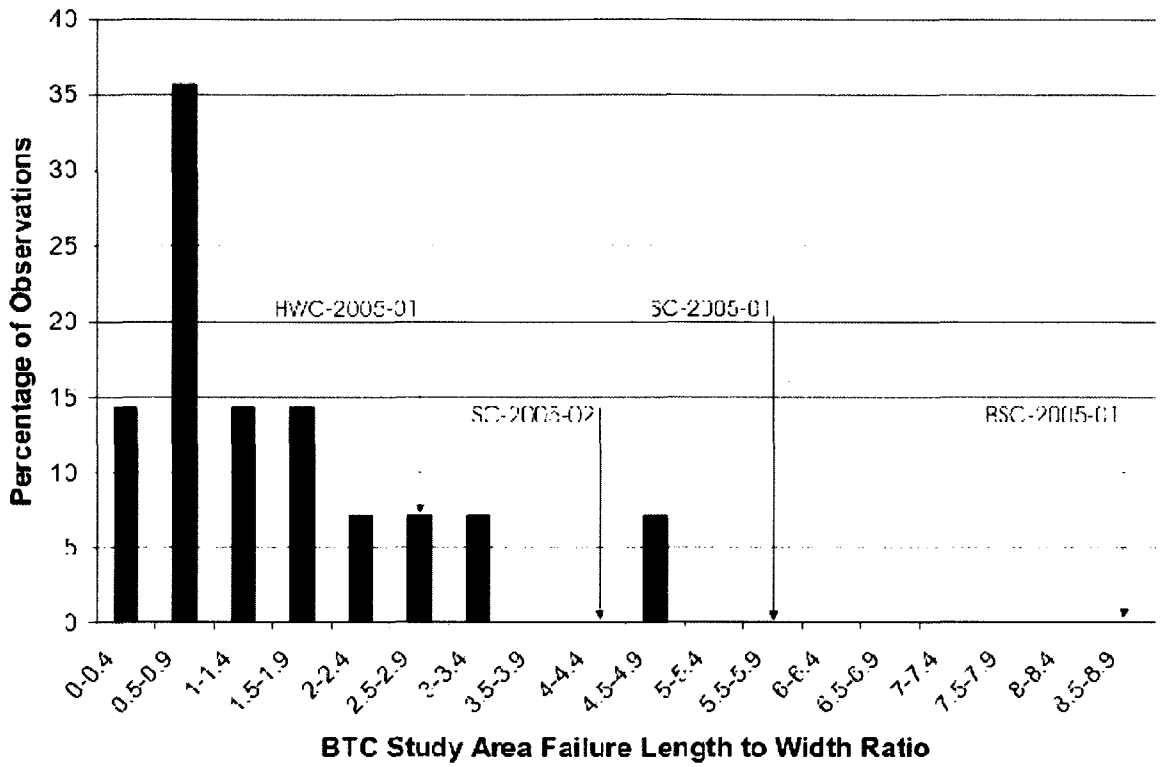

Figure 4-35. Histogram of failure length to width ratio for 2005 active layer detachments at the BTC study area indicating the category into which the failures from the SC, HWC, and BSC study areas would fall.

Table 4-3. Correlation coefficients for dimensions of 2005 active layer detachments from the BTC study area.

Study Area	Length vs. width	Width vs. overall failure angle	Length vs. overall failure angle	Percentage scar length vs. overall failure angle
BTC	0.49	-0.21	-0.46	0.23

The results are similar to those of Lewkowicz and Harris (2005b). As was found in Lewkowicz and Harris (2005b), positive correlations were found between length and width and between percentage scar length and overall failure angle. Lewkowicz and Harris (2005b) suggested that these positive correlations indicate that failures tend to enlarge in both planar dimensions and on steeper slopes, and that the displaced blocks move further relative to the total failure length. As was found in Lewkowicz and Harris (2005b), the negative correlations indicate that the longest and widest failures are

present on the gentlest slopes. Taken together, Lewkowicz and Harris (2005b) suggest that these results show that displaced masses are largest on gentler slopes, but in relation to overall failure length, these masses move shorter distances.

Failures were grouped into the morphological categories of elongate and compact (elongate = length to width ratio > 1; compact = length to width ratio < 1) to investigate differences or similarities regarding average width, length, scar length, deposit length (Figure 4-36A), overall angle, maximum scar zone angle, maximum deposit zone angle (Figure 4-36B), scar length as a percentage of overall length, and ratio of length to width (failure planform; Figure 4-36C).

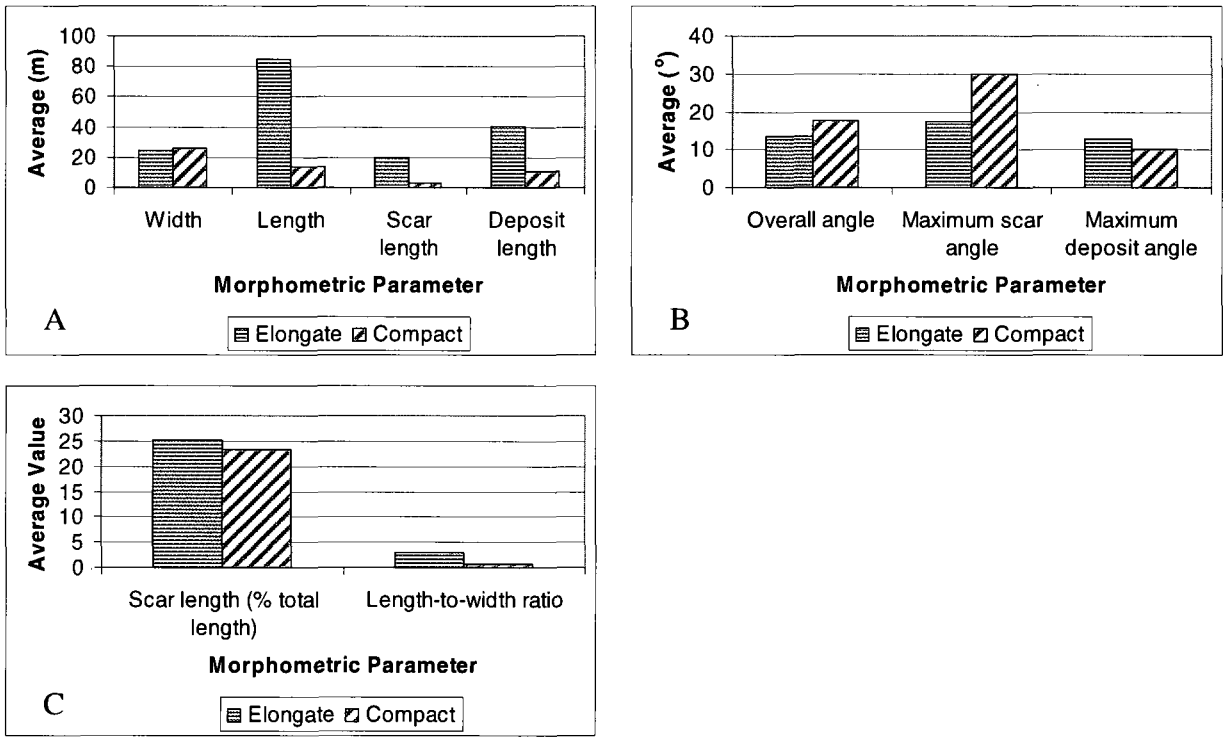

Figure 4-36. Graphs comparing morphometric parameter averages of 2005 active layer detachments grouped into elongate and compact morphologic categories.

Elongate failures exceeded compact failures in terms of length, scar length, deposit length, maximum deposit angle, scar length as a percentage of total length, and length to width ratio. Compact failures exceeded elongate failures in terms of width, overall angle, and maximum scar angle. Figure 4-36 highlights the smaller lengths of

compact failures compared to elongate failures and the overall steeper valley slopes upon which compact failures originate compared to elongate failures.

4.1.5 *In-Situ* Undrained Shear Strength

Field shear vane measurements were taken at several failures (Table 4-4), but numbers of samples are insufficient to allow comparisons of *in-situ* undrained shear strength between locations above and below the shear plane, and within and below the rooting zone. *In-situ* undrained shear strength are only representative of conditions at the moment of sampling and hence do not represent conditions at the time of failure. However, measurements collected during meteorological conditions similar to those encountered at the time of failure can be considered representative of shear strength conditions at the time of failure (although they will generally be greater).

The two sets of measurements from above and below the shear plane display opposite results in terms of *in-situ* undrained shear strength (see Table 4-4). The measurements from within and below the rooting zone illustrate the higher strength of the rooting zone compared to the sediments just below the rooting zone.

Table 4-4. In-situ undrained shear strengths from several locations and failures on the Fosheim Peninsula.

Failure	Location	Depth (cm)	Average In-Situ Undrained Shear Strength (kPa)[1]	Standard Deviation
SC-2005-01	Sphagnum	3	8	4
	Within Rooting Zone	6	28	8
	Just Below Rooting Zone	10	22	9
BTC-2005-04	Ejection Feature - Profile 1	1	13	6
		10	8	5
		20	4	1
		30	3	4
		40	2	1
		50	1	1
	Ejection Feature - Profile 2	1	18	5
		8	12	7
		16	8	9
		24	7	10
		32	2	1
		40	4	2
BTC-2005-08	At Junction of Scar zone and Displaced Mass (area with high pore water pressures)	5	17	3
		22	5	3
BTC-2005-13	TP1 - Above Shear Plane	30	24	5
	TP1 - Below Shear Plane	40	52	12
	TP2 - Above Shear Plane	60	36	4
	TP2 - Below Shear Plane	70	19	4
	Below Scar Floor	5	13	4

Notes: 1. Average of 5 measurements.

Profiles of *in-situ* undrained shear strength were collected at two locations at BTC-2005-04 (see Table 4-4 and Figure 4-37). Both profiles were collected near a mud ejection feature generated by high pore-water pressures. The water table and frost table were encountered at depths of 4 cm and 51 cm (Profile 1), and 5-10 cm and 42 cm (Profile 2), respectively. Near surface *in-situ* undrained shear strengths were 13 and 17 kPa in Profiles 1 and 2, respectively, dropping to 1 and 3.5 kPa at depths of 50 and 40 cm

in Profiles 1 and 2, respectively. The latter sets of measurements were obtained just above the frost table.

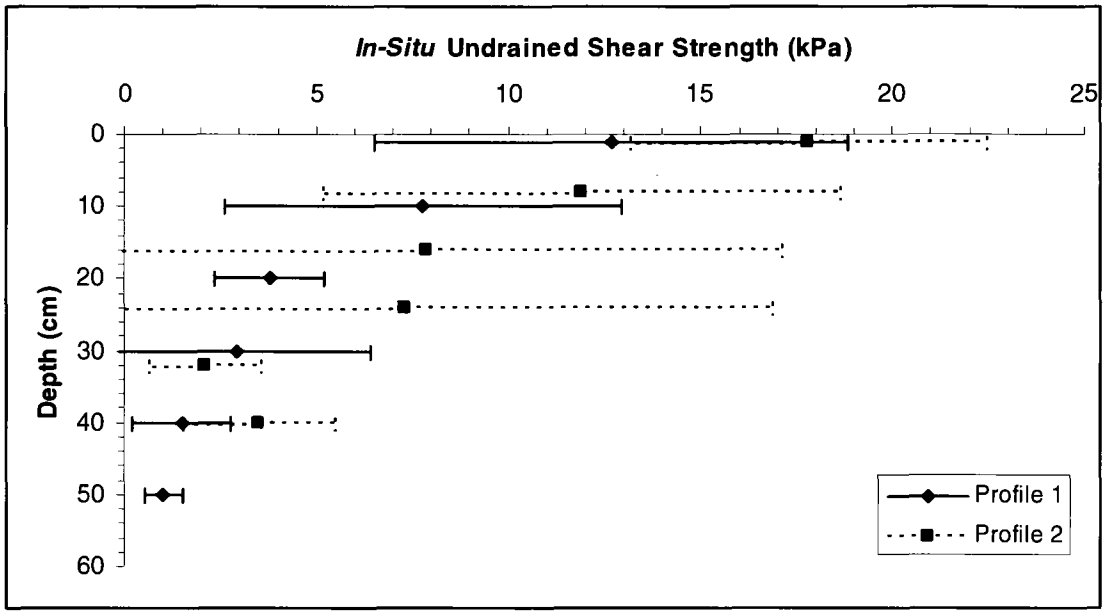

Figure 4-37. In-situ undrained shear strength profiles (mean (n = 5) and standard deviation) measured near mud ejection feature at BTC-2005-04 on July 19, 2006 (after Lewkowicz 2007).

In-situ undrained shear strength results from two previous investigations, Harris and Lewkowicz (2000) and Lewkowicz and Harris (2005b) were combined to allow a comparison with the vertical profiles of the current investigation (Table 4-5). The *in-situ* undrained shear strengths presented in Table 4-5 are from HWC and BSC not BTC, but the patterns are consistent with the current results where vertical profiles display a decrease in *in-situ* shear strength with depth. However, values from the two previous investigations were generally > 90% greater than the values from the two profiles at BTC-2005-04. The difference is likely due to the fact that profiles from previous investigations were collected from cleaned trial pit faces and not the high pore water pressure ejection feature locations of the current investigation.

Table 4-5. In-situ undrained shear strength of soil from previous published investigations on the Fosheim Peninsula (Harris and Lewkowicz 2000, Lewkowicz and Harris 2005b).

Study Area	Depth (cm)	Undrained Shear Strength		n; samples
		Average	Range	
HWC	10	67	57-86	3
	20	71	48-110	3
	30	74	36-120	5
	40	58	28-88	2
	50	55	38-75	3
	60	54	54-55	3
BSC	5	11	11-11	2
	10	46	14-83	3
	20	33	23-43	2
	30	32	13-42	3
	40	43	23-56	3
	50	35	30-38	3
	58-65	21	20-22	3

The vertical profiles of the current and previous investigations both display a decrease in *in-situ* shear strength with depth indicative of the relative high strength of upper crust sediments compared to the low strength of sediments close to the frost table. The presence of a vegetation mat contributes further to the strength of upper crust sediments due to the increased stability provided by the roots. Higher moisture contents associated with sediments close to the frost table contribute to a reduction in *in-situ* shear strength.

4.2 Engineering Properties of Failure Sediments

Various engineering properties of the active layer detachment deposit sediments were obtained from laboratory tests. These include particle-size, moisture content, LOI, bulk density, Atterberg Limits, and shear strength.

4.2.1 Failure Sediment Particle-Size Analysis

Soils subject to active layer detachments on the Fosheim Peninsula were dominantly sandy silts with clay (Table 4-6). Silt contents were high, ranging from a minimum of 50% (2006-07-18-01-BSP; BTC-2005-08) to a maximum of 75% (2006-07-17-03; HWC-2005-01). Clay content ranged from a minimum of 4% (2006-07-18-05-02; BTC-2005-08) to a maximum of 44% (2006-07-21-04-SP, 2006-07-21-04-BSP, and 2006-07-21-07; BTC-2005-13) and sand content ranged from 2% (2006-07-21-04-BSP; BTC-2005-13) to 46% (2006-07-18-01-BSP; BTC-2005-08).

Table 4-6. Textural characteristics of soils from 2005 active layer detachments examined on the Fosheim Peninsula.

Sample ID	Gravel (%)	Sand (%)	Silt (%)	Clay (%)
Station Creek; SC-2005-01				
2006-07-20-02	0	20	62	17
2006-07-20-02-ASP	0	25	58	16
2006-07-20-02-SP	0	19	64	17
2006-07-20-02-BSP	0	21	61	19
2006-07-20-06	0	23	62	15
2006-07-20-07	0	17	69	15
2006-07-20-08	0	26	62	12
Station Creek; SC-2005-02				
2006-07-21-02	0	4	70	25
2006-07-21-03	0	6	72	21
Black Top Creek; BTC-2005-04				
2006-07-18-06-ASP	0	7	63	**31**
2006-07-18-06-SP	**3**	21	57	19
2006-07-18-06-BSP	1	13	60	26
2006-07-19-01	1	16	64	19
2006-07-19-02	1	17	61	21
2006-07-19-05-01	0	29	53	18
2006-07-19-05-02	1	27	54	18
2006-07-19-07-ATP	0	27	56	17
2006-07-19-07-TP	0	29	55	16
2006-07-19-07-BTP	1	27	58	14
2006-07-21-10	0	10	67	23
2006-07-21-11	0	16	62	22
Black Top Creek; BTC-2005-08				
2006-07-17-09	0	7	67	26
2006-07-18-01 ASP	0	17	68	15
2006-07-18-01 SP	0	22	64	13
2006-07-18-01 BSP	0	46	50	5
Black Top Creek; BTC-2005-08 cont'				
2006-07-18-05-01	0	10	66	24
2006-07-18-05-02	0	40	56	4
2006-07-21-08	0	6	69	26
2006-07-21-09	0	6	68	26
Black Top Creek; BTC-2005-13				
2006-07-15-01-ATP	**3**	24	50	23
2006-07-15-02-BTP	0	**29**	51	20
2006-07-15-04 ASP	0	7	63	30
2006-07-15-04 SP	0	7	61	31
2006-07-15-04 BSP	0	8	62	31
2006-07-21-04-ASP	0	3	55	41
2006-07-21-04-SP	0	3	53	44
2006-07-21-04-BSP	0	2	54	44
2006-07-21-05	0	4	58	38
2006-07-21-06	0	5	63	32
2006-07-21-07	0	3	53	44
Hot Weather Creek; HWC-2005-01				
2006-07-17-01	6	21	53	19
2006-07-17-03	1	6	75	18
2006-07-17-03-SP	0	9	66	25
Big Slide Creek; BSC-2005-01				
2006-07-17-04-ASP	0	19	62	19
2006-07-17-04-SP	2	18	58	21
2006-07-17-04-BSP	5	23	54	17
2006-07-17-07-ABOH	12	19	52	17
2006-07-17-07-BOH	1	23	63	14
2006-07-17-07-BOHC	6	27	52	15

Notes: **63** Bold numbers indicates a value greater than two standard deviations above or below average for each failure.

Of the seven failures studied in detail: the sandiest were SC-2005-01 and BSC-2005-01 while SC-2005-02 had the least amount of sand; SC-2005-02 had the highest silt content while BSC-2005-01 and BTC-2005-13 had the lowest silt content; and BTC-2005-13 had the highest clay content while SC-2005-01 had the lowest clay content (Table 4-6). Gravel was not found within the active layer detachments studied at the SC study area, at BTC-2005-08, and with the exception of one sample, was not found at BTC-2005-13. The failure containing the highest percentage of gravel (12%) was BSC-2005-01. Table 4-7 provides the summary statistics (average, standard deviation, and range) of sand, silt, and clay percentages for each failure and study area (if two or more failures were investigated in a study area).

When comparing the four study areas: the sandiest was BSC and the least sandy was HWC; HWC had the highest silt content while BSC had the lowest silt content; and BTC had the highest clay content while BSC had the lowest clay content (Figure 4-38). Particle-size envelopes show a slightly finer and more variable particle size distribution at BTC, but a much larger number of samples were collected at BTC (31) compared to 9 samples at SC, 6 at BSC, and 3 at HWC.

Table 4-7. Average, standard deviation and range for textural characteristics of soils from 2005 active layer detachments examined on the Fosheim Peninsula.

Study area and failure	n; samples	Sand (%; 0.06-2mm)			Silt (%; 0.002-0.06mm)			Clay (%; <0.002mm)		
		Av	Sd	Range	Av	Sd	Range	Av	Sd	Range
SC-2005-01	7	22	3	17-26	62	3	58-69	16	2	12-19
SC-2005-02	2	5	1	4-6	71	1	70-72	23	3	21-25
BTC-2005-04	12	20	8	7-29	59	4	53-67	20	5	14-31
BTC-2005-08	8	19	16	6-46	63	7	50-69	17	9	4-26
BTC-2005-13	11	9	9	2-29	57	5	50-63	34	9	20-44
HWC-2005-01	3	12	8	6-21	65	11	53-75	21	4	18-25
BSC-2005-01	6	22	3	18-27	57	5	52-63	17	3	14-21
SC Study area	9	18	8	4-26	64	5	58-72	18	4	12-25
BTC Study area	31	16	12	2-46	59	6	50-69	24	10	4-44

Notes: Av – Average
Sd - Standard Deviation

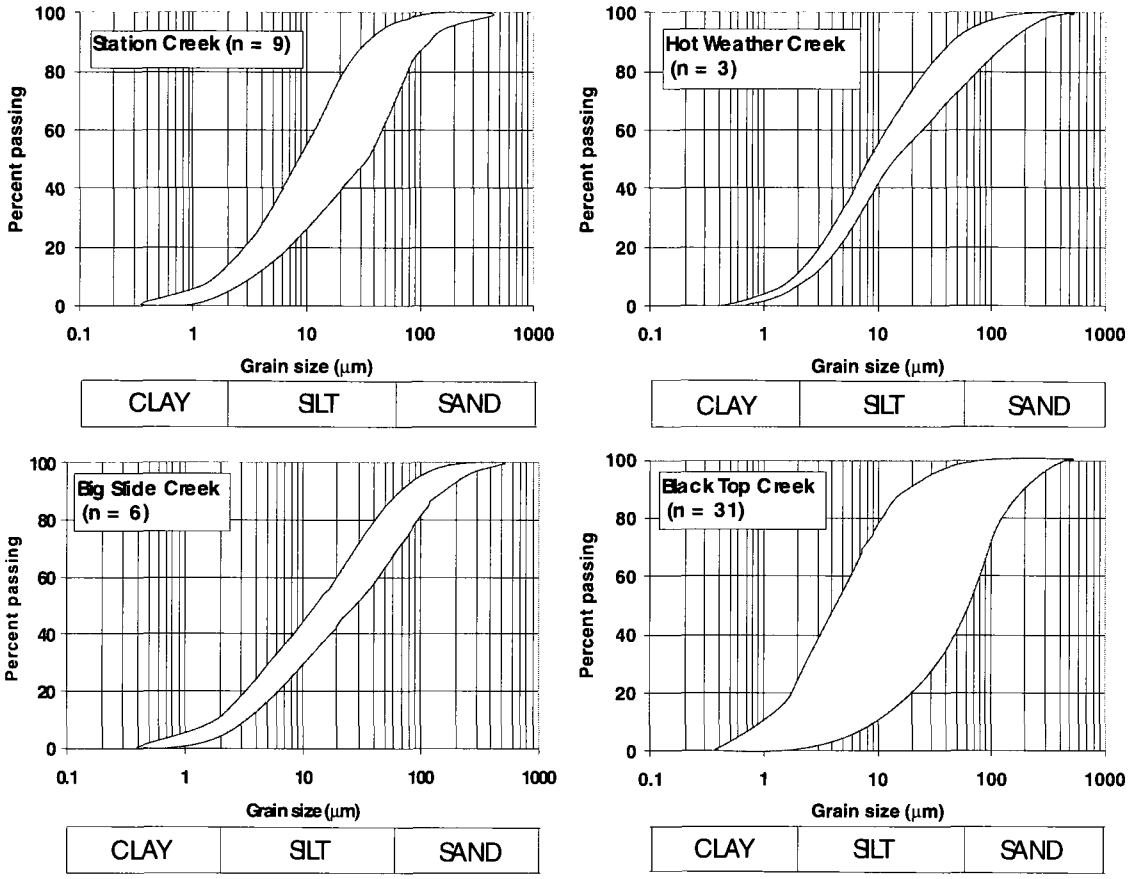

Figure 4-38. Particle-size distribution envelopes of samples collected from 2005 active layer detachments at each of the four study areas on the Fosheim Peninsula.

Table 4-8 provides the inclusive graphic standard deviation and verbal classification of degree of sorting for each failure. Particle size sorting was either poorly or very poorly sorted. Given that both poorly and very poorly sorted particle sizes were reported at SC and BTC (the only areas where more than one failure was studied), it is not possible to determine particle size sorting trends between study areas.

Table 4-8. Inclusive graphic standard deviation and degree of sorting of soils from 2005 active layer detachments on the Fosheim Peninsula.

Study area and failure	n; samples	Inclusive Graphic Standard Deviation (gs; in Φ)	Degree of Sorting
SC-2005-01	7	2.1	very poorly
SC-2005-02	2	1.79	poorly
BTC-2005-04	12	2.2	very poorly
BTC-2005-08	8	1.89	poorly
BTC-2005-13	11	1.99	poorly
HWC-2005-01	3	2.2	very poorly
BSC-2005-01	6	2.5	very poorly

Particle size distribution results were compared to those reported in Lewkowicz and Harris (2005b; Table 4-9). Results from the current investigation are inconsistent with those previously obtained as the current study reports silt contents in all study areas that are much greater, while sand and clay contents are much less.

Table 4-9. Textural characteristics of soils examined during previously published investigation (Lewkowicz and Harris 2005b) on the Fosheim Peninsula.

Study Area	Sand (%; 0.06-2mm)		Silt (%; 0.002-0.06mm)		Clay (%; <0.002mm)		n; samples
	Average	Range	Average	Range	Average	Range	
BTC	15	9-23	37	32-40	48	40-59	5
HWC	23.2	1-44	35.4	28-42	41.4	21-57	5
BSC	22.2	2-37	38.4	27-50	39.4	28-48	5

Since only one failure (BTC-2005-08) of the seven failures studied in detail was identified as compact, it is not possible to compare the particle size distribution of compact failures to elongate failures on the Fosheim Peninsula. However, a direct comparison can be made between the particle size distribution results of BTC-2005-08 and one of the elongate failures within the same study area, BTC-2005-04. Table 4-7 does not indicate a significant difference between the sand, silt, and clay averages of samples collected from the two failures.

Samples were also grouped according to vertical location in the soil profile with reference to the shear or thrust plane (Figure 4-39). Table 4-10 provides the summary

statistics (average, standard deviation, and range) of sand, silt, and clay percentages for each group. At first glance, a comparison of gravel, sand, silt, and clay averages does not indicate a significant difference between the groups. A paired t-test was conducted to examine the probability of real differences existing between the averages of the groups (Table A-1, Appendix A). Computed t-values are less than t-critical for two tails and that the computed p-values are always greater than the significance factor (0.05). These tests confirm that there are no significant differences between particle-size groups for any vertical location in the soil profile with reference to the shear or thrust plane.

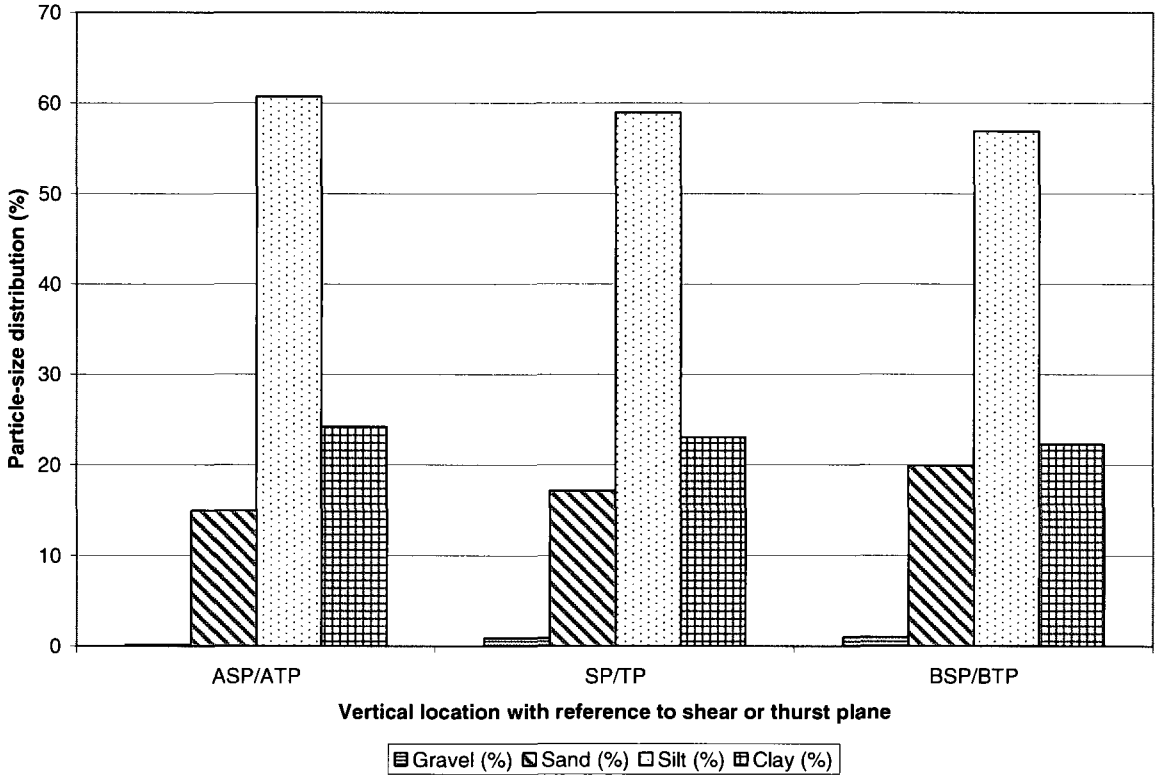

Figure 4-39. Comparison of particle-size distribution based on vertical location in the soil profile with reference to the shear or thrust plane for 2005 active layer detachments examined on the Fosheim Peninsula.

Table 4-10. Average, standard deviation, and range for textural characteristics of soils from 2005 active layer detachments on the Fosheim Peninsula grouped according to vertical location in the soil profile with reference to the shear or thrust plane.

Vertical location in soil profile	n; samples	Sand (%; 0.06-2mm)			Silt (%; 0.002-0.06mm)			Clay (%; <0.002mm)		
		Av	Sd	Range	Av	Sd	Range	Av	Sd	Range
ASP/ATP	7	15	9	3-27	61	4	55-68	24	10	15-41
SP/TP	7	17	9	3-29	59	4	53-64	23	11	13-44
BSP/BTP	7	20	14	2-46	57	4	50-62	22	13	5-44

Av - Average

Sd - Standard Deviation

4.2.2 Failure Sediment Soil moisture and LOI

The soil moisture contents provide information regarding the conditions within the slope and along the shear or thrust planes. However, these samples are not directly comparable to conditions at the time of failure because a year had passed since the failure events. Across all four study areas, moisture content ranged from 13 to 47% while LOI ranged from 2.6 to 12% (Table 4-11). Of the four study areas, SC exhibited the lowest average moisture content (22%) while BTC exhibited the greatest average moisture content (29%; Table 4-12). With reference to individual failures, SC-2005-01 exhibited the lowest average moisture content (21%) while BTC-2005-13 exhibited the greatest average moisture content (32%; see Table 4-12).

The LOI data provides information regarding the organic content of the soil (see Tables 4-11 and 4-12). Across all four study areas, organic content ranged from 2.6 to 12% (Table 4-11). Of the four study areas, SC exhibited the lowest average LOI (6.3%) while BSC exhibited the greatest average LOI (9.7%; Table 4-12). Both the SC-2005-01 and BTC-2005-08 failures exhibited low LOI averages (5.9%) while BSC-2005-01 exhibited the greatest LOI average (9.7%; see Table 4-12). However, the high average LOI value for the BSC-2005-01 failure may be considered unusual since it is influenced

by a high LOI value (12%) from sample 2006-07-17-07-BOH which was from a buried organic horizon.

Table 4-11. Moisture content and LOI of soils from 2005 active layer detachments examined on the Fosheim Peninsula.

Sample ID	Depth (m)	Moisture Content (%)	LOI (%)
Station Creek; SC-2005-01			
2006-07-20-02	0.4	25	7.7
2006-07-20-02-ASP	0.4	18	5.5
2006-07-20-02-SP	0.4	21	5.5
2006-07-20-02-BSP	0.4	21	6.5
2006-07-20-06	0.6	24	5.2
2006-07-20-07	0.01	13	5.5
2006-07-20-08	0.7	27	5.2
Station Creek; SC-2005-02			
2006-07-21-02	0.01	24	8.1
2006-07-21-03	0.65	28	7.1
Black Top Creek; BTC-2005-04			
2006-07-18-06-ASP	0.6	27	8.3
2006-07-18-06-SP	0.6	21	6.5
2006-07-18-06-BSP	0.6	21	7.5
2006-07-19-01	0.15	**39**	6.3
2006-07-19-02	0.15	33	6.1
2006-07-19-05-01	0.6	24	6.5
2006-07-19-05-02	0.6	23	6.5
2006-07-19-07-ATP	0.6	21	6.3
2006-07-19-07-TP	0.6	21	6.0
2006-07-19-07-BTP	0.6	24	5.6
2006-07-21-10	0.01	24	7.8
2006-07-21-11	0.65	25	7.0
Black Top Creek; BTC-2005-08			
2006-07-17-09	0.2	43	8.5
2006-07-18-01-ASP	0.45	24	4.9
2006-07-18-01-SP	0.45	31	5.6
2006-07-18-01-BSP	0.45	22	2.6
Black Top Creek; BTC-2005-08 cont'			
2006-07-18-05-01	0.3	28	7.4
2006-07-18-05-02	0.3	21	2.6
2006-07-21-08	0.7	38	7.7
2006-07-21-09	0.01	35	8.0
Black Top Creek; BTC-2005-13			
2006-07-15-01-ATP	0.35	25	6.8
2006-07-15-02-BTP	0.35	28	6.4
2006-07-15-04-ASP	0.6	28	7.3
2006-07-15-04-SP	0.6	33	7.5
2006-07-15-04-BSP	0.6	34	7.5
2006-07-21-04-ASP	0.5	33	8.7
2006-07-21-04-SP	0.5	35	9.2
2006-07-21-04-BSP	0.5	37	9.1
2006-07-21-05	0.01	19	9.3
2006-07-21-06	0.7	**47**	7.8
2006-07-21-07	0.55	37	9.3
Hot Weather Creek; HWC-2005-01			
2006-07-17-01	0.01	16	9.3
2006-07-17-03	0.17	32	8.3
2006-07-17-03-SP	0.17	31	9.1
Big Slide Creek; BSC-2005-01			
2006-07-17-04-ASP	0.15	29	8.9
2006-07-17-04-SP	0.15	32	11
2006-07-17-04-BSP	0.15	22	8.2
2006-07-17-07-ABOH	0.25	23	8.8
2006-07-17-07-BOH	0.25	34	12
2006-07-17-07-BOHC	0.25	25	9.3

Note: **63** Bold numbers indicates a value greater than two standard deviations above or below average for each failure.

Table 4-12. Moisture content and LOI average, standard deviation and range of samples grouped according to study area and failure.

Study area and failure	n; samples	Moisture content (%)			LOI (%)		
		Av	Sd	Range	Av	Sd	Range
SC-2005-01	7	21	5	13-27	5.9	0.9	5.2-7.7
SC-2005-02	2	26	3	24-28	7.6	0.7	7.1-8.1
BTC-2005-04	12	28	6	21-39	7.0	0.8	5.6-8.3
BTC-2005-08	8	30	8	21-43	5.9	2.4	2.6-8.5
BTC-2005-13	11	32	7	19-47	8.1	1.1	6.4-9.3
HWC-2005-01	3	26	9	16-32	8.9	0.5	8.3-9.3
BSC-2005-01	6	28	5	22-34	9.7	1.5	8.2-12
SC Study area	9	22	5	13-28	6.3	1.1	5.2-8.1
BTC Study area	31	29	7	19-47	7.0	1.6	2.6-9.3
HWC Study area	3	26	9	16-32	8.9	0.5	8.3-9.3
BSC Study area	6	28	5	22-34	9.7	1.5	8.2-12

Av - Average
Sd - Standard Deviation

Average moisture contents calculated for the HWC and BSC study areas as part of the current investigation are similar to results reported in the Lewkowicz and Harris (2005b) investigation (Table 4-13). In both studies, moisture content averages were in the mid-20's with higher contents calculated at BSC than HWC.

Table 4-13. Moisture content of soils examined during previously published investigation on the Fosheim Peninsula.

Study Area	Moisture Content		n; samples	Source
	Average	Range		
BTC	-	-	-	Harris and Lewkowicz (2000)
HWC	23.5	12.5-34	15	Harris and Lewkowicz (2000)
BSC	26	8-37	17	Harris and Lewkowicz (2000)

Note: '-' indicates no data available.

To examine potential differences between the moisture content and LOI of compact and elongate failures a direct comparison was made between the results of BTC-2005-08 and BTC-2005-04. Review of Table 4-12 does not indicate a significant

difference between the moisture content and LOI of samples collected from the two failures.

Samples were also grouped according to vertical location in the soil profile with reference to the shear or thrust plane (Table 4-14). At first glance, a comparison of moisture content and LOI averages does not indicate a significant difference between the groups. A t-test was conducted to examine the probability of real differences existing between the means of the groups (Table A-2, Appendix A). The paired t-tests show that computed t-values are less than t-critical for two tails and that the computed p-values are always greater than the significance factor (0.05). The paired t-tests confirm therefore, that there are no significant differences between moisture content and LOI for any vertical location in the soil profile with reference to the shear or thrust plane.

Table 4-14. Moisture content and LOI average, standard deviation and range of samples grouped according to vertical location in the soil profile with reference to the shear or thrust plane.

Vertical location in soil profile	n; samples	Moisture content (%)			LOI (%)		
		Av	Sd	Range	Av	Sd	Range
ASP/ATP	8	26	5	18-33	7.0	1.5	4.9-8.9
SP/TP	8	28	6	21-35	8.0	2.1	5.5-11
BSP/BTP	8	20	6	21-37	7.0	2.0	2.6-9.1

Av - Average
Sd - Standard Deviation

4.2.3 Failure Sediment Bulk Density and Unit Weight

The bulk density and unit weight of soil were determined to facilitate calculations of shear strength and slope stability. Results indicate that the sample from BTC-2005-13 (2006-07-15-02) exhibited the lowest bulk density and soil unit weight (Table 4-15). Whereas, the sample from HWC-2005-01 (2006-07-17-03) exhibited the highest bulk density and soil unit weight.

Table 4-15. Bulk density and soil unit weight of select samples from 2005 active layer detachments examined on the Fosheim Peninsula.

Failure	Sample ID	Moisture content (ω; %)	Slice mass (M; g)	Volume of slice (V; cm^3)	Bulk density (ρ; M/V; g/cm^3)	Unit weight (γ; $\gamma = \rho * g$; kN/m^3)
SC-2005-01	2006-07-20-02	25	287	144	1.99	19.6
BTC-2005-04	2006-07-18-06	25	278	144	1.93	19.0
BTC-2005-08	2006-07-18-01	28	323	144	2.25	22.0
BTC-2005-13	2006-07-21-07	37	275	144	1.91	18.7
BTC-2005-13	2006-07-15-02	31	253	144	1.76	17.3
HWC-2005-01	2006-07-17-03	32	352	144	2.45	24.0
Average		32	295	144	2.05	20.1

Harris and Lewkowicz (2000) reported an average measured bulk density of 1.73 g/cm^3 for samples from HWC and BSC, corresponding to a moisture content of 23%. Average bulk density and moisture content from the bulk density samples for the current investigation are respectively 16% and 23% greater than those from the Harris and Lewkowicz (2000) investigation.

4.2.4 Failure Sediment Atterberg Limits

As the Atterberg Limit tests are only suitable for cohesive sediments, tests were not conducted on cohesionless samples. These samples included 2006-07-18-01-BSP and 2006-07-18-05-02 where particle-size analyses classified as silt loam sediments. Flow curves were plotted for each sample to determine the Liquid Limit (LL). An example of a graph produced is shown in Figure 4-40 with all other graphs found in Appendix B.

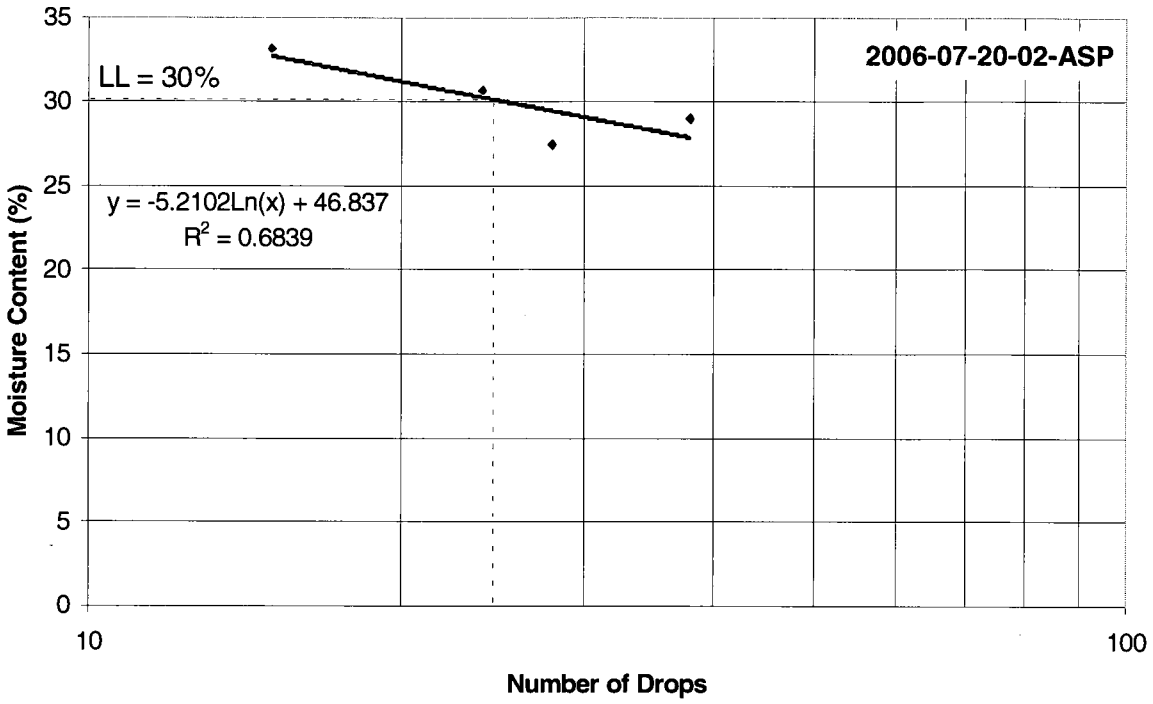

Figure 4-40. Example of a flow curve used to determine Liquid Limit. The result for this sample was a liquid limit of 30%.

Across the study areas, LLs ranged from 24 to 54%, Plastic Limits (PLs) from 16 to 29%, and Plasticity Index (PI) ranged from 6 to 30% (Table 4-16). When comparing the four study areas: HWC had the highest average LL and PL while SC had the lowest average LL and PL (Table 4-17). Both SC and BSC exhibited low average PI while HWC had the highest average PI (see Table 4-17).

Table 4-16. Atterberg limits and plasticity indices of select sediment samples from 2005 active layer detachments examined on the Fosheim Peninsula.

Sample ID	LL (%)	PL (%)	PI (%)
Station Creek; SC-2005-01			
2006-07-20-02-ASP	30	17	13
2006-07-20-02-BSP	32	18	14
2006-07-20-06	31	25	6
2006-07-20-07	31	22	9
2006-07-20-08	27	18	9
Station Creek; SC-2005-02			
2006-07-21-02	44	23	21
2006-07-21-03	38	24	14
Black Top Creek; BTC-2005-04			
2006-07-18-06-ASP	**43**	26	17
2006-07-18-06-BSP	32	20	12
2006-07-19-01	30	19	11
2006-07-19-02	28	17	11
2006-07-19-05-01	30	22	8
2006-07-19-05-02	31	19	12
2006-07-19-07-ATP	27	18	9
2006-07-19-07-BTP	24	16	8
2006-07-21-10	37	27	10
2006-07-21-11	35	21	14
Black Top Creek; BTC-2005-08			
2006-07-17-09	37	24	13
Black Top Creek; BTC-2005-08 cont'			
2006-07-18-01 ASP	29	19	10
2006-07-18-05-01	41	21	20
2006-07-21-08	40	22	18
2006-07-21-09	41	28	13
Black Top Creek; BTC-2005-13			
2006-07-15-01-ATP	35	21	14
2006-07-15-02-BTP	36	21	15
2006-07-15-04 ASP	51	28	23
2006-07-15-04 BSP	46	25	21
2006-07-21-04-ASP	47	27	20
2006-07-21-04-BSP	48	29	19
2006-07-21-05	51	25	26
2006-07-21-06	48	22	26
2006-07-21-07	54	24	30
Hot Weather Creek; HWC-2005-01			
2006-07-17-01	38	19	19
2006-07-17-03	46	29	17
Big Slide Creek; BSC-2005-01			
2006-07-17-04-ASP	40	24	16
2006-07-17-04-BSP	31	20	11
2006-07-17-07-ABOH	30	22	8

Notes: **3**; Bold numbers indicates a value greater than two standard deviations above or below average for each failure.

LL; Liquid Limit

PL; Plastic Limit

PI; Plasticity Index

Table 4-17. Average, standard deviation, and range for Atterberg limits and plasticity indices of soils from 2005 active layer detachments examined on the Fosheim Peninsula.

Study area and failure	n; samples	LL (%)			PL (%)			PI (%)		
		Av	Sd	Range	Av	Sd	Range	Av	Sd	Range
SC-2005-01	5	30	2	27-32	20	3	17-25	10	3	6-14
SC-2005-02	2	41	4	38-44	24	1	23-24	18	5	14-21
BTC-2005-04	10	33	5	24-43	21	4	16-27	12	3	8-17
BTC-2005-08	5	38	5	29-41	23	3	19-28	15	4	10-20
BTC-2005-13	9	46	7	35-54	25	3	21-29	22	5	14-30
HWC-2005-01	2	42	6	38-46	24	7	19-29	18	1	17-19
BSC-2005-01	3	34	6	30-40	22	2	20-24	12	4	8-16
SC Study area	7	33	6	27-44	21	3	17-25	12	5	6-21
BTC Study area	26	38	9	24-54	23	4	16-29	16	6	8-30
HWC Study area	2	42	6	38-46	24	7	19-29	18	1	17-19
BSC Study area	3	34	6	30-40	22	2	20-24	12	4	8-16

Notes: LL; Liquid Limit
PL; Plastic Limit
PI; Plasticity Index
Av; Average
Sd; Standard Deviation

To examine potential differences between the Atterberg Limits and plasticity indices of compact and elongate failures a comparison can be made between the results of BTC-2005-08 and BTC-2005-04 (Table 4-17). Higher Atterberg Limits and a higher plasticity index were associated with the compact failure.

Samples were also grouped according to vertical location in the soil profile with reference to the shear or thrust plane (Table 4-18). At first glance, a comparison of Atterberg Limits and plasticity indices averages does not indicate a significant difference between the two groups. A t-test was conducted to examine the probability of real differences existing between the means of the two groups (Table A-3, Appendix A). The paired t-tests show that computed t-values are less than t-critical for two tails and that the computed p-values are always greater than the significance factor (0.05). The paired t-tests therefore, confirm that there are no significant differences between Atterberg

Limits and plasticity indices for any vertical location in the soil profile with reference to the shear or thrust plane.

Table 4-18. Atterberg limits and plasticity index average, standard deviation and range of samples grouped according to vertical location in the soil profile with reference to the shear or thrust plane.

Vertical location in soil profile	n; samples	LL (%)			PL (%)			PI (%)		
		Av	Sd	Range	Av	Sd	Range	Av	Sd	Range
ASP/ATP	8	38	9	27-51	23	4	17-28	15	5	9-23
BSP/BTP	7	36	9	24-48	21	4	16-29	14	5	8-21

Notes: LL; Liquid Limit
PL; Plastic Limit
PI; Plasticity Index
Av; Average
Sd; Standard Deviation

LL was plotted against PI producing a plasticity chart (Figure 4-41). The majority of the samples, and at least one sample from every failure, fell within the CL or OL range (low-plasticity clay or low plasticity organic soil). All of the samples from SC-2005-02 and BSC-2005-01 fell within this range. Five samples fell within the ML or OL range (low plasticity silt or low plasticity organic soil). These samples were from SC-2005-01, HWC-2005-01, BTC-2005-04, BTC-2005-08, and BTC-2005-13. Three samples, all of which were from BTC-2005-13, fell within the CH or OH range (high-plasticity clay or high plasticity organic soil). Organic soil contains more than 17% organic carbon (about 30% or more organic matter) by weight (Soil Classification Working Group 1998). Given that soils on the Fosheim Peninsula did not contain 30% or more organic matter, samples can be classified as CL, ML or CH and not OL or OH. The very low sand contents of the three samples in question compared to other samples is likely the reason for the highly plastic nature of these three samples.

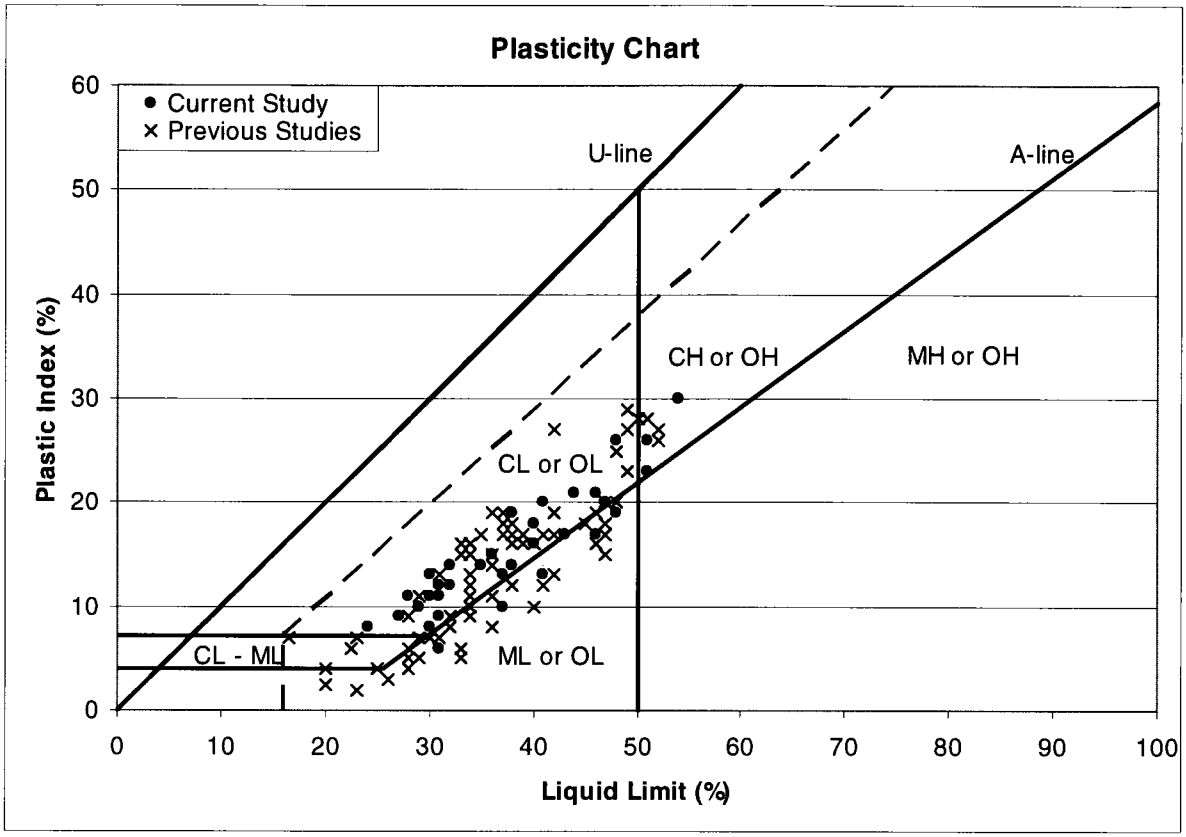

Figure 4-41. Plasticity chart of sediments from active layer detachments examined on the Fosheim Peninsula during the current study and previous studies (Harris and Lewkowicz 2000; Lewkowicz and Harris 2005b).

Atterberg limits from the current study were compared to those measured in previous investigations (Harris and Lewkowicz 2000, Lewkowicz and Harris 2005b). Atterberg limits and plasticity indices from BTC soil samples analyzed and reported in previous investigations are consistent with results from the current study (Table 4-19). Atterberg limits and plasticity indices from soil samples collected from HWC and BSC during the current study are most similar to soil samples collected from depths at or greater than 40 cm below ground surface during previous investigations. In both the current study and previous investigations, soil at depth from HWC and BSC study areas are characterized by lower Atterberg limits and plasticity indices indicating that low moisture contents are sufficient to create soil liquid and plastic states. To allow comparison, results from previous investigations are plotted on the same plasticity chart

as results from the current study (see Figure 4-41). The comparison indicates results from the current study are consistent with results from previous studies.

Table 4-19. Atterberg limits and plasticity indices of soils from previously published investigations on the Fosheim Peninsula.

Study area	Depth (cm)	PL (%)	LL (%)	PI (%)	Source
BTC	Nt	Nt	~17-53[a]	~3-26[a]	Lewkowicz and Harris (2005b)
HWC	Nt	Nt	~38-53[a]	~17-28[a]	Lewkowicz and Harris (2005b)
HWC	20	22-23	49-51	27-28	Harris and Lewkowicz (2000)
HWC	40	21	38	17	Harris and Lewkowicz (2000)
HWC	50	21-25	36-42	15-17	Harris and Lewkowicz (2000)
BSC	Nt	Nt	~23-50[a]	~3-28[a]	Lewkowicz and Harris (2005b)
BSC	20	15	42	27	Harris and Lewkowicz (2000)
BSC	30	13-17	38-42	16-19	Harris and Lewkowicz (2000)
BSC	50	22	38	16	Harris and Lewkowicz (2000)
BSC	60	18-22	36-37	14-19	Harris and Lewkowicz (2000)

Notes: LL; Liquid Limit
PL; Plastic Limit
PI; Plasticity Index
nt; Not tabulated.
[a] Data approximate as read from graph.

4.2.5 Failure Sediment Shear Strength

Peak shear strengths of the undisturbed samples were measured in a 6 cm^2 shear box. Two to three 6 cm x 6 cm x 3 cm specimens were cut along the shear or thrust plane from the original 12 cm x 12 cm x 12 cm undisturbed sample. Care was taken to locate the shear or thrust plane as exactly as possible in the shear plane of the box and to arrange the specimen so that shearing followed the natural direction of movement. Where feasible, an additional two to three specimens were cut from the soil above and below the shear or thrust plane and subjected to direct shear tests.

As described in Section 3.3.5, each specimen was subject to an initial run, at effective stresses of; 4.2, 7.2, or 10.8 kPa, to determine peak effective cohesion and peak effective internal angle of friction. Each specimen was then subject to three additional

runs, at effective stresses of; 30, 60, and 120 kPa, to determine residual effective internal angle of friction (residual effective cohesion is assumed to be zero). Stress-displacement curves were used to determine the peak and residual maximum shear stresses.

Determination of the peak and residual maximum shear stresses from the stress-displacement curves proved difficult. A noticeable maximum shear stress followed by a drop in shear stress with additional displacement was not present. Generally shear stresses increased rapidly with displacement, eventually reaching a displacement at which the rate of increase reduced. Attempts to determine maximum peak and residual shear stress using the conventional method appeared somewhat subjective. In an attempt to eliminate subjectiveness from the selection process, the shear stress corresponding to a horizontal displacement of 4 mm was chosen to represent the maximum peak and residual shear stress. A horizontal displacement of 4 mm was chosen because in all tests, at least 4 mm of horizontal movement was attained. Where more than one test was conducted for a particular effective stress (as was the case in residual tests) the lowest shear stress at a 4 mm horizontal displacement of the two or three tests was chosen as representative of residual shear stress. The lowest value was chosen because in theory, residual shear stresses should be less than peak shear stresses and concern that higher values were related to friction that developed within the sample during the tests due to gravel and/or drying of the sample.

Examples of peak and residual curves produced by the tests are shown in Figure 4-42 with all other curves portrayed in Appendix C. A graph was produced by plotting the maximum shear stress (τ) from each run against the corresponding effective stress (σ) of that run (4.2, 7.2, and 10.8 kPa in the case of the peak direct shear tests, and 30, 60, and 120 kPa in the case of the residual direct shear tests) to determine cohesion and internal angle of friction (peak and residual). An example of such a graph is shown in Figure 4-43 with all other graphs found as an insert within the corresponding stress-displacement curve in Appendix C.

Table 4-20 presents the peak and residual maximum shear strength values, obtained from shear stress (τ) versus horizontal displacement graphs (see Appendix C). As would be expected, the maximum shear strength values increased with increasing vertical load for most samples for both peak and residual tests.

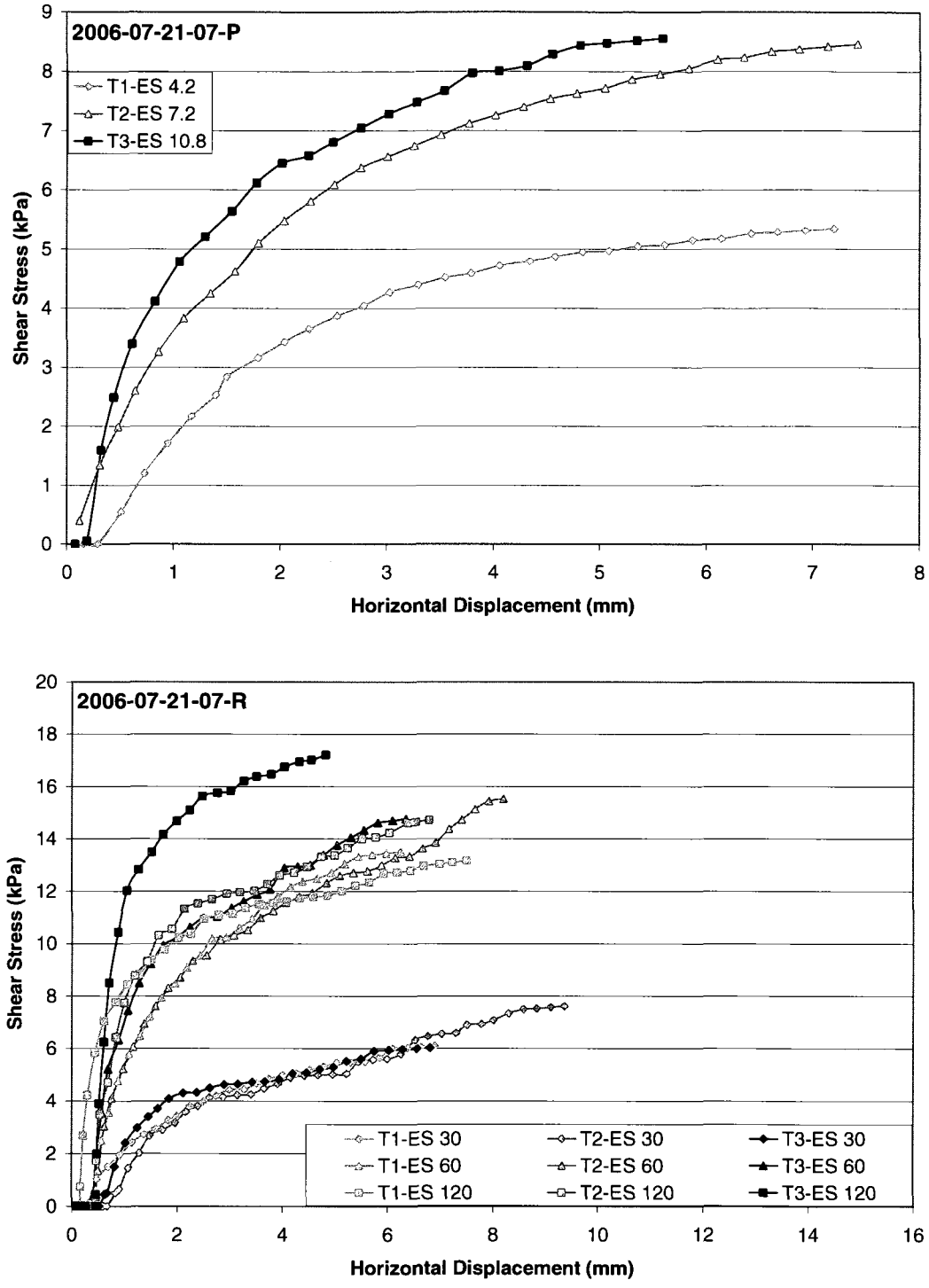

Figure 4-42. Example of peak and residual stress-displacement curves used to determine peak and residual maximum shear stress.

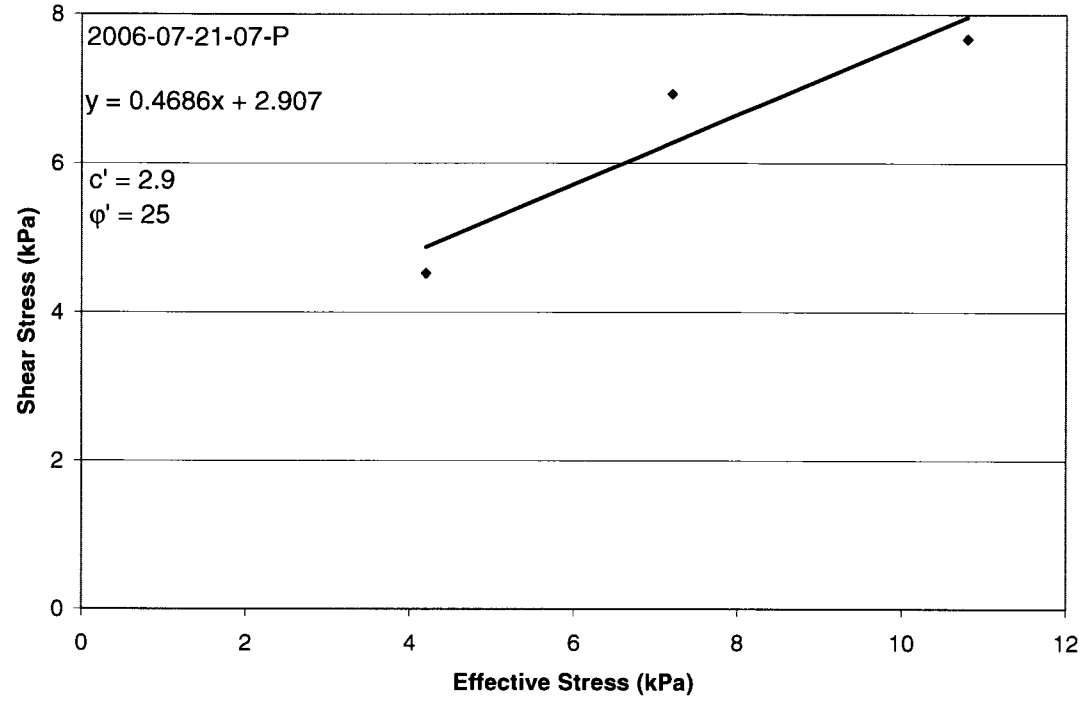

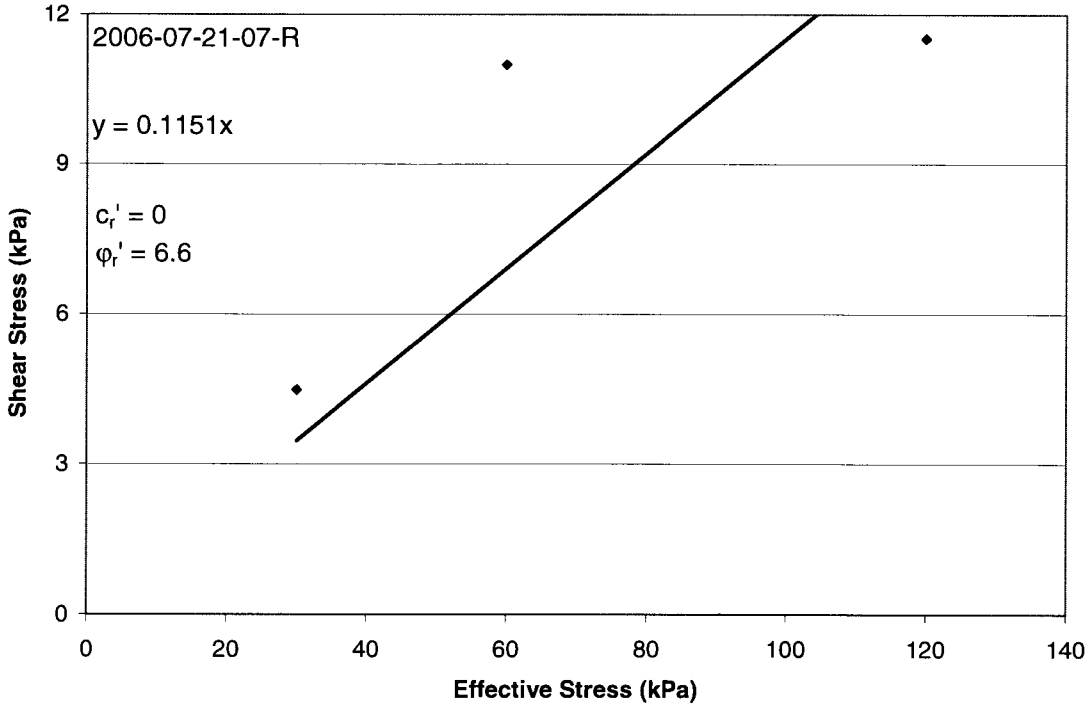

Figure 4-43. Example of a graph used to determine cohesion and internal angle of friction (peak and residual).

Table 4-20. Peak and residual maximum shear strength values from 2005 active layer detachments examined on the Fosheim Peninsula.

Sample ID	Peak Maximum Shear Strength (kPa)		
	4.2kN	7.2kN	10.8kN
Station Creek; SC-2005-01			
2006-07-20-02-ASP-P	2.6	-	8.1
2006-07-20-02-BSP-P	1.0	-	11.6
Black Top Creek; BTC-2005-04			
2006-07-19-07-ATP-P	-	8.4	13.3
2006-07-19-07-BTP-P	4.4	4.4	7.4
Black Top Creek; BTC-2005-08			
2006-07-18-01-ASP-P	2.2	-	7.2
Black Top Creek; BTC-2005-13			
2006-07-15-01-ATP-P	19.5	18.8	26.3
2006-07-15-02-BTP-P	9.9	12.6	-
2006-07-15-04-BSP-P	13.4	-	18.5
2006-07-21-04-ASP-P	9.4	-	15.5
2006-07-21-04-BSP-P	8.6	12.2	11.4
2006-07-21-07-P	4.5	6.9	7.7
Hot Weather Creek; HWC-2005-01			
2006-07-17-03-P	5.7	10.6	12.0
Big Slide Creek; BSC-2005-01			
2006-07-17-04-ASP-P	10.6	15.7	17.9
2006-07-17-04-BSP-P	11.6	14.2	17.6
2006-07-17-07-OH-P	7.8	8.6	14.0

Sample ID	Residual Maximum Shear Strength (kN)		
	30kN	60kN	120kN
Black Top Creek; BTC-2005-04			
2006-07-18-06-SP-R	8.7	19.9	46.8
2006-07-19-05-TP-R	8.4	8.7	28.3
2006-07-19-07-TP-R	9.8	15.1	42.6
Black Top Creek; BTC-2005-13			
2006-07-15-04-SP-R	7.2	-	24.6
2006-07-21-04-SP-R	-	14.5	15.8
2006-07-21-07-R	4.5	11.0	11.5
Hot Weather Creek; HWC-2005-01			
2006-07-17-03-R	8.4	16.2	35.9
Big Slide Creek; BSC-2005-01			
2006-07-17-04-SP-R	9.4	15.5	30.5

Sample ID	Residual Maximum Shear Strength (kN)		
	4.2kN	7.2kN	10.8kN
Station Creek; SC-2005-01			
2006-07-20-02-SP-R	0.6	0.9	3.8
Black Top Creek; BTC-2005-08			
2006-07-18-01-SP-R	1.1	-	3.5

Notes: P; Peak

R; Residual

'-' indicates not analyzed.

Table 4-21 summarizes the shear strength parameters, cohesion and internal angle of friction (peak and residual) that were obtained from the maximum shear stress (τ) versus effective stress (σ') graphs (see Appendix C). Correlation analysis was conducted to determine if statistically significant relationships exist between the shear strength parameters and clay content. The analysis did not indicate statistically significant relationships between the peak shear strength parameters and clay at the 5% level. However, the analysis indicated a strong negative relationship between residual internal angle of friction and clay content (-0.82; p-value of 0.003) indicating that the residual strength of soil previously subject to failures decreases with increasing clay content.

Table 4-21. Peak and residual shear strength parameters from 2005 active layer detachments examined on the Fosheim Peninsula.

Peak Shear Strength Parameters			Residual Shear Strength Parameters		
Sample ID	c' (kPa)	ϕ' (°)	Sample ID	c_r' (kPa)	ϕ_r' (°)
Station Creek; SC-2005-01			Station Creek; SC-2005-01		
2006-07-20-02-ASP-P	0	36	2006-07-20-02-SP-R	0	15
2006-07-20-02-BSP-P	0	44	Black Top Creek; BTC-2005-04		
Black Top Creek; BTC-2005-04			2006-07-18-06-SP-R	0	21
2006-07-19-07-ATP-P	0	51	2006-07-19-05-TP-R	0	12
2006-07-19-07-BTP-P	2.0	25	2006-07-19-07-TP-R	0	19
Black Top Creek; BTC-2005-08			Black Top Creek; BTC-2005-08		
2006-07-18-01-ASP-P	0	33	2006-07-18-01-SP-R	0	17
Black Top Creek; BTC-2005-13			Black Top Creek; BTC-2005-13		
2006-07-15-01-ATP-P	14	47	2006-07-15-04-SP-R	0	12
2006-07-15-02-BTP-P	6.1	42	2006-07-21-04-SP-R	0	8.7
2006-07-15-04-BSP-P	10	38	2006-07-21-07-R	0	6.6
2006-07-21-04-ASP-P	5.5	43	Hot Weather Creek; HWC-2005-01		
2006-07-21-04-BSP-P	7.7	22	2006-07-17-03-R	0	16
2006-07-21-07-P	2.9	25	Big Slide Creek; BSC-2005-01		
Hot Weather Creek; HWC-2005-01			2006-07-17-04-SP-R	0	15
2006-07-17-03-P	2.5	43			
Big Slide Creek; BSC-2005-01					
2006-07-17-04-ASP-P	6.7	47			
2006-07-17-04-BSP-P	7.7	43			
2006-07-17-07-OH-P	3.0	44			

Notes: P; Peak
R; Residual

The average peak cohesion value and peak internal angle of friction for all samples were 4.5 kPa and 39°, respectively (Table 4-22). Averages for peak cohesion and peak internal angle of friction for each failure (with the exception of BTC-2005-08 and HWC-2005-01 because only one sample was collected from these failures) and study area (with the exception of the HWC study area because only one sample was collected from the HWC-2005-01 failure) are displayed on Figure 4-44. Separated into failures, the average peak cohesion value was greatest for BTC-2005-13 (7.7kPa) and lowest for SC-2005-01 (0kPa). The differences correspond to grain-size distribution where the higher clay content of BTC-2005-13 (34%) than SC-2005-01 (16%) contributes to the higher peak cohesion values reported for BTC-2005-13. Separated into failures, the average peak internal angle of friction was greatest for BSC-2005-01 (45°) and lowest for BTC-2005-13 (36°). The differences may correspond to grain-size distribution where the higher sand content of BSC-2005-01 (22%) than BTC-2005-13 (9%) may contribute to the higher peak internal angle of friction values reported for BSC-2005-01.

Table 4-22. Average, standard deviation, and range for peak and residual shear strength parameters of soils from 2005 active layer detachments examined on the Fosheim Peninsula.

Study area and failure	n	Peak Shear Strength Parameters						n	Residual Shear Strength Parameters		
		c' (kPa)			ϕ' (°)				ϕr' (°)		
		Av	Sd	Range	Av	Sd	Range		Av	Sd	Range
SC-2005-01	2	0	0	0	40	5.7	36-44	-	-	-	-
BTC-2005-04	2	1.0	1.4	0-2	38	18	25-51	3	17.3	4.7	12-21
BTC-2005-13	6	7.7	3.9	2.9-14	36	10	22-47	3	9.1	2.7	6.6-12
BSC-2005-01	3	5.8	2.5	3-7.7	45	2.1	43-47	-	-	-	-
SC Study area	2	0	0	0	40	5.7	36-44	-	-	-	-
BTC Study area	9	5.4	4.7	0-14	36	10	22-47	7	13.8	5.4	6.6-21
BSC Study area	3	5.8	2.5	3-7.7	45	2.1	43-47	-	-	-	-
All samples	15	4.5	4.2	0-14	39	8.9	22-51	10	14.2	4.5	6.6-21

Notes: '-' not calculated, only one sample.

n - Number of Samples

Av - Average

Sd - Standard Deviation

Averages not calculated for BTC-2005-08, HWC-2005-01, and for the HWC study area due to insufficient number of samples.

Separated into study areas, the average peak cohesion was greatest for BSC and lowest for SC while the average peak internal angle of friction was greatest for SC and lowest for BTC. While it is not possible to definitively offer suggestions for the differences observed in peak cohesion, differences in peak internal angle of friction may be attributed grain-size distribution where the coarser materials reported for the SC study area contribute to higher internal angle of friction values.

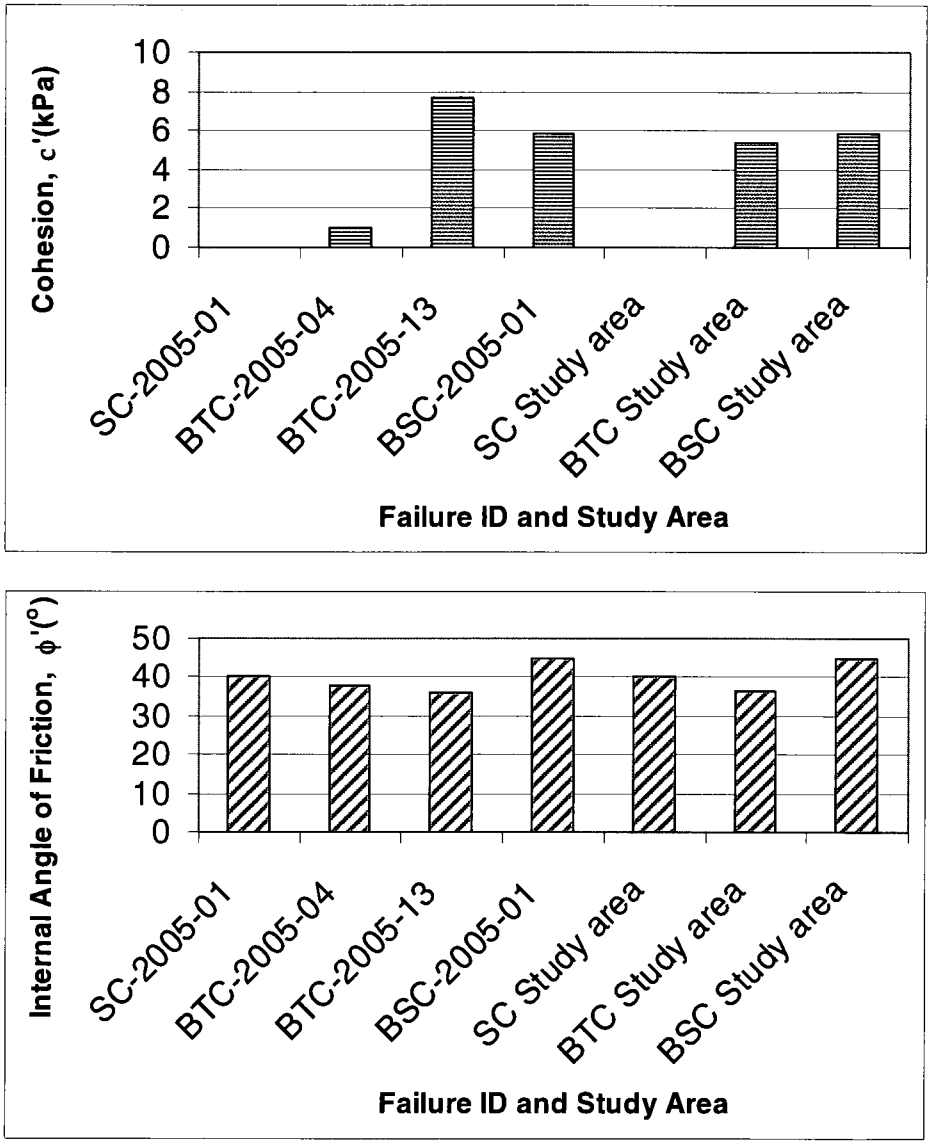

Figure 4-44. Comparison of peak cohesion and internal angle of friction for four of the 2005 active layer detachments and three of the study areas examined on the Fosheim Peninsula.

The average residual internal angle of friction for all samples was 14°. Due to an insufficient number of samples collected from the SC-2005-01, BTC-2005-08, HWC-2005-01, and BSC-2005-01 failures, average, standard deviation, and range were not calculated for these sites, nor for the SC, HWC, and BSC study areas.

To examine potential differences between peak and residual shear strength parameters of compact and elongate failures a comparison can be made between the results of BTC-2005-08 and BTC-2005-04 (see table 4-21). Only one peak and one residual sample from BTC-2005-08 are available for comparison with BTC-2005-04. Since the peak sample from BTC-2005-08 (2006-07-18-01-ASP-P) is representative of a vertical position in the soil profile that is above the shear plane, it was compared to a sample from BTC-2005-04 (2006-07-19-07-ATP-P) that is representative of the soil profile above a thrust plane. While peak cohesion was 0 kPa for both samples, a higher peak internal angle of friction was associated with the elongate failure. Since the residual sample from BTC-2005-08 (2006-07-18-01-SP-R) is representative of a shear plane and not a thrust plane, it was compared to a similar sample from BTC-2005-04 (2006-07-18-06-SP-R). Similar to the comparison of peak shear strength parameters, the elongate failure was associated with a higher residual internal angle friction than the compact failure.

Peak and residual shear strength parameters from the current study were compared to those measured in previous investigations (Harris and Lewkowicz 2000, Lewkowicz and Harris 2005b). Peak shear strength parameters from the single sample analyzed from the HWC study area and from the average of samples from the BSC study area are inconsistent with results from previous investigations (Table 4-23). The HWC study area peak cohesion result from the current study is nearly 50% less than those reported in previous studies. On the other hand, the BSC study area peak cohesion result from the current study area is nearly 50% greater than those reported in previous studies. Peak internal angle of friction values from both the HWC and BSC study areas in the

current study are significantly greater than those reported in previous studies. The residual shear strength parameter, residual internal angle of friction, from both the HWC and BSC study areas in the current study are less than, yet comparable to, those reported in previous studies. Differences, particularly those relating to the greater peak internal angle of friction values reported in the current study, may be related to the higher silt contents reported during the current study than in previous studies (see Tables 1-1 and 4-9).

Table 4-23. Shear strength parameters of soils from the current investigation compared to previously published investigations on the Fosheim Peninsula.

Study area	c' (kPa)	ϕ' (°)	ϕ_r' (°)	Source
SC	0	40	15*	This study
BTC	5.4	36	14	This study
HWC*	2.5	43	16	This study
HWC	4.8	26.5	20	Harris and Lewkowicz (2000)
HWC	5	26	20	Lewkowicz and Harris (2005b)
BSC	5.8	45	15*	This study
BSC	2	26	18	Harris and Lewkowicz (2000)
BSC	2-2.5	23-26	18	Lewkowicz and Harris (2005b)
KP182 Failure 28 Pit 1	0	28	-	Lewkowicz and Harris (2005b)
KP182 Failure 33 Pit 3	0	29	-	Lewkowicz and Harris (2005b)

Notes: * denotes result from single sample rather than average of several samples.
- denotes not reported or calculated.

Table 4-24 compares the peak cohesion and internal angle of friction values for samples separated into whether the sample was collected from above or below the shear/thrust plane. Table 4-24 also compares the peak internal angle of friction values of samples collected from above or below the shear/thrust plane with residual internal angle of friction values of samples collected from within the shear/thrust plane.

Significant differences were not noted between the average peak cohesion and internal angle of friction values of samples collected from above or below the shear/thrust plane. However, as would be expected, residual internal angle of friction values of samples collected from within the shear/thrust plane are significantly less than

peak internal angle of friction values from samples collected from above or below the shear/thrust plane.

Table 4-24. Peak and residual shear strength parameter average, standard deviation and range of samples grouped according to vertical location in the soil profile with reference to the shear or thrust plane.

Vertical location in soil profile	n; samples	Peak Shear Strength Parameters					
		c' (kPa)			ϕ' (°)		
		Average	Standard deviation	Range	Average	Standard deviation	Range
ASP/ATP	6	4.4	5.6	0-14	43	7.0	33-51
BSP/BTP	6	5.6	3.8	0-10	36	9.7	22-44
					Residual Shear Strength Parameters		
					ϕ_r' (°)		
SP/TP	8				15	4.0	8.7-21

4.3 Particle Size Distribution/Atterberg Limit and Morphometry Correlation Analysis

Particle size distribution and Atterberg Limits of sediments determined during laboratory tests were correlated with failure morphometry (length, width, and scar length) measured during fieldwork (Table 4-25). While correlation analysis between shear strength parameters and morphometry might have been illuminating, this analysis was not conducted because sufficient numbers of shear strength samples were not available to calculate average cohesion and internal angle of friction values for each failure.

Table 4-25. Correlation coefficients for dimensions and failure sediments of 2005 active layer detachments examined on the Fosheim Peninsula.

	Length (m)	Width (m)	Scar Length (m)
Gravel (%)	0.65	0.10	-0.23
Sand (%)	0.60	0.11	0.24
Silt (%)	-0.37	0.33	0.23
Clay (%)	-0.51	-0.44	-0.40
Liquid Limit	-0.74	-0.60	-0.63
Plastic Limit	-0.69	-0.56	-0.67

Notes: Sample sizes are variable for different pairs of data.

The analysis did not indicate any statistically significant relationship at the 5% level but some general inferences may be drawn. The positive correlation between gravel and sand percentage and failure length suggests that as the gravel and sand percentage of slope sediment increases so does failure length. The negative correlation between clay percentage and failure length suggests that shorter failures are associated with slopes containing high percentages of clay. Negative correlations between LL and PL and all three morphometric parameters suggests that as LL and PL of sediments increase, failure length, width and scar length decrease.

4.4 Slope Stability Analysis

The geotechnical properties of failure sediments, slope morphology, and pore water pressure are considered to influence slope stability and were used in an assessment of slope stability.

4.4.1 Factor of Safety Calculations

The analysis of slope stability was performed using a deterministic method (El Ramly 2001). This method makes use of the Limit Equilibrium theory to derive the Factor of Safety against sliding for the slope. The Factor of Safety is defined as the ratio between resisting and disturbing forces involved in the slope stability problem (Eqns.

[15] through [18]). When the Factor of Safety approaches unity, failure is assumed to be imminent.

The stability of failed slopes is assessed using an effective stress analysis based on an infinite slope model, with a planar failure surface immediately above the frost table (Skempton and DeLory 1957; Chandler 1972; Hutchinson 1974; Harris and Lewkowicz 2000). Application of this model to thawing slopes assumes the following:

- transitional sliding occurs under approximately undrained conditions because the rate of thawing of ice-rich sediments is rapid relative to the rate of drainage (Harris and Lewkowicz 1993a); and
- edge effects are considered negligible since maximum width to maximum depth ratios are significantly greater than 4:1 (Chandler 1972; Harris and Lewkowicz 2000; in the current study ratios were measured as between 25:1 and 70:1 for all studied failures).

Although pore water pressure was not measured directly at the time of failure, the first assumption was satisfied because observations at BSC-2005-01 in 2005 shortly after failure initiation indicated nearly artesian water levels (Lewkowicz 2007). At the same time, water was present 10-20 cm below ground surface in tension cracks upslope of the head scarp of a second failure observed in 2005 in the BSC study area (Lewkowicz 2007).

Tables 4-26 and 4-27 present Factors of Safety calculated for peak and residual conditions along with the corresponding measured values for peak effective cohesion (c' and c_r'), peak and residual effective angle of friction ($\phi'$and ϕ_r'), depth to slip surface (z), slope angle (β; for four cases: sample collection location, overall average, scar zone average, and track zone average), and unit weight of soil (γ). Based on the fact that ice contents are high at the base of the active layer in continuous permafrost areas, an assumed value of 1.0 was selected as the height of the piezometric surface above the

shear plane expressed as a fraction of the total thawed layer thickness (m; artesian conditions reported in Lewkowicz 2007).

All Factors of Safety calculated from peak values are greater than unity with the exception of the sample from BTC-2005-08 with a slope representative of the scar zone (Table 4-26). However, when calculated with the actual slope at the location of collection, the Factor of Safety for the sample from BTC-2005-08 is also greater than unity. Table 4-26 indicates, with the exception of BTC-2005-08, that even with the worst combination of the parameters (greatest slope - scar zone and highest pore water pressure - m=1), peak shear strength parameters from the Fosheim Peninsula do not produce Factors of Safety less than unity. Therefore, based on Factor of Safety calculations, peak effective stress stability analysis indicates that Fosheim Peninsula slopes should be stable if pore-water pressures are not artesian.

Table 4-27 indicates that, with the exception of two samples from BTC-2005-04, Factor of Safety is less than unity or equal to unity for some combination of parameters at each of the detachment failures under residual conditions. The two samples from BTC-2005-04 had the two highest residual internal angles of friction of all samples analyzed. Table 4-27 indicates that slopes greater than 6° were required to produce Factors of Safety less than unity. Based on these Factor of Safety calculations, residual effective stress stability analysis indicates that slopes greater than 6° on the Fosheim Peninsula are unstable even if pore-water pressures are not artesian.

Table 4-26. Peak effective stress stability analysis for samples collected from 2005 active layer detachments on the Fosheim Peninsula based on the infinite slope model (Slope 1 – Slope angle where sample collected, Slope 2 – Overall slope average, Slope 3 – Scar zone slope average, Slope 4 – Track zone slope average).

Sample ID	c' (kPa)	ϕ' (°)	Depth to slip plane (z; m)	Slope 1 (β; °)	Slope 2 (β; °)	Slope 3 (β; °)	Slope 4 (β; °)	Unit weight (γ; kN/m³)	Fs Slope 1	Fs Slope 2	Fs Slope 3	Fs Slope 4
Station Creek; SC-2005-01												
2006-07-20-02-ASP-P	0	36	0.6	4	4	7.5	4	19.6	5.2	5.2	2.8	5.2
2006-07-20-02-BSP-P	0	44	0.6	4	4	7.5	4	19.6	6.9	6.9	3.7	6.9
Black Top Creek; BTC-2005-04												
2006-07-19-07-ATP-P	0	51	0.8	3	7	8.5	11.5	19.0	11.4	4.9	4.0	2.9
2006-07-19-07-BTP-P	2.0	25	0.8	3	7	8.5	11.5	19.0	6.3	2.9	2.4	1.8
Black Top Creek; BTC-2005-08												
2006-07-18-01-ASP-P	0	33	0.3	5	13	20	9.5	22.0	4.1	1.6	1.0	2.2
Black Top Creek; BTC-2005-13												
2006-07-15-01-ATP-P	14	47	0.7	6	8	16	6	17.3	18.4	11.7	6.0	15.6
2006-07-15-02-BTP-P	6.1	42	0.7	6	8	16	6	17.3	9.8	6.4	3.3	8.6
2006-07-15-04-BSP-P	10	38	0.7	10	8	16	6	18.7	12.1	8.2	4.2	10.9
2006-07-21-04-ASP-P	5.5	43	0.7	8	8	16	6	18.7	8.7	6.2	3.1	8.3
2006-07-21-04-BSP-P	2.9	22	0.7	8	8	16	6	18.7	4.3	3.0	1.5	4.0
Hot Weather Creek; HWC-2005-01												
2006-07-17-03-P	2.5	43	0.6	8	15	21	8	24.0	6.4	2.8	2.0	5.2
Big Slide Creek; BSC-2005-01												
2006-07-17-04-ASP-P	6.7	47	0.6	5	8	17	5	22.0	13.5	7.9	3.8	12.7
2006-07-17-04-BSP-P	7.7	43	0.6	5	8	17	5	22.0	13.6	7.9	3.8	12.6
2006-07-17-07-OH-P	3.0	44	0.6	5	8	17	5	22.0	9.1	5.5	2.6	8.6

Table 4-27. Residual effective stress stability analysis for samples collected from 2005 active layer detachments on the Fosheim Peninsula based on the infinite slope model (Slope 1 – Slope angle where sample collected, Slope 2 – Overall slope average, Slope 3 – Scar zone slope average, Slope 4 – Track zone slope average).

Sample ID	c_r' (kPa)	ϕ_r' (°)	Depth to slip plane (z; m)	Slope 1 (β; °)	Slope 2 (β; °)	Slope 3 (β; °)	Slope 4 (β; °)	Unit weight (γ; kN/m^3)	Fs Slope 1	Fs Slope 2	Fs Slope 3	Fs Slope 4
Station Creek; SC-2005-01												
2006-07-20-02-SP-R	0	15	0.6	4	4	7.5	4	19.6	1.9	1.9	1.0	1.9
Black Top Creek; BTC-2005-04												
2006-07-18-06-SP-R	0	21	0.8	3.3	7	8.5	4.2	19.0	3.2	1.5	1.2	2.5
2006-07-19-05-TP-R	0	12	0.8	3	7	8.5	4.2	19.0	2.0	0.8	0.7	1.4
2006-07-19-07-TP-R	0	19	0.8	3	7	8.5	4.2	19.0	3.2	1.4	1.1	2.3
Black Top Creek; BTC-2005-08												
2006-07-18-01-SP-R	0	17	0.3	5	13	20	9.5	22.0	1.9	0.7	0.5	1.0
Black Top Creek; BTC-2005-13												
2006-07-15-04-SP-R	0	12	0.7	10	8	16	6	18.7	0.6	0.7	0.4	1.0
2006-07-21-04-SP-R	0	8.7	0.7	8	8	16	6	18.7	0.5	0.5	0.3	0.7
2006-07-21-07-R	0	6.6	0.7	8	8	16	6	18.7	0.4	0.4	0.2	0.5
Hot Weather Creek; HWC-2005-01												
2006-07-17-03-R	0	16	0.6	8	15	21	8	24.0	1.2	0.6	0.4	1.2
Big Slide Creek; BSC-2005-01												
2006-07-17-04-SP-R	0	15	0.6	5	8	17	5	22.0	1.7	1.1	0.5	1.7

4.4.2 Sensitivity Analyses

In the deterministic method used previously to calculate the Factor of Safety, assumed values are used for the slope geometry and pore-water pressure and mean values are used for shear strength parameters. However, it is recognized that these parameters exhibit a degree of variability and, therefore, cannot be fully represented by their assumed or mean values. One way to account for the variability of the parameters is a sensitivity analysis, where one parameter is systematically varied in a sequence of analyses, while the other parameters are held constant. This analysis provides insight into the degree to which a certain parameter affects the stability of a slope. Sensitivity analyses may be used to assess factors affecting initiation of slope failure.

Sensitivity analyses of peak and residual conditions were conducted for each failure using Eqns [18 and 20] in which depth to slip surface and unit weight of soil were kept constant to investigate the relationship between Factor of Safety and the remaining four variables in the equation. The variables of depth to slip surface and unit weight of soil were kept constant because they are assumed to remain constant in space and time for each failure in question. Therefore, the sensitivity analysis for each failure focused on variations in peak and residual internal angle of friction, peak cohesion, slope angle, and the head of water above the slip surface. The selected ranges of peak and residual internal angle of friction and peak cohesion for each failure were based on the maximum and minimum values determined from the direct shear tests of samples collected from each failure. In cases where only one sample was tested for internal angle of friction at a particular failure, a range on either side of the measured value (±5; range shifted upwards if lower bound fell below 0) was used in the sensitivity analysis. The selected range of slope angle used in the sensitivity analysis for each failure was based on the maximum and minimum valued measured along the disturbed profiles of each failure. The head of water above the slip surface was simply varied from 0 to 1.0 (value representative of

artesian conditions; e.g. greater than the distance between the ground surface and the slip surface).

Normalized percent change for each parameter and the corresponding normalized percent change in the Factor of Safety were calculated using Eqns [30 and 31]. Graphs were plotted for each failure displaying all five parameter and corresponding Factor of Safety normalized percent change pairs (ϕ', ϕ_r', c', β and D_w) to assess the change in Factor of Safety relative to a change in the specified parameter (Figures 4-45 to 4-54; Haneberg 2000). When $c' > 0$ (either median value or single value from single analyzed sample), Factor of Safety was calculated using both peak and residual equations [18 and 20] and two graphs were plotted for each failure displaying the five parameter and corresponding Factor of Safety normalized percent change pairs (peak graphs displayed ϕ', c', β, and D_w; residual graphs displayed ϕ_r', β, and D_w). When $c' = 0$ (either median value or single value from single analyzed sample), normalized percent change was only calculated for ϕ_r', because the residual Factor of Safety equation is the same as the peak Factor of Safety equation (normalized ϕ_r' - normalized Factor of Safety pair plotted on peak graph). In this case, the relationship between Factor of Safety and β, and D_w would be the same.

The values of each of the independent variables for SC-2005-01 are assumed to be uniformly distributed over the ranges $36° \le \phi' \le 44°$, $10° \le \phi_r' \le 20°$, $0° \le c' \le 10°$, $2° \le \beta \le 13°$, and $0 \le D_w \le 1.0$ m. Median values were used to determine average peak and residual Factors of Safety.

Sensitivity analysis of the peak and residual infinite slope equations (Figure 4-45) indicates that values of normalized D_w greater than their median value produce unstable slopes whereas the opposite inference may be drawn for normalized c', normalized ϕ' and normalized ϕ_r'. Changes in normalized c' exhibit greater influence on Factor of Safety than normalized ϕ_r', which in turn exhibits greater influence on Factor of Safety than

changes in normalized ϕ'. Values of normalized β significantly less than median values are able to produce stable slopes.

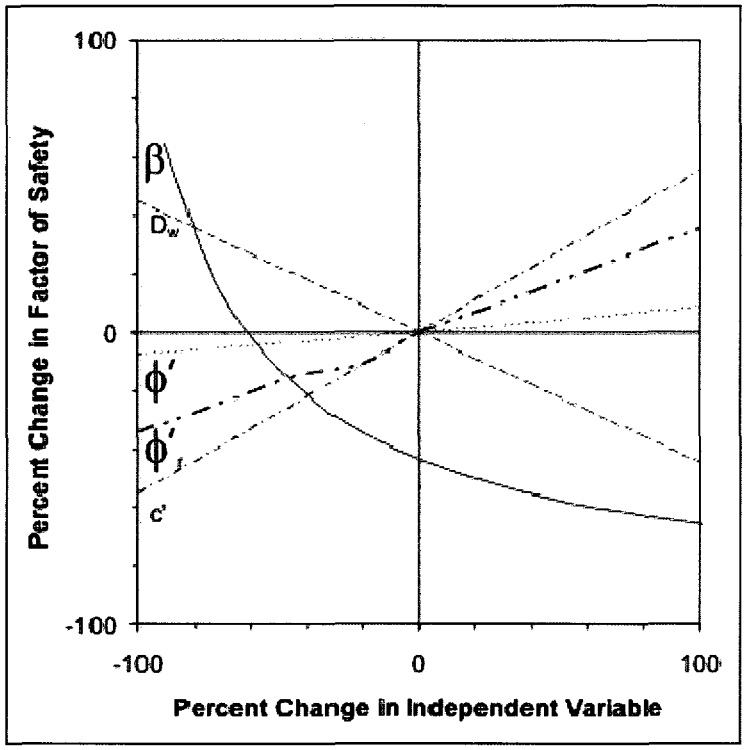

Figure 4-45. Results of sensitivity analysis of the peak and residual infinite slope equation using parameters for SC-2005-01. Since c' = 0, only ϕ_r' is presented because the peak and infinite slope equations yield the same results for the other parameters. Unit weight is 19.6 KN/m³.

The values of each of the independent variables for BTC-2005-04 are assumed to be uniformly distributed over the ranges $25^\circ \le \phi' \le 51^\circ$, $12^\circ \le \phi'_r \le 21^\circ$, $0^\circ \le c' \le 10^\circ$, $6^\circ \le \beta \le 15^\circ$, and $0 \le D_w \le 1.0$ m. Median values were used to determine average peak and residual Factors of Safety.

Sensitivity analysis of the peak infinite slope equation (Figure 4-46) indicates that values of normalized β and normalized D_w greater than their median values produce unstable slopes. The opposite inferences may be drawn for normalized ϕ' and normalized c' where values less than their median values produce unstable slopes.

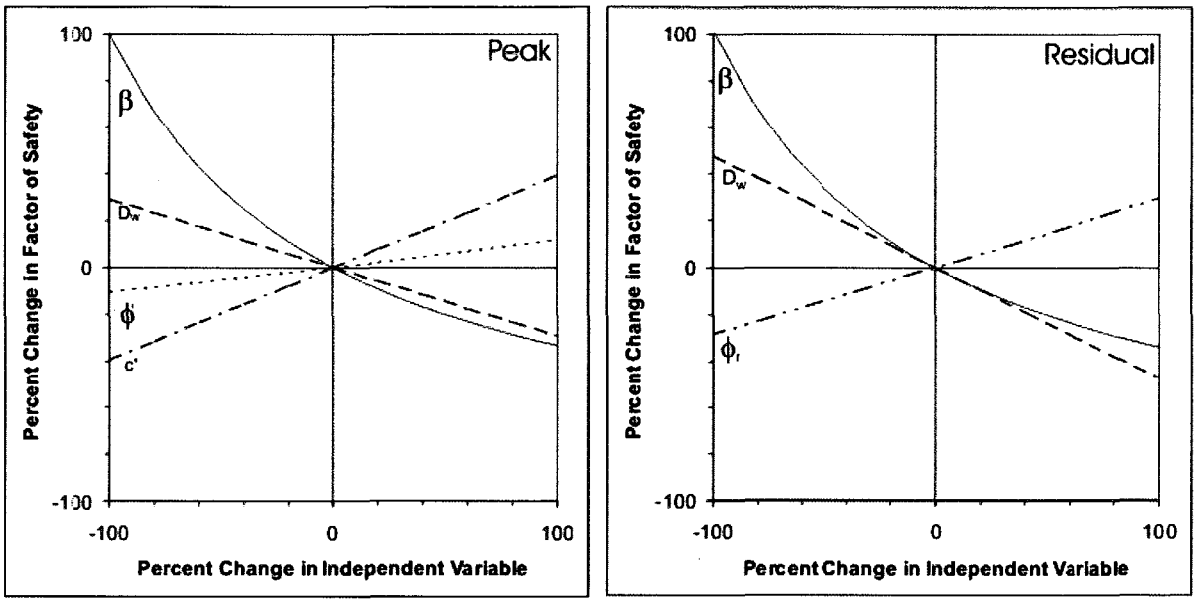

Figure 4-46. Results of sensitivity analysis of the peak and residual infinite slope equation using parameters for BTC-2005-04. Unit weight is 19.0 KN/m³.

Sensitivity analysis of the residual infinite slope equation (see Figure 4-46) indicates that values of normalized β and normalized D_w greater than their median value produce unstable slopes. The opposite inference may be drawn for normalized ϕ_r'where values less than its median value produce unstable slopes.

The values of each of the independent variables for BTC-2005-08 are assumed to be uniformly distributed over the ranges $28^\circ \le \phi' \le 38^\circ$, $12^\circ \le \phi_r' \le 22^\circ$, $0^\circ \le c' \le 10^\circ$, $12^\circ \le \beta \le 24^\circ$, and $0 \le D_w \le 1.0\,\text{m}$. Median values were used to determine average peak and residual Factors of Safety.

Sensitivity analysis of the peak and residual infinite slope equations (Figure 4-47) indicates that values of normalized β and normalized D_w greater than their median value produce unstable slopes whereas the opposite inference may be drawn for normalized c', normalized $\phi'$and normalized ϕ_r'. Changes in normalized D_w exhibit greater influence on Factor of Safety than changes in normalized β. Changes in normalized c'exhibit greater influence on Factor of Safety than normalized ϕ_r', which in turn exhibits greater influence on Factor of Safety than changes in normalized ϕ'. In fact, normalized ϕ'

exhibits very little influence on Factor of Safety for values both greater than and less than its median value.

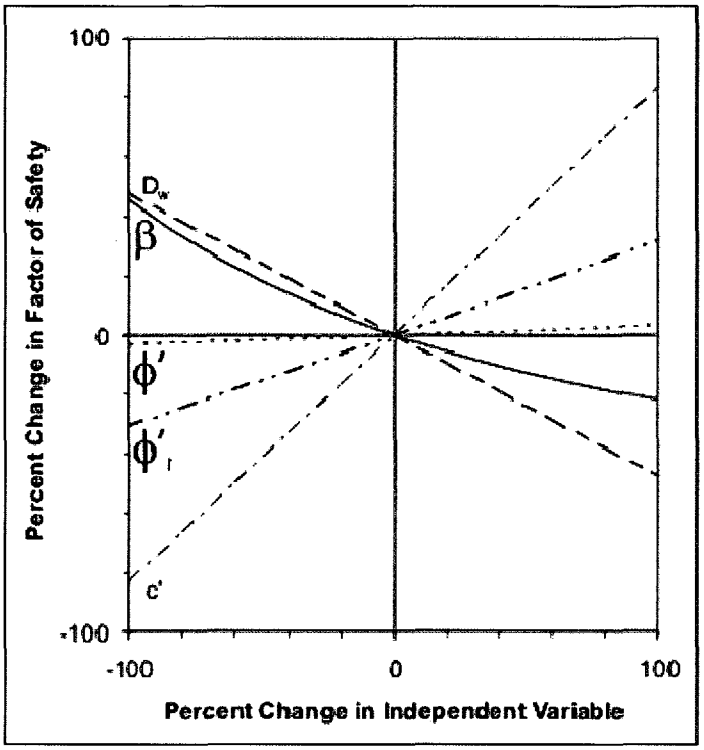

Figure 4-47. Results of sensitivity analysis of the peak and residual infinite slope equation using parameters for BTC-2005-08. Since c' = 0, only ϕ_r' is presented because the peak and infinite slope equations yield the same results for the other parameters. Unit weight is 22.0 KN/m³.

The values of each of the independent variables for BTC-2005-13 are assumed to be uniformly distributed over the ranges $29.5^\circ \le \phi' \le 39.5^\circ$, $4.3^\circ \le \phi'_r \le 14.3^\circ$, $3.5^\circ \le c' \le 13.5^\circ$, $6.5^\circ \le \beta \le 16.5^\circ$, and $0 \le D_w \le 1.0$ m. Median values were used to determine average peak and residual Factors of Safety.

Sensitivity analysis of the peak infinite slope equation (Figure 4-48) indicates that values of normalized β and normalized D_w greater than their median values produce unstable slopes. The opposite inferences may be drawn for normalized ϕ' and normalized c' where values less than their median values produce unstable slopes.

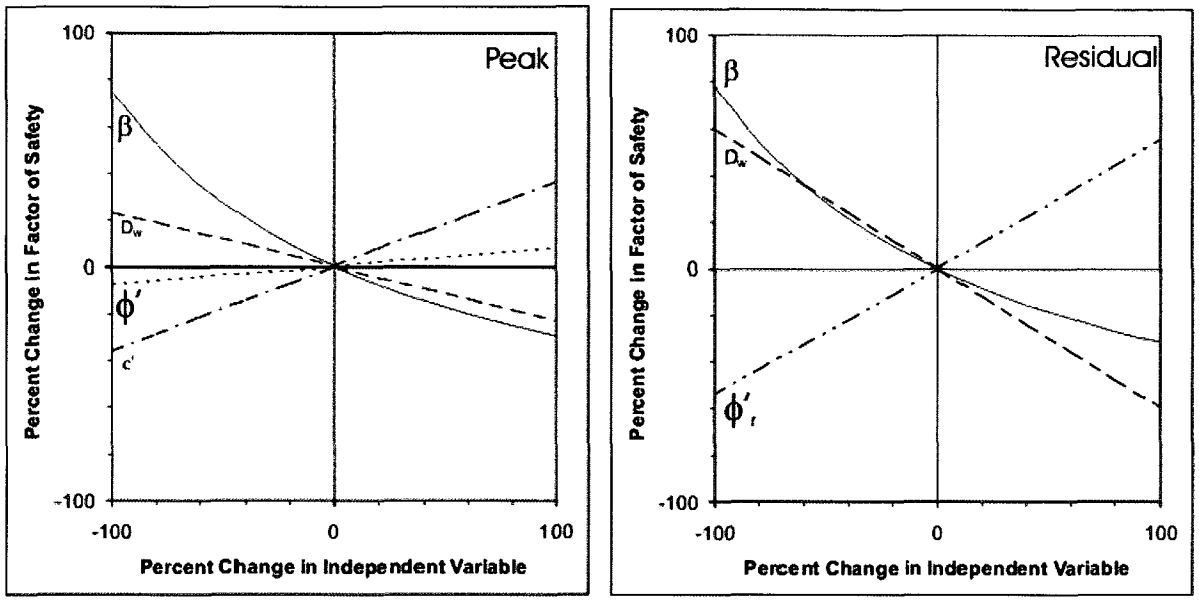

Figure 4-48. Results of sensitivity analysis of the peak and residual infinite slope equation using parameters for BTC-2005-13. Unit weight is 18.7 KN/m³.

Sensitivity analysis of the residual infinite slope equation (see Figure 4-48) indicates that values of normalized β and normalized D_w greater than their median value produce unstable slopes. The opposite inference may be drawn for normalized ϕ_r'where values less than its median value produce unstable slopes.

The values of each of the independent variables for HWC-2005-01 are assumed to be uniformly distributed over the ranges $38^\circ \le \phi' \le 48^\circ$, $11^\circ \le \phi_r' \le 21^\circ$, $0^\circ \le c' \le 10^\circ$, $6^\circ \le \beta \le 16^\circ$, and $0 \le D_w \le 1.0$ m. Median values were used to determine average peak and residual Factors of Safety.

Sensitivity analysis of the peak infinite slope equation (Figure 4-49) indicates that values of normalized β and normalized D_w greater than their median values produce unstable slopes. The opposite inferences may be drawn for normalized ϕ' and normalized $c'$where values less than their median values produce unstable slopes.

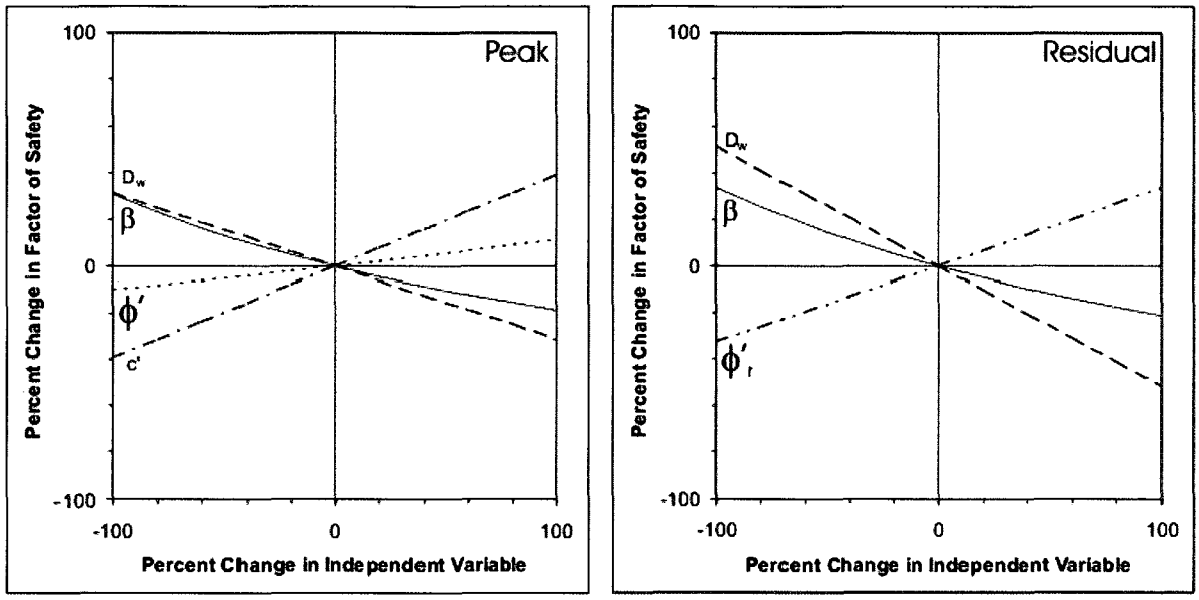

Figure 4-49. Results of sensitivity analysis of the peak and residual infinite slope equation using parameters for HWC-2005-01. Unit weight is 24.0 KN/m³.

Sensitivity analysis of the residual infinite slope equation (see Figure 4-49) indicates that values of normalized β and normalized D_w greater than their median value produce unstable slopes. The opposite inference may be drawn for normalized ϕ_r'where values less than its median value produce unstable slopes.

The values of each of the independent variables for BSC-2005-01 are assumed to be uniformly distributed over the ranges $40^\circ \leq \phi' \leq 50^\circ$, $10^\circ \leq \phi_r' \leq 20^\circ$, $0.5^\circ \leq c' \leq 10.5^\circ$, $11.5^\circ \leq \beta \leq 21.5^\circ$, and $0 \leq D_w \leq 1.0$ m. Median values were used to determine average peak and residual Factors of Safety.

Sensitivity analysis of the peak infinite slope equation (Figure 4-50) indicates that values of normalized β and normalized D_w greater than their median values produce unstable slopes. The opposite inferences may be drawn for normalized $\phi'$and normalized $c'$where values less than their median values produce unstable slopes.

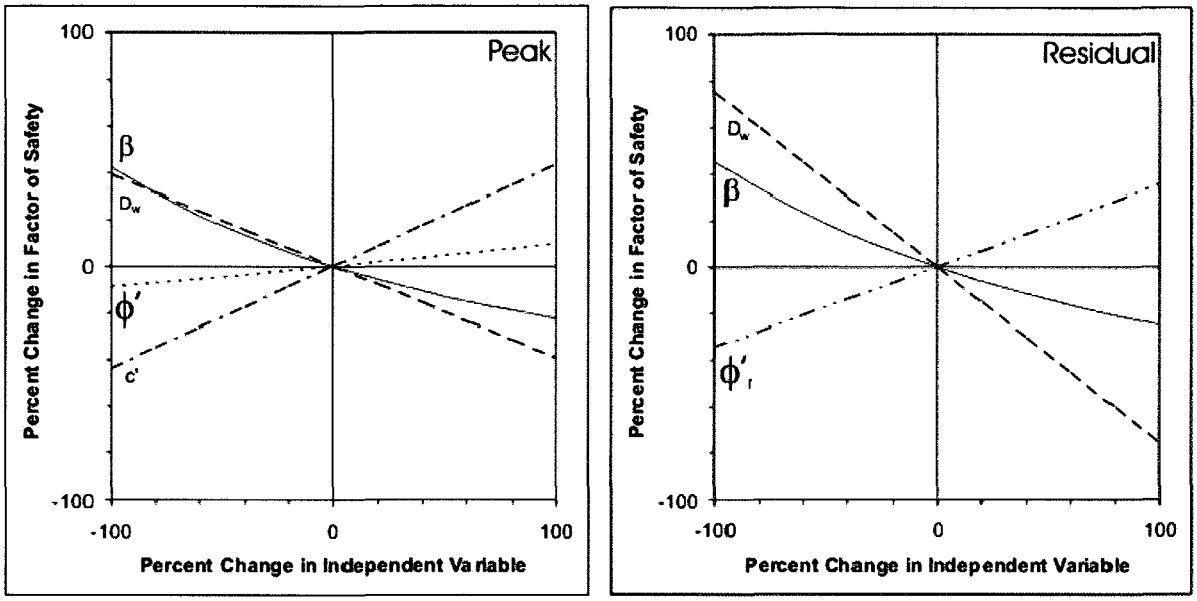

Figure 4-50. Results of sensitivity analysis of the peak and residual infinite slope equation using parameters for BSC-2005-01. Unit weight is 19.0 KN/m³.

Sensitivity analysis of the residual infinite slope equation (see Figure 4-50) indicates that values of normalized β and normalized D_w greater than their median value produce unstable slopes. The opposite inference may be drawn for normalized ϕ_r'where values less than its median value produce unstable slopes.

4.4.2.1 Sensitivity Analyses Summary

Table 4-28 provides a summary of the parameter values about the median required to produce unstable slopes for each failure analyzed on the Fosheim Peninsula. Table 4-28 also summarizes which parameters Factor of Safety is most sensitive to changes to in both peak and residual conditions.

Table 4-28. Summary of parameter location about its median that produces unstable slopes for each failure examined on the Fosheim Peninsula under both peak and residual conditions.

	D_w (m)	β (°)	ϕ' (°)	ϕ_r' (°)	c' (kPa)	Factor of Safety most sensitive to changes in:
SC-2005-01						
peak	>median	>median	<median	<median	<median	β and c', then ϕ_r', then ϕ'
residual						
BTC-2005-04						
peak	>median	>median	<median	NA	<median	β and c'
residual	>median	>median	NA	<median	NA	β
BTC-2005-08						
peak	>median	>median	<median	<median	<median	D_w and c', then ϕ_r', then ϕ'
residual						
BTC-2005-13						
peak	>median	>median	<median	NA	<median	β and c'
residual	>median	>median	NA	<median	NA	β
HWC-2005-01						
peak	>median	>median	<median	NA	<median	D_w and c'
residual	>median	>median	NA	<median	NA	D_w
BSC-2005-01						
peak	>median	>median	<median	NA	<median	D_w and c'
residual	>median	>median	NA	<median	NA	D_w

Notes:
D_w - Head of water above slide plane
β - Slope angle
ϕ' - Effective internal angle of friction (peak)
ϕ_r' - Effective internal angle of friction (residual)
c' - Effective cohesion
NA - Not applicable

Table 4-28 indicates that in all failures, of the parameters that produced unstable slopes for values less than their median value, Factor of Safety was most sensitive to changes in normalized *c'*. Of the two parameters that produced unstable slopes for values greater than their median value, Factor of Safety was most sensitive to changes in normalized *β* for SC-2005-01, BTC-2005-04 and BTC-2005-13. For the remaining failures, BTC-2005-08, HWC-2005-01 and BSC-2005-01, Factor of Safety was most sensitive to changes in normalized D_w.

5 DISCUSSION

The purpose of this chapter is to discuss the results presented in Chapter 4 with reference to previously published results in an attempt to establish a relationship between active layer detachment deposit morphology, morphometry and sedimentology and active layer detachment dynamics.

5.1 Failure Initiation Location and Morphology

One failure studied in detail was classified as compact, while the remaining six failures studied in detail were classified as elongate (Table 5-1). With the exception of HWC-2005-01, all elongate failures initiated at a mid-slope location. This observation suggests that moist conditions may be required for the development of elongate failures such as those found in cross-slope hollows that are maintained by throughflow in the active layer (Lewkowicz 2007) from upslope locations. Melting of a cross-slope ice wedge at the crest-slope of HWC-2005-01 contributed to the high moisture conditions required to facilitate the formation of an elongated failure.

Table 5-1. Initiation location and failure form of 2005 active layer detachments studied in detail on the Fosheim Peninsula.

Failure Name	Initiation location	Failure Form
SC-2005-01	mid-slope	Elongate
SC-2005-02	mid-slope	Elongate
BTC-2005-04	mid-slope	Elongate
BTC-2005-08	crest-slope	Compact
BTC-2005-13	mid-slope	Elongate
HWC-2005-01	crest-slope	Elongate
BSC-2005-01	mid-slope	Elongate

Table 5.2 summarizes the morphological characteristics observed at each failure. The main morphological differences noted between the elongate failures and the compact failure is the presence of transverse ridges, trailing blocks, and shear gashes at all of the elongate failures and not at the compact failure. In addition, lateral

compression ridges were noted at all elongate failures with the exception of two (BTC-2005-13 and HWC-2005-01) but were not noted at the compact failure.

Table 5-2. Morphological characteristics of 2005 active layer detachments studied in detail on the Fosheim Peninsula.

Failure ID	Transverse Ridges	Lateral Compression Ridges	Lateral Smears	Shear Gashes/Tension Cracks	Side Disturbed Zone	Frontal Disturbed Zone	Collapsed Blocks	Trailing Blocks	Lateral Berm	Toe Berm/Blunt Toe
Elongate Failures										
SC-2005-01	√	√	√	√	√		√	√		
SC-2005-02	√	√	√	√	√	√	√	√		√
BTC-2005-04	√	√	√	√			√	√		√
BTC-2005-13	√			√		√	√	√		
HWC-2005-01	√			√		√	√			√
BSC-2005-01	√	√	√	√	√		√	√		
Compact Failure										
BTC-2005-08				√			√		√	√

Elongate failures are not characterized by consistent toe morphology. Three failures (SC-2005-02, BTC-2005-04, and HWC-2005-01) are marked by either blunt toes or a large frontal lobe. The remaining three elongate failures (SC-2005-01, BTC-2005-13, and BSC-2005-01) are characterized by toe zones that gradually meet or ease into the downslope undisturbed terrain. In addition, elongate failures are not characterized by similar track zone lengths. While SC-2005-01, BTC-2005-04, and BSC-2005-01 exhibit track zones of significant length, SC-2005-02, BTC-2005-13, and HWC-2005-01 are characterized by track zones with minimal length.

Morpological descriptions of compact and elongate failures studied during previous investigations are similar to those reported in the current study (Harris and

Lewkowicz 2000; Lewkowicz and Harris 2005b). Elongate failures studied at HWC, BSC, and in the MacKenzie Valley in the Northwest Territories were characterized by lateral compression ridges, shear gashes/tension cracks, frontal disturbed zones, and trailing blocks (Harris and Lewkowicz 2000; Lewkowicz and Harris 2005b). A compact failure studied in the MacKenzie Valley was characterized by a short length with a minimal to non-existent track zone and some large secondary displaced blocks (Harris and Lewkowicz 2000).

The above observations from the current study and previously published studies suggest that while failures on the Fosheim Peninsula can be categorized into compact and elongate failures based on overall morphometry, elongate failures display a range of morphological characteristics, some of which are similar to compact failures, suggestive of a morphological continuum connecting compact failures to elongate failures (Figure 5-1). For instance, Lewkowicz and Harris (2005b) suggested that additional loading from mud associated with a retrogressive thaw slump that occurred after the main failure event caused minor movements of the main displaced mass of a compact failure.

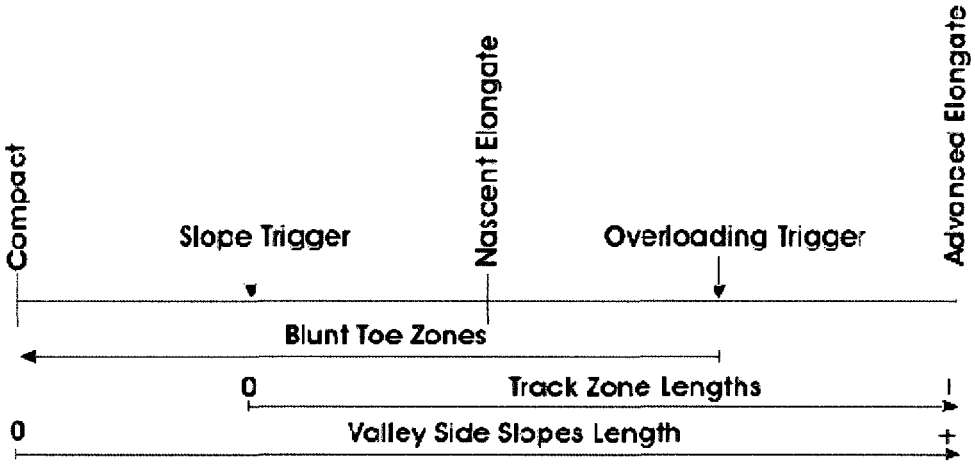

Figure 5-1. Morphological continuum of active layer detachments on the Fosheim Peninsula showing trigger points (slope and overloading) between failure types, other factors (valley side slopes length), and main features distinguishing failure types (blunt toe zone and track zone length).

Trigger points along the continuum may be governed by factors such as slope and overloading. The triggers mark the transitional boundaries between compact failures,

nascent elongate failures and advanced elongate failures. However, it may be prudent to ensure that failures compared along this continuum contain similar grain-size distributions evident by the significantly different failure slope angles observed at HWC (average 22°) compared to BTC (12°) and BSC (14°; Harris and Lewkowicz 2000; Lewkowicz 1990). Harris and Lewkowicz (2000) suggested that the steeper slopes at HWC indicates that slope stability at HWC is controlled by the sandy nature of sediments and corresponding low ice contents compared to the clay and ice-rich sediments of BTC and BSC.

When failures of similar grain-size distributions are compared using this continuum, the geomorphic conditions of increasing slope angles and shorter valley side slope lengths are most likely to display failures of a compact nature (see Figure 4-36). On the other hand, the geomorphic conditions of longer valley side slope lengths and smaller slope angles are most likely to display failures of an elongate nature (see Figure 4-36).

5.2 Failure Stratigraphy

Sediment from the SC study area in addition to sediments near the toe of the compact failure, BTC-2005-08, displayed water escape structures suggestive of high water content conditions and overloading. These features were observed in a trailing block within the scar zone, a transverse ridge within the compression zone, and in terminal compression ridges in the toe zone. Hence, movement involving overloading and deformation occurred along the entire length of SC failures and within the toe zone of the compact failure, BTC-2005-08. Similar water escape structures were reported in transverse ridges by Mathewson and Mayer-Cole (1984), Harris and Lewkowicz (1993a), and Lewkowicz and Harris (2005b).

Sediments associated with the track zone and compression zone of BTC-2005-04 and BTC-2005-13 are characterized by a prevalence of vertically layered (columnar and

prismatic) and regular reticulate (cryoaggregates) cryostructures. Weaknesses or reductions in shear strength associated with these cryostructures may have contributed to the positioning of the failure plane and the location of emergent shear planes. Similar vertical prismatic or vertical blocky cryostructures were reported in sediments associated with elongate failures described by Harris and Lewkowicz (2000) and Lewkowicz and Harris (2005b).

In most cases where toe zone sediments were described, SC-2005-01, BTC-2005-08, BTC-2005-13 (the exception being HWC-2005-01), green buried organics were observed suggesting over-riding of the intact terrain by the failure front. In the case of HWC-2005-01, the absence of green buried organics within the toe zone suggests that the front of the failure pushed into rather than over-rode the downslope intact terrain.

5.3 Failure History

Morphological and sedimentogical observations described above were used to suggest histories and dynamics associated with the seven failures studied in detail on the Fosheim Peninsula. A summary of movement type, number, rate (inferred velocity, temporal and continuity) is provided in Table 5-3.

Table 5-3. Movement types, numbers, and inferred rates, times, and continuity associated with 2005 active layer detachments studied in detail on the Fosheim Peninsula.

Failure	Movement				
	Type	#	Inferred		
			Rate	Time	Continuity
SC-2005-01	Translational + Compressional	2	Slow	Prolonged	Discontinuous
SC-2005-02	Translational + Compressional	3	Rapid	Prolonged	Discontinuous
BTC-2005-04	Translational + Compressional	1	Slow	Prolonged	Continuous
BTC-2005-08	Translational	1	Slow or Rapid	Instantaneous	Continuous
BTC-2005-13	Translational + Compressional	1	Slow	Prolonged	Continuous
HWC-2005-01	Translational + Compressional	1	Slow	Prolonged	Continuous
BSC-2005-01	Translational + Compressional	2	Slow	Prolonged	Continuous

Recent observations by Lamoureux and Lafrenière (2009) indicated that elongate failures, up to 650 m in length, progressed downslope at rates up to 2.5 m/hr over four days. These observations are consistent with those observed by Lewkowicz (2007) at BSC. The elongated failure in question (referred to as BSC-2005-1 in Lewkowicz (2007) and BSC-2005-01 in this study) progressed downslope for a total of 330 m at rates up to 9 m/hr over 3-5 days. These observations along with the current observations suggest that elongate failure movement is typically characterized as: slow, yet sometimes rapid;, prolonged; continuous or discontinuous; with both translational and compressional movement.

BTC-2005-08 is the only failure during the current detailed study that was identified as compact and the only failure believed to have a failure history characterized by solely translational movement that occurred in a nearly-instantaneously fashion. While detailed morphogical and sedimentological information is not available for a small active layer detachment in BSC, BSC-2005-2, described by Lewkowicz (2007), the similar appearance of BTC-2005-08 and BSC-2005-2 suggests that these failures may have similar failure histories. Lewkowicz (2007) reports that BSC-2005-2 stabilized within

approximately 4 hours. This observation along with the current observations suggest that compact failure movement is typically characterized as: slow or rapid; near instantaneous; continuous; with translational movement.

5.4 Failure Sediment Shear Strength

Determination of peak and residual shear strength parameters uncovered a strong negative relationship between residual internal angle of friction and clay content indicating that the residual strength of soil previously subject to failures decreases with increasing clay content. Differences in peak and residual shear strength parameters reported between failures and between study areas correspond reasonably well to grain-size distribution where higher peak cohesion and peak internal angle of friction values correspond to higher clay and sand contents, respectively.

A comparison between a compact and an elongate failure indicates that higher peak and residual internal angle of friction values are associated with elongate failures. This information suggests that in order to generate prolonged elongate failures on Fosheim Peninsula slopes, high pore water pressures are required to sustain the prolonged movement.

While relationships between grain-size distribution and peak and residual internal angle of friction values have been suggested for Fosheim Peninsula sediments, the large variability in grain-size distribution between samples collected from the same failure and the same study area and the very poorly to poorly sorted nature of sediments suggest that differences in slope stability, failure morphology, and failure dynamics are not related to differences in grain-size distribution. It appears that while very general relationships can be suggested, the stability of individual slopes on the Fosheim Peninsula is likely governed by other factors such as: reduction in residual strength by pre-conditioning of the basal shear zone; basal ice contents; rapidity of active layer thaw; pore water pressure; and slope angle (Harris and Lewkowicz 2000; Lewkowicz and Harris 2005b).

5.5 Factor of Safety Calculations

Based on Factor of Safety calculations, peak effective stress stability analysis indicates stable slopes on the Fosheim Peninsula if pore water pressures are not artesian. Based on Factor of Safety calculations, residual effective stress stability analysis indicates that slopes greater than 6° on the Fosheim Peninsula are unstable even if pore water pressures are not artesian. If pore-water pressures are artesian, slopes less than 6° would likely also be unstable under residual conditions. This indicates that in years with high summer temperatures and rapid thawing of the active layer, failure of residual slopes less than 6° is possible.

5.6 Sensitivity Analysis

Sensitivity analyses indicates that Factors of Safety on Fosheim Peninsula slopes are most sensitive to changes in normalized c' when values of c' are less than median values (peak conditions). Hence, under peak conditions, slope instability is related to reductions in cohesion.

The Factors of Safety of slopes associated with three failures (SC-2005-01, BTC-2005-04, and BTC-2005-13) are most sensitive to changes in normalized β when values of β are greater than median values (either peak or residual conditions). Factors of Safety of slopes associated with the remaining three failures for which sensitivity analyses were conducted (BTC-2005-08, HWC-2005-01, and BSC-2005-01) are most sensitive to changes in normalized D_w when values of D_w are greater than median values (either peak or residual conditions). This indicates that under residual conditions, slope instability is related to increases in both β and D_w. The fact that instability on the Fosheim Peninsula under residual conditions could be related to either β or D_w suggests that other site-specific factors such as grain-size distribution, govern residual slope instability.

6 CONCLUSIONS

Active layer detachments on the Fosheim Peninsula, although never observed in motion until recently, had been assumed to develop over periods of minutes to a few hours (Lewkowicz 2007). However, field observations of two failures at 'Big Slide Creek' on the Fosheim Peninsula in August 2005 showed that while one failure conformed to the pre-existing assumption of near-instantaneous formation, movement and cessation of movement, the other failure did not and exhibited progressive expansion over several days (Lewkowicz 2007). Considering this new-found knowledge, opportunities existed to (1) assess whether in plan-form, active layer detachments known to have failed via a prolonged mode and those known to have failed in a near-instantaneous mode display unique sets of morphological characteristics, (2) assess whether in section, the macrostructure of failures known to have failed via a prolonged mode differ from those failures known to have failed in a near-instantaneous mode, and (3) evaluate the ability of the infinite slope model to adequately predict slope stability by back-calculating the slope factor of safety using measured geotechnical properties and by providing a sensitivity analysis. The main findings are the following:

1. Active layer detachments that failed via a prolonged mode display plan-form morphological characteristics that are unique from active layer detachments that failed via a near-instantaneous mode. Prolonged failure modes generate elongate failures which are characterized by greater widths, lengths, scar lengths, deposit lengths, and length to width ratios than compact failures which are generated by a near-instantaneous failure mode. Surficial macro-morphologic features characteristic of elongate failures include: transverse ridges, trailing blocks, shear gashes, and lateral compression ridges. Compact failures are characterized by a lack of the surficial macro-morphological features characteristic of elongate failures described above.

2. That while the trailing edge of the displaced mass of active layer detachments that failed via prolonged modes contains macrostructures that are similar to those of active layer detachments that failed via a near-instantaneous mode, the leading front of failures that failed via a prolonged mode contain macrostructures that are unique from failures that failed via a near-instantaneous mode. Internal macro-morphologic features characteristic of elongate failures are complex folding and deformation of sediments within the compressed zone of the displaced block and downslope disturbed terrain reflective of a high moisture contents and low Atterberg limits. The internal macro-morphology of the trailing edge of the main displaced mass is characterized by a prominent shear plane and minimal deformation above and below the shear plane. This observation suggests that in the upper reaches of the scar zone, sediments are drier, likely due to higher slope angles allowing groundwater to travel downslope and not pond, causing the displaced mass to travel as an intact block with minimal disturbance over a narrowly defined, high moisture content, low friction, low Atterberg limit shear plane. The coincidence of the shear plane with the thaw plane lends to the conditions of high moisture content and low friction necessary for movement to occur on such a thin layer. Groundwater traveling from the upper reaches of the scar zone to the lower reaches of the scar zone and to the lower angled slopes of the track zone serve to create the high moisture content conditions necessary to cause the folding and deformation of sediments present at the leading edge of the displaced mass and of sediments within the disturbed terrain downslope of the displaced mass. Common internal macro-morphologic features to both elongate and compact failures are flame-like intrusions in the displaced mass suggestive of fluid escape associated with overloading of sediments containing high water contents. Other than the above-mentioned fluid escape structures observed in the sediments of displaced masses associated with compact failures, there are no

other significant internal macro-morphologic features associated with compact failures. The internal macro-morphology of the displaced mass is similar to that of the trailing edge of the main displaced mass in elongate failures where sediments are characterized by a prominent shear plane with minimal deformation above and below the shear plane. The dry nature of the intact displaced mass may be due to the high angles characteristic of the slopes upon which compact failures originate causing groundwater to travel efficiently downslope and the relatively dry conditions of crest-slopes where compact failures typically originate compared to mid-slopes where elongate failures typically originate.

3. Based on Factor of Safety calculations, peak effective stress stability analysis indicates thawing slopes are stable on the Fosheim Peninsula if pore water pressures are not artesian. Based on Factor of Safety calculations, residual effective stress stability analysis indicates that thawing slopes greater than 6° on the Fosheim Peninsula are unstable even if pore water pressures are not artesian. If pore-water pressures are artesian, thawing slopes less than 6° would likely also be unstable under residual conditions. This indicates that in years with high summer air temperatures and rapid thaw of the active layer, failure of slopes less than 6° is possible if their shear strengths are residual. Higher peak and residual internal angle of friction values are associated with elongate failures suggesting that in order to generate prolonged elongate failures on Fosheim Peninsula slopes, high pore water pressures are required to sustain the prolonged movement. Sensitivity analyses indicates that Factors of Safety on Fosheim Peninsula slopes are most sensitive to changes in normalized c' when values of c' are less than median values (peak conditions). Hence, under peak conditions, slope instability is related to reductions in cohesion. Under residual conditions, slope instability is related to increases in both β and D_w. The fact that instability on the Fosheim

Peninsula under residual conditions could be related to either β or D_w suggests that other site-specific factors, such as grain-size distribution, govern residual slope instability.

6.1 Recommendations for Future Work

During the preparation of this thesis, alternative methods or additional avenues of research were identified. The following recommendations for future work would help to further understand active layer detachment morphology, sedimentology and mechanisms:

1. Determination of peak and residual shear strength parameters using the triaxial apparatus instead of the direct shear apparatus. Soil conditions on the Fosheim Peninsula can be considered to approximate undrained since the rate of thaw is likely sufficiently rapid relative to the rate of drainage. Triaxial tests are better suited to undrained testing because drainage can be prevented by sealing the test specimens in impermeable membranes and tests are performed slow enough to eliminate undesirable rate effects (Duncan and Wright 2005).
2. Employment of a more sophisticated effective stress analysis whereby the effects of loading on the main displaced mass by the joining of secondary displaced blocks to the trailing edge of the main displaced mass are included.
3. Explore the relationship between failure initiation and sediment geochemistry, especially that of sediment salt content.
4. Additional samples from active layer detachments known to have failed via prolonged and near-instantaneous modes could be collected to allow the important analysis of sediment micro-structure allowing the confirmation or re-interpretation of previously published inferences regarding connections between failure dynamics and microstructure (Lewkowicz and Harris 1993b).

7 REFERENCES

Alt, B.T., Labine, C.L., Atkinson, D.E., Headley, A.N., and Wolfe, P.M. 2000. Automatic weather station results from Fosheim Peninsula, Ellesmere Island, Nunavut. *In* Environmental Response to Climate Change in the Canadian High Arctic. *Edited by* M. Garneau and B.T. Alt. Ottawa: Geological Survey of Canada, Bulletin 529, pp. 37-97.

American Society for Testing and Materials. 2004a. ASTM D2216-98 Standard Method for Laboratory Determination of Water (Moisture) Content of Soil and Rock by Mass. *In* Annual Book of ASTM Standards, Section 4, Volume 04.08, Soil and Rock (I), ASTM International, Pennsylvania. pp. 220-224.

American Society for Testing and Materials. 2004b. ASTM D4318 Standard Test Method for Liquid Limit, Plastic Limit, and Plasticity Index of Soils. *In* Annual Book of ASTM Standards, Section 4, Volume 04.08, Soil and Rock (I), ASTM International, Pennsylvania. pp. 580-591.

Andersland, O.B. and Ladanyi, B. 1994. An Introduction to Frozen Ground Engineering. Chapman and Hall, New York. 352p.

Aylsworth, J. M., Duk-Rodkin, A., Robertson, T., and Traynor, J. A. 2000. Landslides of the Mackenzie valley and adjacent mountainous and coastal regions. *In* The physical environment of the Mackenzie valley, Northwest Territories: a base line for the assessment of environmental change. *Edited by* L. D. Dyke and G. R. Brooks. Geological Survey of Canada, Bulletin 547, pp. 167-176.

Bell, T. 1996. The last glaciation and sea level history of Fosheim Peninsula, Ellesmere Island, Canadian High Arctic. Canadian Journal of Earth Sciences, **33**, pp. 1075-1086.

Bell, T. and Hodgson, D.A. 2000. Quaternary geology and glacial history of Fosheim Peninsula, Ellesmere Island, Nunavut. *In* Environmental Response to Climate Change in the Canadian High Arctic. *Edited by* M. Garneau and B.T. Alt. Ottawa: Geological Survey of Canada, Bulletin 529, pp. 175-196.

Bishop, A. W., and Blight, G.E. 1962. Some aspects of effective stress in saturated and partially saturated soils. Geotechnique, **12**, pp. 177-197.

Bowles, J. E. 1992. Engineering Properties of Soils and their Measurements. McGraw-Hill Publishing, New York.

Brady, N.C. and Weil, R.R. 1996. The Nature and Properties of Soils. Prentice Hall, New Jersey, 740p.

Carter, L. D., and Galloway, J. P. 1981. Earth flows along Henry Creek, Northern Alaska. Arctic, **34**, pp. 325-328.

Chandler, R.J. 1972. Periglacial mudslides in Vestspitsbergen and their bearing on the origin of fossil "solifluction" shears in low angled clay slopes. The Quarterly Journal of Engineering Geology, **5**, pp. 223-241.

Chandler, R.J. 1986. Processes leading to landslides in clay slopes: a review. *In* Hillslope Processes. *Edited by* A. D. Abrahams. The Binghampton Series in Geomorphology: International Series 16, pp. 343-360.

Cogley, J. G., and McCann, S. B. 1976. An exceptional storm and its effects in the Canadian High Arctic. Arctic and Alpine Research, **8**, pp. 105-110.

Craig, R. F. 1997. Soil Mechanics. 6th Edition. Chapman and Hall, London, 485p.

Duncan, J.M. and Wright, S.G. 2005. Soil Strength and Slope Stability. John Wiley and Sons Inc., New Jersey, pp. 297.

Dyke, L. D. 2000. Stability of permafrost slopes in the Mackenzie valley. *In* The physical environment of the Mackenzie valley, Northwest Territories: a base line for the assessment of environmental change. *Edited by* L. D. Dyke and G. R. Brooks. Geological Survey of Canada, Bulletin 547, pp. 177-186.

Dyke, L.D. 2004. Stability of frozen and thawing slopes in the Mackenzie Valley, Northwest Territories. *In* 57th Canadian Geotechnical Conference, Session 1G, pp. 31-38.

Edlund, S.A. and Alt, B.T. 1989. Regional congruence of vegetation and summer climate patterns in the Queen Elizabeth Islands NWT, Canada. Arctic, **42**, pp. 3-23.

Edlund, S. A., Alt, B. T., and Young, K. L. 1989. Interaction of climate, vegetation, and soil hydrology at Hot Weather Creek, Fosheim Peninsula, Ellesmere Island, Northwest Territories. *In* Current Research, Part D, Geological Survey of Canada, Paper 89-1D, pp. 125-133.

El Ramly, H. 2001. Probablistic Analyses of Landslide Hazards and Risks: Bridging Theory and Practice. Unpublished PhD Thesis, University of Alberta, Edmonton, Alberta, 391p.

Environment Canada. 2007. Canadian Climate Data Online. Available from http://www.climate.weatheroffice.ec.gc.ca/climateData/canada_e.html [accessed May 2007].

Fairbridge, R.W. and Bourgeois, J. (Eds.). 1978. The Encyclopedia of Sedimentology. Dowden, Hutchinson and Ross Inc, Stroudsburg, Pennsylvania, 901p.

French, H. M. 1988. Active layer processes. *In* Advances in periglacial geomorphology. *Edited by* M. J. Clark. John Wiley and Sons, Toronto, pp. 151-177.

French, H.M. 1996. The Periglacial Environment. 2nd Edition. Longman Publishers, Singapore, 341p.

Folk, R.L. 1980. Petrology of Sedimentary Rocks. Hemphill Publishing Company, Austin, Texas, 184p.

Geological Survey of Canada, 1971a. Geology of Slidre Fiord, District of Franklin, Scale 1:50,000. Map 1298A, Geological Survey of Canada, Ottawa, Ontario.

Geological Survey of Canada, 1971b. Geology of Eureka Sound North, District of Franklin, Scale 1:250,000. Map 1298A, Geological Survey of Canada, Ottawa, Ontario.

Haneberg, W.C. 2000. Deterministic and probabilistic approaches to geologic hazard assessment. Environmental and Engineering Geoscience, **6**, No. 3, pp. 209-226.

Harris, C., and Lewkowicz, A. G. 1993. Form and internal structure of active-layer detachment slides, Fosheim Peninsula, Ellesmere Island, Northwest Territories, Canada. Canadian Journal of Earth Sciences, **30**, pp. 1708-1714.

Harris, C., and Lewkowicz, A. G. 1993b. Micromorphological investigations of active-layer detachment slides, Ellesmere Island, Canadian Arctic. *In* Proceedings of the Sixth International Conference on Permafrost, Beijing, China, pp. 232-237.

Harris, C., and Lewkowicz, A. G. 2000. An analysis of the stability of thawing slopes, Ellesmere Island, Nunavut, Canada. Canadian Geotechnical Journal, **37**, pp. 449-462.

Harry, D.G., and MacInnes, K.L. 1988. The effect of forest fires on permafrost terrain stability, Little Chicago-Travaillant Lake area, Mackenzie Valley, N.W.T. *In* Current Research, Part D, Geological Survey of Canada, Paper 88-1D, pp. 91-94.

Heginbottom, J.A., Dubreuil, M.A., and Harker, P.A. 1995. Canada-Permafrost. *In* National Atlas of Canada, 5th edition. National Resources Canada, National Atlas Information Service. Plate 2.1. MCR 4177.

Heiri, O., Lotter, A.F. and Lemcke, G. 2001. Loss on ignition as a method for estimating organic and carbonate content in sediments: reproducibility and comparability of results. Journal of Paleolimnology, **25**, pp. 101-110.

Holtz, R. D., and Kovacs, W. D. 1981. An Introduction to Geotechnical Engineering. Prentice Hall, Englewood Cliffs, New Jersey, 733p.

Huscroft, C.A., Lipovsky, P., and Bond, J.D. 2004. A regional characterization of landslides in the Alaska Highway corridor, Yukon. Yukon Geological Survey, Open File 2004-18, 65p.

Hutchinson, J. N. 1974. Periglacial solifluction: an approximate system for clayey soils. Geotechnique, **24**, pp. 438-443.

Kokelj, S.V. and Lewkowicz, A.G. 1999. Salinization of permafrost terrain due to natural geomorphic disturbance, Fosheim Peninsula, Ellesmere Island. Arctic, **52**, pp. 372-385.

Lamoureux, S.F. and Lafrenière, M.J. 2009. Fluvial impact of extensive active layer detachments, Cape Bounty, Melville Island, Canada. Arctic, Antarctic and Alpine Research, **41**, no 1. pp. 59-68.

Leibman, M.O. 1995. Cryogenic landslides on the Yamal Peninsula, Russia: preliminary observations. Permafrost and Periglacial Processes, **6**, pp. 259-264.

Leibman, M.O. and Egorov, I.P. 1996. Climatic and environmental controls of cryogenic landslides, Yamal, Russia. *In* Proceedings of the Seventh International Symposium on Landslides. *Edited by* K. Senneset, Trondheim, Norway, pp.1941-1946.

Leibman, M.O., Kizakov, A.I., Sulerzhitsky, L.D., and Zaretskaia, N.E. 2003. Dynamics of landslide slopes and their development on Yamal Peninsula. *In* Proceedings of the Eighth International Conference on Permafrost. *Edited by* M. Phillips, S.M. Springman and L.U. Arenson, Swets and Zeitlinger: Lisse, pp. 651-656.

Lewis, T., Braun, C., Hardy, D.R., Francus, P., and Bradley, R.S. 2005. An extreme sediment transfer event in a Canadian High Arctic stream. Arctic, Antarctic, and Alpine Research, **37**, pp. 477-482.

Lewkowicz, A. G. 1988. Slope processes. *In* Advances in periglacial geomorphology. *Edited by* M. J. Clark. John Wiley and Sons, Toronto, pp. 325-368.

Lewkowicz, A. G. 1990. Morphology, frequency and magnitude of active-layer detachment slides, Fosheim Peninsula, Ellesmere Island, Northwest Territories. *In* Proceedings Fifth Canadian Permafrost Conference, Quebec City, Universite Laval, Nordicana 54, pp. 111-118.

Lewkowicz, A. G. 1992. Factors influencing the distribution and initiation of active-layer detachment slides on Ellesmere Island, Arctic Canada. *In* Periglacial Geomorphology. *Edited by* Dixon, J. C. and Abrahams, A. D. John Wiley and Sons, Chichester, pp. 223-250.

Lewkowicz, A.G. and C. Harris. 2005a. Frequency and magnitude of active-layer detachment failures in discontinuous and continuous permafrost, northern Canada. Permafrost and Periglacial Processes, **16**, pp. 115-130.

Lewkowicz, A. G. and C. Harris. 2005b. Morphology and geotechnique of active-layer detachment failures in discontinuous and continuous permafrost, northern Canada. Geomorphology, **69**, pp. 275-297.

Lewkowicz, A. G. 2007. Dynamics of active-layer detachment failures, Fosheim Peninsula, Ellesmere Island, Nunavut, Canada. Permafrost and Periglacial Processes, **18**, pp. 89-103.

Mackay, J. R. 1983. Downward water movement into frozen ground, western arctic coast, Canada. Canadian Journal of Earth Sciences, **18**, pp. 1666-1680.

Mackay, J. R., and Mathews, W. H. 1973. Geomorphology and Quaternary history of the Mackenzie River Valley near Fort Good Hope, N.W.T., Canada. Canadian Journal of Earth Sciences, **10**, pp. 26-41.

Mathewson, C.C., and Mayer-Cole, T.A. 1984. Development and runout of a detachment slide, Bracebridge Inlet, Bathurst Island, Northwest Territories, Canada. Bulletin of the Association of Engineering Geologists, **21**, pp. 407-424.

McRoberts, E.C., and Morgenstern, N.R. 1973. A Study of Landslides in the Vicinity of the MacKenzie River, Mile 205 to 660. Environmental-Social Committee, Northern Pipelines, Task Force on Northern Oil Development, Information Canada, Ottawa, Ontario, 96p.

McRoberts, E.C., and Morgenstern, N.R. 1974. The stability of thawing slopes. Canadian Geotechnical Journal, **11**, pp. 447-469.

Murton, J.B. and French, H.M. 1994. Cryostructures in permafrost, Tuktoyaktuk coastlands, western arctic Canada. Canadian Journal of Earth Sciences, **31**, pp. 737-747.

NASA Landsat 7 Geocover, website accessed on July 5, 2009, https://zulu.ssc.nasa.gov/mrsid.

Nash, D. 1987. A comparative review of limit equilibrium methods of stability analysis. *In* Slope Stability. *Edited by* M. G. Anderson and K. S. Richards. John Wiley and Sons Ltd, New York, pp. 11-76.

Ó Cofaigh, C., England, J., and Zreda, M. 2000. Late Wisconsinan glaciation of southern Eureka Sound: evidence for extensive Innuitian ice in the Canadian High Arctic during the Last Glacial Maximum. Quaternary Science Reviews, **19**, pp. 1319-1341.

Prellwitz, R.W. 1994. Soil slopes-transition from deterministic to probabilistic analysis. *In* Slope Stability Reference Guide fro National Forests in the United States, Volume II. *Edited by* D.E. Hall, M.T. Long, and M.D. Rembolt. US Government Printing Office, Washington, DC, pp. 663-642.

Roots, E.F. 1963. Physiography. *In* Geology of the North-Central Part of the Arctic Archipelago, Northwest Territories (Operation Franklin). *Edited by* Y.O. Fortier. Geological Survey of Canada, Memoir 320. pp. 418-426.

Savigny, W., Logue, C., and MacInnes, K. 1995. Forest fire effects on slopes formed in ice-rich permafrost soils MacKenzie Valley, Northwest Territories. *In* 48th Canadian Geotechnical Conference, Preprint Volume 2, Vancouver, British Columbia, Canadian Geotechnical Society, pp. 989-998.

Selby, M.J. 1993. Hillslope materials and processes: 2nd Edition. Oxford University Press, Oxford. 451p.

Skempton, A. W.1985. Geotechnical aspects of the Carsington dam failure. *In* Proceedings of the 11th International Conference on Soil Mechanics and Foundation Engineering, San Francisco, US, Volume 5, pp. 2581-2591.

Skempton, A.W., and DeLory, F.A. 1957. Stability of natural slopes in London Clay. *In* Proceedings of the 4th International Conference on Soil Mechanics, London, Volume 2, pp. 378-381.

Skempton, A.W., Norbury, D., Petley, J., and Spink, T.W. 1991. Solifluction shears at Carsington, Derbyshire. *In* Quaternary Engineering Geology – Geological Society Engineering Group Special Report 7. *Edited by* A. Forster, M.G. Culshaw, J. Cripps, J.A. Little, and C.F. Moon. Geological Society, London, pp. 381-388.

Skempton, A.W. and Vaughan, P.R. 1993. The failure of Carsington Dam. Geotechnique, **43**, No.1, pp. 151-173.

Soil Classification Working Group. 1998. The Canadian System of Soil Classification. 3rd Edition. Agiculture and Agri-Food Canada Publication 1646. 187p.

Stangl, K.O., Roggensack, W.D., and Hayley, D.W. 1982. Engineering geology of surficial soils, eastern Melville Island. *In* Proceedings Fourth Canadian Permafrost Conference. *Edited by* H. M. French. N.R.C.C. Ottawa. pp. 136-147.

Thorsteinnsson, R. and Tozer, E.T. 1970. Geology of the Arctic Archipelago. *In* Geology and Economic Minerals of Canada. *Edited by* R.J.W. Douglas. Geological Survey of Canada, Economic Geology Report No. 1, pp. 547-590.

Towner, G. D.,and Childs, E. C. 1972. The mechanical strength of unsaturated porous granular material. Journal of Soil Science, **23**, pp. 481-498.

Trettin, H.P. 1989. The Arctic Islands. *In* The Geology of North America – An Overview. *Edited by* A.W. Bally and A.R. Palmer. Geological Society of America, The Geology of North America, v. A, Boulder, Colorado. pp. 349-370.

Whitlow, R. 1995. Basic Soil Mechanics. 3rd Edition. Longman Scientific and Technical, Essex, England. 559p.

APPENDIX A – PAIRED T-TESTS

Table A-1. Paired t-test results of comparison of sand, silt, and clay percentages between samples collected from the three groups of vertical location with reference to the shear or thrust plane.

	Sand					
	ASP/ATP	SP/TP	ASP/ATP	BSP/BTP	SP/TP	BSP/BTP
Mean	15.0	17.1	15.0	19.9	17.1	19.9
Variance	85.2	80.1	85.2	207.8	80.1	207.8
Observations	7	7	7	7	7	7
t-Stat	-0.9		-1.2		-0.7	
P(T<=t) on two tail	0.4		0.3		0.5	
t Critical on two tail	2.5		2.5		2.5	
	Silt					
	ASP/ATP	SP/TP	ASP/ATP	BSP/BTP	SP/TP	BSP/BTP
Mean	60.7	59.0	60.7	56.9	59.0	56.9
Variance	19.2	18.9	19.2	19.9	18.9	19.9
Observations	7	7	7	7	7	7
t-Stat	1.3		1.4		0.9	
P(T<=t) on two tail	0.2		0.2		0.4	
t Critical on two tail	2.5		2.5		2.5	
	Clay					
	ASP/ATP	SP/TP	ASP/ATP	BSP/BTP	SP/TP	BSP/BTP
Mean	24.2	23.0	24.2	22.3	23.0	22.3
Variance	95.0	119.7	95.0	161.4	119.7	161.4
Observations	7	7	7	7	7	7
t-Stat	0.6		1.1		0.4	
P(T<=t) on two tail	0.6		0.3		0.7	
t Critical on two tail	2.5		2.5		2.5	

Notes: ASP/ATP – Above shear plane/above thrust plane
SP/TP – Shear plane/thrust plane
BSP/BTP – Below shear plane/below thrust plane

Table A-2. Paired t-test results of comparison of moisture content and LOI between samples collected from the three groups of vertical location with reference to the shear or thrust plane.

	Moisture Content					
	ASP/ATP	SP/TP	ASP/ATP	BSP/BTP	SP/TP	BSP/BTP
Mean	25.6	28.1	25.6	26.1	28.1	26.1
Variance	22.3	36.4	22.3	39.3	36.4	39.3
Observations	8	8	8	8	8	8
t-Stat	0.9		-0.2		0.7	
P(T<=t) on two tail	0.4		0.9		0.5	
t Critical on two tail	2.1		2.1		2.1	
	LOI					
	ASP/ATP	SP/TP	ASP/ATP	BSP/BTP	SP/TP	BSP/BTP
Mean	7.1	7.6	7.1	6.7	7.6	6.7
Variance	2.2	4.4	2.2	3.9	4.4	3.9
Observations	8	8	8	8	8	8
t-Stat	-0.6		0.5		0.9	
P(T<=t) on two tail	0.6		0.6		0.4	
t Critical on two tail	2.1		2.2		2.1	

Notes: ASP/ATP – Above shear plane/above thrust plane
SP/TP – Shear plane/thrust plane
BSP/BTP – Below shear plane/below thrust plane

Table A-3. Paired t-test results of comparison of Atterberg limits and plasticity indices between samples collected from two groups of vertical location with reference to the shear or thrust plane.

	Liquid Limit; LL	
	ASP/ATP	BSP/BTP
Mean	37.8	35.6
Variance	79.1	74.0
Observations	8	7
t-Stat	0.5	
P(T<=t) on two tail	0.6	
t Critical on two tail	2.2	
	Plastic Limit; PL	
	ASP/ATP	BSP/BTP
Mean	22.5	21.3
Variance	18.6	19.2
Observations	8	7
t-Stat	0.5	
P(T<=t) on two tail	0.6	
t Critical on two tail	2.2	
	Plasticity Index; PI	
	ASP/ATP	BSP/BTP
Mean	15.3	14.3
Variance	22.8	20.6
Observations	8	7
t-Stat	0.4	
P(T<=t) on two tail	0.7	
t Critical on two tail	2.2	

Notes: ASP/ATP – Above shear plane/above thrust plane
BSP/BTP – Below shear plane/below thrust plane

APPENDIX B – FLOW CURVES FOR DETERMINATION OF LIQUID LIMIT

SC-2005-01

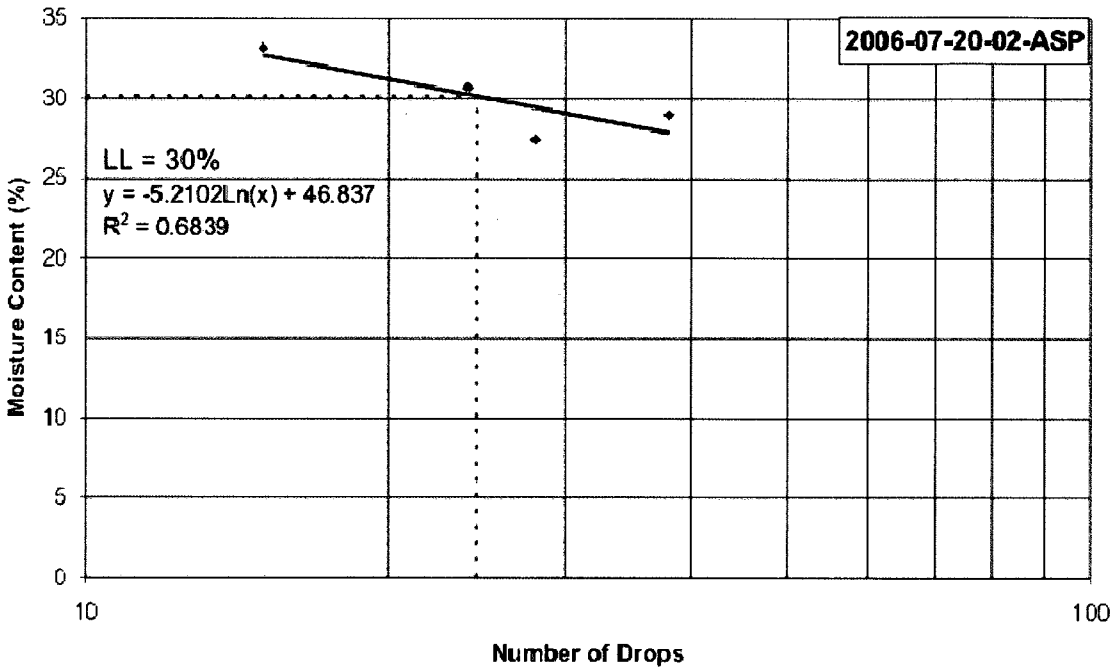

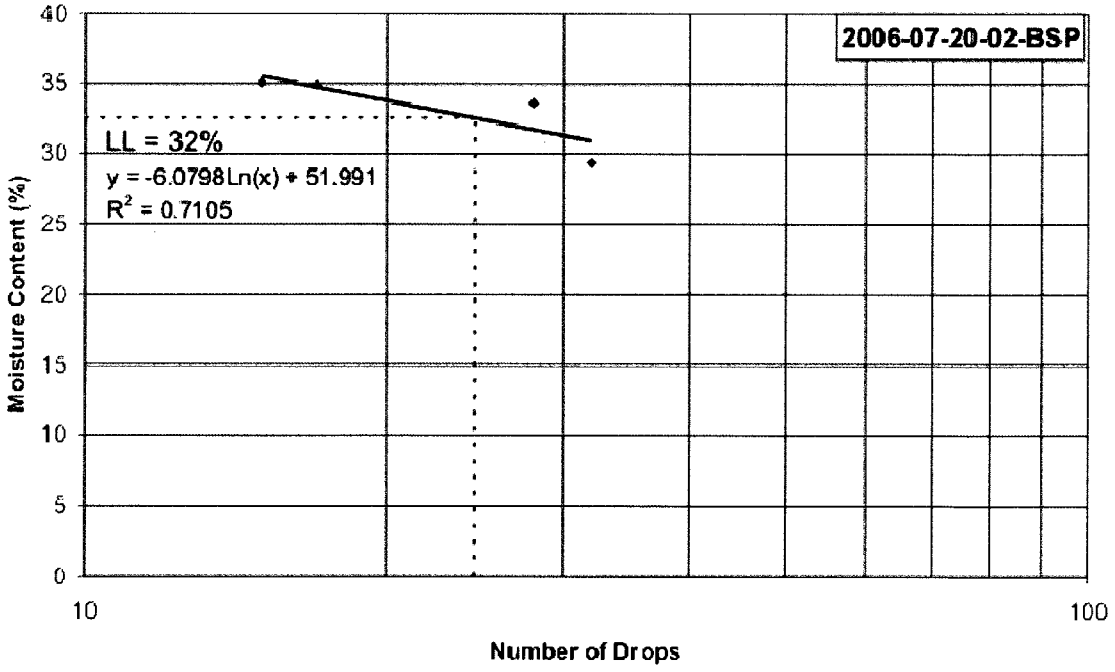

SC-2005-01 Continued

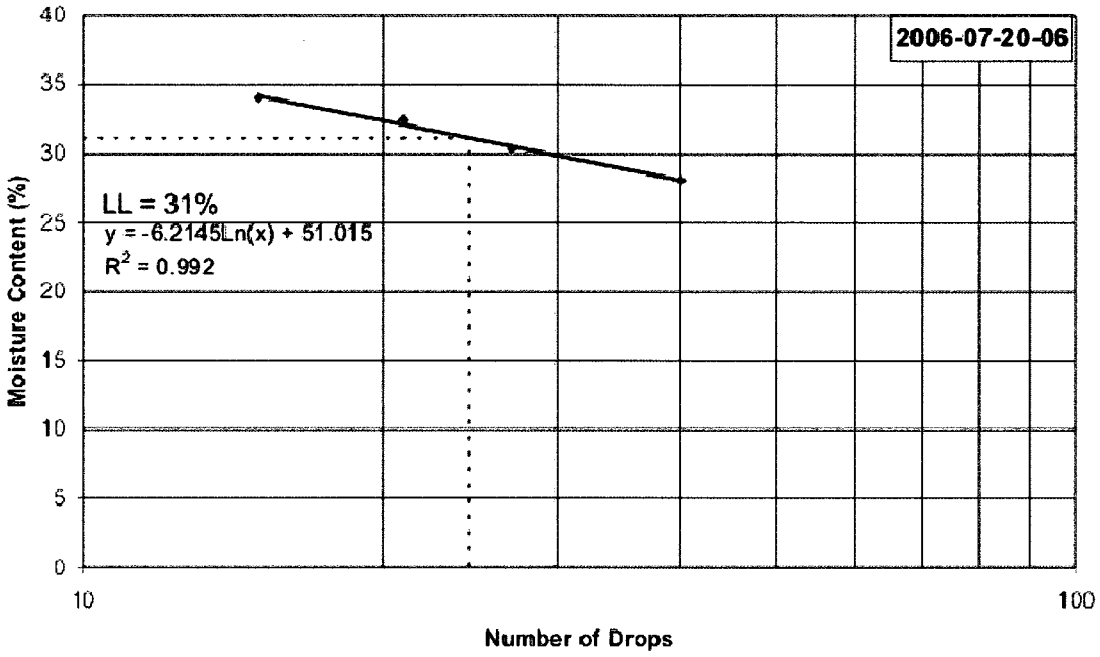

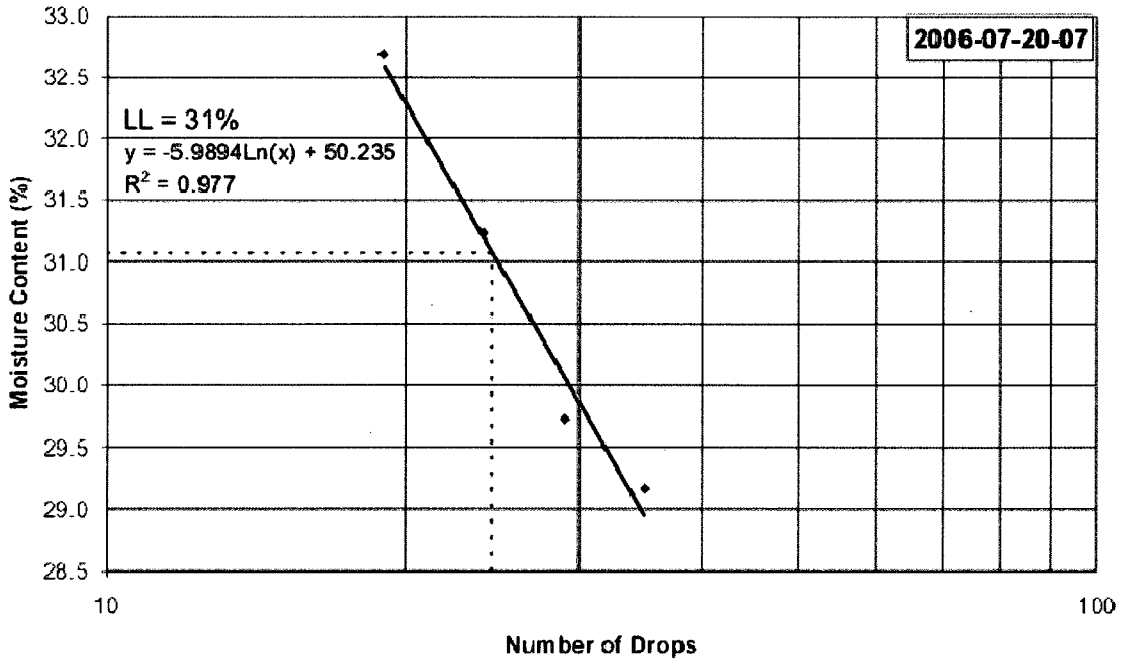

SC-2005-01 Continued

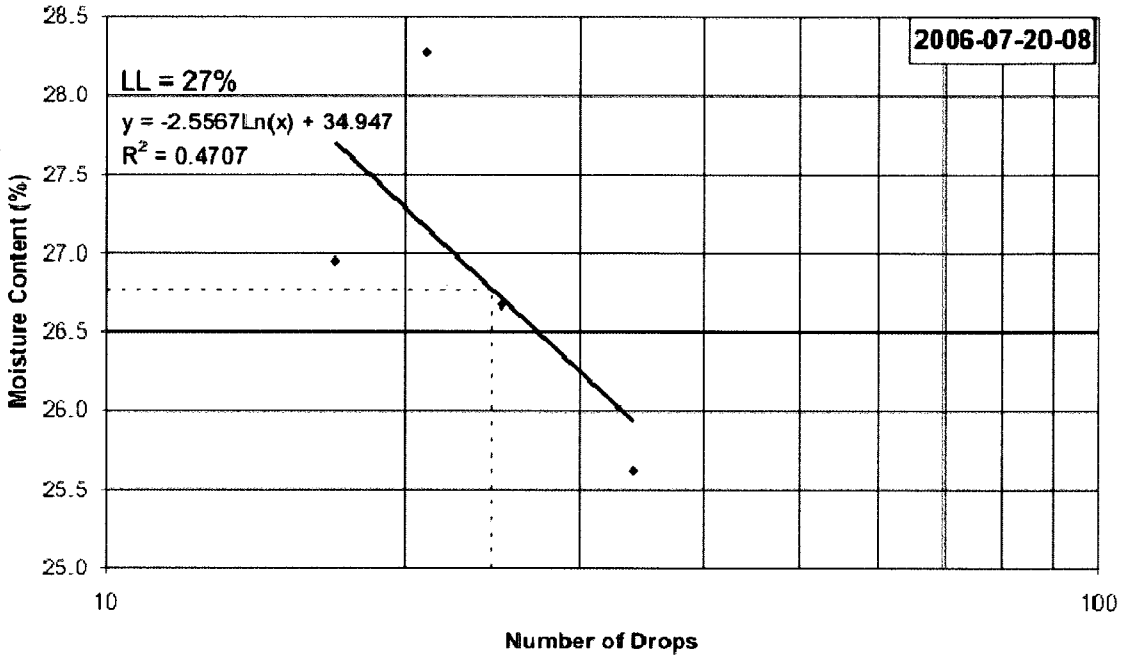

SC-2005-02

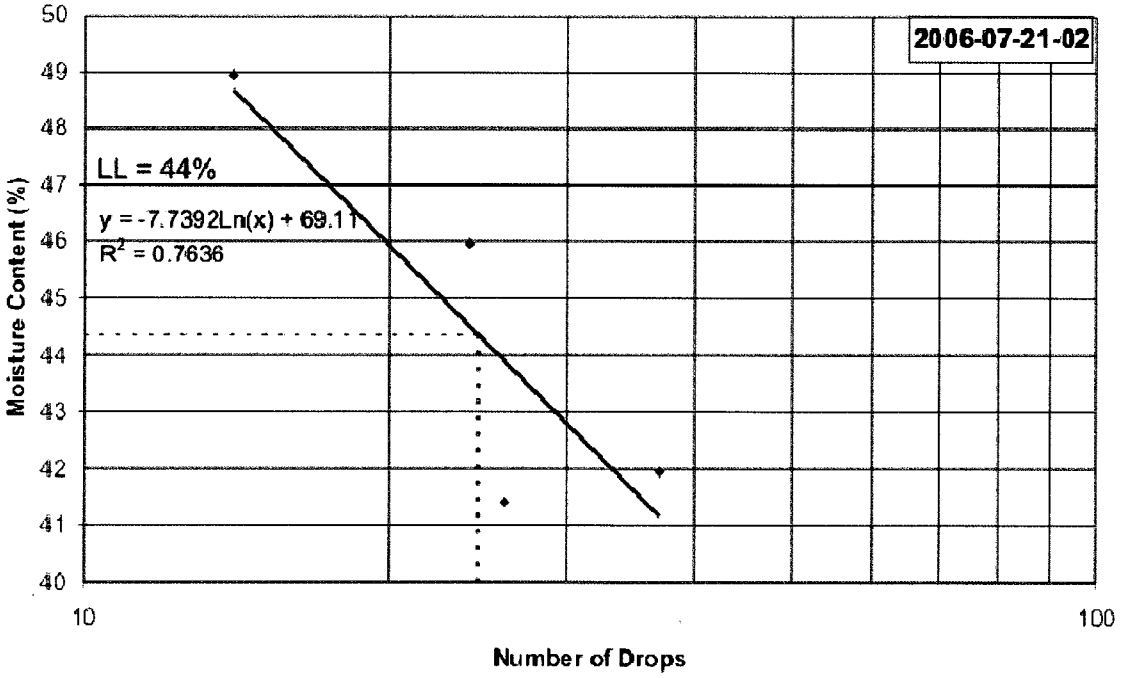

SC-2005-02 Continued

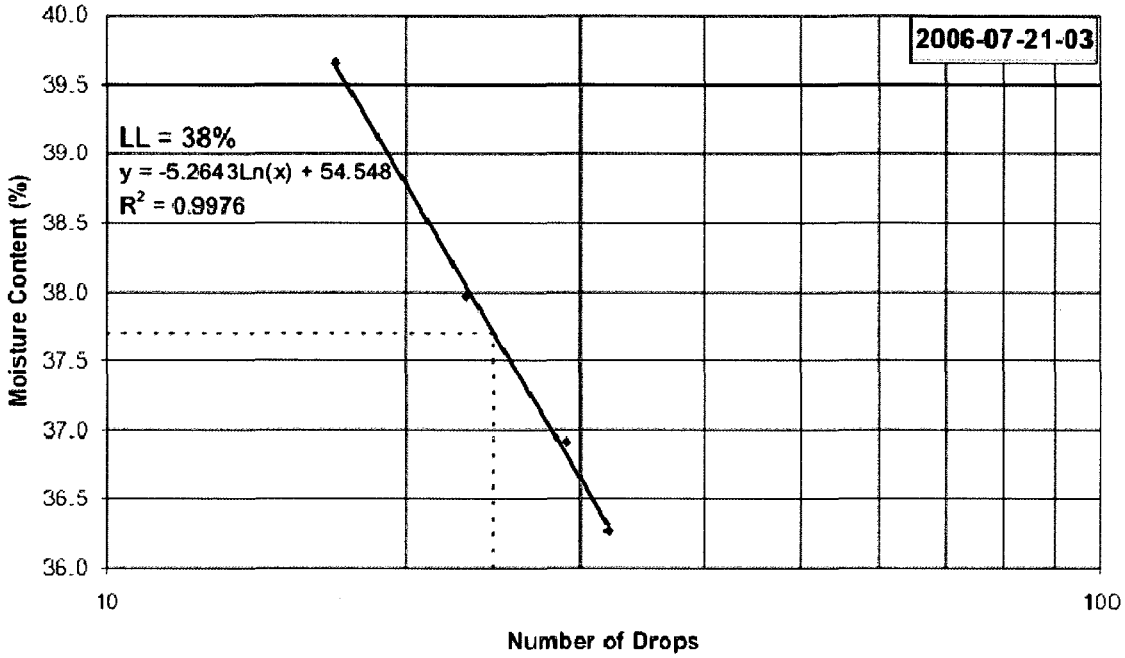

BTC-2005-04

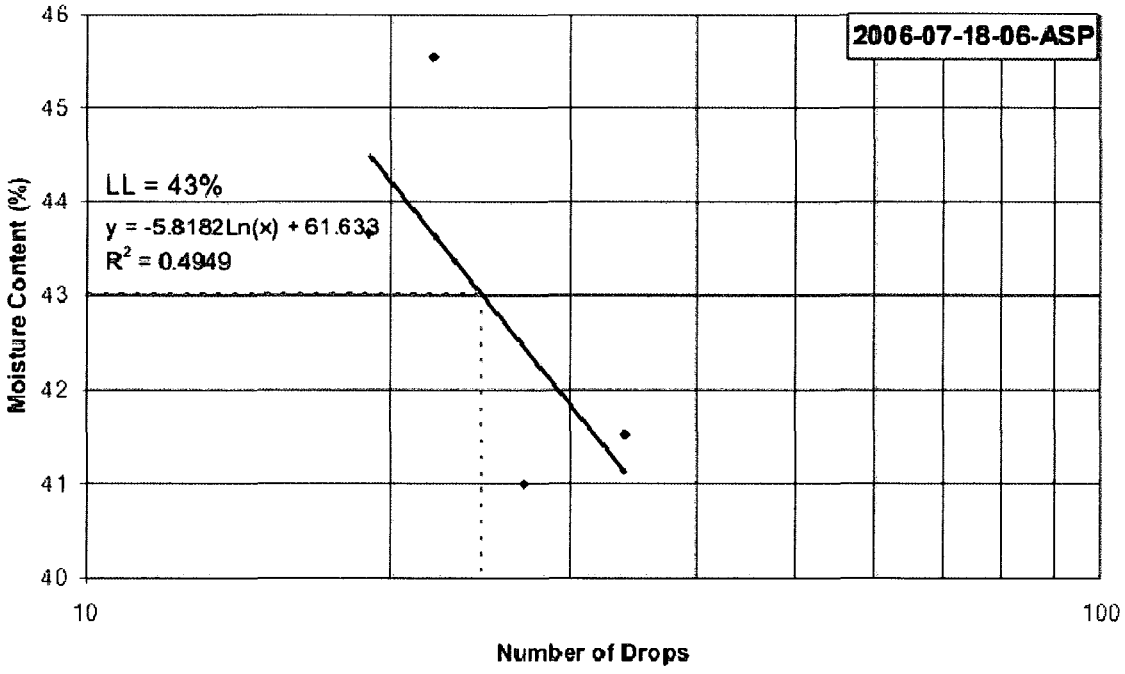

BTC-2005-04 Continued

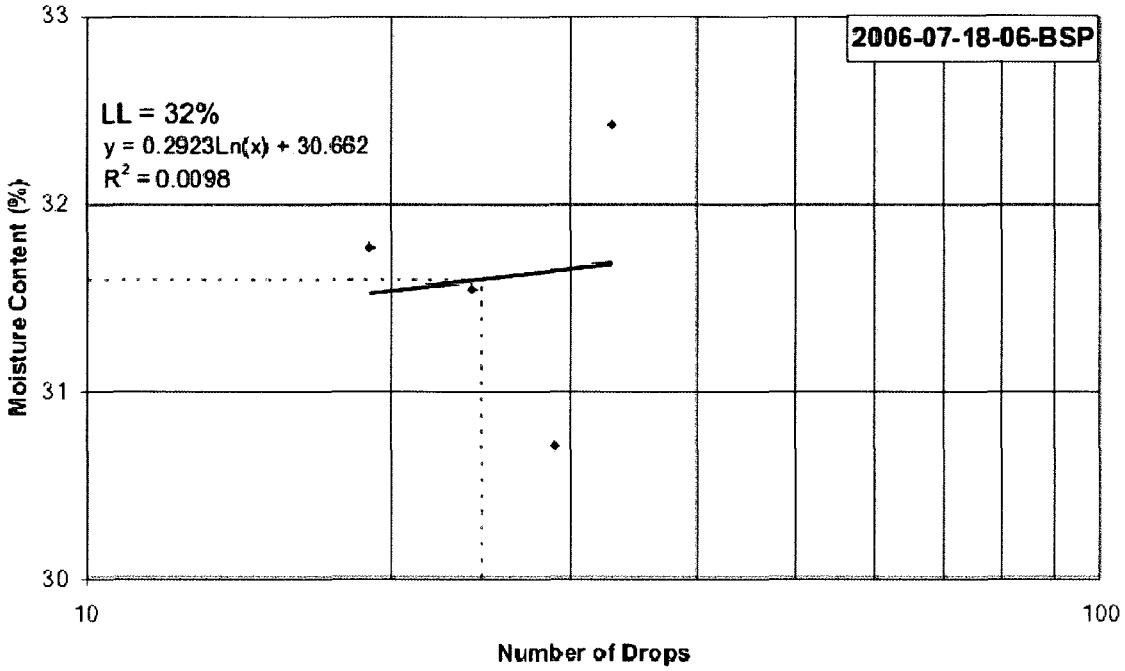

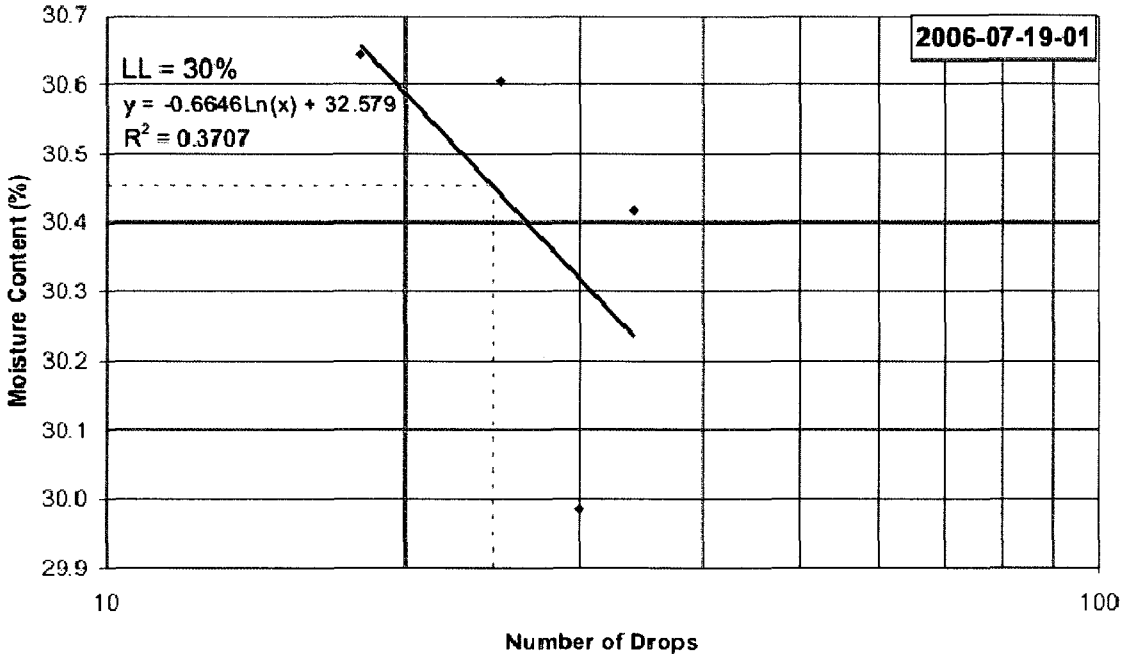

BTC-2005-04 Continued

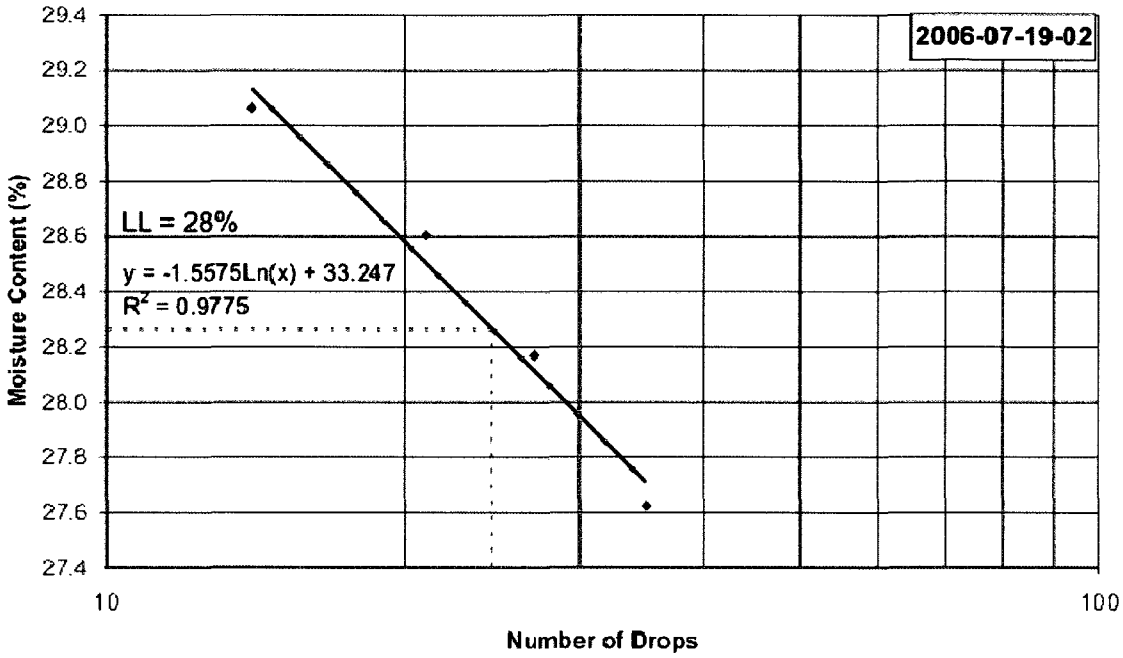

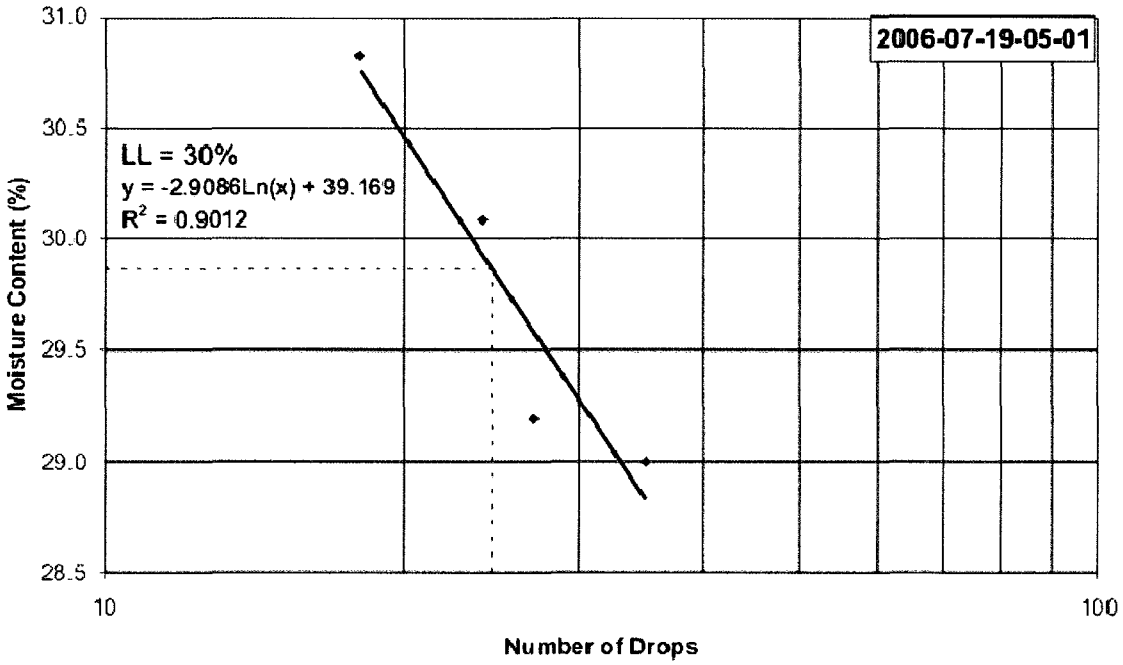

BTC-2005-04 Continued

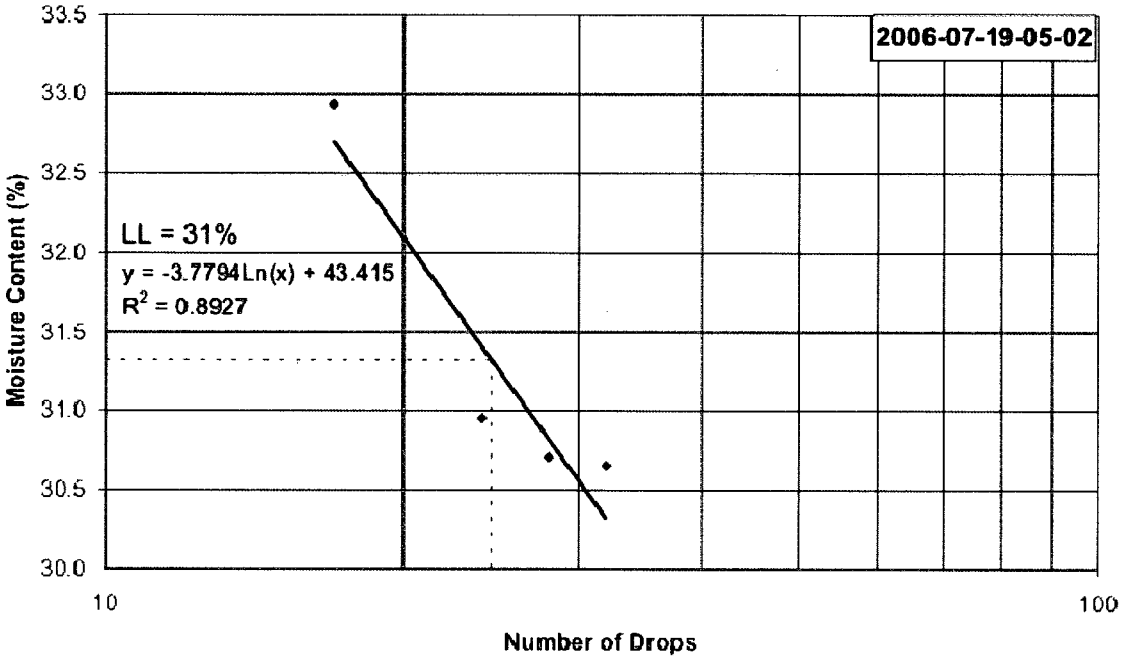

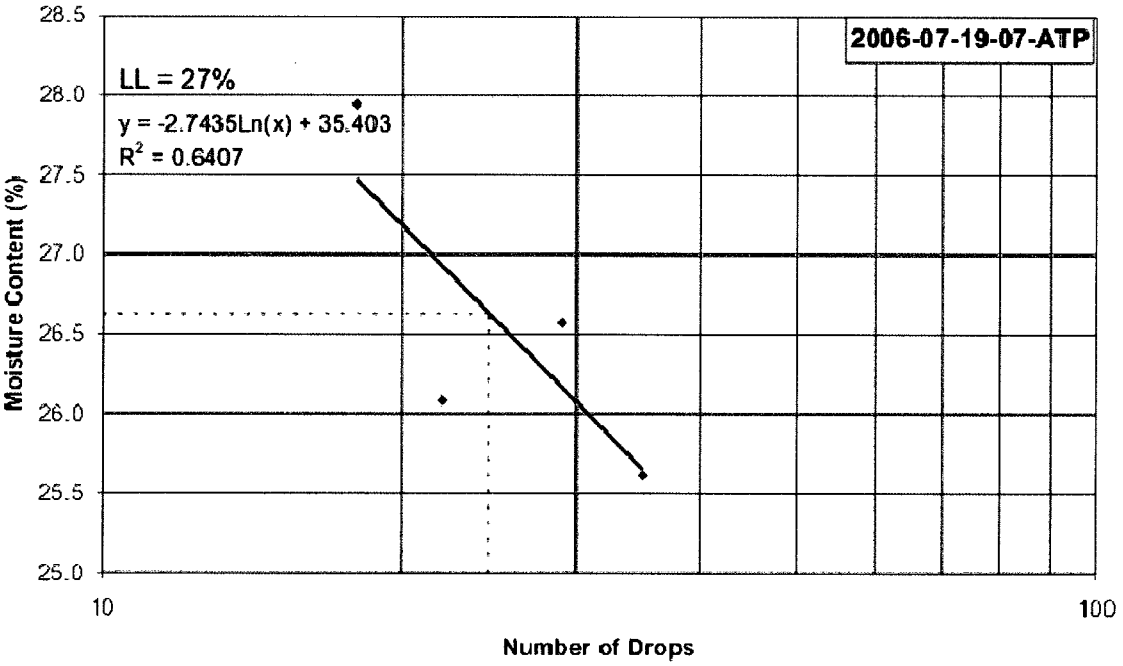

BTC-2005-04 Continued

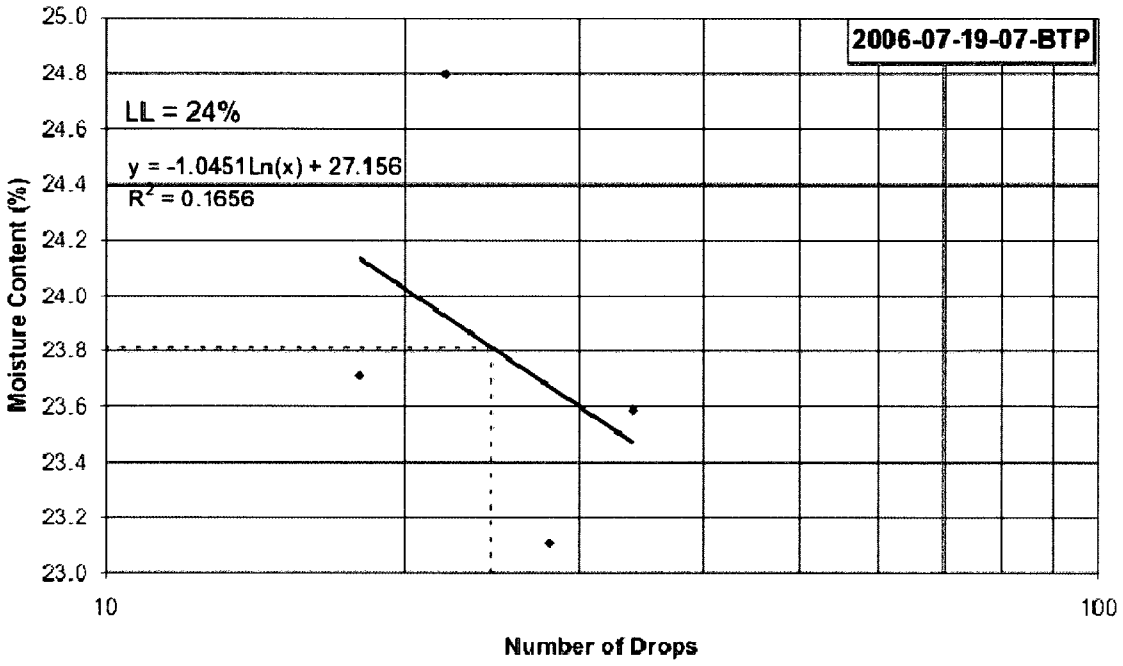

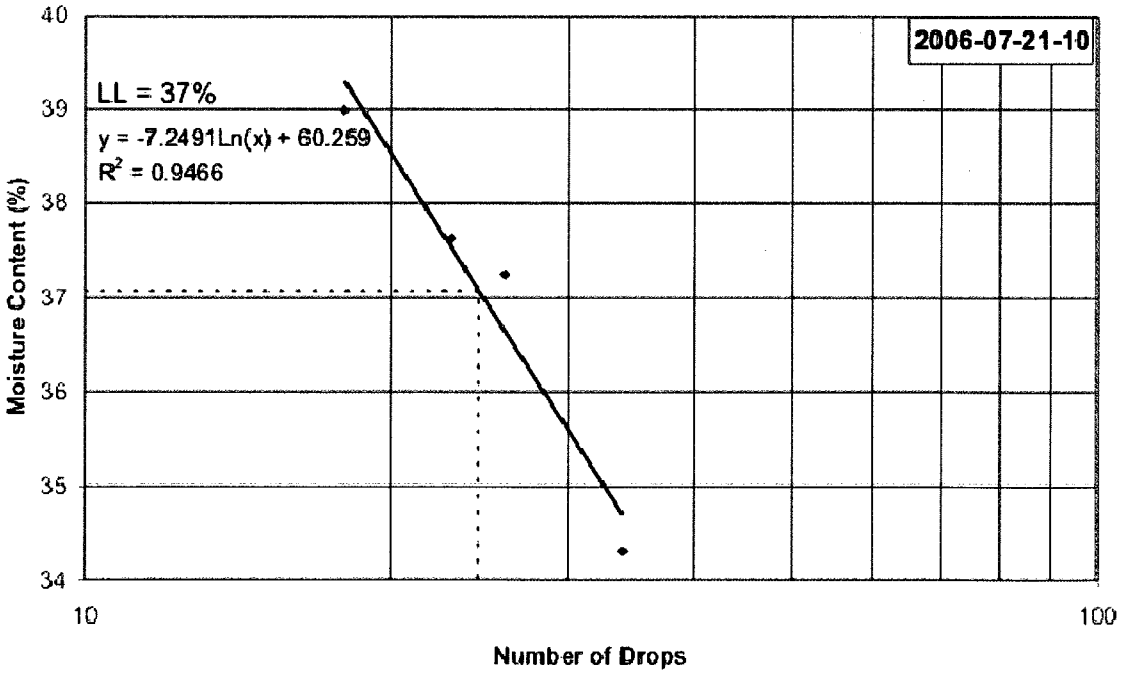

BTC-2005-04 Continued

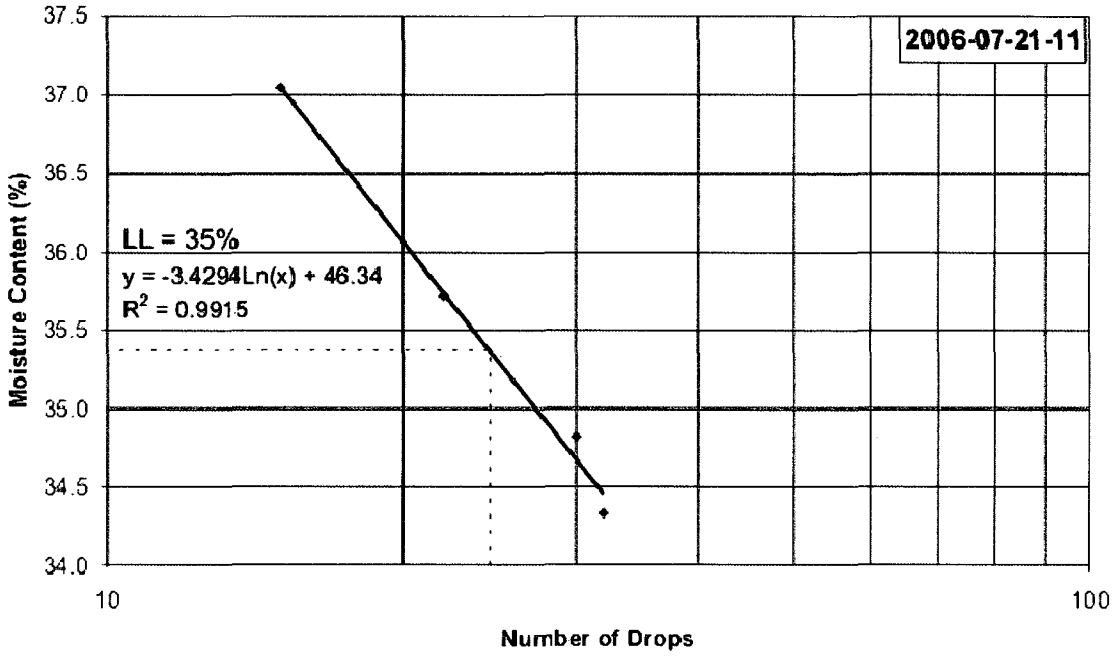

BTC-2005-08

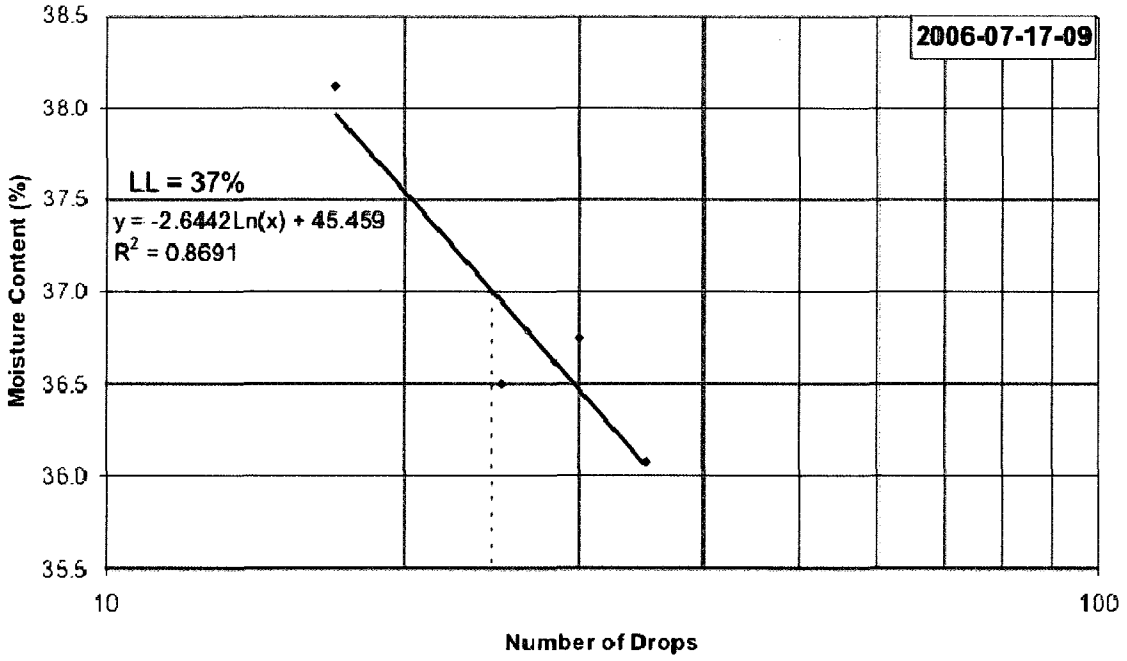

BTC-2005-08 Continued

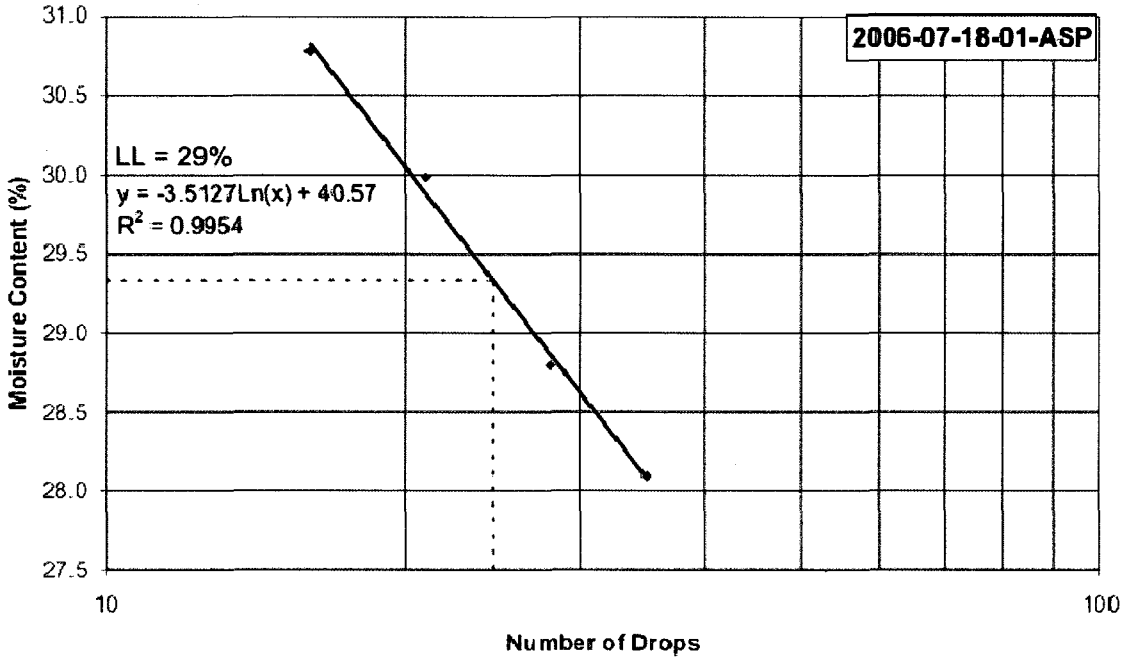

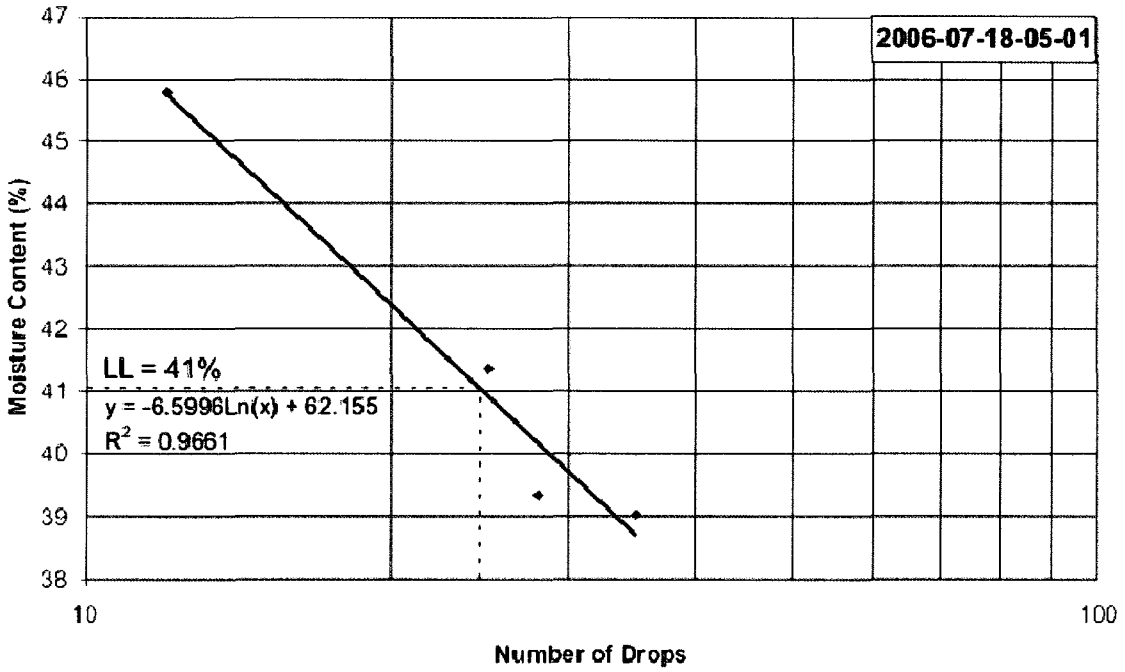

BTC-2005-08 Continued

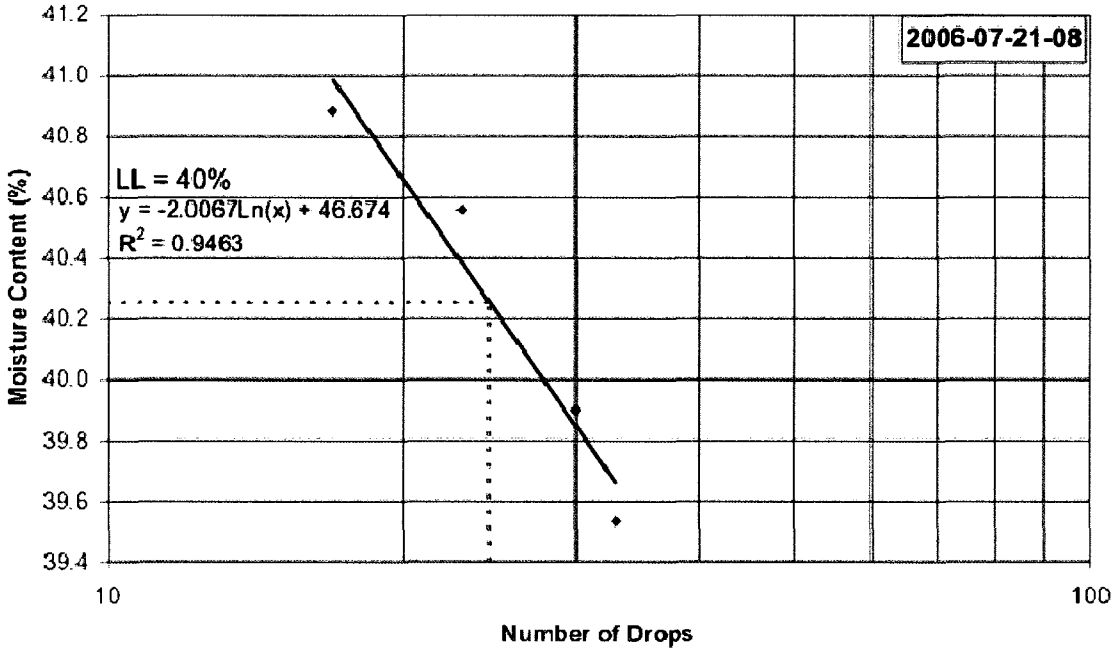

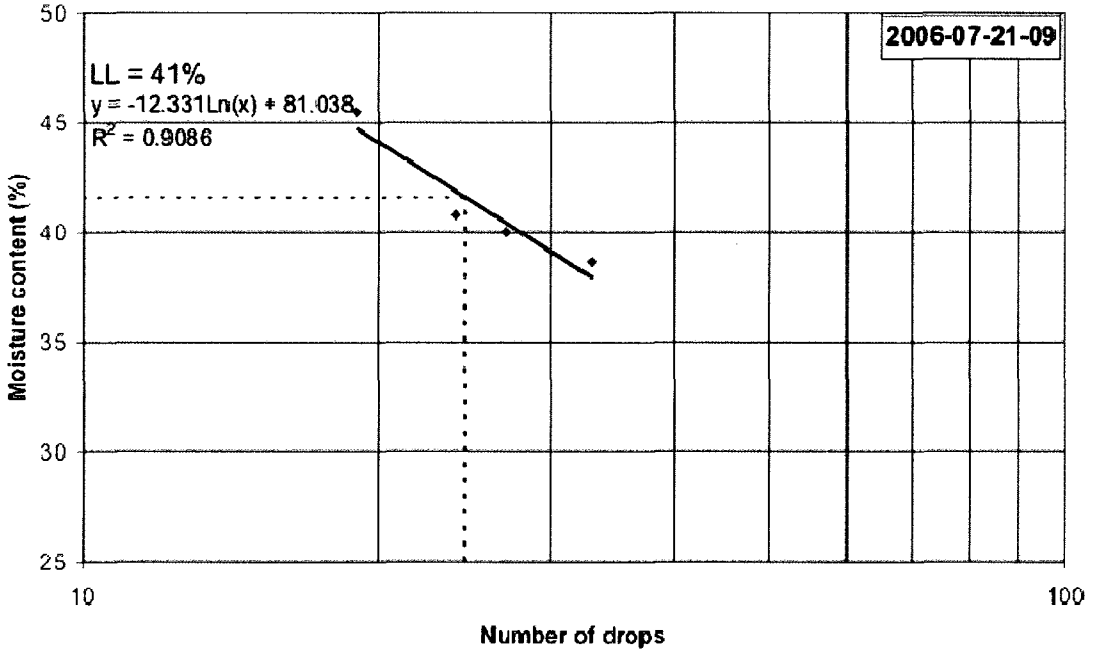

BTC-2005-13

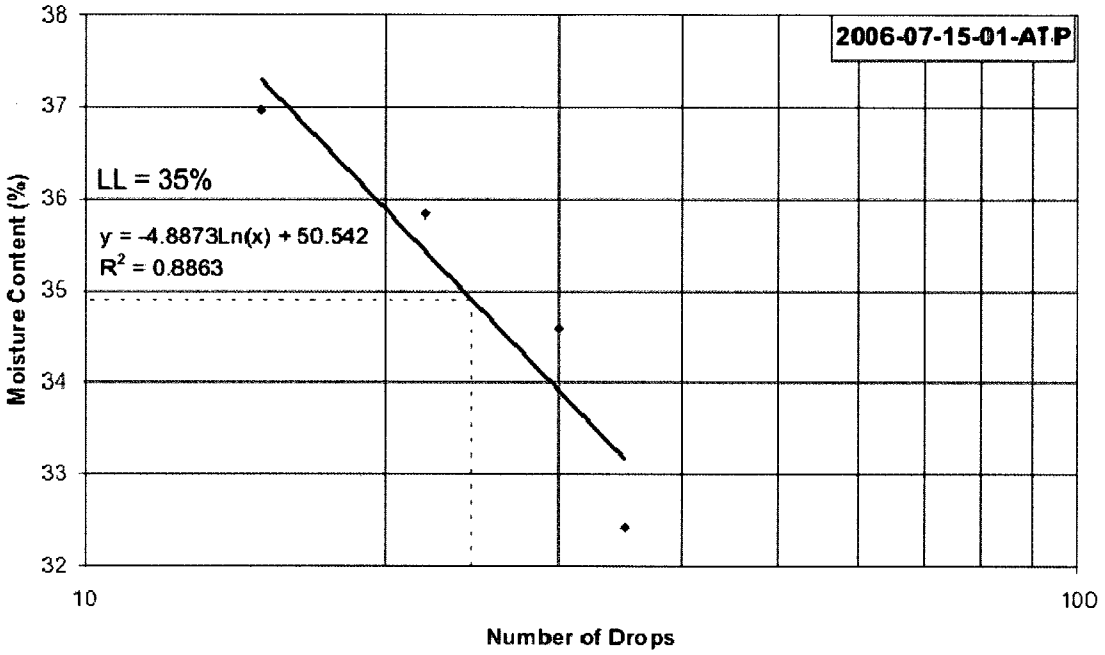
2006-07-15-01-ATP
LL = 35%
y = -4.8873Ln(x) + 50.542
R2 = 0.8863
Moisture Content (%)
38
37
36
35
34
33
32
10
100
Number of Drops

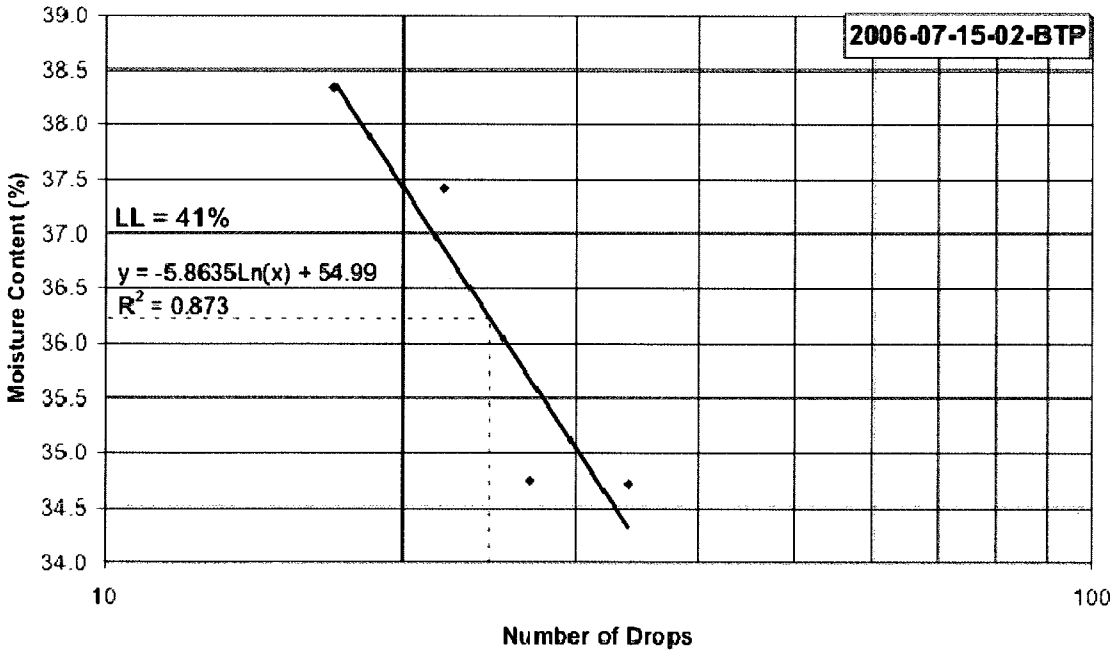
2006-07-15-02-BTP
LL = 41%
y = -5.8635Ln(x) + 54.99
R2 = 0.873
Moisture Content (%)
39.0
38.5
38.0
37.5
37.0
36.5
36.0
35.5
35.0
34.5
34.0
10
100
Number of Drops

BTC-2005-13 Continued

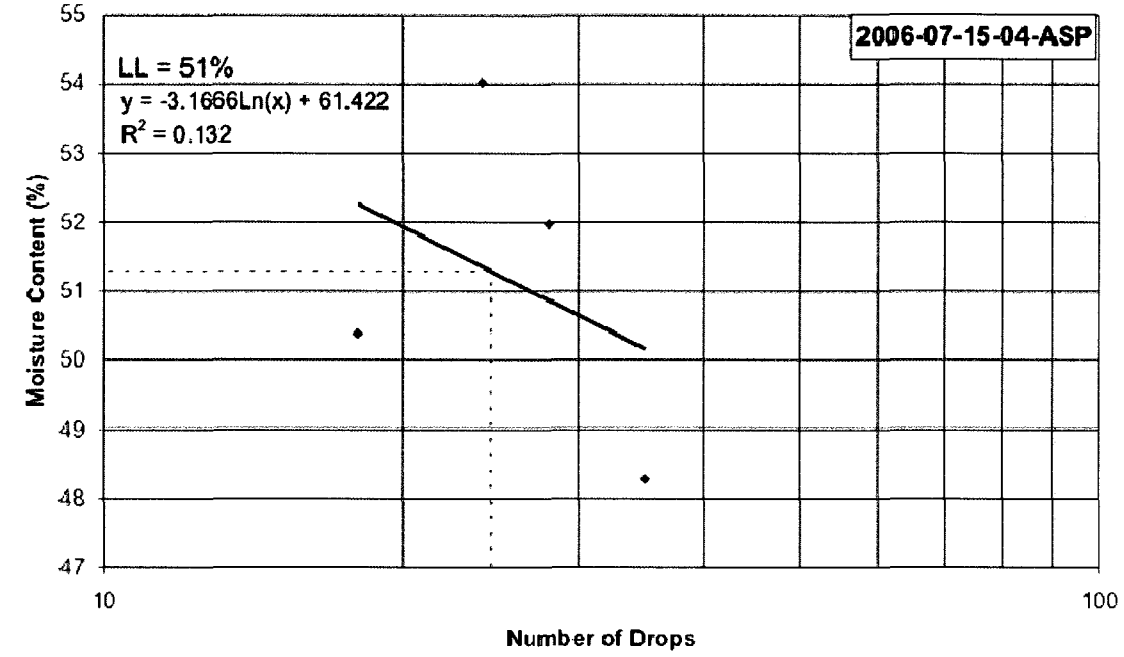

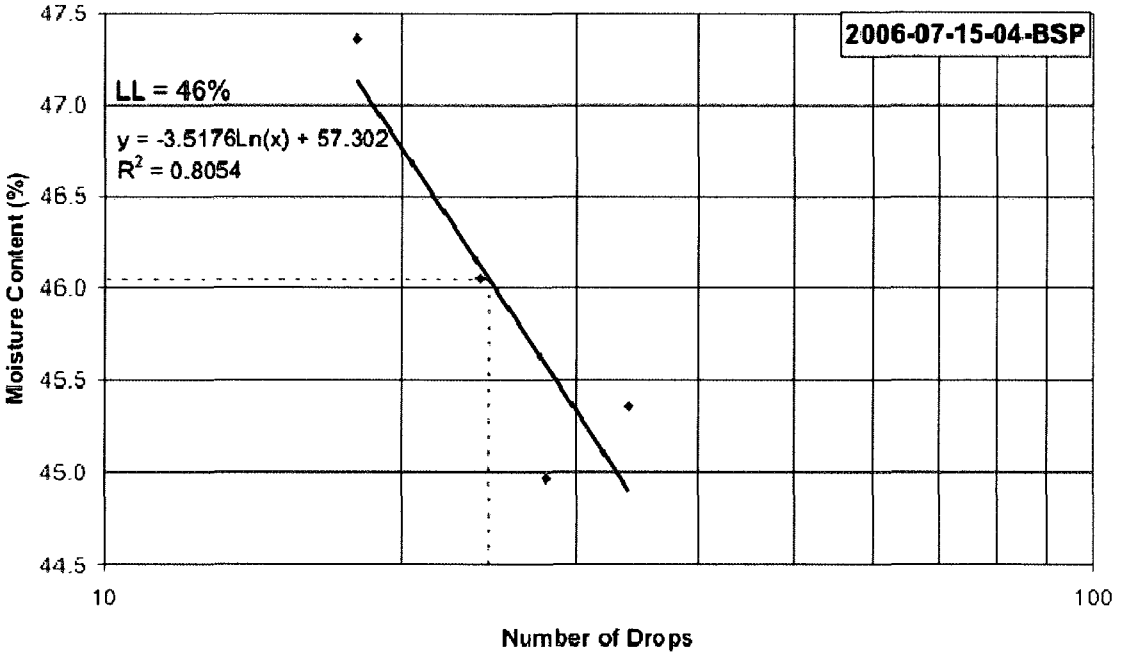

BTC-2005-13 Continued

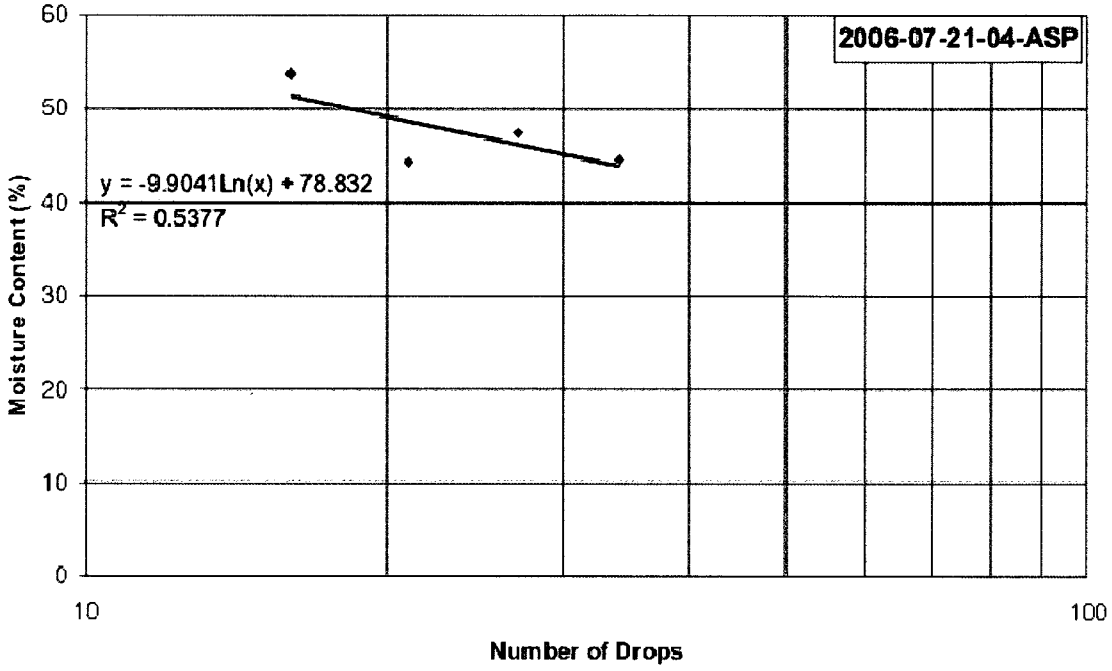

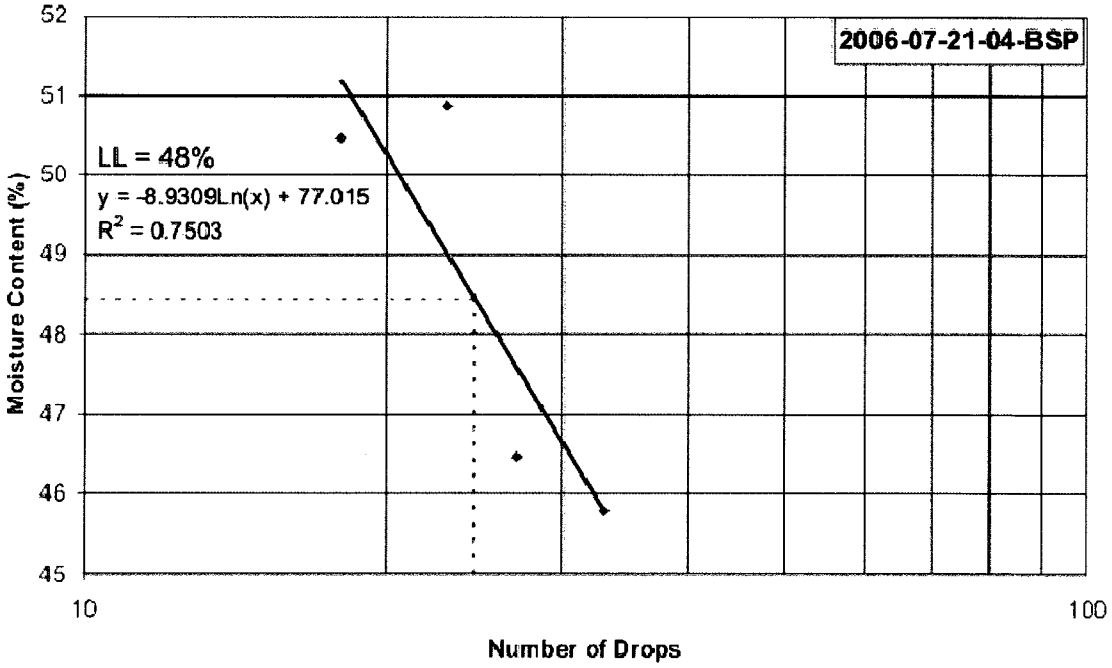

BTC-2005-13 Continued

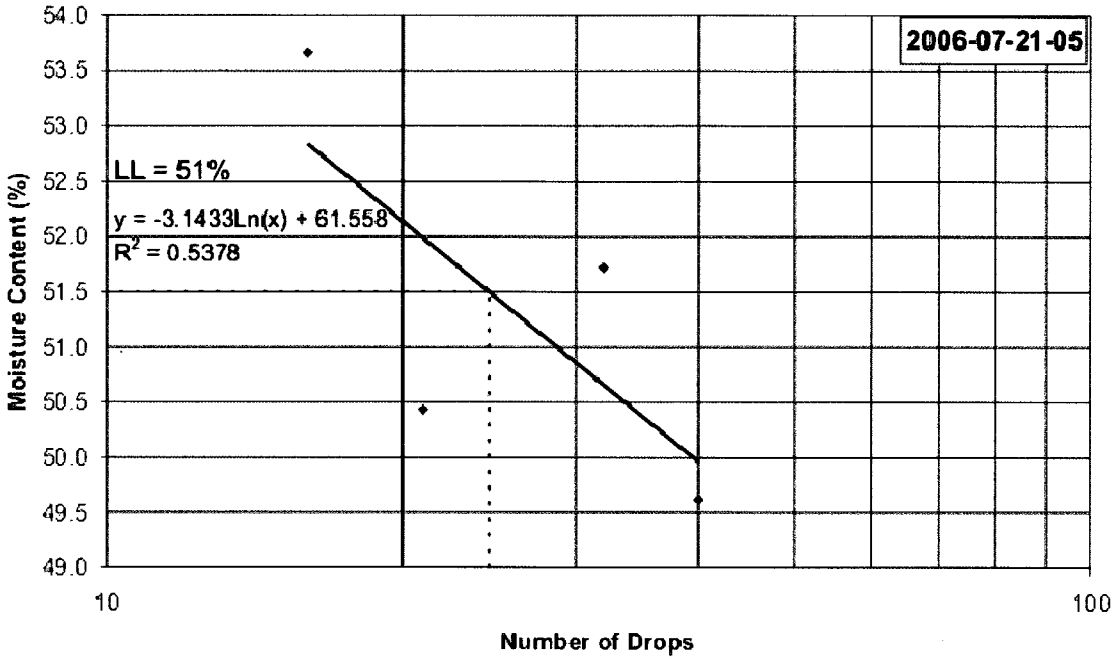

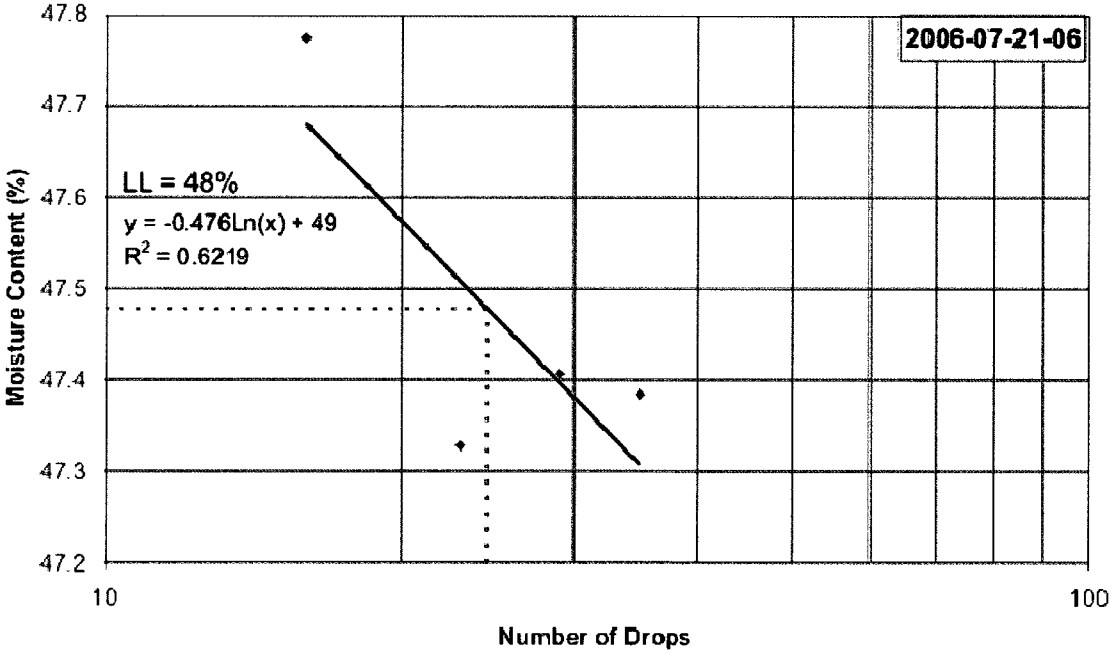

BTC-2005-13 Continued

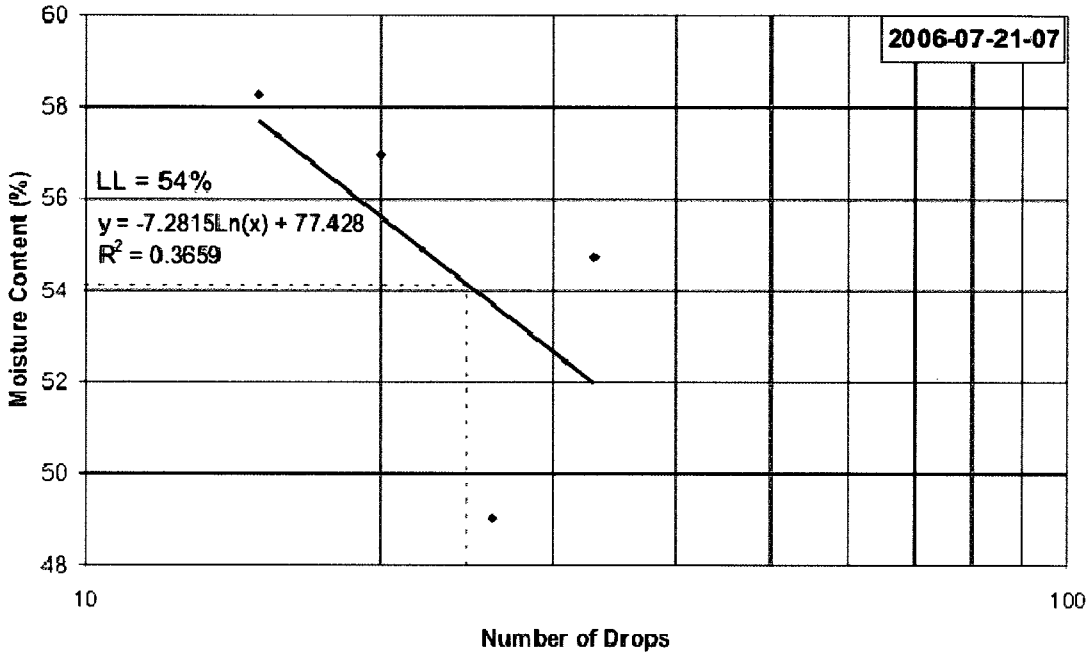

HWC-2005-01

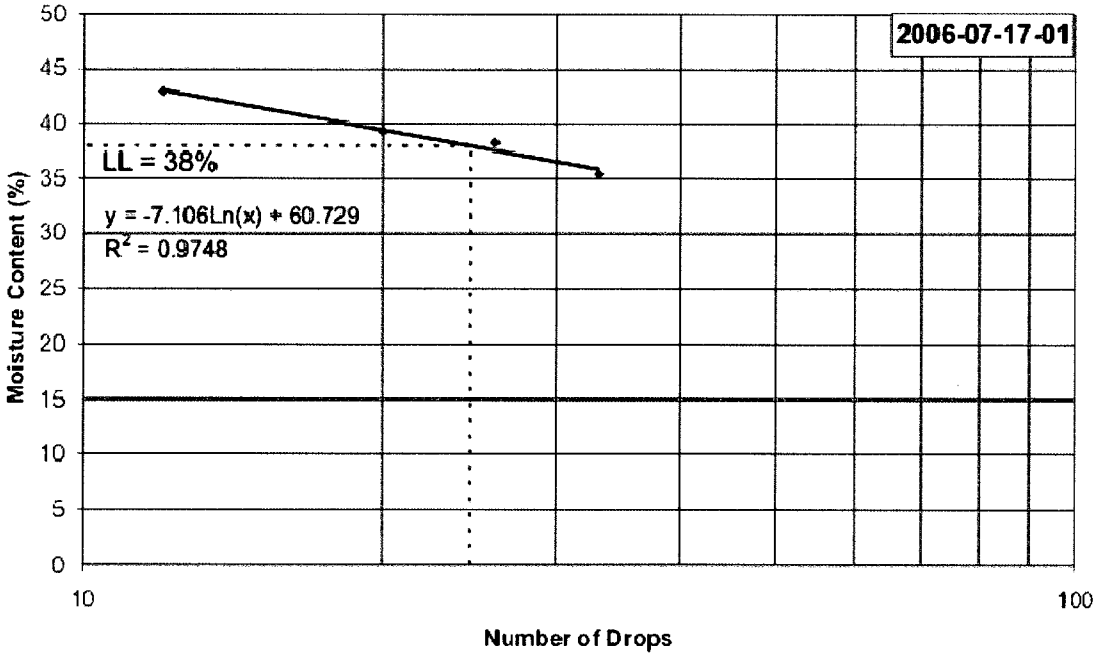

HWC-2005-01 Continued

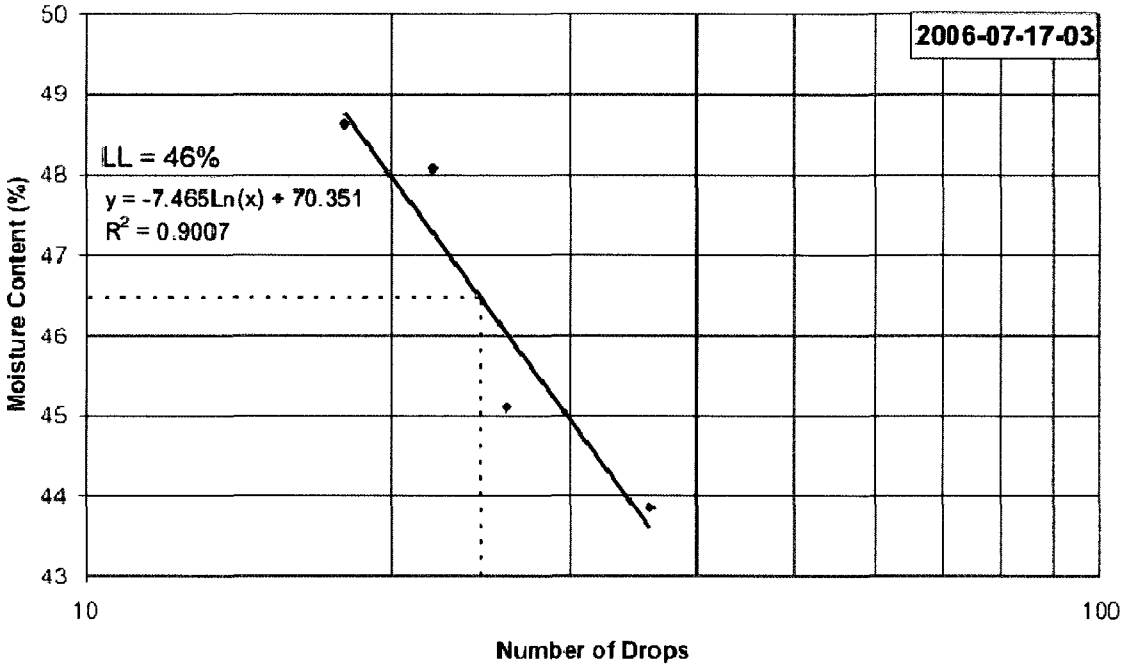

BSC-2005-01

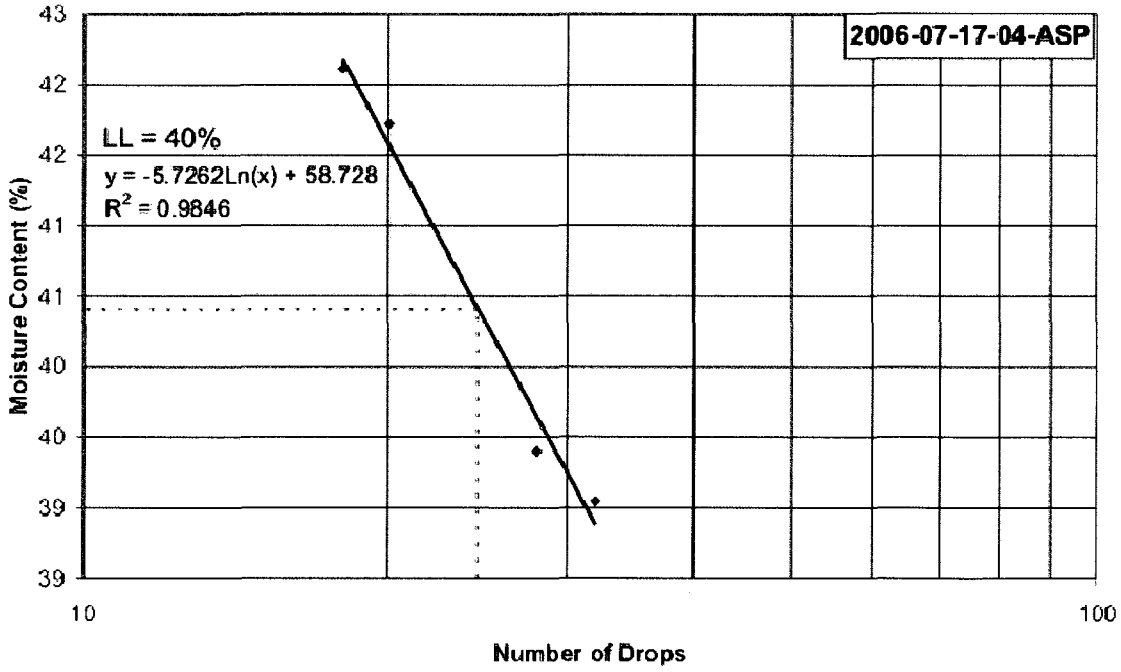

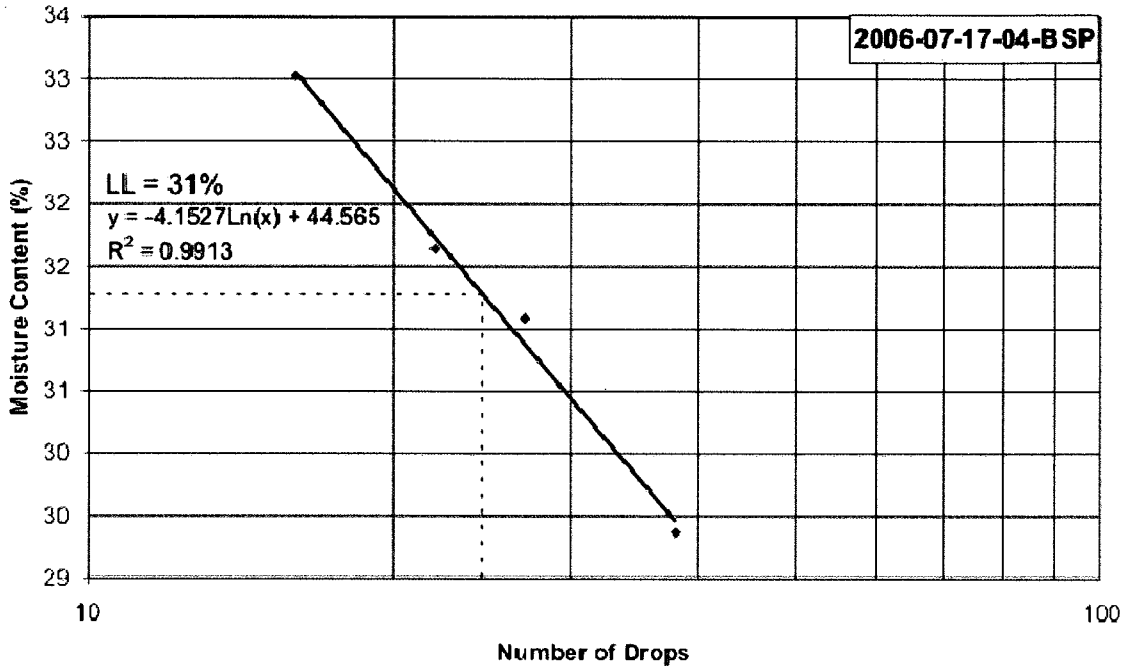
2006-07-17-04-BSP
LL = 31%
y = -4.1527Ln(x) + 44.565
R² = 0.9913
Moisture Content (%)
Number of Drops
34
33
33
32
32
31
31
30
30
29
10
100

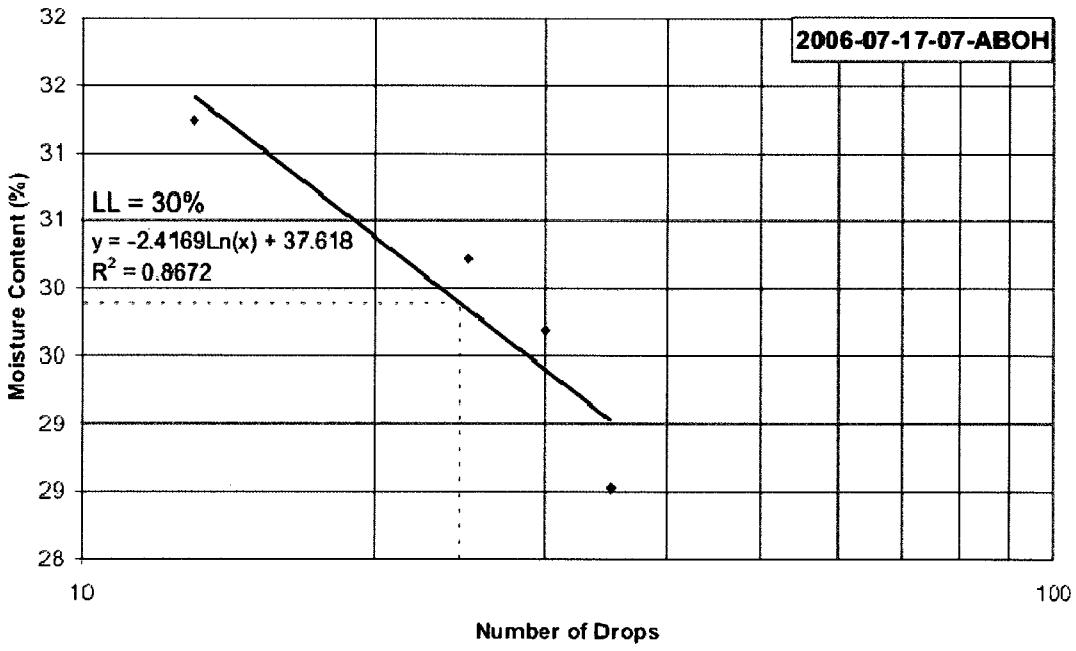
2006-07-17-07-ABOH
LL = 30%
y = -2.4169Ln(x) + 37.618
R² = 0.8672
Moisture Content (%)
Number of Drops
32
32
31
31
30
30
29
29
28
10
100

APPENDIX C – STRESS-DISPLACMENT CURVES AND SHEAR STRENGTH PARAMETER GRAPHS

SC-2005-01

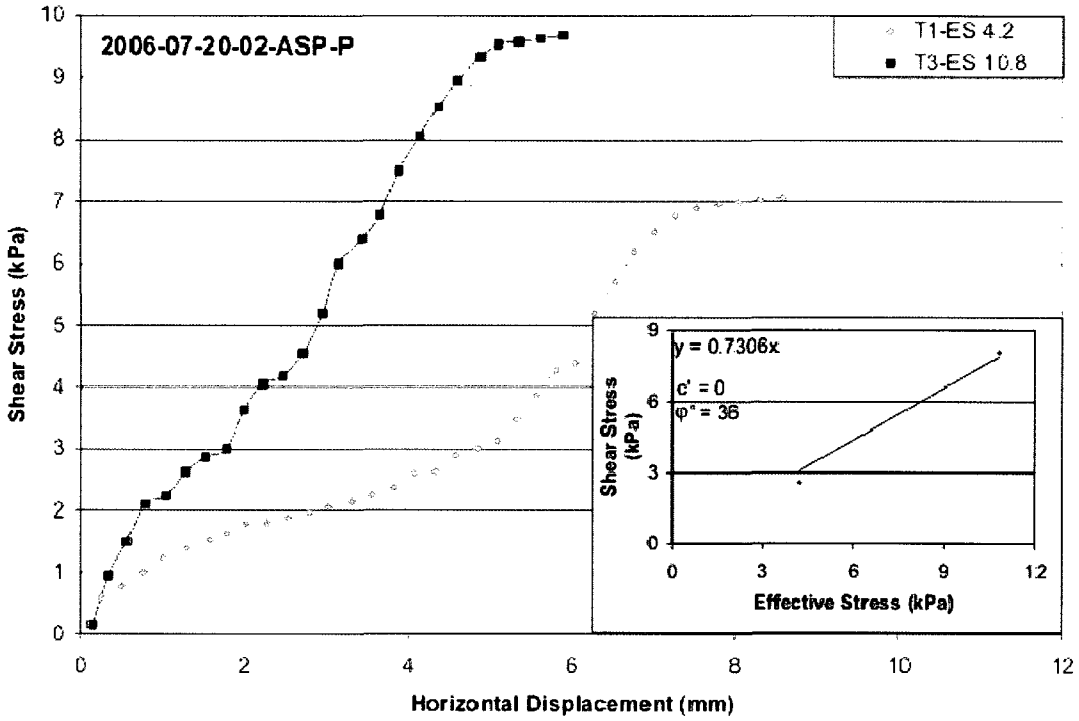

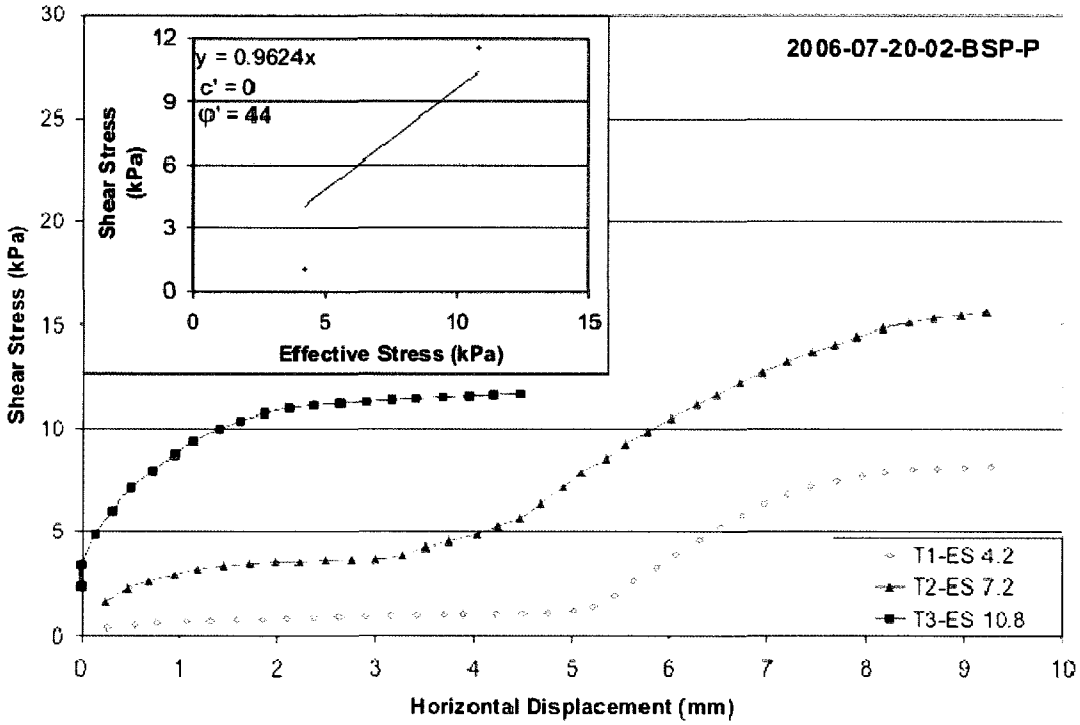

SC-2005-01 Continued

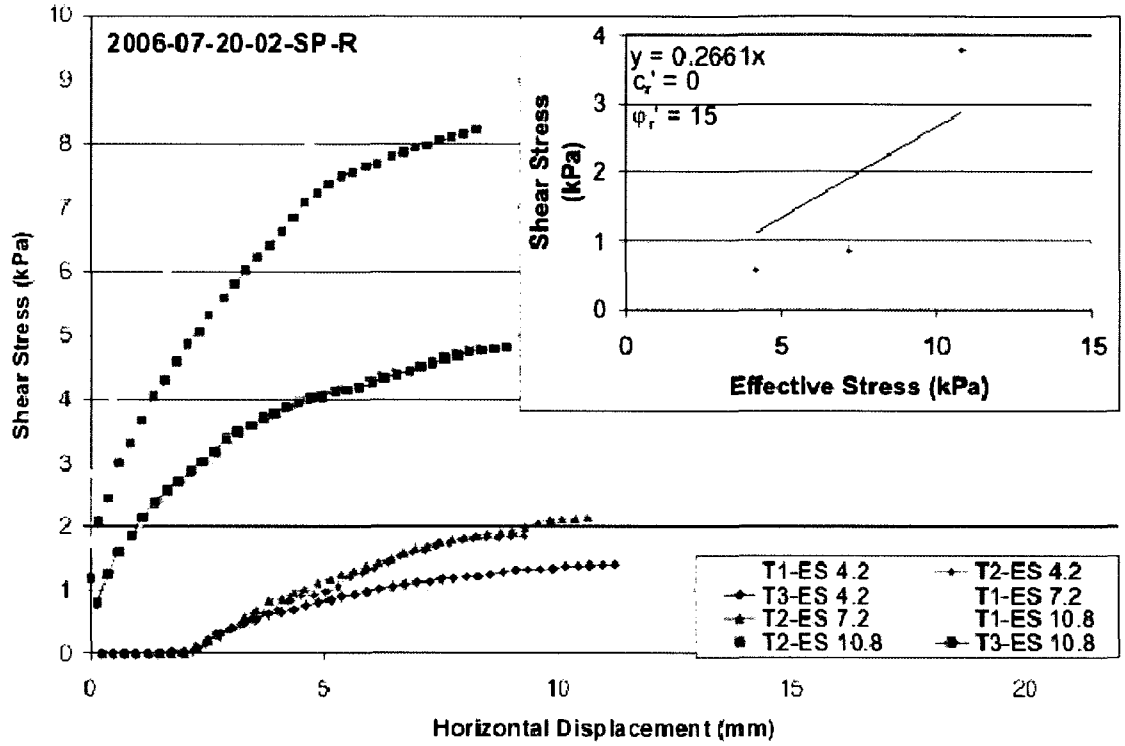

BTC-2005-04

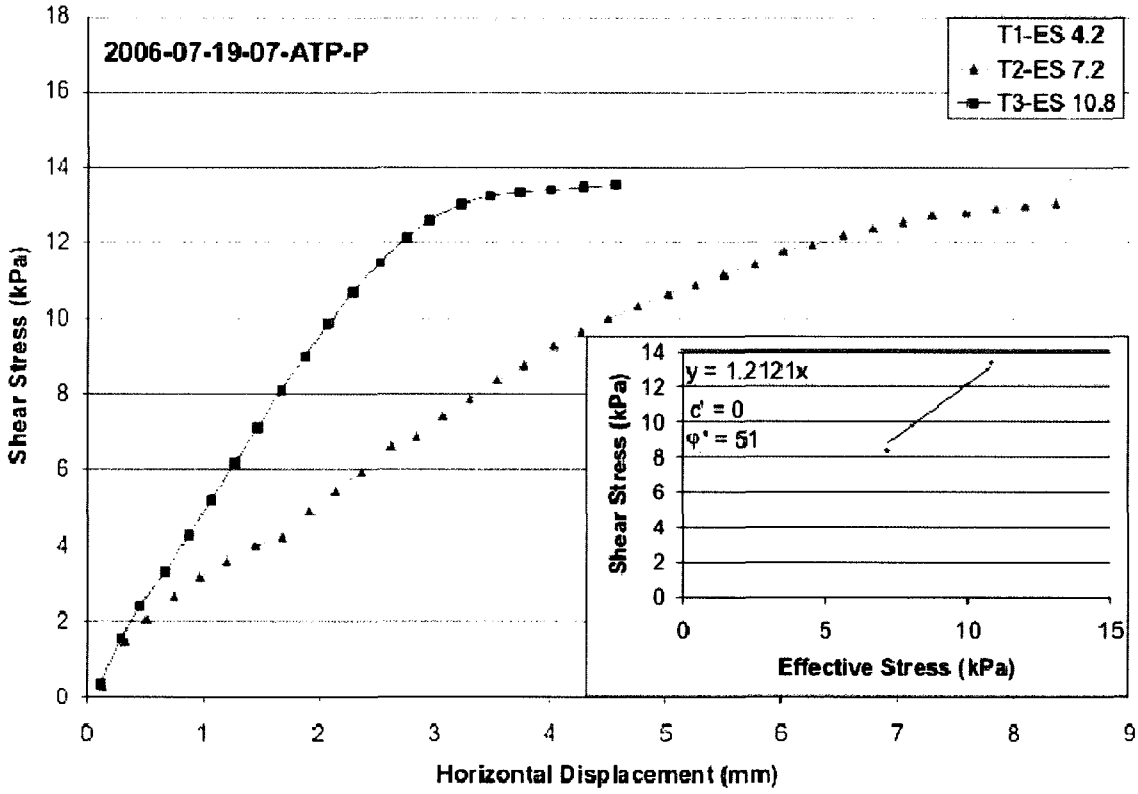

BTC-2005-04 Continued

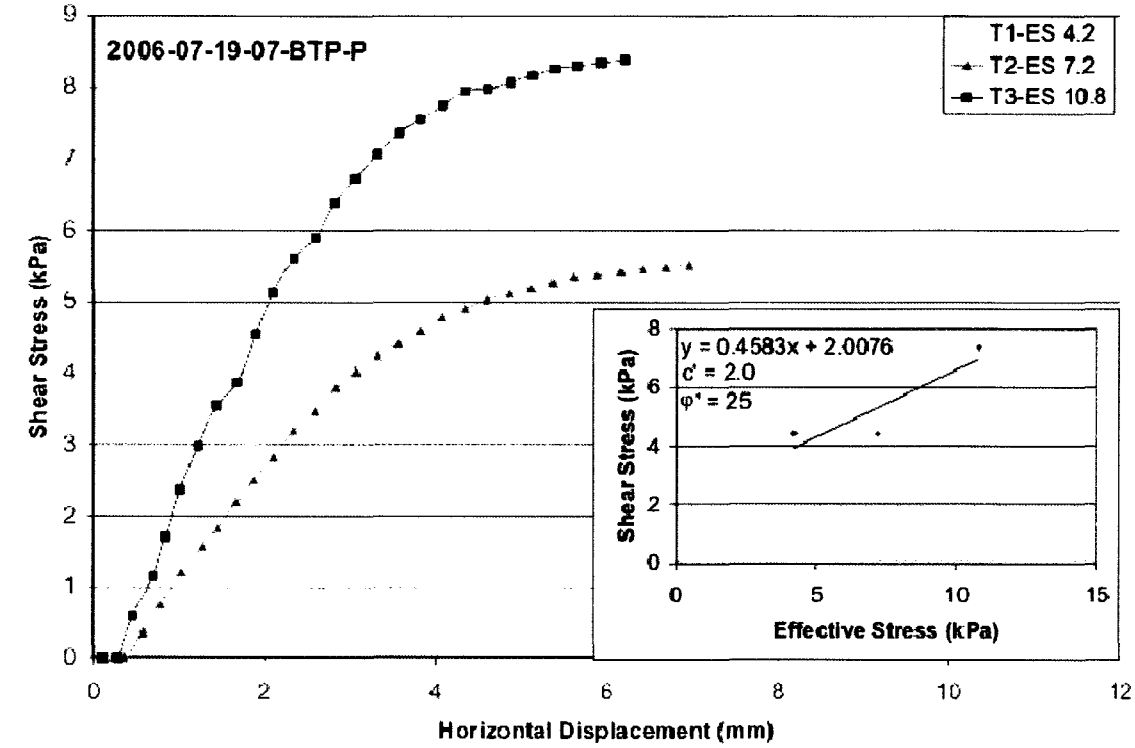

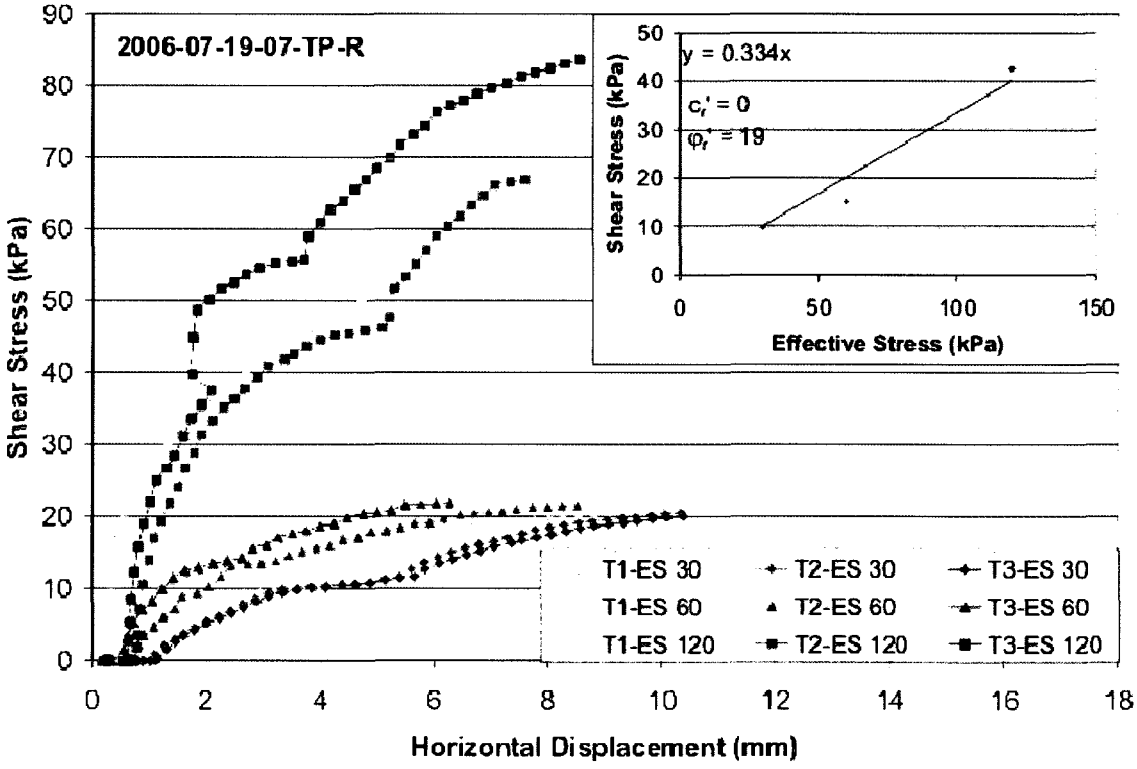

BTC-2005-04 Continued

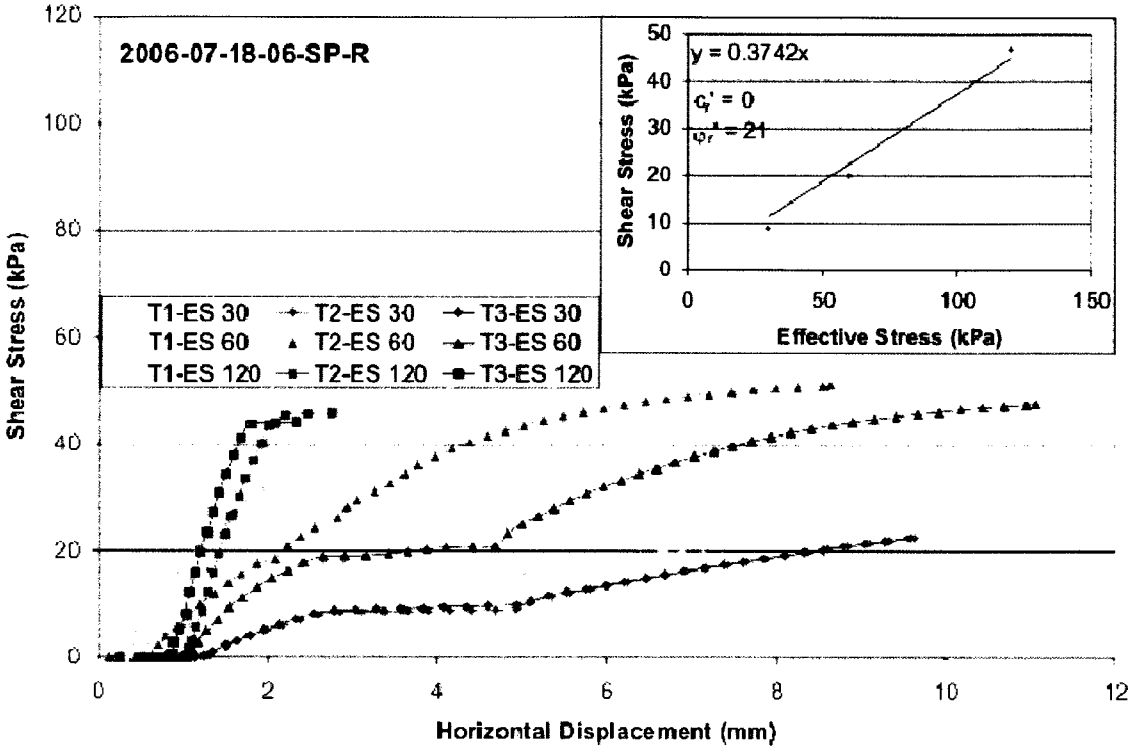

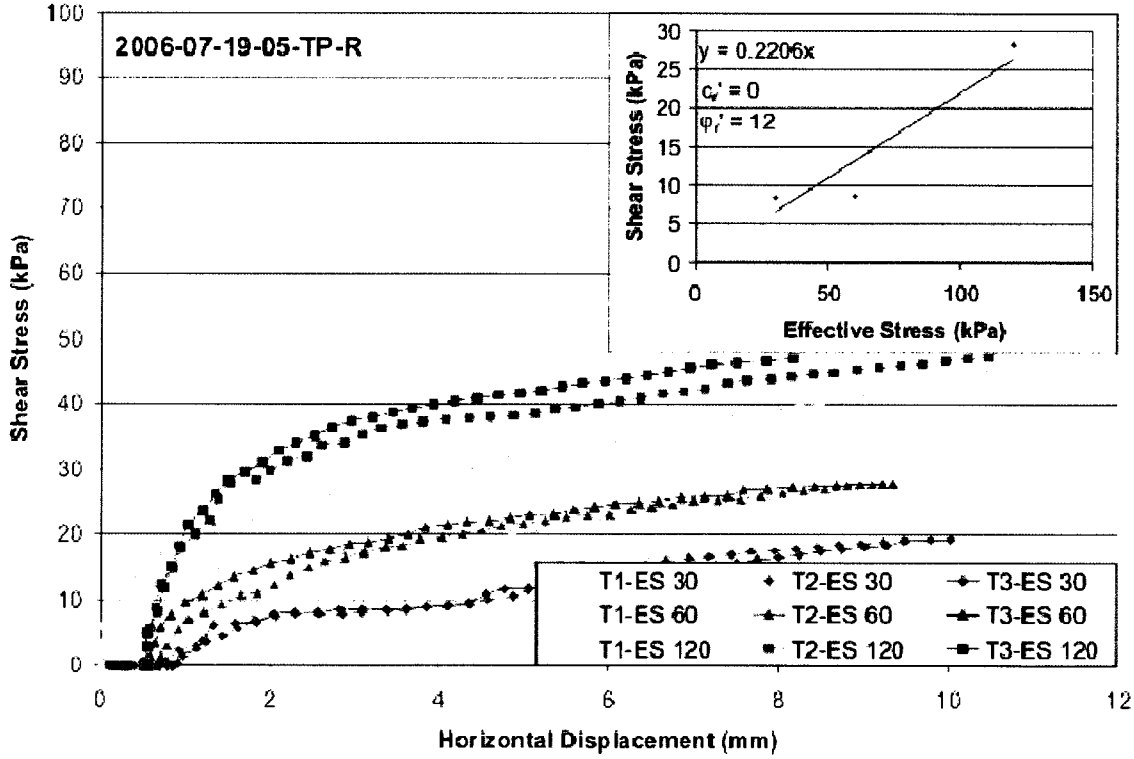

BTC-2005-08

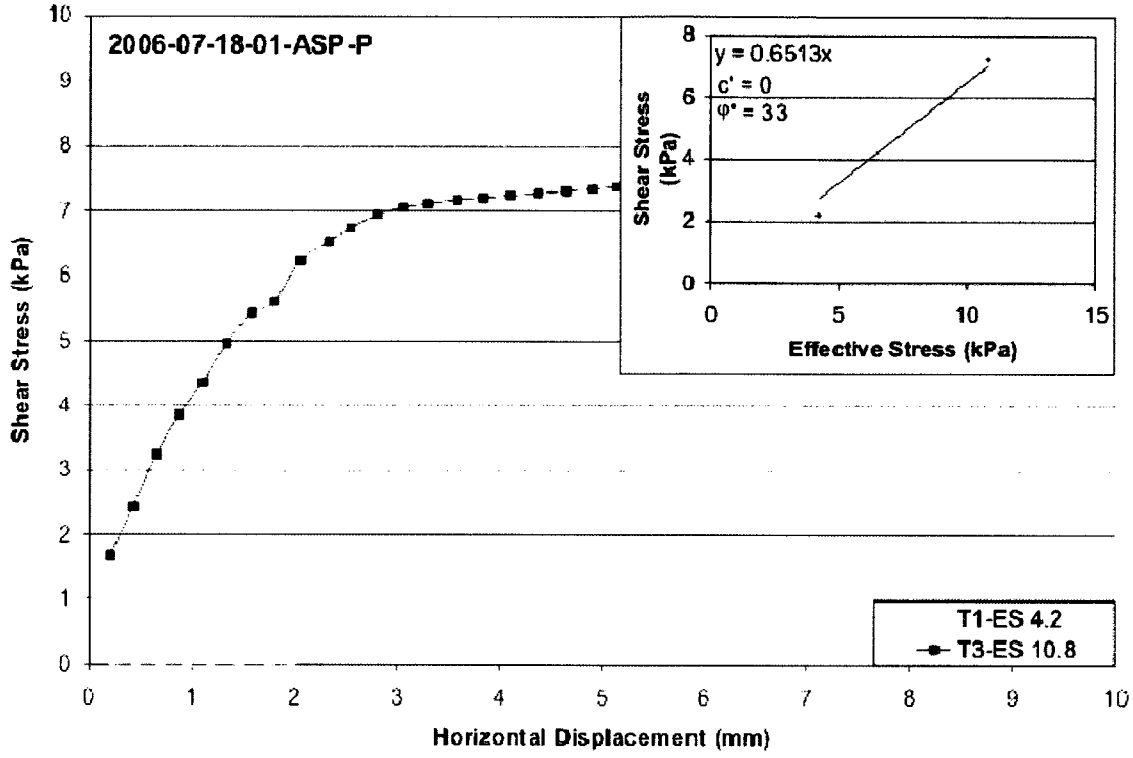
2006-07-18-01-ASP-P
y = 0.6513x
c' = 0
φ' = 33
Shear Stress (kPa)
Effective Stress (kPa)
Shear Stress (kPa)
Horizontal Displacement (mm)
T1-ES 4.2
T3-ES 10.8

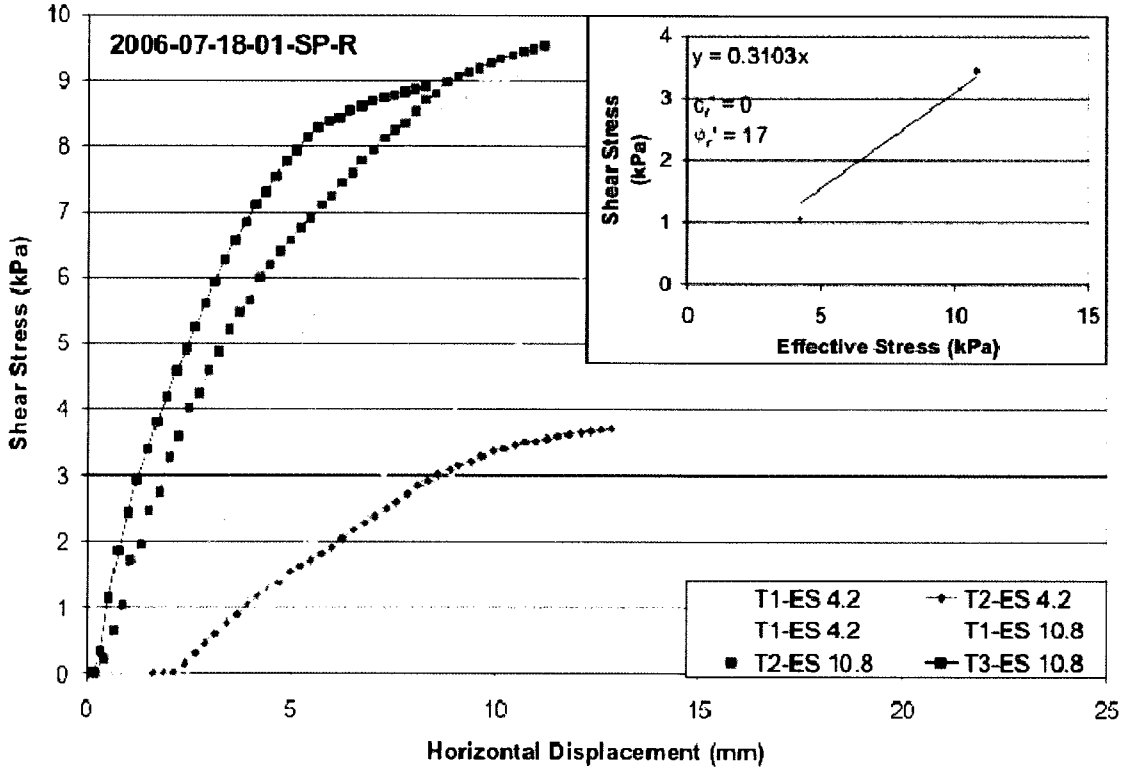
2006-07-18-01-SP-R
y = 0.3103x
c_r' = 0
φ_r' = 17
Shear Stress (kPa)
Effective Stress (kPa)
Shear Stress (kPa)
Horizontal Displacement (mm)
T1-ES 4.2
T2-ES 4.2
T1-ES 4.2
T1-ES 10.8
T2-ES 10.8
T3-ES 10.8

BTC-2005-13

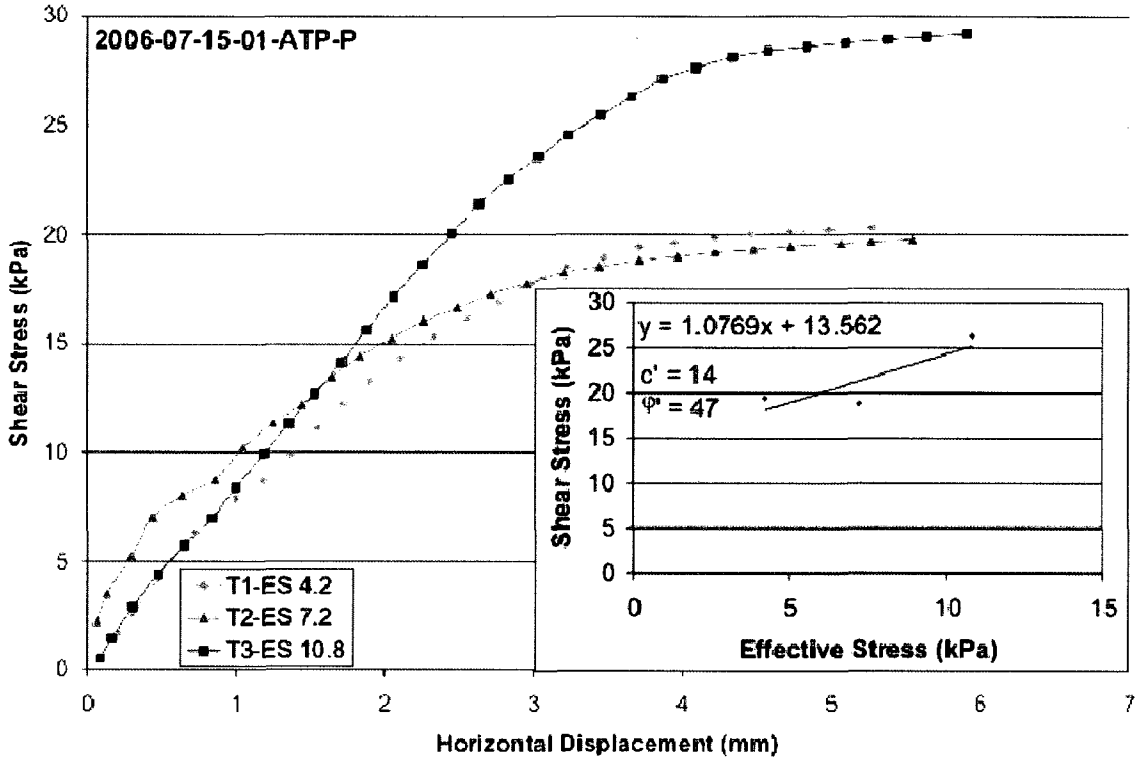
2006-07-15-01-ATP-P
Shear Stress (kPa)
Horizontal Displacement (mm)
T1-ES 4.2
T2-ES 7.2
T3-ES 10.8
y = 1.0769x + 13.562
c' = 14
φ' = 47
Shear Stress (kPa)
Effective Stress (kPa)

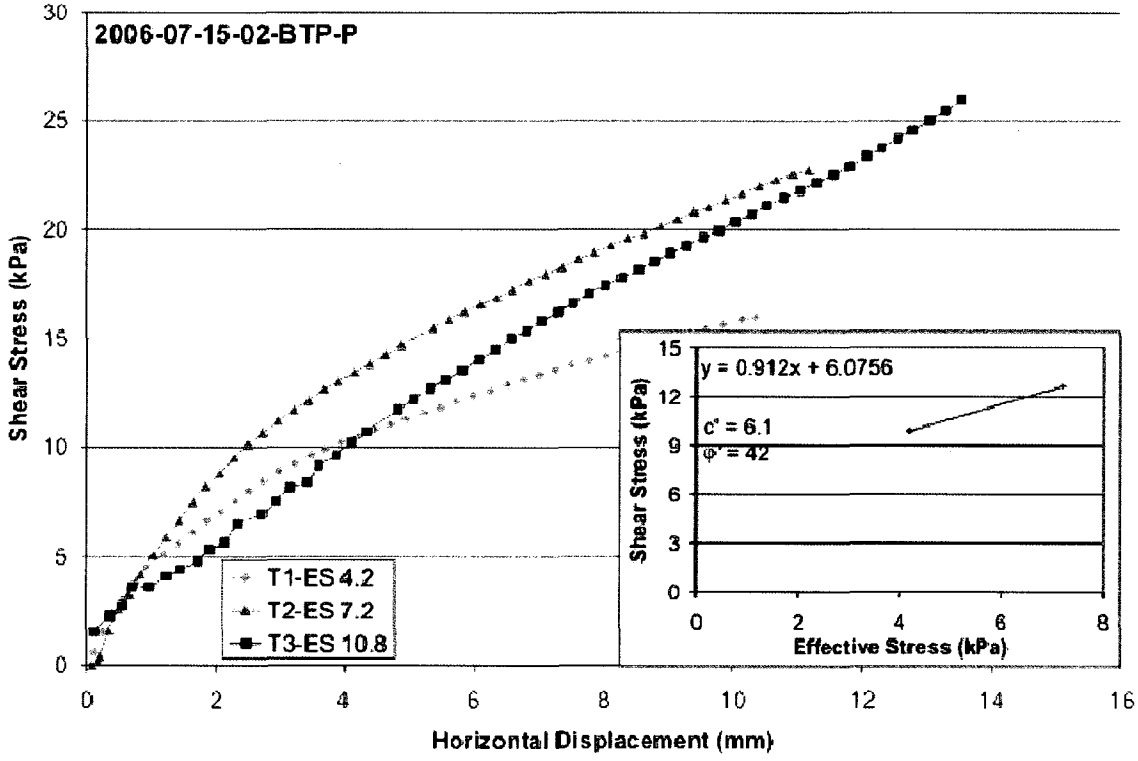
2006-07-15-02-BTP-P
Shear Stress (kPa)
Horizontal Displacement (mm)
T1-ES 4.2
T2-ES 7.2
T3-ES 10.8
y = 0.912x + 6.0756
c' = 6.1
φ' = 42
Shear Stress (kPa)
Effective Stress (kPa)

BTC-2005-13 Continued

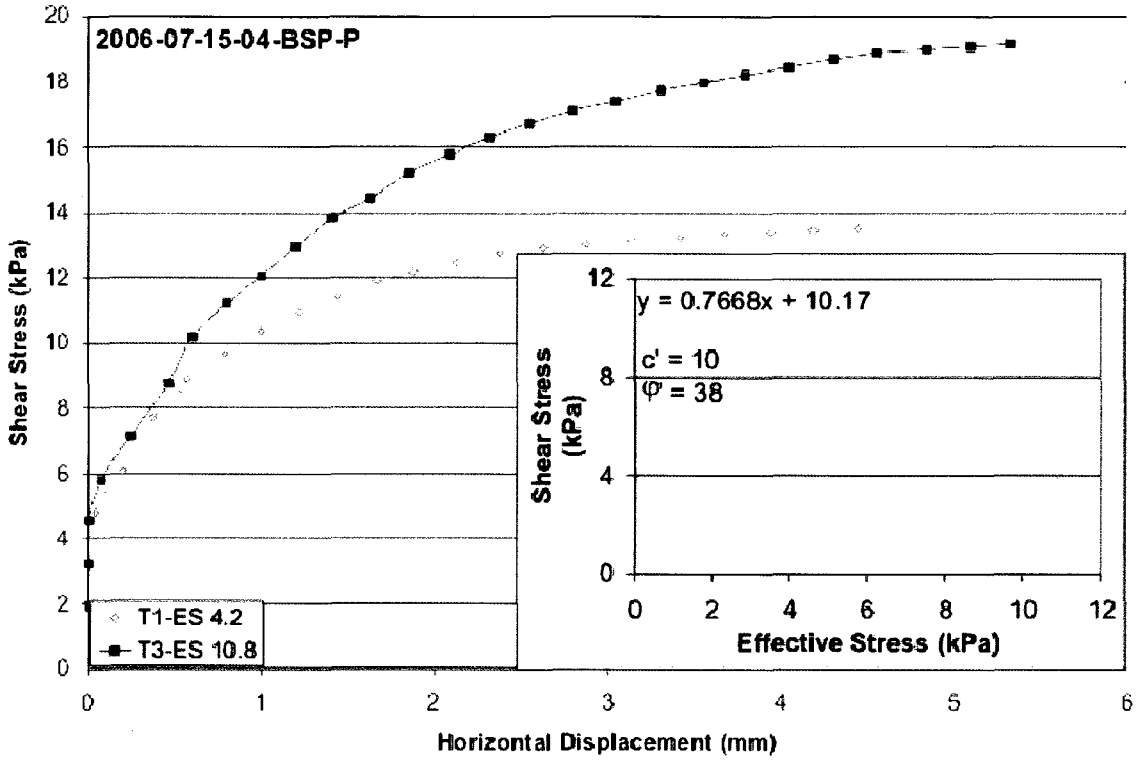

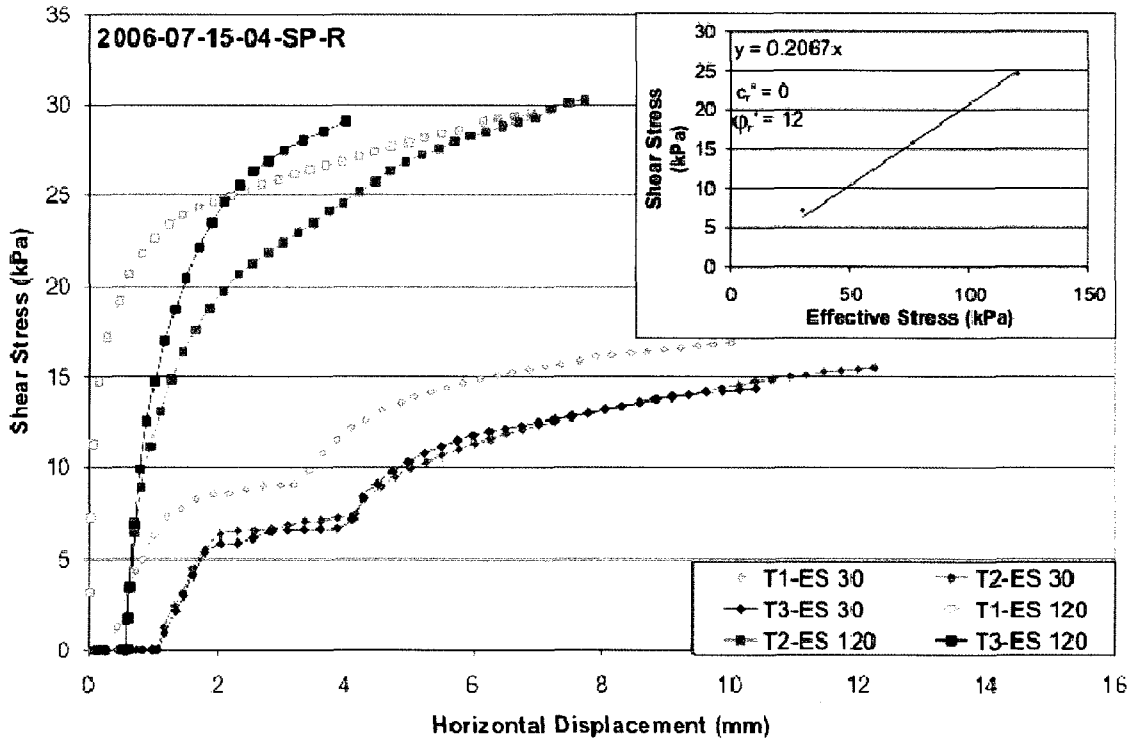

BTC-2005-13 Continued

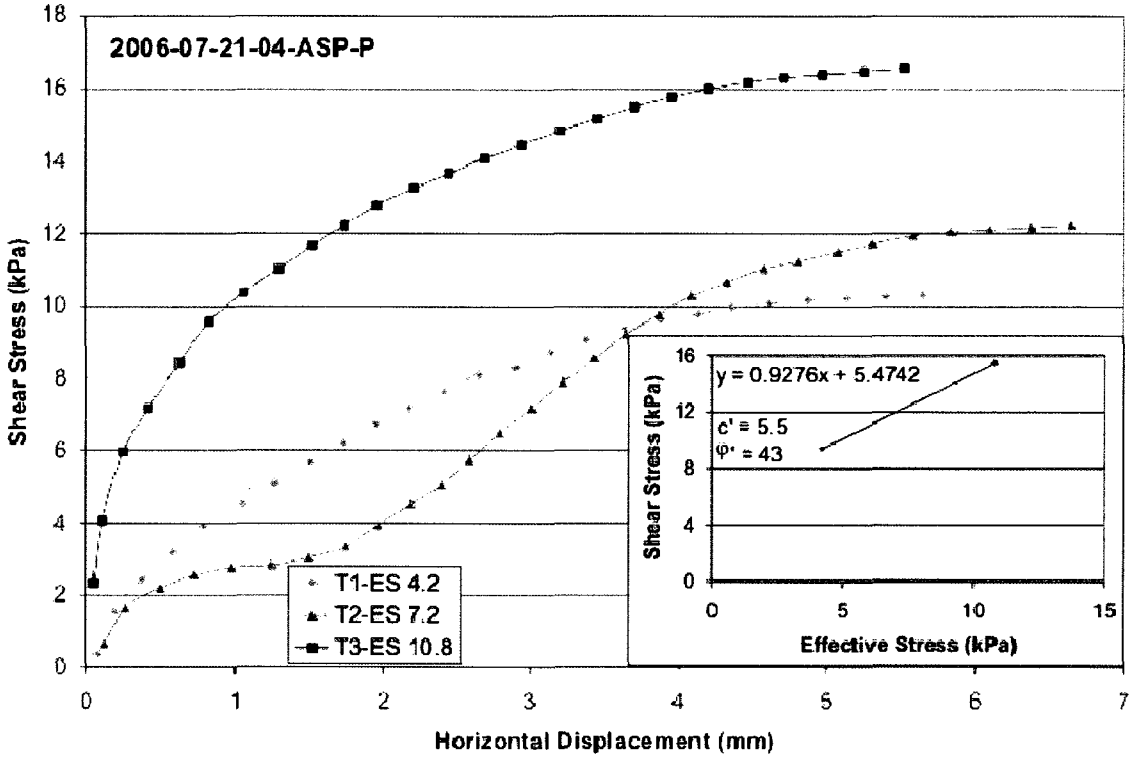

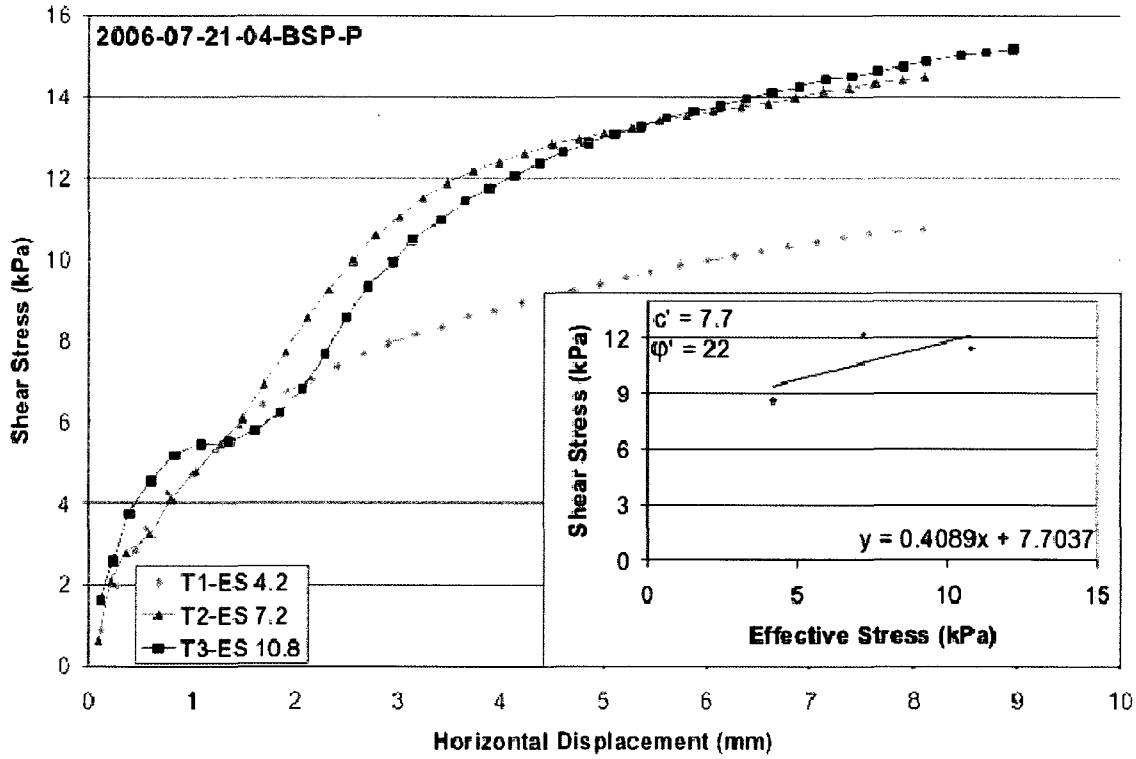

BTC-2005-13 Continued

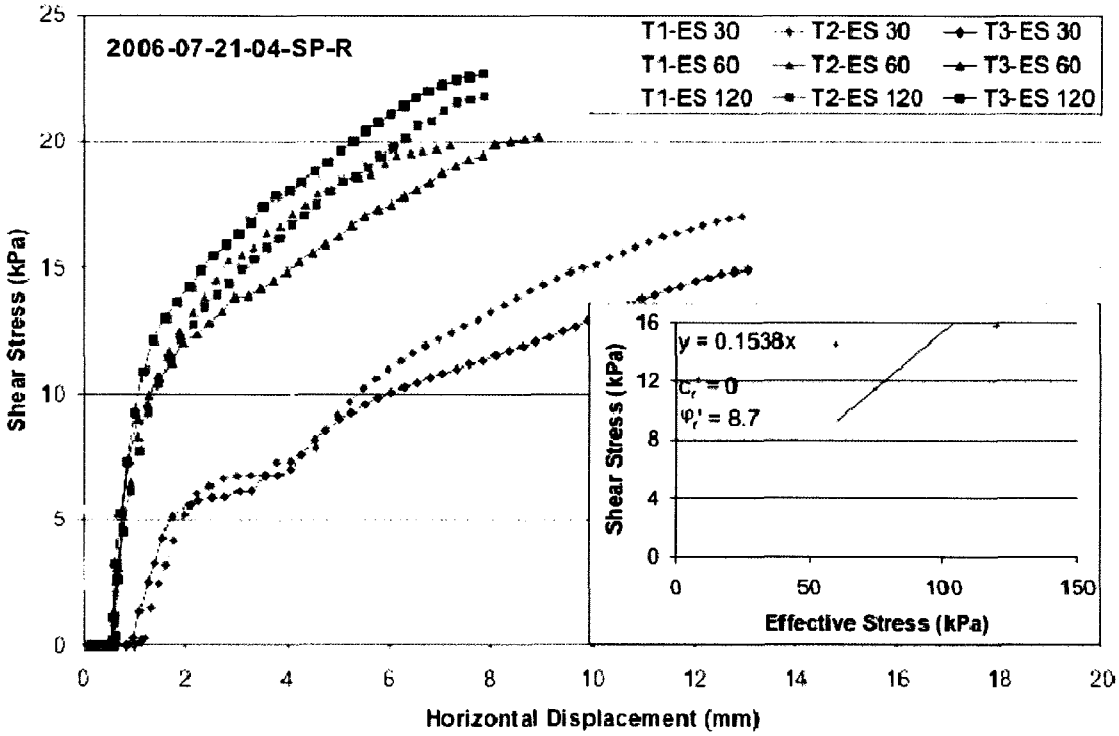

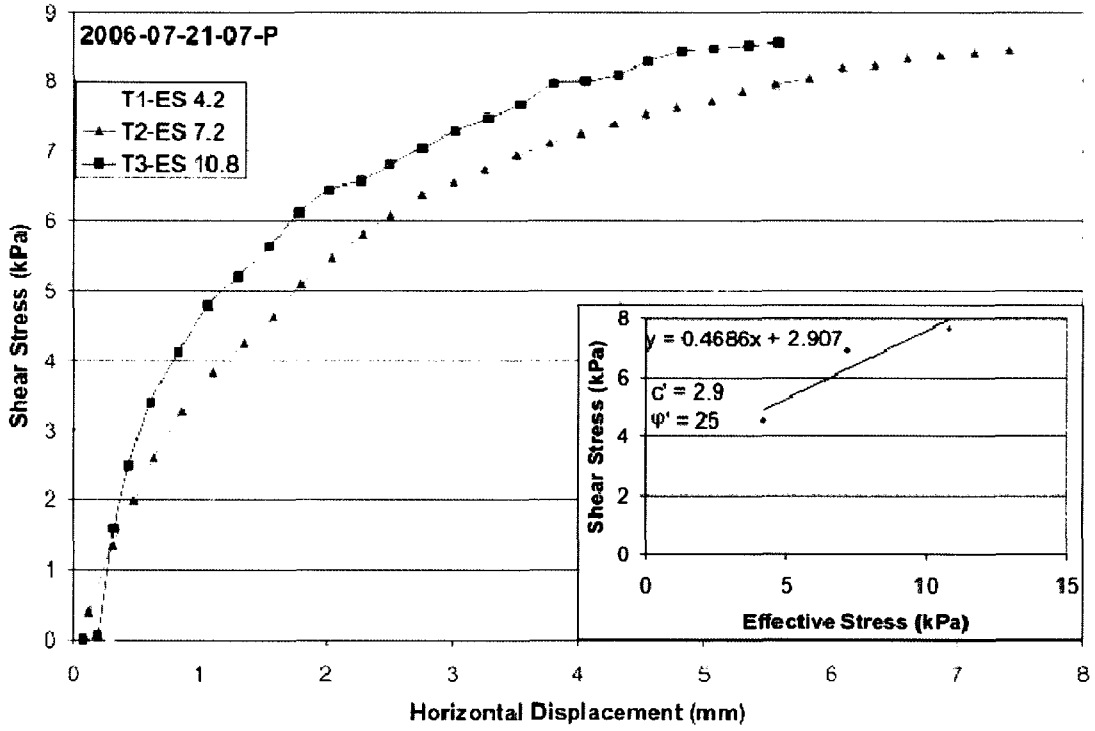

BTC-2005-13 Continued

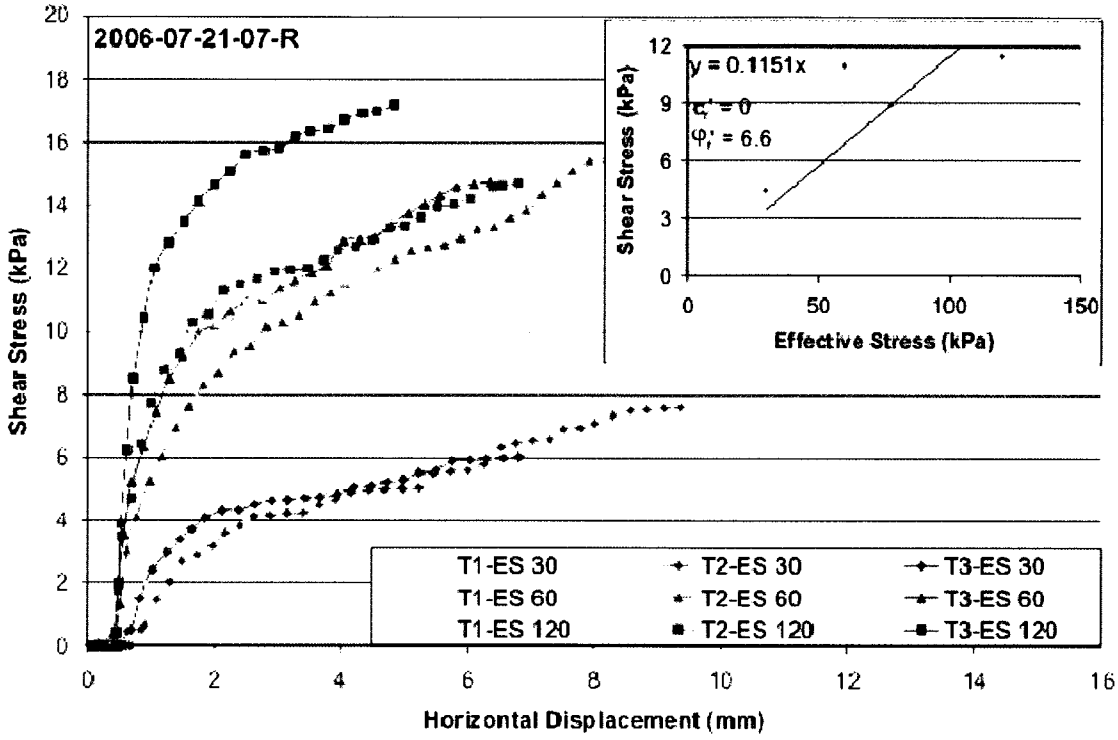

HWC-2005-01

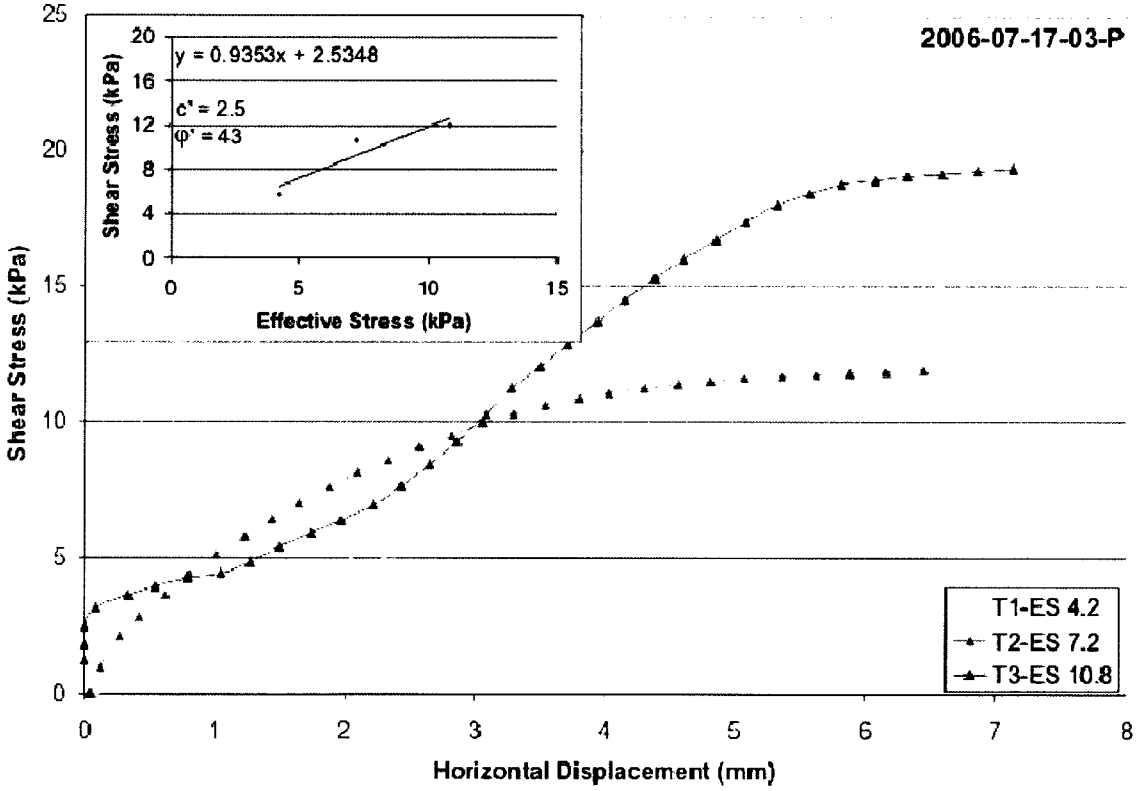

HWC-2005-01 Continued

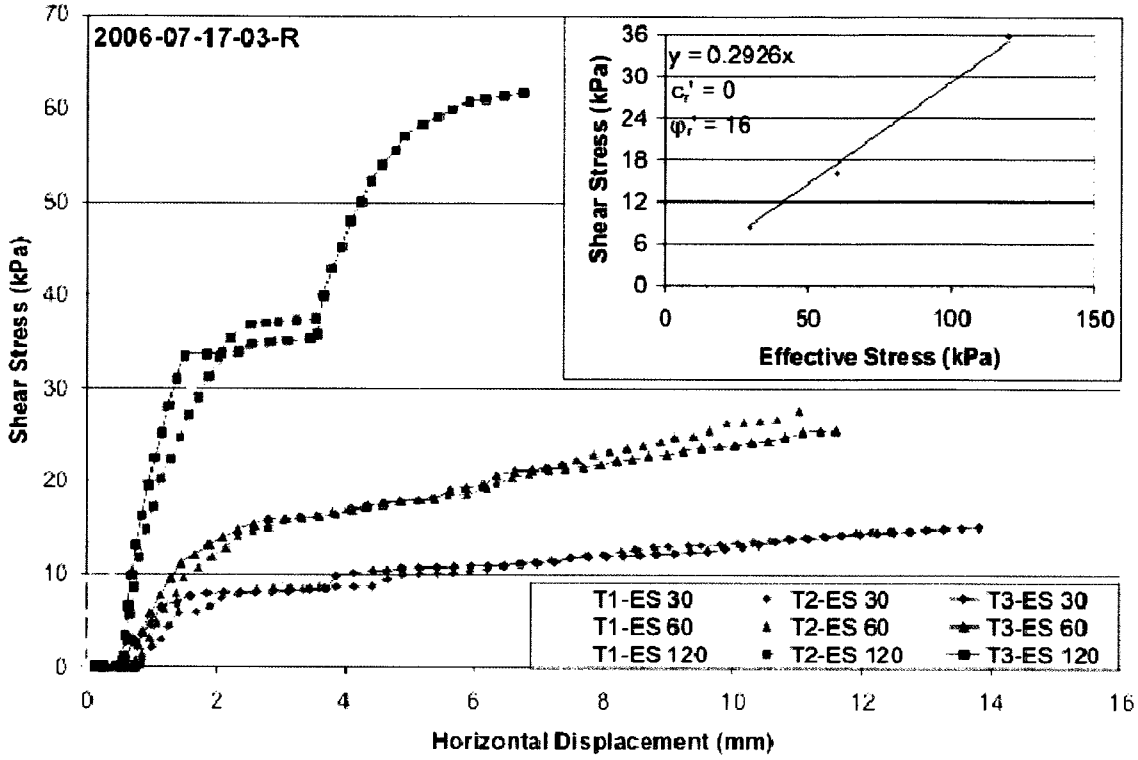

BSC-2005-01

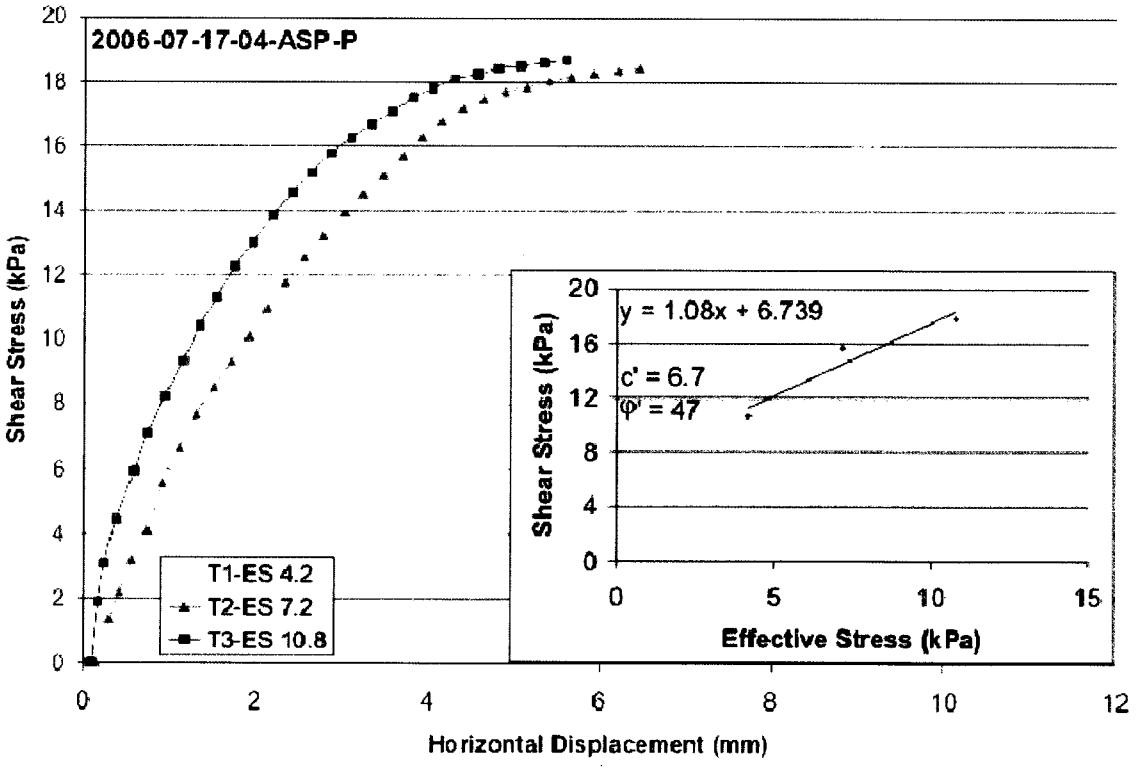

BSC-2005-01 Continued

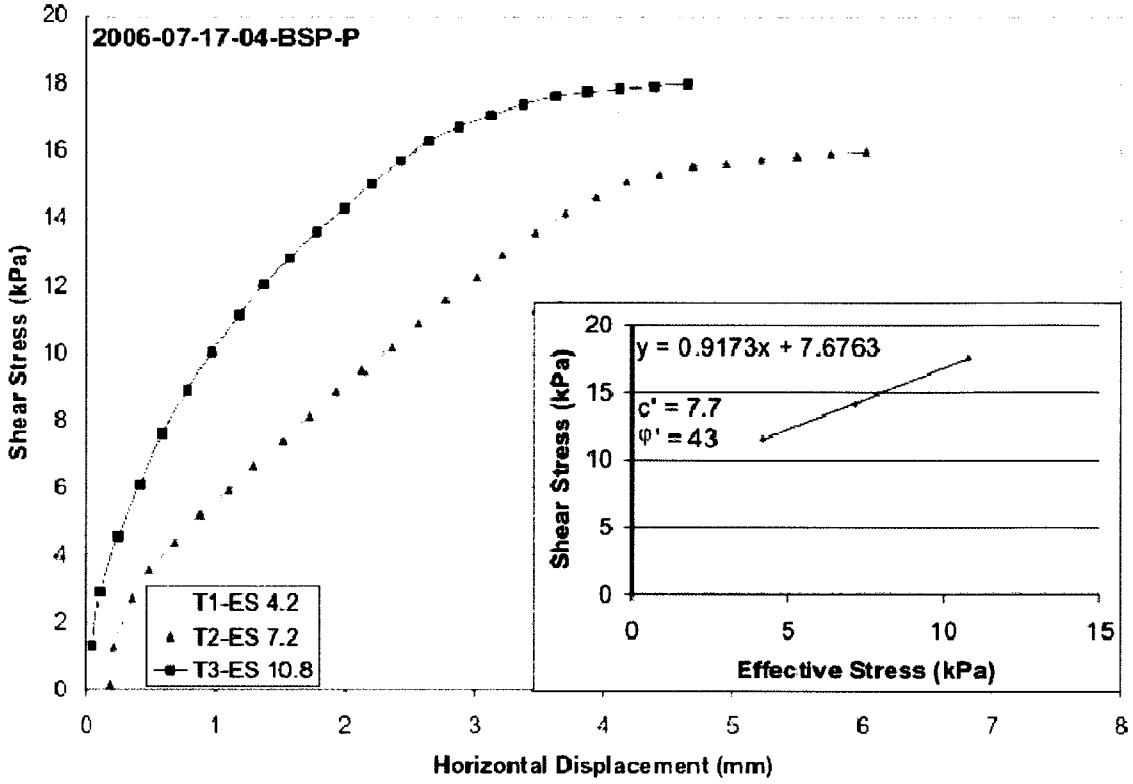

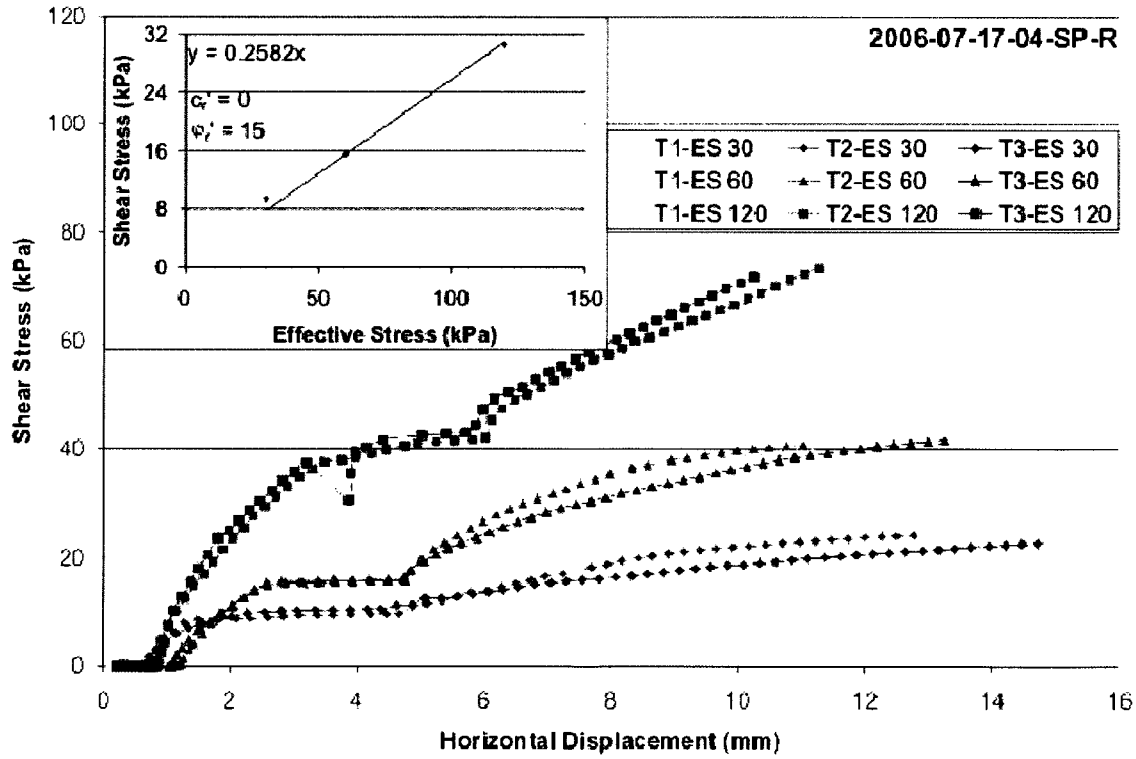

BSC-2005-01 Continued